

Composite Floating 'Point Absorbers' for Wave Energy Converters:  
Survivability Design, Production Method and Large-Scale Testing

Drijvende composiet 'point absorbers' voor golfenergie-converters:  
overlevingsontwerp, productiemethode en grootschalige experimenten

Chris Blommaert

Promotoren: prof. dr. ir. W. Van Paepegem, prof. dr. ir. J. Degrieck  
Proefschrift ingediend tot het behalen van de graad van  
Doctor in de Ingenieurswetenschappen

Vakgroep Toegepaste Materiaalwetenschappen  
Voorzitter: prof. dr. ir. J. Degrieck  
Faculteit Ingenieurswetenschappen  
Academiejaar 2009 - 2010



ISBN 978-90-8578-302-2  
NUR 978  
Wettelijk depot: D/2009/10.500/60

De auteur geeft de toelating dit doctoraatswerk voor consultatie beschikbaar te stellen en delen ervan te kopiëren uitsluitend voor persoonlijk gebruik. Elk ander gebruik valt onder de beperking van het auteursrecht, in het bijzonder met betrekking tot de verplichting uitdrukkelijk de bron te vermelden bij het aanhalen van de resultaten van dit werk.

The author gives the authorization to consult and to copy parts of this work for personal use only. Any other use is limited by the Laws of Copyright. Permission to reproduce any material contained in this work should be obtained from the author.

Copyright © C. Blommaert  
Oostende, Juni 2009



## Promotors:

Prof. dr. ir. Wim Van Paepegem  
Ghent University  
Faculty of Engineering  
Department of Materials Science and Engineering

Prof. dr. ir. Joris Degrieck  
Ghent University  
Faculty of Engineering  
Department of Materials Science and Engineering

## Examination Committee:

Prof. R. Verhoeven (Chair)	Ghent University, Belgium
Prof. W. Van Paepegem (Promotor)	Ghent University, Belgium
Prof. J. Degrieck (Promotor)	Ghent University, Belgium
Prof. J. De Rouck	Ghent University, Belgium
Prof. M. Vantorre	Ghent University, Belgium
Prof. J. Vierendeels	Ghent University, Belgium
Prof. S. Vanlanduit	Free University of Brussels, Belgium
Dr. K. C. Strømsem	Noble Denton Consultants Ltd., United Kingdom

## Research Institute:

Ghent University  
Department of Materials Science and Engineering  
Sint-Pietersnieuwstraat 41  
B-9000 Gent  
Belgium  
Tel. +32 (0)9 264 57 61  
Fax. +32 (0)9 264 35 87  
Chris.Blommaert@gmail.com



## ACKNOWLEDGEMENTS

There are a number of people who have played an important role throughout my research. Without them this work would not have been the same.

The first persons whom I would like to gratefully acknowledge are Prof. Dr. Ir. Joris Degrieck, who gave me the opportunity to do a PhD on a very interesting subject, and Prof. Dr. Ir. Wim Van Paeppegem, for his continuous support and valuable suggestions throughout the years.

A special thank you should go to Luc van den Broecke for his help with the preparation of all laboratory experiments, with the guidance of six thesis students and for the valuable input for the experiments at the '*Watersportbaan*'. Also, special thanks should go to Dr. Ir. Ives De Baere and Dr. Ir. Joost Van Slycken for their help and presence during these outdoor large scale experiments. Others that I should remember for their input for these experiments are Tom Versluys, Dr. Ir. Hans DeBacker and Sam Meurez.

Also, for the discussions about our work and several other things I would like to thank Ir. Griet De Backer as for the nice week at the '*Watersportbaan*'. I believe she is a great person to work with.

Pascal Dhondt from Spiromatic was a great colleague and the several times we discussed about Seewec or life in general I will not easily forget. Also, his work for the production of the buoys was an important input which would not have been possible without him.

Next, I would like to thank Prof. Dr. Ir. Julien De Rouck to fulfil a remarkable job as a coordinator of the European Seewec project.

Additionally, Fred Olsen Ltd. deserves all credit for the general concept of the wave energy converter and therefore I would like to thank them for including Ghent University in the European project.

Then, I should not forget to mention my former colleagues for the interesting and fun conversations about almost everything where I immediately have to think at Ir. Ebrahim Lamkanfi with his views on the world.

Also, each Thursday, during coffee break at 10 o'clock, Ir. Rudy Verhelst surprised the rest of us with very good baking skills. Next to this, I would like to thank him for

## Acknowledgements

---

several new mp3's; I think he is the only person that I have ever met who has a more general knowledge about music and is more addicted to it than me.

Also, a special thanks to Martine Botte for being there whenever a talk was needed.

In fact, I would like to thank all my former colleagues for the 4 years at Ghent University. The way the whole group stuck together was very important for me. Because of them I do not consider those years as mere 'work'.

Of course I would also like to thank my partner for being there during difficult times.

Last but not least I would like to thank my parents for the support they have given me during this Seewec project and especially to encourage me to transform this work into a doctoral thesis.

## ENGLISH SUMMARY

This dissertation is situated within the ‘Seewec’ project funded by the sixth framework program (FP6) of the European Union (EU). Seewec stands for Sustainable Economically Efficient Wave Energy Converter which means that it concerns a device for converting energy out of the sea waves. The Seewec structure is an offshore structure with floating ‘point absorbers’ also called ‘buoys’. These buoys move up and down and they are used to capture the energy from the waves.

The main objectives of this dissertation are the following:

- Establish a finite element model for a specific buoy/point absorber in composite material consisting of several layers that withstands slamming.
- Choosing an effective production method for the buoys.
- Obtain a better understanding of ‘slamming’ on composite materials by performing a literature survey, numerical methods and experiments.
- Comparison between experiments and analysis/literature.

To achieve this, research was necessary in different fields. Until present no research has been carried out to investigate the use of composite materials for point absorbers. In this dissertation Chapters 3, 4, 5, 7 and 9 contain the most relevant issues while Chapters 2, 6 and 8 contain background information. Keeping this in mind a short overview of the different Chapters is given and the main results are mentioned.

In Chapter 2 background information was given about the global energy problem, the use of wave energy converters and about the Seewec project. Today, the global energy problem receives worldwide attention. The Kyoto agreement states that by 2012 an important decrease of greenhouse gasses (GHG), like CO<sub>2</sub>, has to be accomplished. Also, further negotiations about global strategy are currently ongoing for the ‘post-Kyoto’ era. Since the supply of fossil fuels is finite, by 2050, other energy sources will have to be used. The reserves of oil are estimated to last for 40 years, the gas reserves for 60 years and coals for a bit more than 200 years. In any case, the prices will rise simultaneously with decreasing resources. This makes the European Union (EU) economically vulnerable and the development of renewable energy quite urgent. Hence, the EU also ratified the agreement of Kyoto and decided to increase its share in renewables to 12% by 2012. E.g. solar, biomass, wind and

ocean energy can all give a contribution. There should not be any conflict between those. Policy makers should search for the right application for the right purpose or location.

Today, wave energy is a small player on the energy market. However, it has a lot of potential. The European Atlantic coast wave climate is characterised by large energy. Waves can travel for thousands of kilometres with almost no loss of energy. Within the sixth framework program of the EU, the Seewec project has been launched at the end of 2005. The general concept originates from the company Fred Olsen Ltd. in 2001. This concept of the WEC looks like a traditional drill platform. However, there are two factors that differentiate it.

The first one is the presence of point absorbers in the middle of the platform. Point absorbers are defined as oscillating energy converters with horizontal dimensions smaller than the wavelength. They are there to absorb energy out of the waves. At start, the design of the point absorbers looked like buoys of about 4-6 meter height and 3-5 meter diameter. Second, where traditional drill platforms are steel constructions, this platform will be made out of light materials, such as composites and light metals. Composite materials do not corrode like metals. Also, they are a lot lighter than steel. In this way, maintenance or replacements at sea are easier to carry out. The main task of our department within this Seewec project was the survivability design of the point absorbers, their production method and large-scale testing.

For the survivability design a very critical load is 'slamming'. It is a phenomenon, known in the Marine Engineering, as the short impact of water waves on a floating or sailing structure which gives very high local peak pressures. A relevant literature study concerning 'slamming' was done and can be found in Chapter 3. The upward propelling of a structure and the fall back on the water surface, is called straight, vertical or bottom slamming. Also, breaking waves can introduce slamming. This is called lateral or breaking wave slamming. This wave impact can cause damage on the bow of a ship above the waterline. Additionally, breaking wave slamming can occur against a component of an offshore construction. These components have to be designed for impact loads coming from breaking waves. This is quite similar for the buoys within the Seewec project. Also, these buoys are suffering from bottom slamming. In normal to high waves and small penetration depth of a buoy, it is possible that the buoy goes out of the water. The slamming phenomenon was studied in the Marine Engineering on *rigid* bodies but for deformable structures almost no literature is available.

However, in recent years, composite materials are applied more often in ship constructions (catamarans and high speed crafts) and offshore structures because of their corrosion resistance, limited maintenance, long life time and sometimes even cheaper cost. Of course, cost depends on the selected composite material and its production method. Fibre Reinforced Composite (GRP) material consists of several components: fibres for strength and a matrix to bind the material. The fibres are the most important constituent because they carry most loads. They determine the stiffness of the material and limit the tear rate within the matrix. Within the Seewec project, two industrial composite producers were selected: Spiromatic with its knowledge about filament winding for silos and Standfast Yachts for their experience with the sea environment through producing yachts with vacuum infusion. Materials for the point absorbers were proposed by both firms. Plates were made with filament winding as well as with vacuum infusion in order to do a full material characterisation according to the 'American Society for Testing and Materials' (ASTM) standards. Both proposed materials contain glass fibres since cost is an important issue within a design for series production. The characterisation tests resulted in the mechanical properties of the materials which were necessary for finite element calculations. The description of the used composite material, the characterisation tests and the production methods is given in Chapter 4.

At the start of the Seewec project, Fred Olsen Ltd. delivered information to the partners. An important issue was of course the shape of the point absorbers. In the pre-Seewec period (2005), the buoys looked like scaled 'egg' shapes. Due to reasons of severe bottom slamming loads the 'tulip' shape was considered to replace the egg since this tulip shape goes more smoothly into the water. Later on, a so called 'pencil' shape was proposed and several calculations were done on it to assess bottom and breaking wave slamming. For this, In Chapter 5 first a short introduction about the use of the finite element program Abaqus is given. Also, the filament winding software Cadwind is introduced. Within the calculations on several buoys, the influence of using internal stiffeners, a foam core and the kind of material were assessed. It became clear that for survivability conditions, breaking wave slamming was more severe than bottom slamming. Finally, this has lead to the proposal of a smaller 'cone/cylinder/cone' shape which is, again according to several calculations, a suitable shape to withstand the slamming load. The proposed buoy is a sandwich buoy built up with 8 filament wound layers and a foam in between (4 layers/300 mm foam/ 4 layers).

In addition, it seemed useful to perform laboratory scale productions and tests. An existing filament winding machine was updated. Hence, several objects were made on it with glass fibres and epoxy resin. Also, a laboratory slamming set-up was

designed and built at the department. Within Chapter 6 both set-ups are described. Additionally, the proposed production method for the cone/cylinder/cone shape with filament winding is described there. It is called ‘the production method of the cones’. The results of the four test samples are given and compared with literature in Chapter 7. First, a rigid cone was made and tested since a lot of literature exists on its 2D equivalent, the wedge shape. Second, two cylinders were made, one rigid and one deformable. This was done to assess the influence of deformability on the peak pressure. Also, in cooperation with the Department of Fluid Mechanics, fluid structure interaction calculations with use of the Volume of Fluid (VOF) method in Fluent and Abaqus were initiated. There, a rigid cone of 14 degrees was calculated to compare with literature. Next, both numerical and experimental results on the cylinders showed an important decrease (factor two) in the peak pressure for the deformable cylinder in comparison with the rigid cylinder. This is an important conclusion of this Chapter. Finally, a scaled shape (1:10) of a cone/cylinder/cone point absorber was made on the winding machine to experiment with the designed ‘production method of the cones’. It was also tested on the slamming set-up.

Next, the production and testing of two large-scale buoys (about 1:2.29) has been done. The proposed sandwich buoy from Chapter 5 was produced. The second buoy was made more deformable. The more deformable buoy consisted of seven wound layers and contained no foam. The production method that was designed for series production had proven viable during the production of the laboratory scale point absorber and thus was used here as well. Also, an extensive testing program was foreseen on both samples. Fatigue, slamming and fracture tests were done. The fatigue and fracture tests were done indoor in the laboratory Magnel at Ghent University. The slamming tests were done on the ‘*Watersportbaan*’ which is a canal in Ghent. The production and instrumentation of the buoys as well as the preparation of the experiments are described in Chapter 8.

During the large scale experiments, strain gauges, displacement sensors, pressure sensors and accelerometers were measured. An extensive discussion of the comparison between experimental results and simulations of all tests is dealt with in Chapter 9. All signals are discussed and where possible compared with finite element calculations. For the slamming tests it was shown that the peak pressure was again a lot lower for the more deformable buoy (2.23 MPa instead of 3.5MPa). This was less than a factor 2 difference but it is still significant. For the fracture experiment the buoys broke near the predicted failure load value and location which is also an important finding.

## English summary

---

In Chapter 10 the main conclusions of this dissertation are given. In general, it can be concluded that the peak pressure occurring on a cone of 45 degrees is very similar to the value of the proposed constant DNV pressure. Hence, for the cone DNV seems quite conservative. However, for more flat objects such as cylinders, the occurring peak pressure is a lot higher than the constant pressure proposed by DNV. Hence, for this kind of structures the effect of local high pressures should be taken into account in the design.

English summary

---

## NEDERLANDSE SAMENVATTING

Deze doctoraatsthesis is gesitueerd in het ‘Seewec’ project in het Zesde Kaderprogramma (FP6) van de Europese Unie (EU). Seewec staat voor *Sustainable Economically Efficient Wave Energy Converter* wat betekent dat het gaat om een golfenergieconverter. Het is een offshore structuur met drijvende *point absorbers* die ook boeien worden genoemd. Deze boeien bewegen op en neer en ze dienen om de energie uit de golven op te vangen. De belangrijkste objectieven van dit doctoraat zijn de volgende:

- Een eindig elementen model opstellen voor een specifieke boei/point absorber in composiet materiaal bestaande uit verschillende lagen die bestand is tegen slamming.
- Een effectieve productiemethode voor de boeien selecteren.
- Een betere kennis verkrijgen over slamming op composiet materiaal door een literatuurstudie uit te voeren alsook numerieke methodes en experimenten.
- Vergelijking tussen experimenten en analyse/literatuur.

Om dit te bereiken was er onderzoek nodig in verschillende domeinen. Tot op heden werd er nog geen onderzoek verricht naar het gebruik van composiet materiaal voor *point absorbers*. Hoofdstukken 3, 4, 5, 7 en 9 bevatten de relevante informatie terwijl Hoofdstuk 2, 6 en 8 eerder achtergrondinformatie bevatten.

In Hoofdstuk 2 wordt informatie over het globale energieprobleem, het gebruik van golfenergieconverters en het Seewec project besproken. De energieproblematiek is een actueel probleem. Het verdrag van Kyoto stelt dat de uitstoot van broeikasgassen, zoals CO<sub>2</sub>, drastisch moet dalen tegen 2012. Ook zijn er op dit ogenblik verdere onderhandelingen over de globale strategie voor het post-Kyoto era. Daar fossiele brandstoffen eindig zijn, moet er worden gezocht naar andere bronnen. De oliereserves worden geschat op 40 jaar, die van gas op 60 jaar en die van kolen op iets meer dan 200 jaar. De prijzen zullen blijven stijgen naarmate de voorraden slinken. Dit maakt de Europese Unie (EU) economisch kwetsbaar en de ontwikkeling van hernieuwbare energie zeer dringend. Bijgevolg heeft de EU ook het verdrag van Kyoto geratificeerd en zo beslist om haar aandeel in hernieuwbare energie tot 12 % te verhogen tegen 2012. Hierbij kunnen onder andere zon, wind, biomassa en water een kleine bijdrage leveren. Er moet natuurlijk geen conflict

tussen al deze bronnen zijn. Beleidsmakers moeten erop toe zien dat de juiste toepassing gebruikt wordt waar nodig. Golfenergie is op dit ogenblik een kleine speler op de energiemarkt, maar het heeft wel veel potentieel. Het golfklimaat van de Europese Atlantische kust is gekarakteriseerd door grote hoeveelheden energie. Bovendien kunnen golven zich voortplanten over duizenden kilometers met bijna geen energieverlies. In het Zesde Kaderprogramma van de EU werd het Seewec project gelanceerd eind 2005. Het algemene concept komt van het bedrijf Fred Olsen Ltd. en is ontstaan in 2001. Het concept lijkt op een traditioneel boorplatform, maar het bevat twee verschillende aspecten.

Het eerste verschil is de aanwezigheid van '*point absorbers*' in het midden van de structuur. Point absorbers worden gedefinieerd als oscillerende energieconvertoren waarvan de horizontale dimensies duidelijk kleiner zijn dan de golflengte. Deze dienen om energie uit de golven op te nemen. In het begin van het project werd vooropgesteld om ze te voorzien van typische afmetingen van 4-6 meter hoogte en 3-5 meter diameter. Ten tweede, waar traditionele boorplatforms gemaakt worden uit staal, zou dit platform uit lichte materialen gemaakt worden zoals composieten en lichte metalen. Composieten corroderen niet zoals metalen. Ook zijn ze veel lichter dan staal. Op deze manier is onderhoud op zee (of vervangingen) gemakkelijker uit te voeren. De belangrijkste taak van onze vakgroep binnen het Seewec project was het overlevingsontwerp van de '*point absorbers*', hun productie methode en grootschalige testen.

Voor het overlevingsaspect is '*slamming*' een zeer kritieke conditie. Het is een gekend fenomeen in de scheepvaart en het wordt gedefinieerd als de korte golfimpact op een drijvende of zeilende structuur met hoge lokale piekdrukken tot gevolg. In deze doctoraatsthesis werd een relevante literatuurstudie rond slamming uitgevoerd en dit is terug te vinden in Hoofdstuk 3. Het opwaarts bewegen van een structuur en het terugvallen op het wateroppervlak wordt '*bottom slamming*' of 'neerwaartse slamming' genoemd. Het fenomeen werd al uitgebreid onderzocht in het studiegebied van de scheepvaart. Neerwaartse slamming treedt op door de verschillende bewegingen van een schip op zee. Echter, ook brekende golven kunnen slamming introduceren. Dit wordt '*breaking wave slamming*' of 'zijdelingse slamming' genoemd. Het kan schade veroorzaken aan de boeg van een schip net boven the waterlijn. Zijdelingse slamming kan natuurlijk ook optreden tegen componenten van een *offshore* constructie die bijgevolg ontworpen moeten worden voor dergelijk krachten. Dit alles is zeer gelijklopend met de boeien in het Seewec project. Naast zijdelingse slamming zijn die boeien ook onderhevig aan verticale slamming. In normale tot hoge golven en bij een kleine penetratiediepte is het mogelijk dat de boeien uit het water komen. Zoals gezegd is het

slammingsfenomeen uitvoerig bestudeerd voor *starre* lichamen, maar dit blijft beperkt voor vervormbare constructies. Echter, in de laatste jaren worden composieten steeds meer gebruikt bij het produceren van schepen (o.a. voor catamarans en hoge snelheidsboten) en bij *offshore* structuren door hun corrosiebestendigheid, beperkt onderhoud, lange levensduur en soms zelfs goedkopere kost. Natuurlijk hangt die kost af van het geselecteerde composiet en van de productie methode. Composiet materiaal bestaat uit verschillende componenten: vezels voor sterkte en een matrix om het materiaal te binden. De vezels zijn het belangrijkste onderdeel omdat zij de grootste krachten dragen. Ze bepalen de stijfheid van het materiaal en beperken de mate van scheuren in de matrix. In het Seewec project werden twee industriële producenten van composieten gekozen als partners: Spiromatic met haar kennis over wikkelen van silos en Standfast Yachts met hun ervaring met de zee-omgeving door jachten te maken met vacuüm infusie. Beide bedrijven selecteerden een geschikt composietmateriaal voor de '*point absorbers*' met hun respectievelijke productie methode. Bovendien werden er testplaten gemaakt om een volledige materiaalkarakterisatie te kunnen uitvoeren volgens de '*American Society for Testing and Materials*' (ASTM) standaard. Zowel SMC als STY stelden glasvezel voor doordat lage kost een belangrijke ontwerprichting is. De karakterisatie testen resulteren in de materiaaleigenschappen nodig voor de berekeningen in het eindig elementen programma Abaqus. De beschrijving van het gebruikte composietmateriaal, de karakterisatie testen en de productie methoden gebeurt in Hoofdstuk 4.

Het Seewec project werd ingeleid door een informatieoverdracht door Fred Olsen Ltd. aan de andere partners, zoals ondermeer ook Universiteit Gent. Een belangrijk punt was de vorm van de '*point absorbers*'. In de pre-Seewec periode (2005) hadden de boeien de vorm van een ei. Na de ei-vorm werd snel overgegaan op een tulpvorm omwille van de meer geleidelijke intrede in het wateroppervlak bij deze vorm. Daarna werd de potlood-vorm voorgesteld waarbij verschillende berekeningen uitgevoerd werden om zowel neerwaartse als zijdelingse slamming te beoordelen. In Hoofdstuk 5 werd hiervoor een korte introductie van het eindig elementen programma Abaqus gegeven alsook van de wikkel software Cadwind. In deze berekeningen werd de invloed van interne verstijvers, een schuimkern en het gebruikte materiaal bekeken. Ook werd het duidelijk dat zijdelingse slamming kritischer was dan neerwaartse slamming bij overlevingscondities. Uiteindelijk heeft dit tot een kleinere '*conus/cilinder/conus*' vorm geleid welke een geschikte vorm bleek om aan de voorgestelde slamming overlevingsconditie te weerstaan. De voorgestelde boei is een sandwich boei opgebouwd uit 8 gewikkelde lagen en een schuim in het midden (4 lagen/300 mm schuim/4 lagen).

Naast dit alles, werden ook testen op laboschaal voorbereid. Eerst werd hiervoor een kleine bestaande wikkelmachine geoptimaliseerd. Verschillende objecten werden hierop geproduceerd met glasvezels en epoxy hars. Bovendien werd een slammingsopstelling ontworpen en gebouwd. In Hoofdstuk 6 worden beide opstellingen beschreven. Bovendien wordt de ‘methode van de conussen’ als productiemethode voor de conus/cilinder/conus toegelicht. De resultaten van de valtesten en de vergelijking met de literatuur zijn beschreven in Hoofdstuk 7. Het eerste gekozen object was een starre conus omdat in de literatuur informatie te vinden is over zijn 2D equivalent, namelijk een wig. Daarna werden er twee cilinders geproduceerd, een starre en een vervormbare om de invloed van de vervormbaarheid op de piekdruk na te gaan. Daarnaast werden in samenwerking met de vakgroep Mechanica van Stroming, Warmte en Verbranding, vloeistof-structuur interactieberekeningen met gebruik van de Volume Of Fluid (VOF) methode in Fluent en Abaqus opgestart. Eerst werd een simulatie van een starre conus 14 graden uitgevoerd om te vergelijken met de literatuur. Voor de cilinders toonden zowel de numerieke als experimentele resultaten een belangrijke daling (factor 2) in de piekdruk voor de vervormbare cilinder. Dit is een belangrijke conclusie van dit hoofdstuk. Het vierde en laatste object was een labo-versie (schaal 1:10) van de conus-cilinder-conus vorm. Het werd gemaakt op de wikkelmachine met de ‘methode van de conussen’.

Ook op grote schaal (ongeveer 1:2.29) werden twee boeien gemaakt met het wikkelp proces in SMC. De eerste boei was opgebouwd zoals deze voorgesteld in Hoofdstuk 5. De tweede was opgebouwd uit zeven gewikkelde lagen zonder schuim wat een meer vervormbare boei tot gevolg heeft. De gebruikte productie methode met de twee conussen, die met succes gebruikt werd op labo-schaal, werd hier opnieuw toegepast. Een uitgebreid testprogramma op deze boeien werd voorbereid. Vermoeiing, slamming en breuktesten kwamen aan bod. De vermoeiing en breuktesten werden uitgevoerd in het Magnel laboratorium aan de Universiteit Gent. De slamming testen (valtesten) werden uitgevoerd op de Watersportbaan in Gent. De productie en de instrumentatie van boeien en de voorbereiding van de experimenten zijn beschreven in Hoofdstuk 8. Tijdens deze testen werden rekstrookjes, verplaatsingsmeters, druksensoren en accelerometers opgemeten en waar mogelijk vergeleken met eindige elementen berekeningen. Een uitgebreide discussie van alle experimentele resultaten en simulaties is beschreven in Hoofdstuk 9. De resultaten van de valtesten toonden onder andere dat de piekdruk opnieuw lager was voor de meer vervormbare boei (2.23 MPa in plaats van 3.5 MPa). Tijdens de breukexperimenten zijn beide boeien gebroken dichtbij de voorspelde kracht en lokatie.

## Dutch summary

---

In Hoofdstuk 10 worden de belangrijkste conclusies van deze doctoraatsthesis gegeven. In het algemeen kan besloten worden dat de optredende piekdruk op een conus van 45 graden zeer gelijkend is aan de waarde van de voorgestelde constante DNV druk. Op die manier kan gesteld worden dat DNV conservatief is voor dit object. Echter, bij vlakkere objecten zoals cilinders is de optredende piekdruk een stuk hoger dan de constante druk voorgesteld door DNV. Bijgevolg moet bij het ontwerp van dergelijke structuren rekening gehouden worden met het effect van hoge lokale piekdrukken.

Dutch summary

---

## TABLE OF CONTENTS

CHAPTER 1 INTRODUCTION .....	1
1. 1. BACKGROUND AND OBJECTIVES .....	1
1. 2. OVERVIEW .....	3
1. 3. INNOVATIVE ASPECTS .....	5
1. 4. INDUSTRIAL RELEVANCE .....	5
1. 5. REFERENCES .....	6
CHAPTER 2 THE SEEWEC PROJECT .....	7
2. 1. THE ENVIRONMENTAL POLICY OF THE EU .....	7
2. 2. ELABORATION ON EXISTING WAVE ENERGY PROJECTS .....	10
2. 2. 1. Oscillating water columns .....	10
2. 2. 2. Overtopping Systems .....	11
2. 2. 3. Converters with moving bodies .....	12
2. 3. THE SEEWEC PROJECT .....	17
2. 3. 1. General introduction .....	17
2. 3. 2. Aim of the EU Seewec project .....	21
2. 3. 3. Workpackage four (WP4) .....	22
2. 4. REFERENCES .....	26
CHAPTER 3 DESIGN CRITERIA AND THE SLAMMING PHENOMENON .....	29
3. 1. CHOICE OF DESIGN CRITERIA FOR POINT ABSORBERS .....	29
3. 1. 1. Introduction .....	29
3. 1. 2. Hydrostatic load .....	30
3. 1. 3. Bottom slamming and breaking wave slamming .....	30
3. 2. SLAMMING .....	33
3. 2. 1. Introduction .....	33
3. 2. 2. Velocity: drop velocity or wave celerity .....	36
3. 2. 3. Literature survey .....	37
3. 3. PRESSURE ESTIMATIONS FOR THE FEA ON THE BUOYS .....	48
3. 3. 1. Bottom slamming .....	48
3. 3. 2. Breaking wave slamming .....	50
3. 4. REFERENCES .....	51

Table of contents

---

<b>CHAPTER 4 MATERIAL SELECTION AND BASIC MECHANICAL CHARACTERISATION.....</b>	<b>53</b>
4. 1. COMPOSITE MATERIALS .....	53
4. 2. FILAMENT WINDING .....	55
4. 2. 1. Introduction.....	55
4. 2. 2. Winding patterns.....	56
4. 2. 3. Applications .....	57
4. 3. VACUUM INFUSION.....	59
4. 3. 1. Introduction.....	59
4. 3. 2. Applications .....	60
4. 4. SELECTION OF MATERIALS FOR THE POINT ABSORBERS .....	61
4. 4. 1. Certified materials.....	61
4. 4. 2. Material proposal by SMC.....	61
4. 4. 3. Material proposal by STY.....	62
4. 4. 4. Use of sandwich materials .....	63
4. 5. PREPARATION OF TEST SAMPLES WITH FILAMENT WINDING .....	64
4. 6. TESTS ACCORDING TO ASTM STANDARDS FOR SMC.....	66
4. 6. 1. Stiffness and strength.....	66
4. 6. 2. Characterisation of fibre fraction .....	71
4. 7. PREPARATION OF TEST SAMPLES WITH VACUUM INFUSION.....	73
4. 8. TESTS ACCORDING TO ASTM STANDARDS FOR STY.....	74
4. 9. REFERENCES.....	76
<b>CHAPTER 5 SELECTING SUITABLE LAMINATE LAY-UP WITH FINITE ELEMENT ANALYSIS .....</b>	<b>79</b>
5. 1. INITIAL SHAPES OF THE POINT ABSORBERS .....	79
5. 1. 1. Introduction.....	79
5. 1. 2. Pencil .....	80
5. 2. FINITE ELEMENT SOFTWARE .....	81
5. 2. 1. Introduction.....	81
5. 2. 2. Composite failure criterion .....	82
5. 3. DESCRIPTION OF CADWIND.....	84
5. 3. 1. Introduction.....	84
5. 3. 2. From Cadwind to Abaqus (and other programs for FEA).....	84
5. 4. FEA CALCULATIONS ON PENCIL SHAPE .....	92
5. 4. 1. Introduction.....	92
5. 4. 2. Results for the pencil shape .....	94
5. 5. CONE-CYLINDER-CONE .....	104
5. 5. 1. Introduction.....	104

Table of contents

---

5. 5. 2. Breaking wave slamming: assessing the influence of stiffeners .....	105
5. 5. 3. Breaking wave slamming: assessing the use of foam .....	108
5. 5. 4. Breaking wave slamming: assessing the use of material and production method .....	110
5. 5. 5. Bottom slamming.....	112
5. 6. REFERENCES.....	114

**CHAPTER 6 FILAMENT WINDING MACHINE AND SLAMMING SET-UP AT LABORATORY SCALE..... 115**

6. 1. FILAMENT WINDING SET-UP IN THE LABORATORY .....	115
6. 1. 1. Introduction.....	115
6. 1. 2. The bobbin holders .....	116
6. 1. 3. The pre-tension mechanism .....	117
6. 1. 4. The Resin Bath.....	118
6. 1. 5. The winding robot.....	119
6. 1. 6. Control: Labview and Cadwind .....	120
6. 2. FIRST TRIAL PRODUCTION: CYLINDERS FOR EXTERNAL REINFORCEMENT OF CONCRETE.....	125
6. 2. 1. Introduction.....	125
6. 2. 2. Properties of the cylinders at laboratory scale .....	125
6. 2. 3. The mandrel .....	126
6. 2. 4. The winding patterns for the cylinders.....	127
6. 3. LABORATORY SCALE PRODUCTION OF A POINT ABSORBER.....	131
6. 3. 1. Introduction.....	131
6. 3. 2. The mandrel .....	131
6. 3. 3. Method of the cones.....	132
6. 3. 4. Possible improvement.....	137
6. 4. LABORATORY SLAMMING SET-UP.....	139
6. 4. 1. Introduction.....	139
6. 4. 2. Realisation of the set-up.....	140
6. 4. 3. Ladder .....	140
6. 4. 4. Shaft.....	141
6. 4. 5. Connection between shaft and ladder .....	141
6. 4. 6. Bearings .....	141
6. 4. 7. Support.....	142
6. 4. 8. Water container and well .....	143
6. 4. 9. Floater system .....	146
6. 4. 10. Motor, control and torque moment .....	147
6. 5. REFERENCES .....	151

---

<b>CHAPTER 7 LABORATORY SCALE TEST SAMPLES: PRODUCTION, EXPERIMENTS AND VALIDATION .....</b>	<b>153</b>
7. 1. TEST SAMPLES FOR LABORATORY SLAMMING .....	153
7. 1. 1. Introduction.....	153
7. 1. 2. Instrumentation .....	153
7. 2. TEST CASE ‘CONE’ .....	155
7. 2. 1. Introduction.....	155
7. 2. 2. Production.....	155
7. 2. 3. Instrumentation .....	156
7. 2. 4. Test set-up.....	159
7. 2. 5. Results and validation .....	160
7. 3. TEST CASE ‘FULL AND HOLLOW CYLINDER’ .....	163
7. 3. 1. Introduction.....	163
7. 3. 2. Production of the full cylinder .....	163
7. 3. 3. Instrumentation of the full cylinder .....	165
7. 3. 4. Test set-up full cylinder .....	165
7. 3. 5. Full cylinder: results and validation.....	166
7. 3. 6. Production and instrumentation of the hollow cylinder .....	170
7. 3. 7. Test set-up hollow cylinder.....	174
7. 3. 8. Hollow cylinder: results and validation .....	174
7. 4. TEST CASE ‘POINT ABSORBER’ .....	177
7. 4. 1. Introduction.....	177
7. 4. 2. Production and instrumentation of the laboratory scale point absorber .....	177
7. 4. 3. Test set-up.....	178
7. 4. 4. Laboratory scale ‘point absorber’: results and validation .....	179
7. 5. COMPUTATIONAL FLUID DYNAMICS (CFD) .....	181
7. 5. 1. Introduction.....	181
7. 5. 2. Volume of Fluid.....	181
7. 5. 3. Cone simulation versus literature.....	183
7. 5. 4. Rigid cylinder simulation versus experiments .....	185
7. 5. 5. Coupled hollow cylinder simulation versus experiments.....	186
7. 6. REFERENCES.....	191
 <b>CHAPTER 8 PRODUCTION OF LARGE SCALE BUOYS .....</b>	 <b>193</b>
8. 1. DISCUSSION OF A REPRESENTATIVE DEMONSTRATOR.....	193
8. 1. 1. Buoy.....	193
8. 1. 2. Filament winding method and scaling .....	194
8. 1. 3. Choice of Second buoy .....	195

Table of contents

---

8. 2. TESTING PROGRAM.....	199
8. 2. 1. Fatigue test.....	199
8. 2. 2. Drop test.....	199
8. 2. 3. Fracture test.....	201
8. 3. DISCUSSION OF THE PRODUCTION PROCESS .....	202
8. 3. 1. Introduction.....	202
8. 3. 2. Blow up mandrels .....	202
8. 3. 3. Method of the cones.....	202
8. 4. PREPARATION OF TESTING PROGRAM .....	203
8. 4. 1. Introduction.....	203
8. 4. 2. Steel support tube.....	206
8. 4. 3. Supports .....	208
8. 4. 4. Shell with rubber.....	212
8. 4. 5. Flanges.....	215
8. 5. PRODUCTION OF THE BULDRA-SCALE BUOYS .....	217
8. 5. 1. Introduction.....	217
8. 5. 2. Spray-up cones.....	217
8. 5. 3. Inner composite tubes .....	219
8. 5. 4. First winding phase.....	219
8. 5. 5. Foam .....	220
8. 5. 6. Second winding phase.....	221
8. 5. 7. Coating and markers for the high speed camera .....	222
8. 5. 8. Feedback of production towards FEA.....	222
8. 6. INSTRUMENTATION OF THE LARGE SCALE BUOYS .....	224
8. 6. 1. Introduction.....	224
8. 6. 2. LVDT sensors .....	224
8. 6. 3. Strain gauges.....	225
8. 6. 4. Pressure sensors .....	228
8. 6. 5. Accelerometers .....	230
8. 6. 6. HSC.....	231
8. 7. REFERENCES .....	232
<b>CHAPTER 9 LARGE SCALE BUOYS: EXPERIMENTS .....</b>	<b>233</b>
9. 1. FATIGUE.....	233
9. 1. 1. Introduction.....	233
9. 1. 2. Load .....	234
9. 1. 3. Strain Gauges.....	235
9. 1. 4. LVDT sensors .....	251
9. 2. DROP TESTS FOR LATERAL SLAMMING .....	256

Table of contents

---

9. 2. 1. Introduction.....	256
9. 2. 2. Accelerometers .....	261
9. 2. 3. High Speed Camera .....	264
9. 2. 4. Pressure Sensors .....	265
9. 2. 5. Strain Gauges.....	269
9. 3. DROP TESTS BOTTOM SLAMMING.....	272
9. 4. FRACTURE .....	273
9. 4. 1. Introduction.....	273
9. 4. 2. Load .....	273
9. 4. 3. Strain Gauges.....	276
9. 4. 4. LVDT sensors .....	294
9. 5. REFERENCES.....	298
CHAPTER 10 CONCLUSIONS AND FUTURE RESEARCH.....	301
10. 1. CONCLUSIONS .....	301
10. 2. FUTURE RESEARCH.....	305
PRESSURE TIME HISTORIES OF THE LABORATORY TESTS.....	307
LIST OF PUBLICATIONS.....	315

## LIST OF SYMBOLS AND ABBREVIATIONS

BWF	Buoy With Foam
BWOF	Buoy Without Foam
$c$	Celerity (m/s)
$C_p$	Dimensionless pressure coefficient (-)
$C_{pa}$	Space average slamming pressure coefficient (-)
DNV	Det Norske Veritas
$E_{11,C}$	Compressive modulus of elasticity in the fibre direction (Pa)
$E_{11,T}$	Tensile modulus of elasticity in the fibre direction (Pa)
$E_{22,C}$	Compressive modulus of elasticity in the direction perpendicular to the fibres (Pa)
$E_{22,T}$	Tensile modulus of elasticity in the direction perpendicular to the fibres (Pa)
$G_{12}$	Shear modulus (Pa)
$H_b$	The most probable largest breaking wave height in n years; equal to 1.4 $H_s$ (m)
$H_s$	Significant wave height (m)
$L_b$	Wave length just before breaking; equal to 7 $H_b$ (m)
ML0	Magnel longitudinal strain gauge on the zero degrees meridian of the buoy
ML20	Magnel longitudinal strain gauge on the 20 degrees meridian of the buoy
MD0	Magnel perpendicular strain gauge on the zero degrees meridian of the buoy
MD20	Magnel perpendicular strain gauge on the 20 degrees meridian of the buoy
$p_s$	Space average slamming pressure (Pa)
S	Shear strength (Pa)
$T_z$	Peak period (s)
V	Relative normal velocity between water and member; also U or v (m/s)
WL0	‘Watersportbaan’, longitudinal strain gauge on the zero degrees meridian of the buoy

List of most used symbols and abbreviations

---

WL20	‘Watersportbaan’, longitudinal strain gauge on the 20 degrees meridian of the buoy
WD0	‘Watersportbaan’, perpendicular strain gauge on the zero degrees meridian of the buoy
WD20	‘Watersportbaan’, perpendicular strain gauge on the 20 degrees meridian of the buoy
$X_C$	Compressive strength in the fibre direction (Pa)
$X_T$	Tensile strength in the fibre direction (Pa)
$Y_C$	Compressive strength in the direction perpendicular to the fibre direction (Pa)
$Y_T$	Tensile strength in the direction perpendicular to the fibre direction (Pa)
$\beta$	Deadrise angle (degrees)
$\tau_{ILSS}$	Interlaminar shear strength (Pa)
$\nu_{12}$	Poisson’s ratio, which is the ratio of the strain in the transverse direction of the fibres (2) to the strain in the fibre direction (1), when loaded in the fibre direction (-)
$\nu_{21}$	Poisson’s ratio, which is the ratio of the strain in the fibre direction (1) to the strain in the transverse direction of the fibres (2), when loaded in the transverse direction of the fibres (-)

# Chapter 1

## INTRODUCTION

*In this chapter, the background of this doctoral thesis is given. It shows that there was need for gaining new knowledge. The main objectives of this dissertation are discussed as well as its innovative aspects and its industrial relevance. Also, an overview of the following chapters is given.*

### 1. 1. BACKGROUND AND OBJECTIVES

This dissertation is situated within the ‘Seewec’ project funded by the sixth framework program (FP6) of the European Union (EU). Seewec stands for Sustainable Economically Efficient Wave Energy Converter which means that it concerns a device for converting energy out of the sea waves. The Seewec structure is an offshore structure with floating ‘point absorbers’ also called ‘buoys’. A picture of a test platform (about scale 1:3) at sea is already given in Figure 1-1 to fix thoughts [1-3].



**Figure 1-1** Seewec test platform at sea, called ‘Buldra’ [2].

In this picture five of these point absorbers are present. In operational conditions the buoys move up and down, each along their own rod. The task of the ‘Mechanics of Materials and Structures’ research group at Ghent University within the project mainly concerns these buoys. At the start of the project it was proposed to design them in composite material because this material has some important advantages over steel in a sea environment. In comparison with steel, composites are corrosion resistant and they are a lot lighter for a given strength and stiffness. In this way, maintenance or replacements at sea are easier to carry out [3].

Structures at sea suffer from heavy loads. Within the project it became clear that the ‘slamming’ loads on the buoys are the most severe ones. Slamming is a phenomenon, known in the Marine Engineering, as the short impact of water waves on a floating or sailing structure. This phenomenon has already been studied extensively for wedges which shape resembles the bottom of ships [4]. However, most existing studies concern rigid structures and not deformable ones. This means that there is a need for additional knowledge about the slamming behaviour of deformable structures. Also, other shapes were only scarcely researched at the start of the Seewec project.

The main objectives of this dissertation are the following:

- Establish a finite element model for a specific buoy/point absorber in composite material consisting of several layers that withstands slamming.
- Choosing an effective production method for the buoys.
- Obtain a better understanding of ‘slamming’ on composite materials by performing a literature survey, numerical methods and experiments.
- Comparison between experiments and analysis/literature.

To achieve this, a lot of work has been done concerning production, experiments and modelling. An overview of the main contribution of this dissertation is given in paragraph 1.2 while the innovative aspects can be found in paragraph 1.3.

Test plates of selected composites were made on the filament winding machine of an industrial partner, Spiromatic, in the Seewec project. These plates were used to produce test samples for performing material characterisation tests. Then, the results were used in the numerical models. Several shapes (including internal stiffeners, foam, and other material) were calculated in a finite element program. For establishing these models special attention was needed concerning the fibre orientation, and hence the material properties.

A present laboratory scale filament winding machine was updated and an original slamming set-up was built. Several test samples were produced: a cone, two cylinders and a small buoy. All but the cone were produced on the laboratory scale filament winding machine. On these objects laboratory scale slamming tests were performed on the built set-up. In cooperation with the Department of Fluid

Mechanics at Ghent University coupled simulations with the Volume Of Fluid method (VOF) were performed on the cone and the cylinder.

Finally two large buoys were made in the partner company Spiromatic based on the results of the FEA model. These buoys were instrumented with strain gauges, pressure sensors, an accelerometer, a high speed camera and LVDT sensors. Large scale tests were performed on these buoys: fatigue, slamming and fracture tests.

Considering the work done as explained above, an overview of each chapter in this dissertation is given in the following paragraph.



**Figure 1-2 Slamming phenomenon: ship falls down after wave [5].**

## 1. 2. OVERVIEW

Until present no research has been carried out to investigate the use of composite materials for point absorbers. The most important contributions in this dissertation are the literature survey (Chapter 3), material selection and production (Chapter 4), finite element analysis (Chapter 5), laboratory scale testing (Chapter 7), and large scale tests (Chapter 9). The other chapters contain background information concerning the global energy problem and wave energy in particular (Chapter 2), equipment for filament winding (Chapter 6) and the production and instrumentation of large-scale buoys (Chapter 8).

In Chapter 2 the global energy problem and the policy of the EU concerning this matter are discussed. It seems that the fact that some energy resources are finite (fossil fuels) leads to the increasing use of renewables such as wind, hydro, solar and biomass resources. Also, the discussion whether or not to use nuclear energy

increases. The Seewec project, which concerns wave energy conversion, is explained in this chapter. One of the workpackages within the project, which has led to this thesis, is treated in more detail. Wave energy could be an important energy resource. However, the sea environment still is quite unpredictable and rough. Due to slamming, structures at sea must be able to withstand severe load conditions. More information about this slamming phenomenon and a literature study are given in Chapter 3. Next, in Chapter 4 material issues are dealt with. First, the family of composite materials is discussed. Second, within that family, materials are selected for use on the 'point absorbers'. Next, two possible production methods for those buoys, filament winding and vacuum infusion, are explained. Finally, the standard mechanical characterisation experiments and results, achieved according to the 'American Society for Testing and Materials' (ASTM) norm, are described. These test results are used as input for the material properties in the finite element models. A finite element analysis (FEA) in Abaqus on the point absorbers is discussed in Chapter 5. First, the FEA software program is described. Second, the geometrical filament winding code Cadwind is introduced. The results from a selection of the FEA calculations are given. Hereby, the previously selected materials and production methods are used to design a buoy which withstands slamming. Several shapes were calculated during the project. Also, the use of internal stiffeners is assessed as well as the use of a sandwich material. Finally, this chapter results in a proposal of a buoy that is fit for purpose. It seemed necessary to gain experience about the behaviour of composites under slamming loads. Hence, it was decided to update the existing laboratory-scale filament winding machine to produce test samples. This machine is discussed in Chapter 6. The first trials, made on the machine, are shown. A slamming set-up was designed and built at laboratory scale to perform drop tests on several chosen test samples. These slamming tests are discussed in Chapter 7. First, the production of the chosen test samples – a cone, a full and hollow cylinder and a small scale (1:10) point absorber – is explained. Next, the laboratory scale slamming experiments are discussed. The results are assessed and compared with literature. Additionally, an introduction is given of the Volume of Fluid (VOF) model in the Computational Fluid Dynamics (CFD) software 'Fluent' to simulate the slamming phenomenon numerically. In Chapter 8 the production and instrumentation of two large-scale point absorbers is treated. First, the testing program on those components, which consists of fatigue, slamming and fracture tests, is given. All the preparation steps for the test set-ups as well as for the production of the buoys are given. The instrumentation for each test is discussed in detail. In Chapter 9 the results of all the large-scale tests are given. They are assessed as good as possible with finite element analysis and with the findings from literature. Finally, in Chapter 10 some conclusions are drawn and an outlook for future research is given.

---

### 1. 3. INNOVATIVE ASPECTS

In this dissertation several innovative aspects were dealt with. First, composite material was used in a layered finite element model with special attention to the filament winding technique. Second, until now no research has been performed about the use of composite materials for point absorbers. Third, laboratory scale slamming tests of several objects – a cone, a rigid and a deformable cylinder, and a point absorber – have been done. Strain gauges, pressure sensors and a high speed camera were used. Special attention was paid to the influence on the peak pressure due to the deformability of the cylinder. Next, also large scale testing of two filament wound buoys (fatigue, slamming, and fracture) was done. These buoys were made in interaction with the FEA model with a special selected production method. Strain gauges, LVDT sensors, a high speed camera, pressure sensors and an accelerometer were read out. Again, special attention was paid to the effect of a deformable buoy in comparison with a more rigid buoy on the peak pressure.

### 1. 4. INDUSTRIAL RELEVANCE

The general concept of the Seewec project originates from the company ‘Fred Olsen Ltd.’. They have experience in the area of ship building and offshore platforms for oil- and gas exploitation. With the ‘Buldra’ model (and smaller models) they have proven that the design was adequate. However, still a lot of improvements had to be done. For this, they sought expertise and funding abroad with the ‘Seewec project’. One of the improvements was the survivability at sea of the point absorbers. Meanwhile, it seemed important to gain more knowledge about the behaviour of composites under severe sea loading conditions [1, 3]. Of course, the pool of end-users is not limited to Fred Olsen Ltd. Therefore, other firms in the offshore business which tend to use composites could profit from the results of the research. Additionally, in recent years, composite materials are applied more often in ship constructions (catamarans and high speed crafts) and offshore structures because of their corrosion resistance, limited maintenance, long life time and sometimes even cheaper cost. In the area of Wave Energy Converters (WEC), the survivability of the structure at sea is one of the most important issues to deal with. For now, wave energy is a small player on the energy market and the main reason for this is the difficult survivability at sea. However, waves have a lot of potential in this field. Waves can travel for thousands of kilometres with almost no loss of energy [6]. Within the current discussion about finite energy resources and global warming, this challenging resource of energy should be researched intensively.

## 1. 5. REFERENCES

1. Official website Seewec. [cited 2009 27/04]; Available from: <http://www.seewec.org>.
2. Visit to Buldra, Norway, April 2006.
3. SEEWEC - Sustainable Economically Efficient Wave Energy Converter. Sixth Framework Program (FP6), Specific Targeted Research Project (STREP), Priority 6-1: Sustainable Energy Systems, 2005-2008(contract nr. SES6-CT2005-019969).
4. M. Vantorre, Manoeuvrer- en Zeegangsgedrag van Maritieme Constructies, Course at Ghent University, Faculty of Engineering, Chapter 4. 2005-2006. p. 15 - 24.
5. Safehaven Marine Website. [cited 2009 19/03]; Available from: <http://www.safehavenmarine.com/NEWSLETTER%20JAN%202009.htm>.
6. G. DeBacker, Golfenergie op het Belgisch Continentaal Plat: droom of werkelijkheid? Analyse van de bestaande golfenergieconvertoren, Ghent University. Faculty of Engineering, Master thesis academic year 2004-2005.

## Chapter 2

### THE SEEWEC PROJECT

*In this chapter, the Seewec project which was performed within the 6<sup>th</sup> framework of the European Union (EU) and lead to this doctoral thesis is presented. First, a short overview of the policy of the EU towards renewable energy is given followed by a short elaboration on some wave energy converter projects. Next, a general introduction about the Seewec project and its partners is mentioned. Finally, a more detailed description of the tasks of workpackage four within Seewec and the link with this research are given.*

#### 2. 1. THE ENVIRONMENTAL POLICY OF THE EU

Today, the energy issue receives worldwide attention. The use of traditional fossil fuels can and will lead to global warming with climate changes as a consequence. This final reason is gaining more importance with the Kyoto agreement. The Kyoto agreement states that by 2012 an important decrease of greenhouse gasses (GHG), like CO<sub>2</sub>, has to be accomplished. Further negotiations about global strategy are currently ongoing for the 'post-Kyoto' era. Several causes have lead to this. Fossil fuel, is not infinite and is about to run out in coming decades. Second, growing economies like China and India will even increase the global use of those resources. Also, according to the former president of the United States of America, George W. Bush at his State of the Union of February 1<sup>st</sup> 2006, the US is addicted to oil. They use 25.5 % of the total world production which is more than Europe and Russia together (24.9 %). Additionally, wars like the one in Iraq and the quarrel about gas in Russia were fuel based [1] and an unstable political situation in the 'Organisation of Petroleum Exporting Countries' (OPEC) is not desirable for the rest of the world. Also, as a more economic reason, the EU is dependent on import for 50% of its energy supply. By 2030 this could easily become 70 % [2]. This import consists almost exclusively out of fossil fuels (oil, gas and coal). The reserves of oil are estimated to last for 40 years, the gas reserves for 60 years and coals for a bit more than 200 years by 2050, other energy sources will have to be used. In any case, the prices will rise simultaneously with decreasing resources. This makes the EU economically vulnerable and the development of renewable energy quite urgent. Hence, the EU made a strong effort to promote renewable energy. It also ratified the agreement of Kyoto and decided to increase its share in renewables to 12% by 2012 [3-5].

In 2001 the renewable energy sector in Belgium contributed only 2% to the electricity production in the country. Solar, biomass, wind and ocean energy can all

give a contribution. There should not be any conflict between those. Policy makers should search for the right application for the right purpose or location.

At this moment, wave energy is a small player on the energy market. However, it has a lot of potential. The European Atlantic coast wave climate is characterised by large energy. Waves can travel for thousands of kilometres with almost no loss of energy. Wave energy has some advantages: in comparison with solar energy, waves are more present, certainly at times when energy is needed the most (winter). Of course, for wind this is the same. However, waves have more energy per square meter (3000 to 4000 W/m<sup>2</sup>) than wind (400-600 W/m<sup>2</sup>) and solar energy (100-200 W/m<sup>2</sup>) [6]. The total consumption of energy in the EU was nearly 2800 TWh in 2003 and the overall future potential market for wave energy was estimated in 1998 as 2000 TWh [7].

To improve the transition from technology to real wave energy converters and to insure their value on the global energy market, extensive research is necessary on basic research as well as on applied level. The most critical aspect of the development of a Wave Energy Converter (WEC) is the structural design. It needs to be very solid but, at the same time, the material and fabrication costs have to be limited. This clarifies why wave energy is at the moment not exploited on large scale.

Next to renewables, discussions whether or not nuclear energy is a clean energy form or whether or not it can be our salvation, are going on all levels. Since nuclear energy provides 55% of the Belgian energy consumption, it is an important energy source for our country. The question could rise whether it could play a major role worldwide.

In Belgium, the law 'exit of nuclear power' of 2003 determines that all nuclear plants need to be closed between 2015 and 2025. The general opinion concerning the use of nuclear energy is sceptic because the plants hold a potential risk and the storage of nuclear waste is still a problem. In addition, also Uranium is a finite source. According to estimations, it will still be available for about 40 years [8]. Nuclear energy is a difficult matter, but nevertheless has a strong potential which should not be neglected, at least not at any cause. The following three points are important to emphasize to refine this.

First, sustainable development includes 'ecology' but also the quality of human life, which includes certain standards of social behaviour, economy, politics and culture, are important factors. Ecology sets the limits to the possibilities human beings have

---

in space and time. The emphasis should be in harmony between the different factors. In this case, e.g. without energy, the value of human life goes down. However, a sensible use of energy should be encouraged because fossil fuels have an impact on ecology and finite resources have to (and will) disappear in a not so far future. Thus, the first steps worldwide should be the closure of plants using fossil fuels e.g. by replacing them step by step with renewables. Doing so, it is possible not to decrease the quality of life. Also, existing nuclear plants should not be closed at this stage because they do not contribute to the GHGs. They should receive the fitting maintenance to ensure safety. However, the winning of uranium is a costly, contaminating and energy absorbing process. But, it is only fair to consider that the production of steel and aluminium to build e.g. wind mills is equally energy consuming. Also, the dismantling and recycling of wind turbine blades is not optimised yet [9]. But again, also decommissioning of nuclear power plants is very expensive as a recent study in the UK has shown [10, 11].

Second, since only few countries (Belgium, France, etc.) have large nuclear energy plants, the issue whether or not to invest massively, within the EU or even worldwide, in nuclear energy could rise. However, the author does not believe that this is 'the' global answer. First, there are potential dangers as the ones mentioned above. Those are the main source of general criticism. But also warfare should not be excluded from this issue. Next, and maybe even more important within the discussion, also uranium is a finite resource, and will eventually run out. Considering all these remarks it is clear that there is no easy solution for the global problem.

Finally, the author emphasises the distinction between two kinds of nuclear energies. The first one is fission which is mentioned above. The second one is fusion e.g. out of hydrogen. In opposition to fission, fusion is not a chain reaction. The process needs very high temperatures and pressures (as are present near stars) to keep it going. Fusion could become a safe and clean renewable energy but there is still a long way to go to know this for sure and eventually reach this [4]. Fusion is certainly a worthwhile process for further research. However, this discussion would lead us too far and is not treated further in this work.

## 2. 2. ELABORATION ON EXISTING WAVE ENERGY PROJECTS

Energy generated from ocean waves could provide electricity on a similar scale as nuclear or hydroelectricity sectors, according to the World Energy Council. There are three classifications of wave energy converters (WEC) [12]. In following paragraphs these three types are shortly discussed to supply general background information. This is relevant information since a new kind of WEC, Seewec, explained in paragraph 2. 3. has lead to this doctoral thesis. The main link between both is the survivability of certain components at sea. Within this dissertation it is shown that survivability conditions are crucial and hence robust concepts are necessary. It is also shown that DNV standards in combination with flat surfaces should be used with caution. In relation to this, the local peak pressures can be very high. Finally, further on several production methods are proposed for series production which could also be useful for other WECs. Hence, it is useful having additional information about possible other WEC concepts and the same/different problems within these. To fix thoughts, this is done by means of (an) example(s) of (an) existing device(s).

### 2. 2. 1. Oscillating water columns

The first class is the oscillating water columns (OWC). The water moves up and down in a hollow chamber as a result of the waves. Above the water an air column, which also oscillates, controls an air turbine. The Ocean Energy buoy (OE buoy) is an example of this class. The air contained in the chamber is pumped out and drawn in through the turbine duct by the movement of the water free surface within the device as is shown in Figure 2-1 [13, 14].

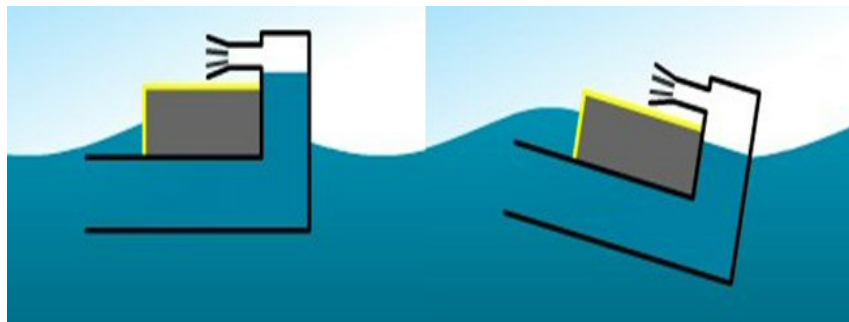


**Figure 2-1** Movement of the free water surface within the device [13, 14].

An air turbine converts the air flow into rotational energy which drives the generator. All of the power take-off is above the waterline and not in contact with the seawater. The air chamber is fitted with a relief valve to protect the turbine from overpressure in extreme wave conditions.

A picture of the actual device is shown in Figure 2-2. OceanEnergy Limited is a specialised commercial company developing wave energy technology. Over the last decade its OE Buoy was developed and tested. The device has the advantages of a robust and practical design, namely 1 moving part. It also has a proven survivability having withstood more than 2 years of live sea trials in Atlantic waves. The company is Irish based and is perfectly situated for its research and development work as Ireland has one of the world's most favourable climates for wave energy power [13, 14].



**Figure 2-2** Ocean energy buoy concept [13, 14].

Another example of the OWC technique is LIMPET (Land Installed Marine Powered Energy Transformer) in Scotland. A schematic view is shown in Figure 2-3. Limpet 500 was installed in 2000 and has a capacity of 500 kW that it supplies to the grid on the Island of Islay off the west coast of the United Kingdom. Limpet is a shoreline unit and ideally placed to generate electricity in areas exposed to strong wave energy. The technology used is currently developed to build a series of commercial power generators and to increase its power performance [15].

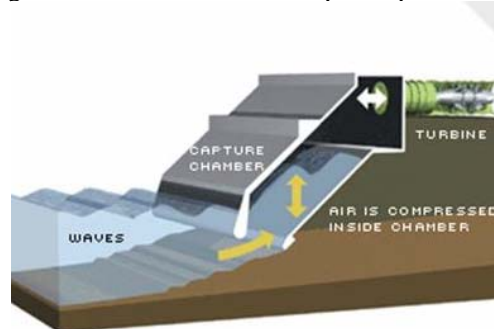


**Figure 2-3** Schematic view of the Limpet 500.

### 2. 2. 2. Overtopping Systems

Next, there are the overtopping systems. These systems use the kinetic energy in the waves which is converted in potential energy. The waves are captured in a reservoir and through the means of turbines lead back to the sea and in this way transformed into electricity. In other words, overtopping systems consist of an overtopping (absorption), a storage (reservoir) and a power-take-off (low-head hydro turbines) phase.

A well known example of this type is the Wave Dragon (Denmark) as is shown in Figure 2-4. The Wave Dragon is a large floating structure that produces energy directly from the power of the water. The only moving parts in the entire structure are the turbines. The Wave Dragon works by facing its collector arms towards the oncoming waves which concentrate 300 metres of wave front towards 140 metres of ramp at the front of the structure. This focusing increases the wave height at the ramp, which in turn acts like a beach and causes the waves to break over its top and into the reservoir behind it. By this action the water is elevated and has potential energy, which is turned into electricity by simply running the water down through turbines in the bottom of the structure [16]. The most distinctive aspects of the Wave Dragon are the two long slender arms mounted to the front corners of the reservoir platform. These are designed to reflect the oncoming waves towards the ramp. A wider section of wave is available to be exploited with only a moderate increase in capital cost. The overtopping volume in a wave is dependent on the wave height. Therefore, by providing only a moderate increase in height, much more energy can overtop the ramp. However, these ‘reflectors’ suffer a lot from peak loads caused by waves and should have a good fatigue resistance [16, 17].



**Figure 2-4** Picture of an installed Wave Dragon model in Denmark [16].

### 2. 2. 3. Converters with moving bodies

Finally, the last class consists out of converters with moving bodies. A possible design is based on the relative movement between different bodies as is the case with the Pelamis Wave Power (PWP) from Scotland.

The Pelamis is a semi-submerged structure composed of four cylindrical sections linked by hinged joints as shown in Figure 2-5 [12, 13, 18]. The wave-induced motion of these joints is contracted by hydraulic rams, which pump high-pressure fluid through hydraulic motors and accumulators. The hydraulic motors drive electrical generators to produce electricity. Power from all the joints is connected with a single cable to a junction on the sea bed. Several devices can be connected together and linked to shore through a single seabed cable. During the summer and autumn 2008, PWP successfully commissioned the World's First Wave Farm off the coast of Portugal. Three Pelamis units make up the Aguçadoura wave farm (in Portugal) of 2.25 MW. They are the world's first, multi-unit, wave farm and also the first commercial wave energy converters. PWP proved for the first time that wave energy could be harnessed, transmitted to shore and into the Portuguese grid in a fully controlled manner using multiple machines. For now, only the Pelamis is in a further stage than the prototype stadium [18]. However, important to mention is that the joints and the connection of the mooring cable suffer from mechanical problems.



**Figure 2-5** Pelamis.

## Composite floating point absorbers for wave energy converters

---

In this WEC class of ‘moving’ bodies also devices with absolute movement of a system with respect to a reference point e.g. seabed, exists. An example of this is the Archimedes Wave Swing (AWS) of Scotland. This is a submerged cylinder shaped buoy, moored to the seabed as shown in a ‘farm’ in Figure 2-6.

As a wave crest approaches, the water pressure on the top of the cylinder increases and the upper part compresses the gas within the cylinder to balance the pressures. The reverse happens as the wave passes and the cylinder expands. This mechanism is shown schematically in Figure 2-7. The relative movement between the floater and the lower part or silo is converted to electricity by means of a hydraulic system and motor-generator set. The power-absorption concept has been proven at full-scale in 2004 in a pilot plant that was installed off the coast of Portugal. Detailed engineering for a 250kW optimised pre-commercial demonstrator is now ongoing. From 2011 on, the AWS should be commercially available with an average power output of 1MW in rough sea conditions [19].

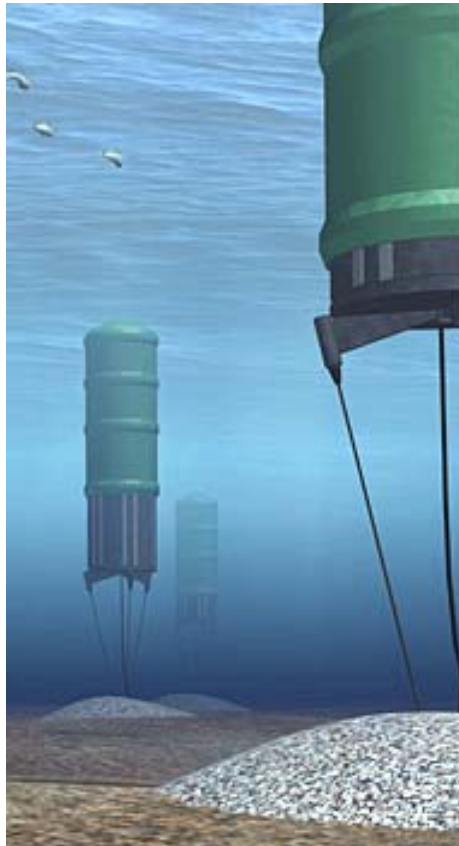


**Figure 2-6** Archimedes Wave Swing [20].

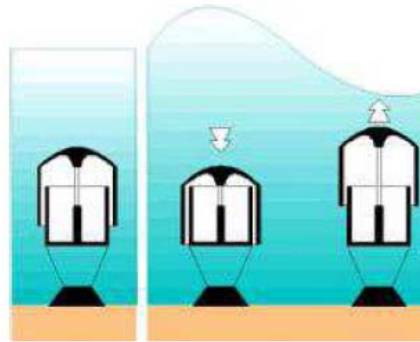


**Figure 2-7 Principle of the Archimedes Wave Swing [20].**

Next, another WEC belonging to this class is the Wave Star. The basic concept behind it is fundamentally different from many other wave power models. The machine does not form a barrier against the waves to capture all of their energy, but it cuts in at right angles to the direction of the wave. In operational conditions the waves run through the length of the machine, and their energy is exploited continuously. The Wave Star consists out of a 240 meter platform with 20 floating hemi-spheres on each side as is shown in Figure 2-8. In severe storm conditions, the machine does not work and is put in ‘safe modus’ as is shown in Figure 2-9.



**Figure 2-8 Scale model of Wave Star [21].**

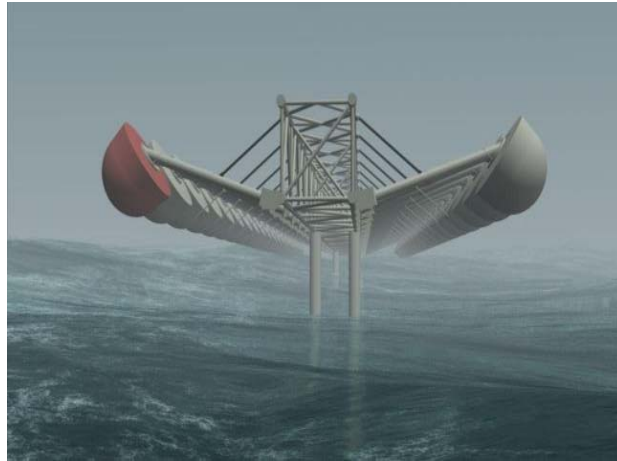


**Figure 2-9 Wave Star model in storm condition [21].**

The 20 floating hemi-spheres are partially submerged in the water. When a wave rolls in, the first float is lifted upwards, and then the second and so on. In this way oil is pumped into a transmission system through a piston in the cylinder at the end of each floater arm. There, a pressure is built up (up to 20 MPa) which drives a hydraulic motor, connected to a generator that produces electricity.

In the long run this WEC should produce 6 MW. Now, a prototype of scale 1:10 was extensively tested in Denmark (grid connected since 2006) and the construction of a 1:2 scale was initiated. The prototype of scale 1:10 already survived 15 storms without any damage [13, 21].

## 2. 3. THE SEEWEC PROJECT

### 2. 3. 1. General introduction

The Seewec device belongs to the moving bodies WEC category. Seewec stands for Sustainable Economically Efficient Wave Energy Converter. Within Framework Six of the EU, the project has been launched at the end of 2005. At that moment, Ghent University entered as a coordinator in the project. Before, Ghent University did not take part in design of the general concept which originates from the company Fred Olsen Ltd. in 2001. This concept of the WEC looks like a traditional drill platform as is shown in Figure 2-10 but there are two factors that differentiate it [22-25].

The basic concept consists of the presence of point absorbers in the middle of the platform. They are there to absorb energy out of the waves. Second, where traditional drill platforms are steel constructions, this platform will be made out of light materials, such as composites and light metals. Furthermore, composite materials do not corrode like metals. In this way, maintenance or replacements at sea are easier to carry out.

The dimensions of such a platform were proposed at 36 x 36 square meters and 15 meters high. In the platform there are 21 point absorbers present as was shown in Figure 2-10. These buoys move up and down in the waves. By damping these motions electricity is produced. This might be realised by means of a hydraulic intermediate stage and a generator or directly with a linear generator. Fred Olsen Ltd. has experience in the area of ship building and offshore platforms for oil- and gas exploitation.



**Figure 2-10** Concept WEC platform.

A major design criterion was the use of known technology as much as possible. The Seewec structure is designed to stay the whole year long at sea. However, in extreme conditions called the Ultimate Limit State (ULS), it should not operate anymore. The operational conditions are called the Serviceability Limit State (SLS).

Seewec is suitable in areas near shore with moderate energetic waves of about 30 kW/m. Point absorbers have a large efficiency in small waves. Also, the absorbed power can be higher than the input power over the diameter of the point absorber since also sideward absorption of power is possible. Hence, these systems are more suitable for large energetic waves than overtopping systems and oscillating water columns.

Waves are initiated through the wind that blows over the sea. As long as the wind velocity just above the water surface is higher than the wave velocity, there is a transport of energy from wind to the highest waves. These waves have the highest energy. The height of the waves increases with increasing wind velocity, duration of the presence of this wind velocity and the free path length where the wind blows at sea. In general, large waves are the most powerful ones. The energy content of the waves is dependent of the wave height, its velocity, its period and the density of the water. However, at a given wind velocity there is a maximum energy content. This means that for a longer duration of the same wind velocity the wave height will not increase any longer at a certain moment. The average transport velocity of this horizontal energy through a vertical surface per unit length in the width of the wave is the energy flux. Equation 2-1 gives the wave energy flux in deep water. This means at a water depth larger than half of the wave length (i.e. deep water).

$$P = \frac{\rho g^2}{32\pi} H_s^2 T$$

**Equation 2-1 Energy flux per unit length wave front in function of the significant wave height, the wave period, Earth's gravitational constant and the density of the seawater [25].**

With  $\rho$  [kg/m<sup>3</sup>] the density,  $g$  [m/s<sup>2</sup>] the gravitational constant,  $H_s$  [m] the significant wave height and  $T$  [s] the wave period.  $H_s$  is the average height of the highest one-third part of the measured waves.

A good WEC converts as much as possible of this flux hence the significant wave height decreases after the WEC [22-25]. According to preliminary calculations, before the Seewec project started, a full scale platform with 21 buoys (of 6 m high and 3.5 m diameter) would produce 2.52 MW out of waves of 6 meter significant

wave height and 9 seconds peak period. This wave size corresponds with the 'yearly storm' of the sea climate at Karmøy. The output of 2.52 MW is comparable with a middle scale wind turbine.

The device should have an installed cost/MW lower than the equivalent for offshore wind (estimated at 1.75-1.9 million Euro/MW) and, once installed, an energy price comparable to onshore (330-370 Euro/MWh) and offshore wind (400-430 Euro/MWh). The main target of the EU is to decrease the cost of electricity production for these kinds of technologies (renewable energy) to 50 Euro/MWh by 2020.

Also, the idea of a WEC farm was born. A schematic view is depicted in Figure 2-11. Due to this reason it should be kept in mind that it concerns large series production of all components especially for the buoys (21 per platform).



**Figure 2-11** Concept of a possible farm of Seewec platforms.

The proposed maximum allowed cost of the construction of each platform was estimated at about 3 to 4 million Euros.

The first steps for the initial design concept were taken at the University of Oslo and at the Norwegian University of Science and Technology (NTNU) in Trondheim. In 2003, a project group was set up and the most important patents were achieved. A year later, in 2004, the concept evolved to a general design and a 1:20 scale model was tested in a wave tank of the Ocean Basin Laboratory at Sintef in Trondheim. It was tested in operational and extreme conditions. The tests confirmed the concept and the excellent properties of the structure in the sea. The 1:20 scale model is seen in Figure 2-12.



**Figure 2-12** 1:20 scale model of the FO<sup>3</sup>.

Following the positive outcome of the first tests, the construction of a research platform of scale 1:3 (Figure 2-13), named 'Buldra', was also built and the point absorbers were tested in the Ocean Basin Laboratory. Buldra has dimensions of 12 x 12 square meters and is 9 meter high. The hydraulic towers on the platform are 7 meter high. The test was designed with a total of five point absorbers a complete hydraulic system, a generator and an electrical load. A monitoring system was also developed for the tests. The major objectives of these tests were to verify the system design, measure actual power production capability versus the theoretical calculations, identify and measure energy loss components and to give input to the control algorithms. The 1:3 scale system tests proved the production potential of the platform. After these basin tests, Buldra was ready for sea trials. It was launched in the sea in January 2005 off the southern coast of Norway.



**Figure 2-13** 1:3 scale testing platform "Buldra".

---

### 2. 3. 2. Aim of the EU Seewec project

Fred Olsen Ltd. has proven with these scale models that the design works. However, still a lot of improvements had to be done. For this, they sought expertise and funding abroad in form of the ‘Seewec project’. The main word for the Seewec project is ‘optimisation’. Since it concerns a sustainable project, it should take into account the ecological, social and economic impact (i.e. sustainability). Hence, the construction, operation and maintenance costs should be reduced as far as possible. Of course, Seewec is mainly a research project thus issues other than economic ones are also very important. Within the project, the power output should be maximized. Different shapes for the point absorbers should be calculated, other designs for the platform considered, composite material assessed, etc. Also, from the electric point of view both rotating and linear generators are considered to decide how to increase the maximum converted energy in a given climate. Additionally, the behaviour of a farm of platforms is studied: e.g. the intermittence effect and how to interconnect them [22-25].

The different partners participating in the project were universities and companies from five EU countries (Belgium, Netherlands, Portugal, United Kingdom and Sweden) and one associated country (Norway). The participants are:

- Ghent University (Belgium)
- Spiromatic NV (SMC) (Belgium)
- ABB (Sweden)
- Standfast Yachts (STY) (Netherlands)
- Brevik Engineering A.S. (BRE) (Norway)
- Marintek (SINTEF) (Norway)
- Norwegian University of Science and Technology (NTNU) (Norway)
- Instituto Superior Técnico (IST) (Portugal)
- Chalmers University of Technology (Sweden)
- Fred Olsen Ltd. (FOL) (UK, Norway)
- Natural Power Consultants Ltd. (UK)

The project is divided in eleven workpackages with several partners working on them. Workpackage four (WP4) is the one that lead to this doctoral thesis and is explained in the following paragraph. A list of all workpackages is given:

- WP1. General methodology and progress assessment
- WP2. Field testing and data collection
- WP3. Wave climate and environmental study
- WP4. Material design for large scale manufacturing

- WP5. Refining of platform design
- WP6. Farm design and characteristics
- WP7. Power generation efficiency
- WP8. Design and manufacturing of 2<sup>nd</sup> generation systems and components
- WP9. Financial viability
- WP10. Synthesis and results
- WP11. Dissemination and exploitation

This ‘floating’, ‘offshore’ platform has the advantage that it can be used in deeper water where there is more energy available. This study can give a contribution to the use of ocean energy worldwide. Also, for the EU, this can mean a further reduction of our independence of the oil producing countries.

### 2. 3. 3. Workpackage four (WP4)

This workpackage focuses mainly on the point absorbers [22-25]. A picture of a point absorber around its rod, installed on the Buldra platform is given in Figure 2-14, which is a picture taken during a visit to this platform in Norway [26]. The typical dimensions of such a full scale buoy are a height of 4-6 meters and a diameter of 3-5 meters. Since the Buldra platform is only a scaled one (about 1:3) the buoys are of course also scaled. The main loads on this buoy are the ‘slamming loads’ at its bottom and at its side. Slamming is a phenomenon known in the maritime environment as the repeated short impact of water on a floating or sailing structure as is explained in Chapter 3. According to the “Project description” and the “General methodology” documents, the partners involved in this workpackage are: Ghent University (Ghent University, work package leader), Spiromatic (SMC), Standfast Yachts (STY), Fred Olsen (FOL) and Brevik (BRE).



**Figure 2-14** Point absorber with part of rod.

Ghent University takes the overall responsibility for this workpackage, and performs the numerical analyses for estimating the mechanical behaviour, as well as the experimental coupon and subcomponent testing. Also, Ghent University assists in the selecting and evaluation phases. The university was chosen as a partner for its experience with composites and numerical finite element analysis (FEA) calculations. SMC and STY evaluate and set-up the design for an actual production process for the point absorbers, and produce laminates and subcomponents for testing. Both firms were chosen for their experience with composites. SMC has the experience of making axisymmetrical objects (storage silos). The point absorbers are also axisymmetric and moreover, their diameter is within the same order of magnitude as the silos made at SMC. The production process of SMC is called 'filament winding' and is explained in detail in Chapter 4. STY produces composite sailing yachts; hence it has a lot of experience with behaviour of composites in sea conditions. Due to this they serve as an advisor within the project for the selection of resin, anti-fouling and bearings. Their production method is vacuum infusion, which is assessed to use for the point absorbers. It is also explained in Chapter 4. FOL and BRE provide continuous input on global methodology and assist in evaluation and decision phases.

The main objectives of WP4 were defined in the description of the 'General methodology' of the EU project as 'The selection and development of composite material for point absorbers (and other components) and the design of the manufacturing process for cost effective large scale production'. It was extended into six different subtasks, defined as:

1. Choice of basic material constituents of the buoys
2. Determination of basic mechanical properties
3. Determination of candidate production processes for the buoys
4. Actual design of absorbers
5. Subcomponents: production and testing
6. Gaining of expertise for production of full composite rig

The first subtask is about the evaluation and selection of basic material constituents for the point absorbers as a whole: the choice of reinforcing fibres, matrices, gel coats, protective surface layers, stiffeners, etc. to fulfil demands. These demands are mainly the environmental conditions such as sea water, UV, sea fauna and flora, the mechanical properties like stiffness, strength, fatigue life, mechanical impact and finally, the achievement of minimum cost for maximum lifetime.

The material static properties were determined experimentally within the second subtask. First, fabrication of test laminates made from the basic constituents (fibres and matrices), selected in subtask 1, has been done. Second, test specimens were prepared with the application of 'end tabs' and strain gauges. Finally, testing was done according to ASTM standards to determine the stiffness and strength in all directions (orthotropic material) as well as the specific mass. The selection and determination of these materials is discussed in detail in Chapter 4.

The third subtask is about the evaluation and the selection of possible manufacturing processes for the point absorbers, in view of fabrication of large components, production at high rates, ease of transportation and of installation, producing and installing at lowest possible costs. For axisymmetric components, with currently existing production facilities for large components as well as with current polymer costs, filament winding and vacuum infusion with thermosetting resins are candidate processes. Both processes are explained in detail in Chapter 4. Important aspects are processing possibilities of selected basic components, choice of moulds/mandrels, necessity/possibility of use of internal stiffeners, use of sandwich or monolithic laminates, ease of assembling, etc.

The determination of the final shape is done within subtask four and is decided in consent with workpackage five which deals, among other things, with the power output as a function of the shape of the buoy. Within this subtask, the required wall thicknesses, the composite stacking sequences (number of layers, fibre reinforcement and orientation, sandwich concept or not, etc.), the need for extra stiffeners and possible bearings for the connection absorber/rod were researched.

Next, within subtask five a subcomponent is made. The first task was the choice which one to make like a full or scaled point absorber or only parts of it. Also, the lay up of the buoy was determined with means of finite element calculations done in Chapter 5. Finally, fabrication and experimental testing of subcomponent sample(s) were done for verification of calculated strength and stiffness.

As mentioned higher, in the Seewec project, WP4 focused on the point absorbers (and rod) [22-25]. However, during the course of the project, some useful expertise was gained for the future production of the full rig from composite materials as well within subtask six.

During all subtasks the financial viability of the point absorbers was also taken into account and given as an input for workpackage nine. The link with this doctoral thesis is the research for suitable materials for the point absorbers and the design

---

(lay-up, stiffeners, etc.) to survive certain design conditions. Further on, within this work the behaviour of composite structures and the influence of deformable objects on the peak slamming load are researched.

## 2. 4. REFERENCES

1. T. Seifert and K. Werner, Het zwarte goud: olie als bron van hebzucht, oorlog, macht en geld. Translated to Dutch by M. Hofstede, P. Hofstede, published by 'Centraal Boekhuis', 2007. p. 320.
2. European Communities (2002): Energy Let us overcome our dependence, ISBN 92-894-1349-2, (p. 1-39).
3. OECD (2003): Energy Policies of IEA Countries: 2003 Review; International Energy Agency.
4. C. Blommaert, Globale Energieproblematiek - Inleidend onderzoek naar hernieuwbare energie in Latijns-Amerika met case study over Colombia', Hoofdstuk 2, blz 11-28, Ghent University. Faculty of Political and Social Sciences, Master after master thesis in Conflict and Development, 2009.
5. C. Blommaert and T. Vernailen, Het gebruik van koolzaadolie en gebruikte frituurolie voor transportdoeleinden, Hoofdstuk 1, blz 1-8, Free University of Brussels. Faculty of Engineering, Master thesis, academic year 2004-2005.
6. G. DeBacker, Golfenergie op het Belgisch Continentaal Plat: droom of werkelijkheid? Analyse van de bestaande golfenergieconvertoren, Ghent University. Faculty of Engineering, Master thesis academic year 2004-2005.
7. T. Thorpe, The wave energy programme in the UK and the European Wave Energy Network. 4th EWEC, Aalborg, Denmark, 2000.
8. I. Broeckmeyer, De nucleaire renaissance. De Tijd, zaterdag 3 september 2005.
9. K. Larsen, Recycling wind turbine blades. Renewable Energy Focus Volume 9, Issue 7., 28/02/2009.
10. Nuclear decommissioning. [cited 2009 20/04]; Available from: [http://en.wikipedia.org/wiki/Nuclear\\_decommissioning](http://en.wikipedia.org/wiki/Nuclear_decommissioning).
11. The economics of nuclear power, (November 2008). World Nuclear Association, Information Papers.
12. . Abaqus Insights 02/2008 - Harvesting the Ocean's Power with Pelamis and Realistic Simulation p. 10-11.
13. European Ocean Energy Association Finance Seminar: Wave and Tidal Energy Finance Experience and Opportunity in Brussels - Presentations about Wave Star, Pelamis and Ocean Energy Buoy, 29/05/2008.
14. Official website Ocean Energy Buoy [cited 2008 30/05]; Available from: [www.oceanenergy.ie](http://www.oceanenergy.ie).
15. Official website Limpet. [cited 2009 20/04]; Available from: [http://www.wavegen.co.uk/what\\_we\\_offer\\_limpet.htm](http://www.wavegen.co.uk/what_we_offer_limpet.htm).
16. Official website Wave Dragon. [cited 2009 16/04]; Available from: [www.wavedragon.net](http://www.wavedragon.net).
17. J. Tedd, Doctoral Thesis, Aalborg University, November 2007, Testing, Analysis and Control of Wave Dragon, Wave Energy Converter, Chapter 7 - Section 'Wave Reflector Wings' p 36-38

- 
18. Official website Pelamis. [cited 2009 21/04]; Available from: [www.pelamiswave.com](http://www.pelamiswave.com).
  19. Official website Aws Ocean Energy. [cited 2009 21/04]; Available from: <http://www.awsocan.com>.
  20. Renewable Energy gadgets in the UK, website. [cited 2009 21/04]; Available from: <http://www.reuk.co.uk/Archimedes-Wave-Swing-Machines.htm>.
  21. Official website Wave Star. [cited 2009 21/04]; Available from: [www.wavestarenergy.com](http://www.wavestarenergy.com).
  22. SEEWEC - Sustainable Economically Efficient Wave Energy Converter. Sixth Framework Program (FP6), Specific Targeted Research Project (STREP), Priority 6-1: Sustainable Energy Systems, 2005-2008(contract nr. SES6-CT2005-019969).
  23. Official website Seewec. [cited 2009 27/04]; Available from: <http://www.seewec.org>.
  24. A. Leirbukt and P. Tubaas, A wave of renewable energy. ABB Review, 3, 2006.
  25. K. Stoop and S. Vermeulen, Numerieke simulatie van de vloeistof-structuur interactie bij hydrodynamische impact, Ghent University. Faculty of Engineering, Master thesis academic year 2007-2008.
  26. Visit to Buldra, Norway, April 2006.



## Chapter 3

### DESIGN CRITERIA AND THE SLAMMING PHENOMENON

*In this chapter the design criteria for the point absorbers are given. Next, the phenomenon of slamming is explained. Also, the relevant literature concerning this subject is discussed. Finally, the used formulas for the finite element calculations are given and justified.*

#### 3. 1. CHOICE OF DESIGN CRITERIA FOR POINT ABSORBERS

##### 3. 1. 1. Introduction

As was mentioned in Chapter 2 several design criteria have to be taken into account for the point absorbers. The most important one is the survival of each of these buoys for about 25 years at sea with low maintenance cost.

It is not necessary that the buoys are operational during severe winter storms. However, they should stay at sea. Hence, they have to survive certain load conditions within that particular environment. One of the proposed shapes within the Seewec project, the tulip shape, is depicted in Figure 3-1 with a schematic view of all loads working on a structure in a sea environment [1]. In the following paragraphs all used symbols will be explained.

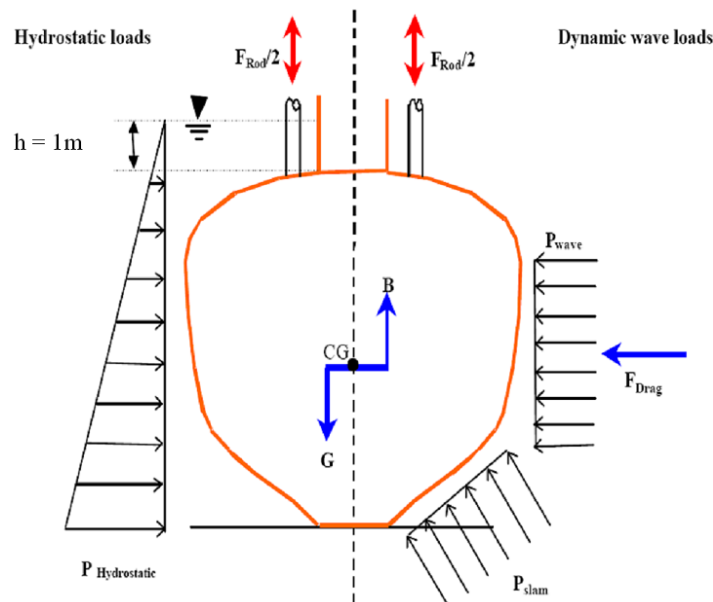


Figure 3-1 Point absorber ‘tulip’ with working loads at sea [1].

Second, operating in a sea environment, the point absorbers should be able to withstand moisture and salt. This is one of the advantages of composites over e.g. steel since no corrosion will occur for that kind of material. Also, this composite material is a lot lighter than steel or concrete. In this way, maintenance or replacements at sea are carried out more easily. Finally, the production method should be suitable to make these point absorbers in series production at lowest cost possible. A more detailed material selection within the composites family is given in Chapter 4.

### 3. 1. 2. Hydrostatic load

Each object that is submersed in water is subject to the hydrostatic load. This pressure is equal to the product of the density [ $\text{kg/m}^3$ ] of the fluid (for seawater this is  $1025 \text{ kg/m}^3$ ), the gravitational constant  $g$  [ $\text{m/s}^2$ ] and the height  $h$  [ $\text{m}$ ] of the object as is shown in Equation 3-1.

$$\Delta p = \rho g \Delta h$$

**Equation 3-1    Formula of the hydrostatic load at a certain depth.**

As was shown in Figure 3-1 (left) the hydrostatic load increases along the penetration depth of the object. However, for a point absorber of maximum 6 meters height (in this case depth) this gives only about 60330 Pa when it is completely submersed. Hence, the slamming phenomenon discussed in following paragraphs is a far more crucial load as will be seen in the used criteria for the loads further in this Chapter.

### 3. 1. 3. Bottom slamming and breaking wave slamming

The slamming at the bottom, called ‘bottom slamming’ (represented with the symbol  $P_{\text{slam}}$ ) or ‘straight slamming’ (represented with the symbol  $P_{\text{wave}}$ ), means that a structure hits a water surface and can be severely damaged due to local high impact pressures. The slamming of a breaking wave, called ‘breaking wave slamming’ or ‘lateral slamming’, occurs when a wave hits the structure laterally at a certain moment in its breaking phase. Brevik, one of the partners in the Seewec project (Chapter 2), performed measurements at Karmøy to determine the sea climate [1].  $H_s$  is the significant wave height and  $T_z$  the zero up-cross period.  $H_s$  is the average height of the highest one-third part of the measured waves.  $T_z$  is the mean time interval between upward or downward zero crossings on a wave record. In Table 3-1 the significant wave heights ( $H_s$ ) and peak periods ( $T_z$ ) are given for 1, 10, 25 and 100 years. These are called ‘the return level of  $n$  years’ which means the characteristics of a storm that occurs once in  $n$  years. Return level 25 years is set

forward within the project as an extreme state where the point absorbers should survive the load. Return level 1 and 25 are called within this doctoral thesis the yearly and 25-year storm. The yearly storm is seen as an operational condition. Next, in Table 3-2 the 25, 50 and 95 percentiles are given based on a yearly scatter diagram. Also, the 95 percentile values are chosen as an operational criterion. It means that for 95 % the waves are equal or lower to these values.

Year	Hs [m]	Tz [s]
1	6.6	8.4
10	8.5	9.4
25	9.6	9.9
100	10.4	10.2

**Table 3-1** Return level of 1, 10, 25 and 100 years at Karmøy.

Percentile	Hs [m]	Tz [s]
25	0.4	3.8
50	0.9	4.6
95	3	6.7

**Table 3-2** The 25, 50 and 95 percentile at Karmøy.

Next, the symbol CG stands for ‘Centre of Gravity’ where the ‘Gravity’ G goes down and the ‘Buoyancy’ B goes up. The centre of buoyancy is the centre of the volume of water which the hull displaces. This point is referred to as B in Marine Engineering. The buoyancy is explained later on in Chapter 8 since it was a necessary check-up for outdoor experiments.

Further,  $F_{drag}$  represents the maximum drag force which occurs when a wave breaks just in front of the point absorber and the breaking wave washes in over the point absorber. A conservative approach is to assume that the whole point absorber is exposed to this flow and that the flow velocity is equal to the wave celerity. For the 25-yearly storm this is 12.1 m/s as will be explained in paragraph 3. 2. 2. In reality there will be a velocity gradient through the flow. For the tulip shape the drag force for a 25 year storm was calculated by Brevik with the help of Equation 3-2 and equals 1460 kN.

$$F_{drag} = C \frac{\rho v^2}{2} A$$

**Equation 3-2** Formula for the drag force.

## Composite floating point absorbers for wave energy converters

---

There,  $C$  is the drag coefficient (-),  $\rho$  is the density of seawater ( $1025 \text{ kg/m}^3$ ),  $v$  is the free stream velocity (m/s) and  $A$  the projected frontal area ( $\text{m}^2$ ). The highest drag coefficient from the DNV classifications notes for circular cylinders (1.2) in steady flow is used to calculate the maximum drag force. Finally, the symbol  $F_{\text{rod}}$  represents the sum of the maximum dynamic vertical force.

It seems that slamming is a crucial load for the point absorber. The concept of ‘slamming’ is elaborated in the following paragraphs together with a relevant literature survey of the phenomenon.

## 3. 2. SLAMMING

### 3. 2. 1. Introduction

Slamming is a phenomenon, known in the maritime environment, as the short impact of water on a floating or sailing structure. Slamming loads are local and could introduce very high local stresses but not necessarily large global loads.

The upward motion of a structure and the fall back on the water surface, is called straight, vertical or bottom slamming. The phenomenon was already extensively studied in the Marine Engineering and it takes place due to the several movements of a ship at sea which are all six shown in Figure 3-2.

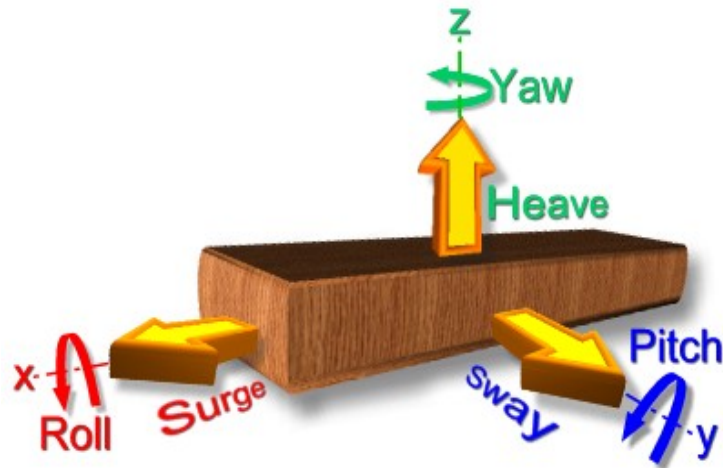


**Figure 3-2** Degrees of freedom of a ship at sea.

In state of extreme loads slamming has been the reason for ship damage. This occurs due to the heave and pitch movement of a ship which initiates vertical slamming loads. Figure 3-3 shows a picture of a ship falling down after the passing of a wave. Figure 3-4 shows the slamming of a wave on the buoy of a ship.

It happens quite frequently that the bow and the bottom are damaged. Sometimes this even leads to fracture of the ship. The probability of slamming of a ship is highest at the front part where the relative velocity between the ship and the waves is most pronounced. Slamming on the bottom of the ship occurs especially in ballast condition, which means that the cargo holds or cargo tanks are empty, but the ballast tanks are filled. The slamming loads are mainly dependent on the shape of the sections in the fore body of the ship, not directly on the block coefficient although

there is a correlation between both. The block coefficient is the ratio of the immersed volume of a vessel to the product of its immersed draft, length, and width.



**Figure 3-3** Ship falls down after wave [2].



**Figure 3-4** Slamming on the bow of a ship [3].

Also, breaking waves can introduce slamming. This is called lateral or breaking wave slamming. This wave impact can cause damage on the bow of a ship above the

waterline. Sometimes it is decided to reduce the speed of the ship to limit any kind of slamming. This is done as soon as more than three of the hundred occurring waves lead to slamming [4]. Additionally, breaking wave slamming can occur against a component of an offshore structure. These components have to be designed for impact loads (up to 10 bar and more, lasting for milliseconds) coming from breaking waves. This is quite similar for the buoys within the Seewec project.

The buoys are also suffering from bottom slamming. In normal to high waves and small penetration depth of a buoy, it is possible that the buoy goes out of the water. The penetration depth is the submerged vertical distance when an object enters a water surface. This can happen when there is a phase shift between the wave and the movement of the buoy. When the buoy falls back into the water, it can be damaged severely due to hydrodynamic impact on the bottom of the buoy. As mentioned, these impact pressures last only for some milliseconds. There are several possibilities to avoid bottom slamming on point absorbers. First, through external control of the movement of the buoy the chance of slamming is kept as small as possible. When nevertheless slamming occurs, it is important that the point absorber has an optimised shape to keep the slamming pressures as low as practically possible. For the simulations it is of course necessary to understand which pressures are built up in these both kinds of slamming. Figure 3-5 shows a schematic view of a buoy subject to bottom slamming (left) and breaking wave slamming (right). In paragraph 3. 2. 3. the literature survey on the slamming phenomenon is presented. However, first a short note on the celerity of waves is given in the following paragraph.

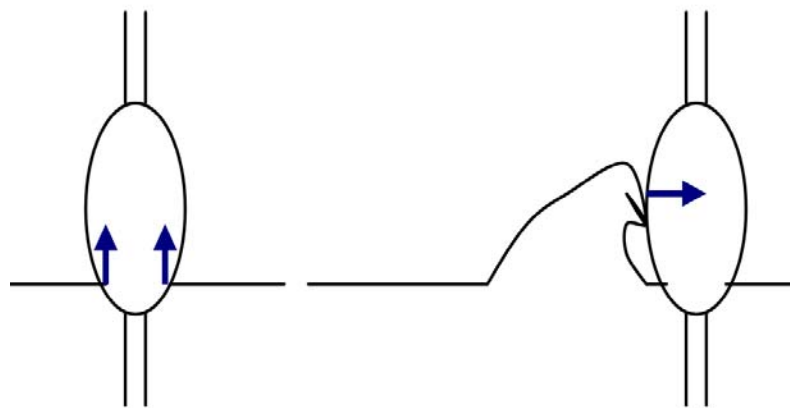


**Figure 3-5** Schematic view of bottom slamming on a point absorber (left) and of breaking wave slamming (right).

### 3. 2. 2. Velocity: drop velocity or wave celerity

For bottom slamming the drop velocity is used in all formulae. However, for breaking waves this is not so straight forward. Waves can not become infinitely steep: when the ratio height/length is higher than 1:7 they break. Just before breaking, the wave length is  $L_b = 7 * H_b$  [5].  $H_b$  is, according to DNV, the most probable largest breaking wave height in n years and it is equal to  $1.4 H_s$  [6]. For the yearly storm, the 25 year storm and the 95 percentile the values of  $L_b$  are given in Table 3-3.

	$H_s$ [m]	$L_b$ [m]
25 year storm	9.6	97.1
1 year storm	6.6	64.7
95 percentile	3	29.4

**Table 3-3 Overview of the wave length for the 1 and 25 year storm and for the 95 percentile.**

Now, with the help of the dispersion equations the celerity  $c$  (which is the velocity) of a breaking wave is determined. First, Equation 3-3, which is valid for regular waves, is introduced.  $L$  is the wave length,  $T$  the wave period,  $\omega$  the circular frequency (i.e.  $2\pi/T$ ),  $k$  the wave number (i.e.  $2\pi/L$ ) and  $c$  the celerity (i.e. the velocity of the wave). Next,  $k$  and  $\omega$  are also related with the dispersion relation shown in Equation 3-4. This equation expresses the relation between the wavelength  $L$  and the wave period  $T$ . The gravitational constant  $g$  (i.e.  $9.81 \text{ m/s}^2$ ) and the water depth  $h$  are used in this relation. When the depth is infinite the hyperbolic tangent ( $\tanh$ ) becomes equal to one which simplifies the calculations. However, in the case of the Seewec structure a water depth of 30 meter was proposed for its location.

$$c = \frac{L}{T} = \frac{\omega}{k}$$

**Equation 3-3 Relation between the wave length, the wave period, the pulsation, the wave number and the celerity [5].**

$$k \tanh(kh) = \frac{\omega^2}{g}$$

**Equation 3-4 Relation between the wave number and the pulsation [5].**

Out of Equation 3-4 (after the substitution of  $k$  by  $2\pi/L$ )  $\omega$  can be calculated which leads to the wave period  $T$  (i.e.  $2\pi/\omega$ ). Finally, with the help of Equation 3-3 this

gives the celerity. An overview of the wave period and celerity for the 1 and 25 year storm and the 95 percentile is shown in Table 3-4.

	T [s]	c [m/s]
25 year storm	8	12.1
1 year storm	6.63	9.75
95 percentile	4.34	6.8

**Table 3-4 Overview of the wave period and the celerity for the 1 and 25 year storm and for the 95 percentile.**

### 3. 2. 3. Literature survey

First, it has to be noted that this survey was done with the proposed shapes in mind. Several shapes were studied for use as a point absorber within the Seewec project [7]. Note that for these shapes both bottom and breaking slamming had to be taken into account. To set the mind all four of them are given in following figures: the egg, the tulip, the pencil and the cone-cylinder-cone.

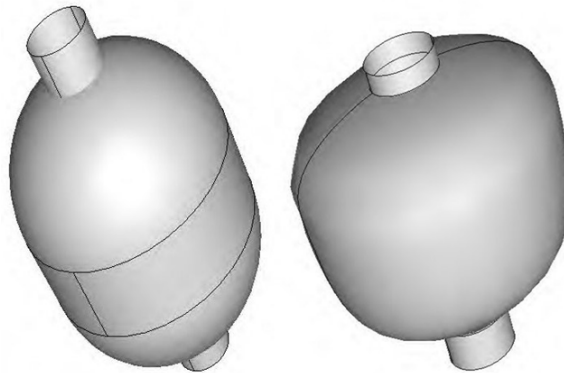


**Figure 3-6 Egg shape (left) and tulip shape (right) [7].**

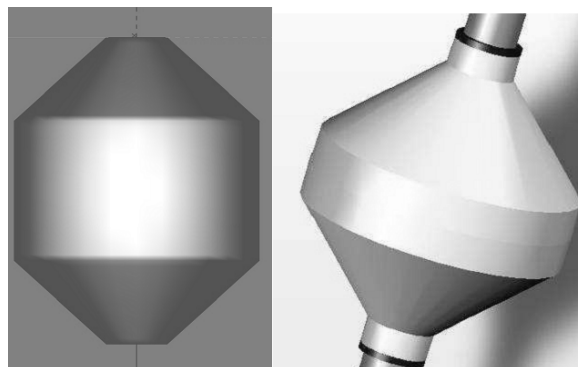


**Figure 3-7 Pencil shape (left) and cone-cylinder-cone shape (right) [7].**

Until a few decades ago, the use of fibre-reinforced composite in Marine Engineering was limited to sport vessels (speedboats, jet skis and sailing yachts) and a number of military applications. The composite structure was designed very stiff and as rigid as possible in order to resist the slamming wave and bottom impact. In that case the calculation of the peak pressure of the slamming is based on the theory of Von Karman (1929) or Wagner (1932), who calculated the maximum line load on a wedge shaped rigid 2D body for bottom slamming [8, 9]. In recent years however, composite materials are applied more often in ship constructions (catamarans and high speed crafts) and offshore structures because of their corrosion resistance, limited maintenance, long life time and sometimes even cheaper cost. Composite materials have also been used for minesweepers for their magnetic properties.

As already mentioned, the slamming phenomenon was studied in the Marine Engineering on *rigid* bodies. The most studied shape was a 2D wedge since the bow of a ship has about this shape. It all started with Von Karman (1929) and a few years later Wagner (1932) who set up a theory which can calculate the hydrodynamic pressure distribution on a rigid wedge when the deadrise angle is not very small. This angle is defined as the angle of the bottom of the object to the horizontal. Wagner's detailed description of the flow at the intersection of the free water surface and the body surface is not given here. This local flow describes a jet flow which ends in a spray. Within this doctoral thesis the emphasis lays on the pressures in the outer flow domain shown in Figure 3-8 because they are most important for the structure. The spray root is the intersection of the outer free surface and the wedge.

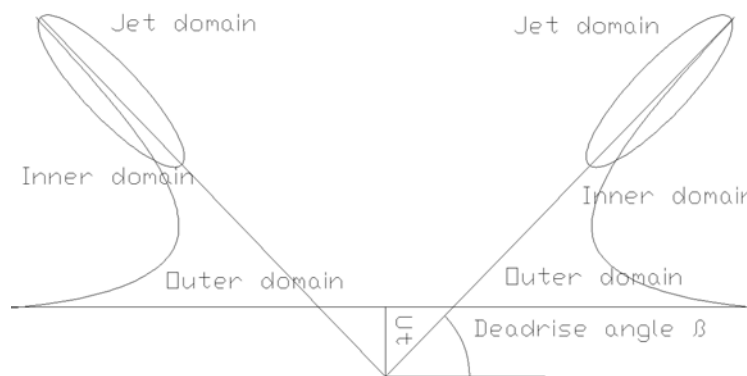


**Figure 3-8 Jet domain, inner domain and outer domain – wedge.**

As said, Von Karman was the first to study theoretically water impact. The problem was analysed by using equivalent plates to picture the falling object. In other words, In other words, the object was approximated by a flat plat for 2D. Von Karman

idealized the impact as a 2D wedge entry problem on a calm water surface and used this theory to estimate the water impact load on a seaplane during landing. Since the impact is so rapid, Von Karman assumed very small water surface elevation during impact and negligible gravity effects. However, not including the water elevation, the impact load is underestimated, particularly for small deadrise angles. The difference between both methods (Von Karman and Wagner) lays in the fact that Wagner includes this elevation. Hence, Wagner derived a more realistic water impact theory.

Note, when the deadrise angle  $\beta$  is assumed quite small and gravity neglected, the flow under the wedge can be approximated by the flow around an expanding flat plate in a uniform flow with velocity  $V$ . However, the theory was found to be not suitable for  $\beta < 3^\circ$ , since in that case air trapping and compressibility of water plays an increasingly important role. This was shown by Takemoto (1984) and Yamamoto (1984) [10, 11]. However, for angles between 3 and 15 degrees the Wagner theory and experiments matched quite well. For deadrise angles smaller than 20 degrees, the pressure distribution shows a peak near the spray root of the water elevation and for higher deadrise angles, the distribution becomes smoother. First, to fix thoughts, the value of the horizontal axis  $Z/Vt$  (and  $Y/Vt$ ) is a dimensionless distance as can be seen on Figure 3-9.  $Z$  equals zero at the height of the calm water surface.  $Vt$  (i.e.  $Ut$ ) is the penetration depth.  $Z/Vt$  equals minus 1 at the lowest point of the object. The definition of the pressure coefficient is function of the position  $y$  and time  $t$  and is given in Equation 3-5 [12].

$$C_p(y,t) = \frac{P(y,t)}{\frac{\rho V^2}{2}}$$

**Equation 3-5 Definition of the pressure coefficient.**

The pressure peak moves towards the bottom (lowest point) of the 2D wedge with increasing deadrise angles, certainly for deadrise angles higher than 45 degrees as is shown in Figure 3-10 (Zhao & Faltinsen, 1993 & 1996) [13, 14]. Mei et al. (1998) developed an analytical 2D method using the potential theory of Wagner. Their objective was to create a model which is solvable in an analytical way instead of only numerically as was the case for Zhao. The location and magnitude of the maximum pressure in function of the deadrise angle and its accompanying free water surface is seen in Figure 3-11 for different deadrise angles larger than 3 degrees (10, 30, 45 and 81 degrees). On the right the shape of the jet, formed along the surface of the wedge, is seen. Note the strongly different scales from  $Y/Vt$  which

shows again that the peak pressures moves towards the lowest point of the wedge with increasing deadrise angles.

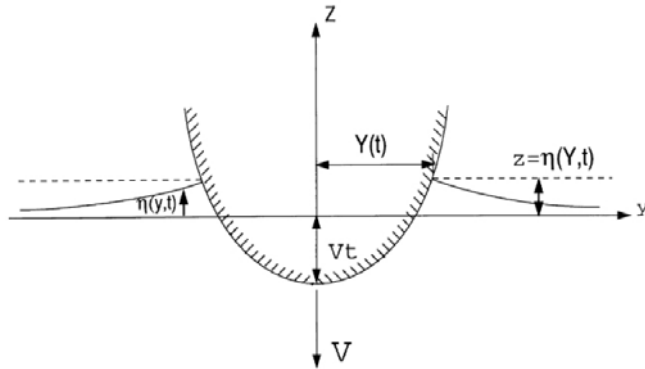


Figure 3-9 Sketch of the impact of an object on a water surface [12].

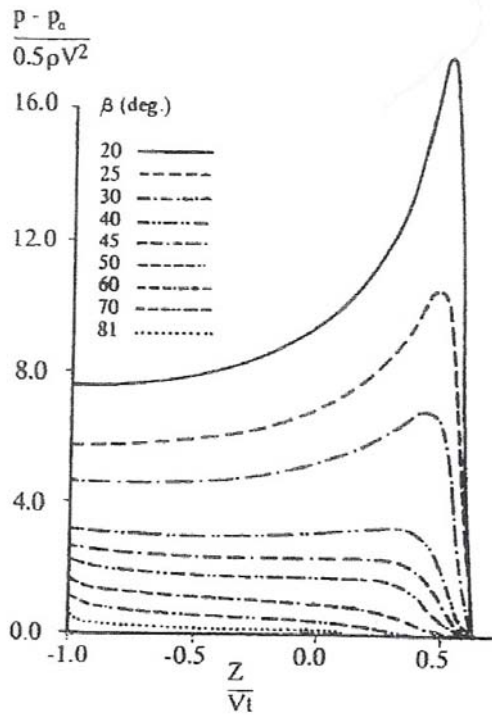
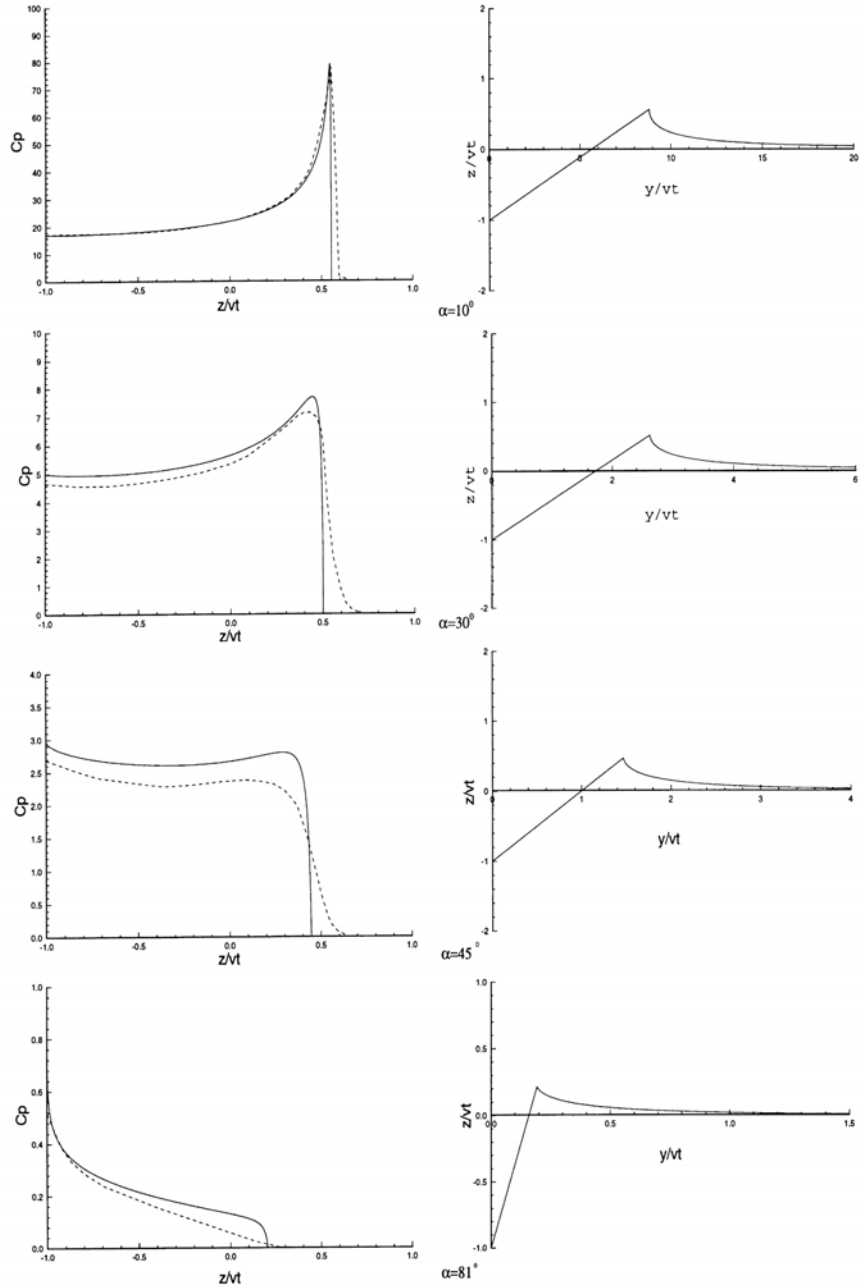
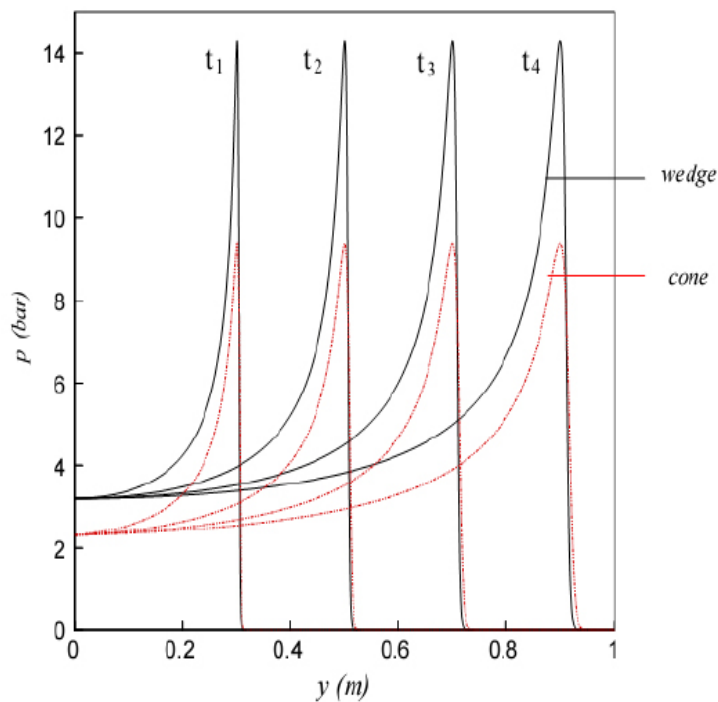


Figure 3-10 Pressure coefficient distribution on a 2D rigid wedge with constant impact speed  $V$  for different deadrise angles, the remote pressure  $p_a$  is zero in this case since it is the pressure before impact [13].



**Figure 3-11** Pressure distribution on a wedge falling on a free water surface; analytical solution according to Mei in continuous lines and of Dobrovolskaya (1969) in dot lines for several deadrise angles ( $\alpha = \beta$ ) [12].

A numerical method was proposed by Peseux et al. (2005) for rigid and deformable wedges with small deadrise angles (6, 10 and 14 degrees). Simulations were done in 2D (wedge) and 3D (cone) which gave higher pressures in 2D as is shown in Figure 3-12 for drop tests with a deadrise angle of 10 degrees at 6 m/s. Next, experiments were done and compared with the numerical solution. There, it was concluded that there is a good correspondence between both but that the numerical model is conservative. First, a peak pressure occurs on the cone and second, it decreases until a constant value is reached. However, the numerical method is conservative which means that the numerical peak pressures are higher than the experimental ones. A possible explanation is the trapped air under the object for small deadrise angles. Next, according to the analytical solution the peak pressure is constant on the cone but the experiments show that this is not the case due to the deceleration of the object. Finally, the experiments with a deformable object show larger differences with the simulations [15].



**Figure 3-12** Comparison between the simulation on a 2D wedge and a 3D cone with a deadrise angle of 10 degrees and a start velocity of 6m/s at four different times by Peseux et al. (2005) [15];  $y(m)$  is the distance on the edge of the wedge or cone starting from its bottom.

Experimental data for the drop of a wedge are described by Yettou et al. [16]. The influences of drop height, deadrise angle and mass are researched. A comparison is made with the analytical solution of Mei et al. [12] and Zhao and Faltinsen [13, 14]. A wedge moving with constant velocity results in a  $C_p$  only depending on the deadrise angle. The measured maximum values match very well with the analytical solutions (5% deviation) but the pressure after impact is overestimated by Mei et al. The mass of the wedge does not have any influence on the maximum pressure coefficient when a constant velocity is assumed. However, the velocity of the wedge decreases fast after impact and this phenomenon is more pronounced for smaller deadrise angles (i.e. larger wedge angles).

Lin and Shieh (1997) [17] measured the flow field with a high speed camera and calculated the velocity field. Also, the pressure was measured on certain locations on the objects (flat plate and 2D cylinder). The dimensionless impact pressure for the cylinder at several impact velocities is given in Figure 3-13. Two acrylic cylinders were used both with a length of 0.2 m, one with a diameter of 0.2 m and the other one with a diameter of 0.3 m. The results at zero degrees have a large deviation with a maximum  $C_p$  value of about 120. Of course, it can not be stated whether or not this is the real maximum. For the experiments at 30 degrees of the cylinder the pressure coefficient is about the same for all impact velocities.

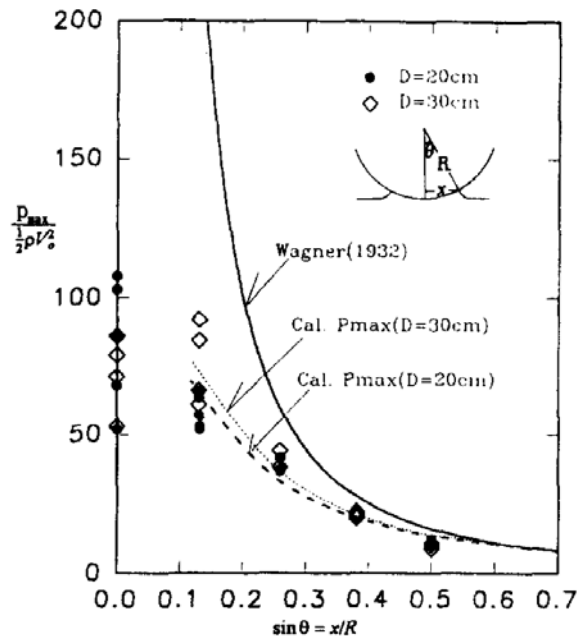
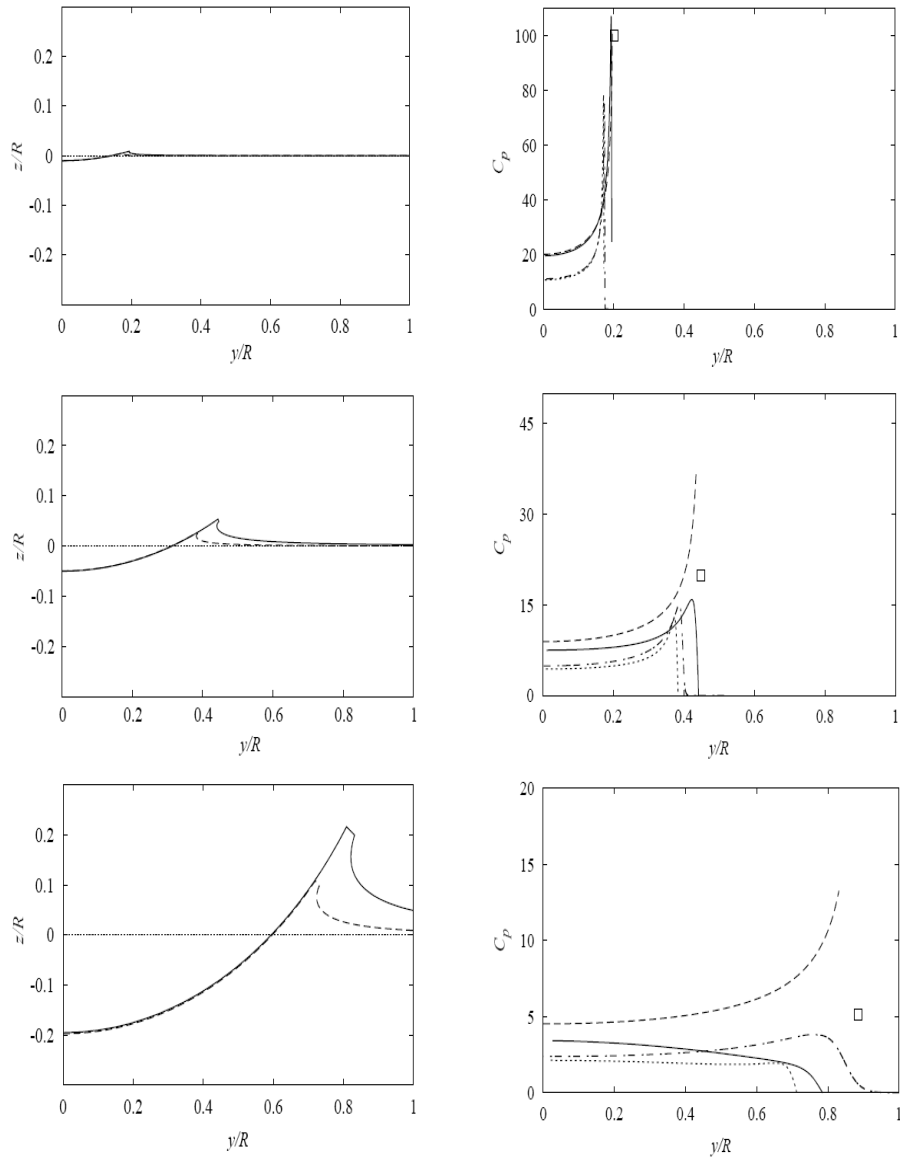


Figure 3-13 Results of Lin and Shieh; dimensionless pressure coefficient[17].

Battistin and Iafrati performed numerical research about the water entry of symmetric and axisymmetric bodies, with focus on the pressure distribution and the total hydrodynamic load on these bodies [18]. An incompressible fluid was used in a one phase model. The influences of the gravity and the surface tension were neglected in this work. The calculations were compared with experimental data. The results for a 2D cylinder and a 3D hemi-sphere are given in Figure 3-14 at three values of the dimensionless penetration depth  $z/R$  with  $R$  the diameter of the cylinder and  $z$  the depth of the cylinder relative to the free water surface. The corresponding pressure distributions are also depicted and compared with the asymptotic estimate provided by Faltinsen and Zhao (1997). Numerical results of Battistin and Iafrati are in good agreement with the asymptotic theory only during the initial stage of the impact. Later, as mentioned, due to the increased deadrise angle, the asymptotic solution is unable to provide a good estimate. The horizontal axis is the ratio  $y/R$  with  $y$  the arc length of the cylinder starting from the bottom. Due to the three-dimensional effect in the case of the hemi-sphere, a reduction of the wetted portion of the body contour and of the overall pressure distribution is noted. The research field of slamming for 3D objects stays quite limited. For this reason additional research was done at the Department of Coastal Engineering of Ghent University as a result of the Seewec project. In the master thesis of S. Victor (2007) the 2D-Wagner theory for wedges was extended to 3D-theory for axisymmetric objects. The object was approximated by a flat circle-shaped plate with increasing radius for 3D. The most important achievements were the formulated equations for a cone with deadrise angle 45 degrees which is given in Equation 3-6 and a hemi-sphere which is given in Equation 3-7 [19, 20]. In this equation  $r$  is the variable radius of the cone as it is entering the fluid,  $\rho$  the density of the fluid ( $1025 \text{ kg/m}^3$  for seawater),  $t$  the time and  $U$  the drop velocity. The product  $U \cdot t$  is the penetration depth of the cone. Figure 3-15 shows how this distribution looks like along the edge of the cone at a fixed time. The symbols in the formulae of the hemi-sphere have the same definition. However, there is one extra symbol,  $R$ , which is the constant radius of the hemi-sphere.

In a study by J. Wiencke (2001 & 2005) [21, 22], the slamming impact from breaking waves on a vertical cylinder has been both theoretically and experimentally investigated. Analytical expressions were proposed for the impact force, the pressure distribution and the wetted surface as a function of time. For the slamming phenomenon, the pressure distribution is most relevant hence it is given in Equation 3-8. Explanation of most geometrical symbols is done with the help of Figure 3-16 which still leaves the density  $\rho$  ( $\text{kg/m}^3$ ) and a dimensionless factor  $u$  which is a function of  $c$ . The distance  $c$  is a function of the time  $t$ .



**Figure 3-14** Comparison between the impact of a 2D cylinder and a 3D hemi-sphere. Left: free surface at impact with a cylinder (—) and a hemi-sphere (---) at three penetration depths  $z/R = 0.01$ ,  $0.05$  and  $0.2$ . Right: pressure distribution for the same penetration depths for the cylinder, Battistin and Iafrati (—) and Faltinsen and Zhao (--- and  $\square$ ) and for the hemi-sphere, Battistin and Iafrati (...) and Faltinsen and Zhao (-·-) [18].

$$P_{45} = \frac{1}{2} \rho U^2 \left[ 1 - \frac{4 \left( \frac{r}{U.t} \right)^2}{\pi^2 \left( \frac{16}{\pi^2} - \left( \frac{r}{U.t} \right)^2 \right)} + \frac{64}{\pi^3 \sqrt{\frac{16}{\pi^2} - \left( \frac{r}{U.t} \right)^2}} \right]$$

**Equation 3-6** Pressure distribution along the edge of a cone of 45 degrees [19].

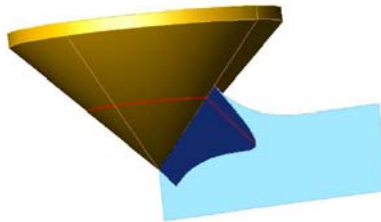


**Figure 3-15** Pressure distribution on a cone with a deadrise angle of 45 degrees; 3D Wagner according to S.Victor [19].

$$P_{bol} = \frac{1}{2} \rho U^2 \left[ 1 - \frac{4 \left( \frac{r}{U.t} \right)^2}{\pi^2 \left( \frac{3R}{U.t} - \left( \frac{r}{U.t} \right)^2 \right)} + \frac{6}{\pi \sqrt{\frac{3U.t}{R} - \left( \frac{r}{R} \right)^2}} \right]$$

**Equation 3-7** Pressure distribution along the edge of a hemi-sphere [19].

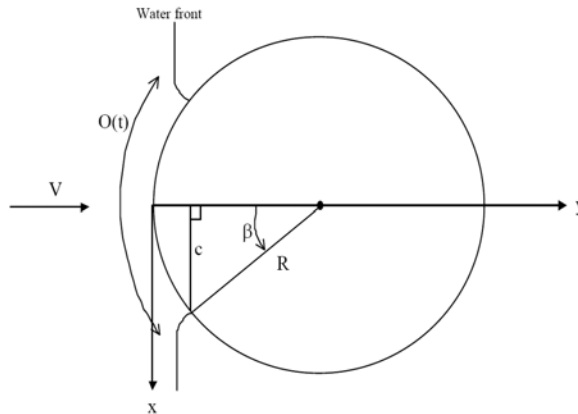


**Figure 3-16** Schematic top view of the section of a breaking wave on a cylinder; explanation of the geometrical symbols used in the pressure distribution of Wiencke.

$$p(x,t) = \rho V^2 \left[ \frac{1}{u \sqrt{1 - \left(\frac{x}{c}\right)^2}} - \frac{1}{2 \left(1 - \left(\frac{x}{c}\right)^2\right)} \right]$$

**Equation 3-8 Pressure distribution in space (x) and time (t) on cylinders according to Wiencke; c is a function of time.**

Finally, the Det Norske Veritas (DNV) norm has proposed a conservative ‘average pressure’ formula for slamming. This is the one used within the calculations since DNV is a world wide accepted norm [6]. More explanation about DNV norms for slamming conditions is given in paragraph 3. 3.

In conclusion it can be stated that the most important parameters for the distribution of the pressure are the local deadrise angle, the impact speed, the drop height of the object, the weight, stiffness and 3D effects of the falling object [23].

### 3. 3. PRESSURE ESTIMATIONS FOR THE FEA ON THE BUOYS

#### 3. 3. 1. Bottom slamming

A constant pressure, calculated using DNV classification notes 30.5, was used to dimension the buoys in a conservative way. Also, the highest possible point absorber velocity is taken as the one caused by a free fall of 5 meter. This 5 meter is the maximum stroke of the buoys on the full scale platform. The equivalent static slamming pressure can be calculated from Equation 3-9 according to DNV. This norm states that structural members near the water surface are exposed to forces caused by wave slamming.

$$p_s = 0.5 \rho C_{pa} v^2$$

**Equation 3-9 Space average slamming pressure [6].**

With

$p_s$  = space average slamming pressure [Pa]

$\rho$  = the mass density of the fluid [kg/m<sup>3</sup>], here seawater which is 1025 kg/m<sup>3</sup> at 15°C

$v$  = relative normal velocity between water and member [m/s]

$C_{pa}$  = space average slamming pressure coefficient [-]

According to DNV, the average slamming pressure coefficient is (or should be) determined using recognised theoretical and/or experimental methods. Further in this paragraph the values for a wedge and a cylindrical shape are given. Coefficients for local peak pressures could be considerably larger than these average ones.

Here,  $v$  can be considered as the drop speed. As mentioned, the maximum drop height  $h$  is 5 meters and the gravitational constant  $g$  is 9.81 m/s<sup>2</sup>, hence  $v^2$  is about 98.1 m<sup>2</sup>/s<sup>2</sup> according to Equation 3-10.

$$v^2 = 2 g h$$

**Equation 3-10 Square of the theoretical drop speed.**

For flat bottom slamming taking into account cushioning and 3D effects, the slamming coefficient should not be taken less than  $2\pi$  according to DNV.

An example of the creation of an aircushion is shown in Figure 3-17 where the entry of a rigid body with a horizontal bottom is depicted.

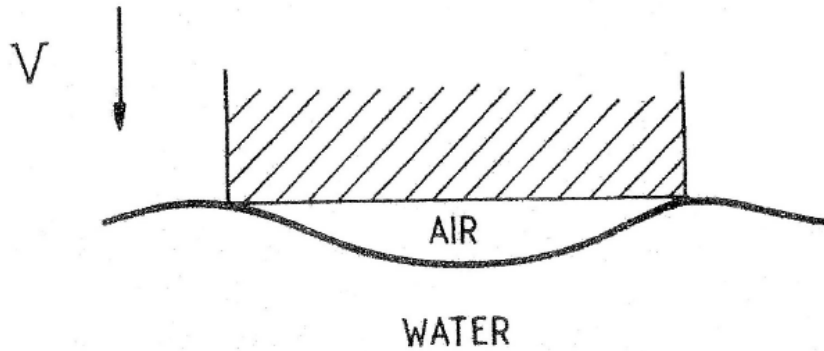


**Figure 3-17 Deformation of the free water surface and the creation of an air cushion at entry of a rigid object with horizontal bottom.**

For bodies with a horizontal bottom or with small deadrise angle this air cushion is formed. It is pushed in the water and due to the compressibility of air, air bubbles are formed in the water. The air cushion effect results in lower slamming pressures in comparison to the Wagner theory.

Equation 3-9 results in a pressure of 0.316 MPa. The vertical height of this sector is about 1 meter independent of the shape, chosen in consent with Brevik. The background can also be found in the DNV code where this height is taken equal to  $0.25 * H_b$  with  $H_b$  equal to  $1.4 * H_s$ .

These loads are used in finite element calculations discussed in Chapter 5. Nevertheless it should be mentioned that DNV states that for a smooth cylinder the  $C_{pa}$  coefficient can be taken lower than  $2\pi$  however not lower than 3. For a wedge shaped body with deadrise angle  $\beta$  above 15 degrees the slamming factor should not be taken less than:

$$C_{pa} = \frac{2.5}{(\text{tg } \beta)^{1.1}}$$

**Equation 3-11 Space average slamming pressure coefficient for wedges with  $\beta > 15$  degrees.**

Further on in this doctoral thesis (Chapter 5) the formula of the 45 degrees cone out of the work of S. Victor (2007) has also been assessed with calculations on the final

chosen shape since the bottom of that point absorber was such a '45-cone'. However, this is discussed in Chapter 5 as soon as this case occurs.

### 3. 3. 2. Breaking wave slamming

The DNV classification notes 30.5 was also used for the breaking wave calculations. The space average pressure can again be calculated as in Equation 3-9. However, the drop velocity is now interpreted as the wave celerity. The maximum considered celerity is the one of the 25 year storm and equals 12.1 m/s which results in a pressure of 0.472 MPa. The pressure is applied on a circle segment of 60 degrees. The chosen height is slightly different from the one for bottom slamming and is given in Chapter 5 for the several shapes.

In Chapters 7 and 9 the results of laboratory as well as large scale testing experiments are discussed and feedback is given towards the used DNV norm and some of the other literature mentioned in paragraph 3. 2. 3.

---

### 3. 4. REFERENCES

1. SEEWEC - Internal report from Brevik Engineering. FO3 - Prototype 1:1. Engineering and Construction. Section 3 Loads. 2006.
2. Safehaven Marine Website. [cited 2009 19/03]; Available from: <http://www.safehavenmarine.com/NEWSLETTER%20JAN%202009.htm>.
3. Hydrolance Website. [cited 2009 19/03]; Available from: <http://www.hydrolance.net/Page%2031%20-%20Ocean%20Bathtubs.htm>.
4. M. Vantorre, Manoeuvrer- en Zeegangsgedrag van Maritieme Constructies, Course at Ghent University, Faculty of Engineering, Chapter 4. 2005-2006. p. 15 - 24.
5. J. DeRouck, Zee- en havenbouw. Course at Ghent University, Faculty of Engineering, Chapter 4. 2005-2006.
6. Det Norske Veritas (DNV). Classification notes No. 30.5 "Environmental conditions and environmental loads". Section 6 "Wave and current loads". March 2000.
7. SEEWEC - Sustainable Economically Efficient Wave Energy Converter. Sixth Framework Program (FP6), Specific Targeted Research Project (STREP), Priority 6-1: Sustainable Energy Systems, 2005-2008(contract nr. SES6-CT2005-019969).
8. vonKarman, The impact on seaplane floats during landing. 1929: p. 321.
9. H. Wagner, Uber Stoss- und Gleitvorgänge an der Oberfläche von Flüssigkeiten. Zeitschrift für Angewandte Mathematik und Mechanik, 1932. 12(4): p. 193-235.
10. Takemoto, Water impact test of a wedge with rectangular plates and its analysis. J. Soc. Nav. Arch. Japan 156, 1984.
11. Y. Yamamoto, Okada et al., Cushioning action for horizontal water impact of a at plate. J. Soc. Nav. Arch. Japan 153, 1983.
12. X. M. Mei, Y. M. Liu et al., On the water impact of general two-dimensional sections. Applied Ocean Research, 1998. 21(1): p. 1-15.
13. R. Zhao and O. M. Faltinsen, Water entry of two-dimensional bodies. Journal of Fluid Mechanics, 1993. 264: p. 593-612.
14. R. Zhao, O. M. Faltinsen et al., Water entry of arbitrary two-dimensional sections with and without flow separation. Proceedings of the 21<sup>st</sup> Symposium on Naval Hydrodynamics, Trondheim, Norway, June 24-28, 1996.
15. B. Peseux, L. Gornet et al., Hydrodynamic impact: numerical and experimental investigations. Journal of Fluids and Structures, 2005. 21: p. 277-303.
16. Yettou, Desrochers et al., Experimental study on the water impact of a symmetrical wedge. Fluid Dynamics Research, 2006. 38: p. 47-66.
17. M.-C. Lin and L.-D. Shieh, Flow visualization and pressure characteristics of a cylinder for water impact. Applied Ocean Research, 1997. 19: p. 101-112.

18. D. Battistin and A. Iafrati, Hydrodynamic loads during water entry of two-dimensional and axisymmetric bodies. *Journal of Fluid and Structures*, 2003. 17: p. 643-664.
19. S. Victor, Onderzoek naar slammingsverschijnselen bij point absorbers: experimenteel en literatuurstudie, Ghent University. Faculty of Engineering, Master thesis academic year 2006-2007.
20. G. DeBacker, M. Vantorre et al., Experimental Investigation of Water Impact on Axisymmetric Bodies. 2008.
21. J. Wienke and H. Oumeraci, Breaking wave impact force on a vertical and inclined slender pile - theoretical and large-scale model investigations. *Coastal Engineering*, 2005. 52: p. 435-462.
22. J. Wienke, Druckschlagbelastung auf schlanke zylindrische bauwerke durch brechende wellen - theoretische und großmaßstäbliche Laboruntersuchungen, in Technische Universität Carolo-Wilhelmina zu Braunschweig. PhD thesis. 2001.
23. O. M. Faltinsen, Hydrodynamics of High-Speed marine vehicles - chapter 8: Slamming, whipping and springing. Norwegian University of Science and Technology, Trondheim., 2006.

## Chapter 4

### MATERIAL SELECTION AND BASIC MECHANICAL CHARACTERISATION

*In this chapter a short introduction on composite material is given. Next, the filament winding production method is discussed. The necessary finite element software is introduced and some difficulties inherent to the production method mentioned. Also, the vacuum infusion production method is explained. For both kinds of production methods specific materials were selected for use on the buoys within the Seewec project. Material characterisation tests were done according to ASTM standards for the suggested materials. Finally, those results are discussed.*

#### 4. 1. COMPOSITE MATERIALS

Fibre reinforced composite materials consists out of several components: fibres for strength and a matrix (i.e. the resin) to bind the material. The fibres are the most important constituent because they carry most loads. They determine the stiffness of the material and limit the tear rate within the matrix. Different architectures exist to embed the fibres in the matrix [1]. On the upper left of Figure 4-1 a microscopic image of unidirectional (UD) fibres is shown, on the lower left an image of a stack of woven fabric layers is depicted. Both are pictured schematically on the right in the figure. Additionally, on the upper right a layer of chopped fibres (which has quasi isotropic properties in-plane) is seen. Finally, the lower right of the figure depicts a laminate where all kinds of layers (UD, chopped fibres and textures) can be put together in a certain lay-up to achieve the desired properties of the material.

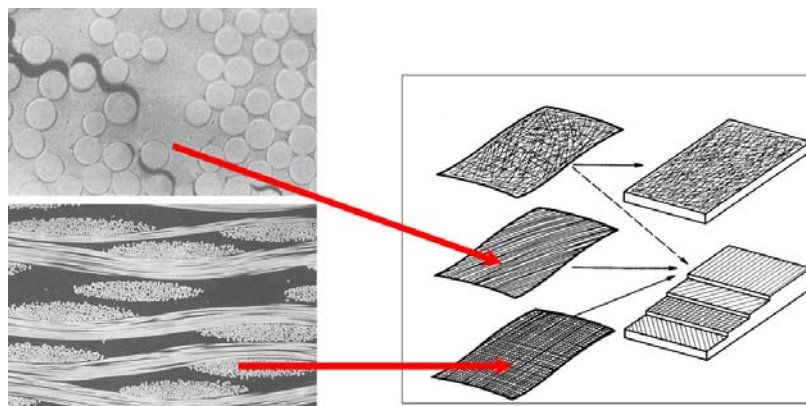


**Figure 4-1 Composite material: orientations fibres within the matrix [1].**

The matrix keeps the fibres together, protects them and takes care of the load transfer. The most occurring class of the resins is the one of the polymers. There are two kinds of matrices in this family: thermoplastic and thermoset materials. Thermoset materials cure by means of a chemical reaction after some time or after heating. They can not be re-melted. Until now, thermoset resins are most applied because of their workability at room temperature, low viscosity and good ‘wetting’ of the fibres. Thermoplastics become liquid again after heating and they could be re-used. Nevertheless the recycling of reinforced thermoplastics is in reality not straight forward. Research towards thermoplastics is certainly worthwhile [1].

For now the well known methods of thermoset resins are considered. The fibres and the matrix are separated by a boundary surface. This can be a subsequent treatment of the fibres or a coating and is very important for the bond of matrix and fibres. The boundary layer increases the wetting of the fibre and plays a role in the transfer of the load between fibre and matrix.

The properties of a composite structure are dependent on those of their components, namely they are dependent on the chosen fibres and of the chosen matrix. However, they also depend on the production method [2]. Filament winding (used at SMC for silos) is the cheapest and fastest method to produce fibre reinforced cylindrical or axisymmetric components. With vacuum infusion (used at STY for yachts) it is possible to make almost any shape. These methods are explained in the next paragraphs.

## 4. 2. FILAMENT WINDING

### 4. 2. 1. Introduction

Within the filament winding technique a set of continuous fibres is impregnated in a resin bath and is wound around a rotating mandrel. The main advantage of filament winding is low production and labour cost [3]. The disadvantage is a relative high initial cost of the winding machine and a limited choice of shapes. The concept of filament winding was introduced at the beginning of the nineteen forties and the first applications were there from the nineteen fifties on. At the time, a winding machine had only two moving axes: one responsible for the spindle rotation and one for horizontal carriage. The first improvement consisted out of a mechanical system which allowed the operator to program the machine with the help of transmissions, belts, pulleys and chains. These machines had limited possibilities and capacity. In the mid seventies the design was improved a lot because of the introduction of servo technology. The desired path of the fibres was converted into a machine movement with the help of a black and white interface on a drum. Later on, this was replaced by a photo-optic device which made it possible to control the machine. Again some years later a third moving axis (perpendicular to the horizontal carriage) was introduced: the crossfeed carriage. The eighties and the nineties were marked with an enormous progress within the field of computer technology. Hence, a faster interpretation of data resulted in a smoother movement of the machine and a far more accurate placement of the fibre. Now, computers take over all functions previously done by chains and belts. The control systems specify positions and velocities in a very accurate way. In addition, the number of moving axes increased and today, winding machines up to six of them exist. An example is shown in Figure 4-2. In the mean while, software (e.g. Cadwind from Belgium) that automatically determines the best fibre path was designed in the industry. With the help of this software more complex geometries can be wound, even non-axisymmetric parts such as T-shapes.



**Figure 4-2** Example of a 6-axes winding machine [4].

#### 4. 2. 2. Winding patterns

The properties of a wound structure vary with the used fibre pattern. The different sorts of patterns are helical winding, circumferential or hoop winding and polar winding. In helical winding, the mandrel rotates at a constant speed while the fibre feed carriage transverses back and forth at a speed regulated to generate the desired helical angles as shown in Figure 4-3.

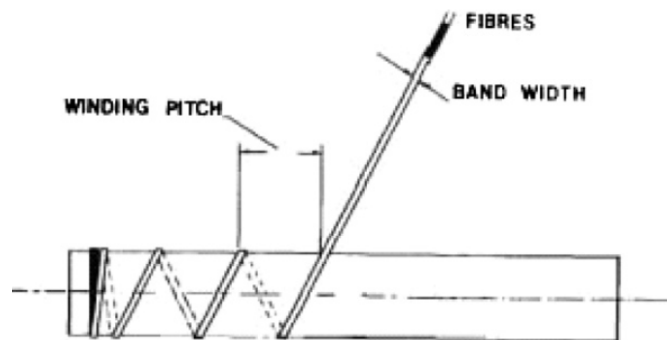


Figure 4-3 Helical winding [2].

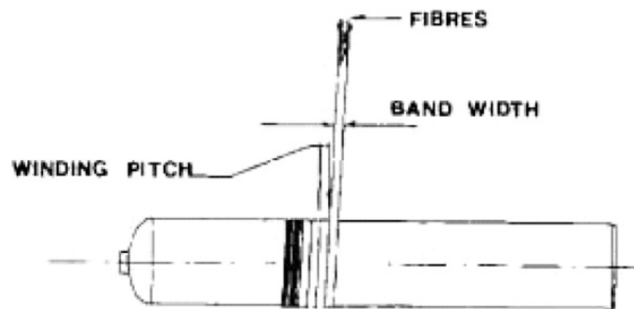


Figure 4-4 Hoop winding [2].

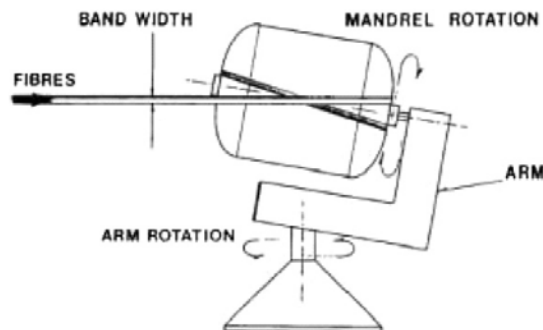


Figure 4-5 Polar winding [2].

Hoop winding is known as circumferential winding. In hoop winding, a high-angle helical winding approaches an angle of 90 degrees. Each full rotation of the mandrel advances the band delivery by one full bandwidth as shown in Figure 4-4. In polar winding, fibres are wrapped from pole to pole, as the mandrel arm rotates about the longitudinal axis as shown in Figure 4-5. It is used to wind almost axial fibres on domed end type of pressure vessels.

#### 4. 2. 3. Applications

Examples of some applications are pressure vessels, pipelines, fuel tanks, and wind turbine blades. Figure 4-6 shows the winding of a wind turbine blade.



**Figure 4-6 Winding of a wind turbine blade [4].**

Silos (made e.g. at SMC) are easily made with this production method. Some are shown in Figure 4-7 [5].



**Figure 4-7 Applications filament winding: silos [5].**

Next, an example of made pressure vessels is shown in Figure 4-8. Finally, it is possible to make tubes or pipes in all sorts. Again a picture is shown (Figure 4-9). Of course this is a non-limited list of possible applications with this production method.

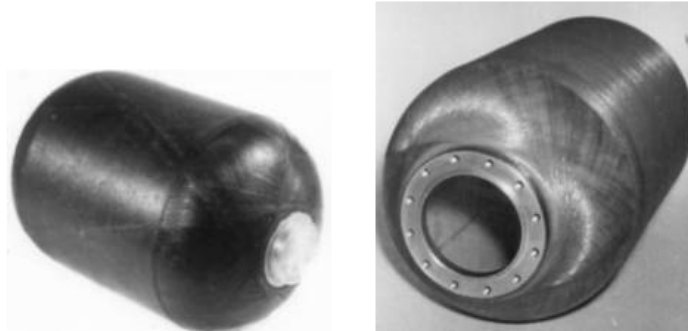


**Figure 4-8 Applications filament winding: pressure vessel [6].**



**Figure 4-9 Applications filament winding: tubes [7].**

More explanation about the filament winding production method can be found in Chapter 6 where the working of a particular winding machine at laboratory scale is discussed.

### 4.3. VACUUM INFUSION

#### 4.3.1. Introduction

The vacuum infusion production method is a technique that uses vacuum pressure to drive resin into a mould. Materials are laid dry into the mould and a vacuum is applied before the resin is introduced. Once complete vacuum is achieved, the resin is literally sucked into the mould via carefully placed tubing. The resin fills the open spaces created by the vacuum; it wants to take the path of least resistance. A schematic view of this technique is shown in Figure 4-10. To fix thoughts, a general concept with the resin infused into the laminate at a centre point is shown in Figure 4-11. From there on the resin is transported through vacuum pressure [8].

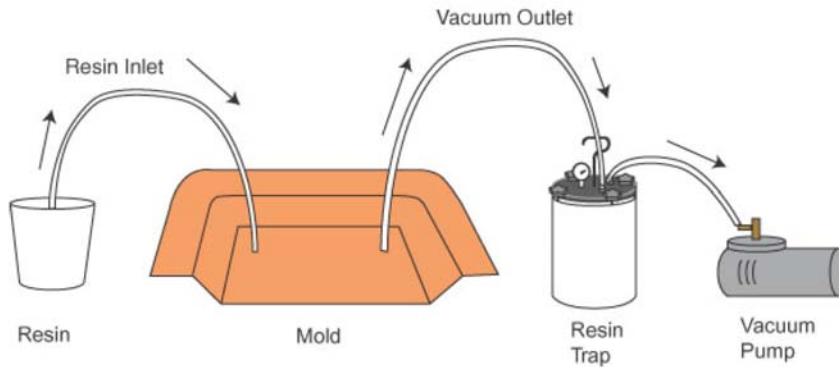


**Figure 4-10 Schematic view of the vacuum infusion production method [8].**

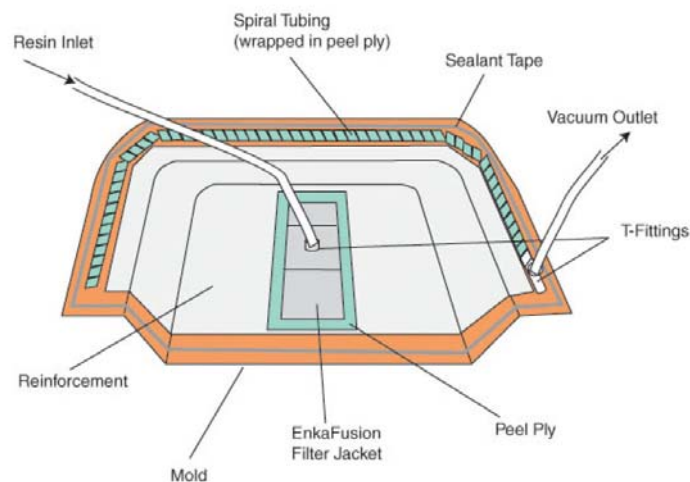


**Figure 4-11 General concept of vacuum infusion with the resin infused into a centre point [8].**

### 4. 3. 2. Applications

As for filament winding, for vacuum infusion several applications are available. The first one is used by one of the production partners in the project, STY. They make e.g. hulls of ships with this production method which are shown in Figure 4-12 [9].

Next, wind turbine blades can also be made by vacuum infusion and a picture of those is shown in Figure 4-13. As is seen before, filament winding is also used for wind turbine blades. The company LM Glasfiber uses both production methods for it [10]. Again, as for filament winding, the examples are of course numerous. Vacuum infusion is used for several kinds of shapes, other examples are e.g. car parts, surfing boards, etc.



**Figure 4-12 Applications for vacuum infusion: hull of a boat [9].**



**Figure 4-13 Applications for vacuum infusion: wind turbine blade [10].**

## 4. 4. SELECTION OF MATERIALS FOR THE POINT ABSORBERS

### 4. 4. 1. Certified materials

It was proposed both by SMC and STY to use only materials with certified specifications over different production batches which means that the manufacturing of composites with constant properties is guaranteed. As was explained there was opted to go for composite material due to its light weight, no corrosion and cheap cost. Hence, within WP4 of the Seewec project, the pool of materials was limited to the composite family. A feasibility approach for the point absorbers concerning the use of certain composite materials has been done. An extended research has been done concerning technical issues (simulations and experimental) and overall cost/benefit issues.

### 4. 4. 2. Material proposal by SMC

Several materials are suitable for winding applications. Concerning the fibres, E-glass, S-glass, aramide fibres and carbon fibres are used. A short overview is given of their respective properties in [1]. E-glass fibres are used for commercial and industrial applications including winding. S-glass is used for pressure vessels and aviation. Aramide fibres have good properties for impact, bad for compressive and shear stress. Carbon fibres are good for tensile stress and stiffness.

	Tensile strength (MPa)	E-modulus (GPa)	Cost
E-glass	3000	70	low
S-glass	4000	85	higher
Carbon	3000	130	higher
Aramide	1700-3000	200-500	higher

**Table 4-1 Overview of some properties of E-glass, S-glass, Carbon and Aramide.**

Next, also several resin types exist. The most used resin families (thermoset resins) are polyester and epoxy resins [1].

Polyester: low cost, curing at room temperature, only compatible with glass fibres.

Epoxy: higher cost, curing at increased temperature, good chemical resistance and higher viscosity; it is known in the marine industry for its bonding strength.

Vinylester: stronger than polyester resins, cheaper than epoxy resins, hybrid form of polyester resin which has been toughened with epoxy molecules within the main molecular structure; bonding issues due to its continuous curing as it ages

After an extensive internal study and after discussions with its material suppliers, SMC has proposed a material combination that fits well with its present filament winding process and that is compatible with a marine environment.

First, for the fibres, SMC has proposed to use E- glass Vetrotex RO99 P192 because of its good price, its suitability for filament winding and good processability (e.g. wetting with the resin) [11]. Second, concerning the resin, two resin systems were compared, of which DSM Synolite 1717-N-1 has finally been proposed because of its better property/price ratio [12]. This basic resin is a standard unsaturated polyester resin based on isophthalic acid in solution with styrene. It has good mechanical properties, corrosion resistance properties which is good for seawater conditions, and it has been used for a range of special marine related projects. Applications in a similar environment are guaranteed to reach a lifetime of up to 40 years [13]. The second resin, DSM Atlac 430, is a vinyl ester, based on bisphenol-A epoxide, dissolved in styrene. The mechanical properties are better than Synolite 1717-N-1. The chemical resistance is extremely high. The resin is also available for winding applications [14]. Nevertheless this resin is more expensive and since the main design criteria are low cost and series production, the Synolite 1717-N-1 was chosen.

#### 4. 4. 3. Material proposal by STY

STY suggested using Lloyds certified resins, since these are commonly used in marine applications and because it has positive experiences with those resins. In order to keep some degree of freedom (related to stiffness, strength, production rate and cost) STY has proposed to start with a benchmark test on different material combination samples, measuring bending stiffness and mechanical strength of each composite. The following most commonly used combinations were proposed:

- glass fibre – polyester resin
- glass fibre – epoxy resin
- carbon fibre – epoxy resin
- carbon fibre – vinyl ester resin
- glass fibre – vinyl ester resin

Based on the results of these benchmark tests, the purpose was to choose two composites to be tested in full as happened for the material of SMC.

As a result of the proposed candidate production processes (winding process at SMC and vacuum resin infusion at STY), the laminate of SMC consists out of a typical winding pattern of unidirectional fibres, whereas the laminate of STY consists out of stacked layers of fibre textile fabrics.

#### 4. 4. 4. Use of sandwich materials

In view of guaranteeing good local and global mechanical properties (bending stiffness and bending strength) at the lowest possible material consumption, and, because of the required resistance against continuous water slamming, the laminates of the point absorbers could consist of a sandwich construction. A sandwich structured composite is a special class of composite materials and it is fabricated by attaching two thin skins to a lightweight but thick core. The core material is normally low strength material, but its higher thickness provides the sandwich composite with high bending stiffness. A schematic view of a sandwich material is shown in Figure 4-14.



**Figure 4-14 Sandwich structure with a honeycomb core.**

STY has a long experience with the use of sandwich construction, and has for the purpose of Seewec performed a comparison of some frequently used materials: balsa wood, plywood, PVC-foam and honeycomb. Of these suggested materials, PVC foam seems by far the best choice and hence is proposed. It is easy to handle and to shape in comparison with e.g. plywood and honeycomb, it comes in different densities, and is therefore easy to optimize for different applications, again in comparison with plywood. Additionally, it has a closed cell structure, and is thus not water absorbent as balsa wood and plywood are. The open cells at the surface guarantee a very good cohesion with the composite skins. Finally, it has proven resistance to damage.

Specific tests on different sandwich samples were not done since this would have lead too far. However, in Chapter 5 finite element calculations were done on sandwich buoys with PVC foam as the core material to assess an improvement in resisting the loads. In Chapter 8 and 9 the production and testing of a sandwich buoy is discussed.

#### 4. 5. PREPARATION OF TEST SAMPLES WITH FILAMENT WINDING

Different plates were made with filament winding from the material proposed by SMC in order to do a full material characterisation according to the ‘American Society for Testing and Materials’ (ASTM) standards. On the left of Figure 4-15 the fibres are going through the resin bath, on the right the winding over the mandrels for the flat plates is shown. The procedure for making flat plates with filament winding went as follows [15]. Three flat mandrel plates were fixed on a silo-mandrel at SMC. Next, the mandrel turned at a constant velocity and the fibres were wound on the mandrel plates almost unidirectional. Finally, the plates were removed from the mandrel and cut. In this way the 0 and 90 degrees plates were produced at the desired thickness according to the ASTM standards. For the +/- 45 degrees plate the same method was used, but instead of a unidirectional pattern, the machine was steered to cross wind the plates with an angle of 45 degrees.

The glass fibre used for all test plates was the one proposed by SMC, namely the E-glass Vetrotex RO99 P192 with a 2400 tex value. The unit tex is the amount of mass per unit length; 1 tex is  $10^{-6}$  kg/m. The Synolite 1717-N-1 resin was used due mainly for reasons of cost, as explained in paragraph 4. 4. 2. It cured at room temperature after thirty minutes. For these test plates no top coat was applied.



**Figure 4-15** Filament winding process at SMC while making the test plates.

Figure 4-16 gives an example of a laminate from which the specimens for the transverse compression tests were obtained. On the left of the figure the side view of the plate is depicted. There the thickness of the plate is depicted (10 mm) and the aluminium tabs. The front view of the plate is shown on the right. There, ten 90 degrees compressive samples are shown in the lower left corner of the plate. For

each kind of test, a different recommended lay-out exists in the ASTM standards. The specimens were cut from the laminates by water jet. Where imposed by the standards, end aluminium tabs were glued onto the specimens for adequate gripping and strain gauges were applied for the measurement of strains.

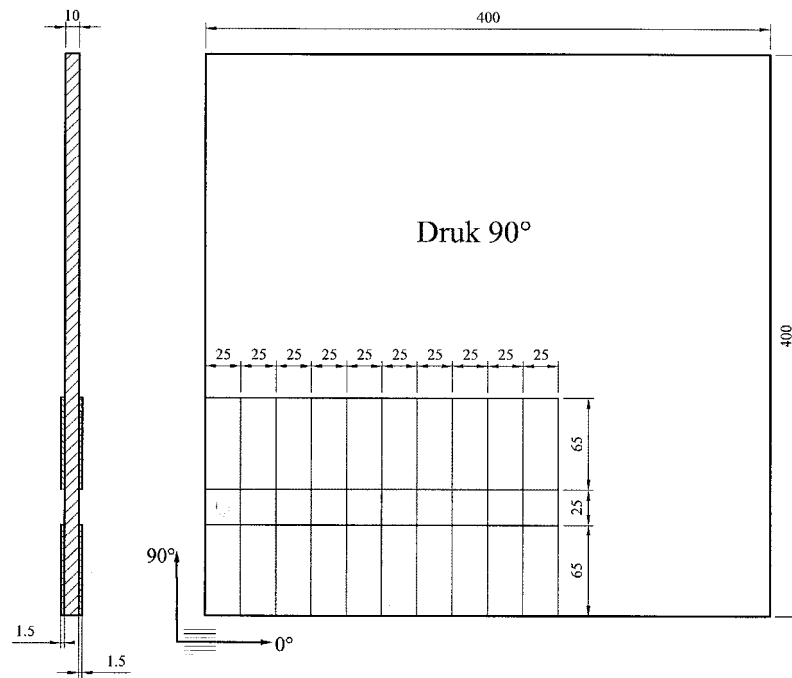


**Figure 4-16** Layout of laminate for characterisation of transverse compression [16, 17].

## 4. 6. TESTS ACCORDING TO ASTM STANDARDS FOR SMC

### 4. 6. 1. Stiffness and strength

For the determination of the stiffness and the strength of the unidirectional material (UD), the ASTM standards of Table 4-2 are used. The left column states which kind of test it is, the middle one shows the ASTM standard test number, and in the right column the experimentally determined material properties for each test are mentioned.

Test type	ASTM standard	Material properties
tensile test [0°]	ASTM D3039/D3039M	$E_{11,T}$ , $\nu_{12}$ , $X_T$
tensile test [90°]	ASTM D3039/D3039M	$E_{22,T}$ , ( $\nu_{21}$ ), $Y_T$
tensile test [+/-45°]2S	ASTM D3518/D3518M	$G_{12}$ , $S$
short beam test	ASTM D2344/D2344M	$\tau_{ILSS}$
compressive test [0°]	ASTM D3410/D3410M	$X_C$ , ( $E_{11,C}$ )
compressive test [90°]	ASTM D3410/D3410M	$Y_C$ , ( $E_{22,C}$ )

**Table 4-2 ASTM standards for stiffness and strength [15].**

With

$E_{11,T}$  = Tensile modulus of elasticity in the fibre direction

$\nu_{12}$  = Poisson's ratio, which is the ratio of the strain in the transverse direction of the fibres (2) to the strain in the fibre direction (1), when loaded in the fibre direction

$$= - \frac{\epsilon_{22}}{\epsilon_{11}}$$

$E_{22,T}$  = Modulus of elasticity in the direction perpendicular to the fibres

$\nu_{21}$  = Poisson's ratio, which is the ratio of the strain in the fibre direction (1) to the strain in the transverse direction of the fibres (2), when loaded in the transverse direction of the fibres

$$= - \frac{\epsilon_{11}}{\epsilon_{22}}$$

$G_{12}$  = Shear modulus

$\tau_{ILSS}$  = Interlaminar shear strength

$E_{11,C}$  = Compressive modulus of elasticity in the fibre direction

$E_{22,C}$  = Compressive modulus of elasticity in the direction perpendicular to the fibres

$X_T$  = Tensile strength in the fibre direction

$X_C$  = Compressive strength in the fibre direction

$Y_T$  = Tensile strength in the direction perpendicular to the fibre direction

$Y_C$  = Compressive strength in the direction perpendicular to the fibre direction

S = Shear strength  
in axes of orthotropy.

The tensile tests of 0, 90 and 45 degrees and the short beam tests have been done on the electromechanical Instron 4505 in the lab, shown at the left in Figure 4-17. The compressive tests of 0 and 90 degrees have been carried out on the servohydraulic Instron 8801, shown at the right on Figure 4-17.



**Figure 4-17 Mechanical instron (left) and the hydraulic instron (right) in the lab of Ghent University.**

For several tests, two strain gauges and an extensometer were used. The strain gauges have been ordered from the Measurements Group Company. The type of the strain gauges is CEA-06-250UN-350. These strain gauges have a 350  $\Omega$  resistance and are temperature-compensated for composites. They have been bonded with the M-Bond 200 adhesive kit. The extensometer is an Instron 2620-603 dynamic strain gauge extensometer with an absolute travel of  $\pm 1$  mm. Pictures of the extensometer and of strain gauges are given in Figure 4-18.



**Figure 4-18 Strain gauges (left) and extensometer (right).**

All signals have been read out with a National Instruments NI DAQPAD–6052E measurement card and Labview software. The sampling frequency of all signals is 20 Hz. Each strain gauge is calibrated before use with a precision shunt resistance of 60 kΩ, simulating a strain of 0.2900 %. The thickness and width of all specimens were measured with a digital micrometer.

As mentioned in Table 4-2 the tensile tests of 0 degrees should give the axial stiffness  $E_{11}$ , the Poisson ratio  $\nu_{12}$  en  $X_T$  [18]. The axial strain was measured by the extensometer and the longitudinal strain gauge, while the transverse strain was measured by the perpendicular strain gauge. The Poisson ratio is calculated from both strain signals. Figure 4-19 shows a test sample of the tensile test 0 degrees after fracture. The tensile test 90 degrees should give  $E_{22}$ , ( $\nu_{21}$ ) and  $Y_T$  [18]. The axial strain is measured by the extensometer, while the transverse strain is measured by the strain gauge. The Poisson ratio ( $\nu_{21}$ ) was calculated from both strain signals. Next, with this ratio a check-up with  $E_{11}$ ,  $E_{12}$  and  $\nu_{12}$  according to Equation 4-1 was done. Instead of 1 this relation equals 0.92 which is a very good match.

$$\frac{\frac{\nu_{12}}{E_{11,T}}}{\frac{\nu_{21}}{E_{22,T}}} = 1$$

**Equation 4-1 Relation between the longitudinal and transverse E moduli and Poisson coefficients [1].**

Figure 4-20 shows a test sample after fracture. Next, the test in tensile direction of +/- 45 degrees gives  $G_{12}$  and  $S$  [19]. The shear strain is calculated from the strain gauge signals. It is only valid until one of the strain gauges saturates. All specimens failed in shear failure mode as is shown in Figure 4-21. The short beam test should give us  $\tau_{ILSS}$  [17]. In Figure 4-22 the set-up is shown. Due to this short beam testing, the influence of the shear force is very large and the specimen fails by interlaminar shear, with cracks starting from the vertical end faces of the specimen. The corresponding “Interlaminar Shear Strength” (ILSS) is calculated with [17]:

$$\tau_{ILSS} = \frac{3}{4} \cdot \frac{P}{b \cdot d}$$

where  $P$  is the maximum load [N] and  $b$  and  $d$  are the width [mm] and thickness [mm].



**Figure 4-19** Test sample tensile 0 degrees after fracture.

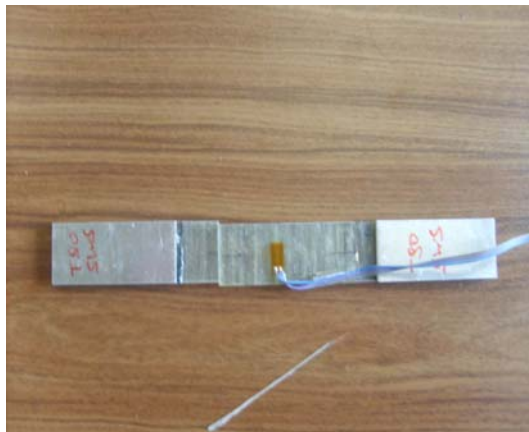


**Figure 4-20** Test sample tensile 90 degrees after fracture.



**Figure 4-21** Test sample tensile 45 degrees after fracture.

Next, the compressive test in 0 degrees gives  $X_C$  and  $E_{11,C}$  [16]. During the tests, it became obvious that the test samples broke because of buckling and not because of the compression. With those (4 test samples were already tested)  $E_{11,C}$  could still be calculated. This is done with the linear part of the stress-strain curve. However, additional measurements for the calculation of  $X_C$  were done on shortened test samples (also 4 samples) to avoid buckling. This worked quite; hence the buckling occurred probably due to too much deviation on the desired thickness (below the minimum) of the samples.

Finally, the compressive test in 90 degrees should give  $Y_c$  and  $E_{22,C}$  [17]. As buckling occurred, this measured maximum is not the real compressive maximum. For this test shortening the samples did not solve the problem. In this case some shape imperfections in the test samples were the reason for buckling. This is inherent to the production method of the test plates since they did not have a perfect finishing. All that can be said is that the real maximum is at least above this one.  $E_{22,C}$  is again calculated from the linear part of the stress-strain curve.

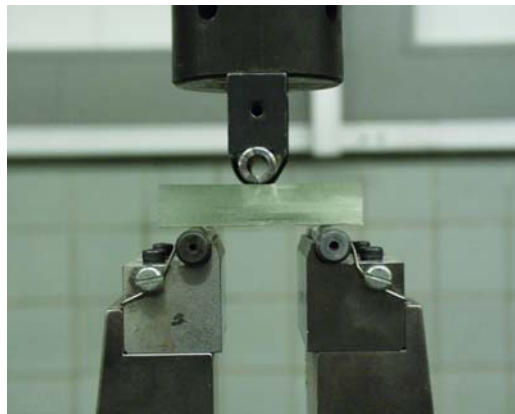


**Figure 4-22** Experimental set-up of the 0 degrees specimens for short beam test.

The overall test results (average value and standard deviation) for these ASTM tests are given in Table 4-3. Those values are used in finite element calculations as material properties. The FEA calculations on different point absorbers are discussed in Chapter 5.

	Average	Standard Deviation	# Test Samples
$E_{11,T}$	25770 MPa	1750 MPa	5
$\nu_{12}$	0.38	0.02	
$X_T$	575.7 MPa	48.4 MPa	
$E_{22,T}$	6251.5 MPa	686.12 MPa	5
$\nu_{21}$	0.10	0.02	
$Y_T$	20.73 MPa	6.95 MPa	
$E_{11,C}$	23260 MPa	1950 MPa	4
$X_C$	419 MPa	88.1 MPa	4
$E_{22,C}$	6688 MPa	518 MPa	5
$Y_C$	>> 72.76 MPa	1.53 MPa	
$G_{12}$	4195 MPa	71.5 MPa	
$S$	71.43 MPa	3.23 MPa	4
$\tau_{LSS}$	45.2 MPa	1.89 MPa	5

**Table 4-3 Results for ASTM standards for stiffness and strength.**

#### 4. 6. 2. Characterisation of fibre fraction

This test determines the volume and mass fraction of glass fibres and resin in a laminate structure. First, at Spiromatic, test samples of 70 x 40 x 4 mm are cut and the mass is determined. The size depends on the available oven. Next, the samples are heated in the oven for about 45 minutes at 650°C to burn the resin. This oven is shown in Figure 4-24. Finally, the mass of glass fibres is measured and the mass fraction calculated. The material used for winding the silos, consists out of 52 % fibre mass fraction, which is an average value out of five test samples. The standard deviation is 0.9 %. The volume fraction of the fibres is determined, now through the use of Equation 4-2. The average value of the fibre mass,  $m_F$ , equals 9 g. The density of the fibres,  $\rho_F$  is 2540 kg/m<sup>3</sup>.  $V_F$  is 31.6 %. However, it has to be kept in mind that within the ignition loss there is probably a small fraction of glass fibres burnt as well [20].

$$V_F = \frac{m_F}{\rho_F} \times \frac{100}{V_T}$$

**Equation 4-2 Volume fraction in function of its mass and density.**



**Figure 4-23** Making of test samples.



**Figure 4-24** Oven at Spiromatic.

#### 4. 7. PREPARATION OF TEST SAMPLES WITH VACUUM INFUSION

STY has made plates of different materials with vacuum infusion (Figure 4-25). For this partner, four-point bending tests were done, again according to ASTM standards, on the test samples of the selected five different materials [21]. Thus, STY has made five different plates with vacuum infusion, which are shown in Figure 4-26. All plates have about 9 mm thickness and are produced with all layers having the same orientation of the textile fabrics of 0/90 degrees.

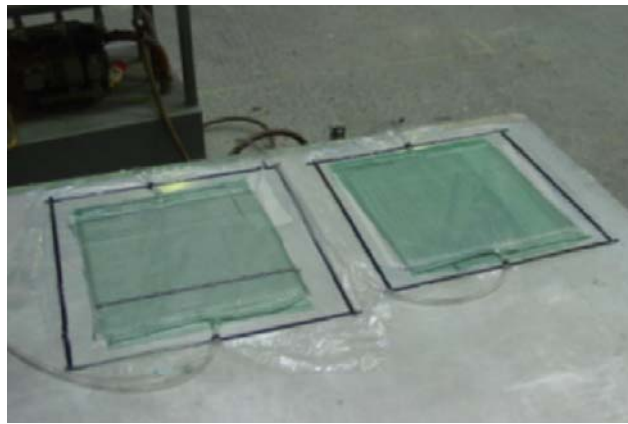


**Figure 4-25** Plates made with vacuum infusion by STY.



**Figure 4-26** Resulting plates made by STY; 5 combinations.

#### 4. 8. TESTS ACCORDING TO ASTM STANDARDS FOR STY

For STY four-point bending tests were done for the five different materials mentioned in 4. 4. 3. This was chosen since a full characterisation for five materials is a quite extensive work. These four-point bending tests are considered as screening tests to provide a general idea of the maximum tensile strength and the E-modulus. Again, the experiments were done according to ASTM standards [21]. The testing of a sample is shown in Figure 4-27. For each material five samples were tested.

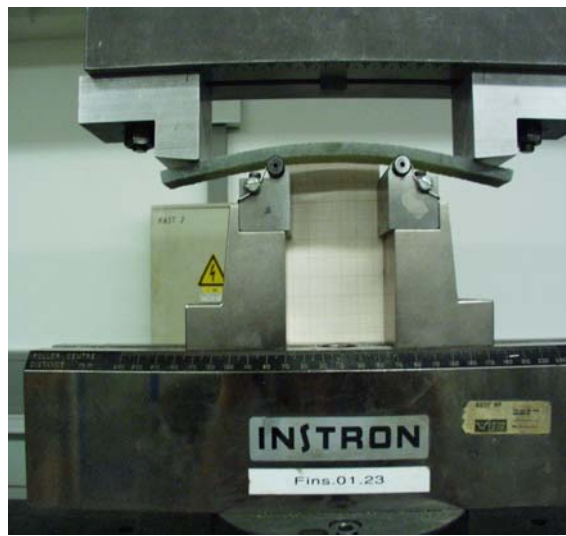


**Figure 4-27 Test set-up for four-point bending sample of STY.**

The average results and their standard deviations for the different materials are given in Table 4-4.

	$\sigma_{xx, \max}$ (MPa)	Standard Deviation $\sigma_{xx, \max}$ (MPa)	$E_{xx}$ (GPa)	Standard Deviation $E_{xx}$ (GPa)
<b>carbon fibre / epoxy</b>	391.79	24.3	63.45	6.1
<b>carbon fibre / vinyl ester</b>	288.99	6.6	66.87	2.1
<b>glass fibre / polyester</b>	342.6	21.4	21.32	1.3
<b>glass fibre / vinyl ester</b>	396.59	30	22.59	1.6
<b>glass fibre / epoxy</b>	346.32	36.6	21.55	1.2

**Table 4-4 Results four point bending tests for STY.**

At the start of the Seewec project, it was planned to do a similar full characterisation of one or two chosen materials for STY, as with the material of SMC. However, the material properties measured from the four point bending tests for STY were used as a sufficient estimation for the STY materials in FEA calculations. The results of these simulations are discussed more in detail in Chapter 5.

Glass fibre was chosen before carbon fibre for reasons of cost. The epoxy resin was chosen instead of the other resins because STY had a lot of experience with it and, in any case, the properties do not differ a lot. In Table 4-5 the allowable maximum tensile strength and the tensile E moduli of the chosen SMC and STY materials are summarised in both the 0 and 90 degrees direction.

	$\sigma_{xx, \max}$ (MPa)	$E_{xx}$ (MPa)	$\sigma_{yy, \max}$ (MPa)	$E_{yy}$ (MPa)
<b>STY</b>	346.32	21550	346.32	21550
<b>SMC</b>	575.7	25770	20.73	6251.5

**Table 4-5 Comparison of the available experimental properties of the chosen STY and SMC materials.**

#### 4. 9. REFERENCES

1. J. Degrieck, Composieten, Course at Ghent University, Faculty of Engineering, 2006-2007.
2. F. H. Abdallah and S. A. Mutasher (2005) Design and fabrication of a low cost filament winding machine, Universiti Putra Malaysia.
3. M. S. Babu, G. Srikanth et al. Composite fabrication by filament winding, an insight. 2000 [cited 2007 03/03]; Available from: <http://www.tifac.org.in/news/acfil.htm>.
4. Entec. Brochure winding machines. [cited 2007 24/02]; Available from: <http://www.entec.com/brochures/filament.pdf>
5. Spiromatic. [cited 2006 25/04]; Available from: [www.spiromatic.com](http://www.spiromatic.com).
6. Adoptech. Advanced Design and Optimization Technologies. [cited 2009 25/03]; Available from: <http://www.adoptech.com/pressure-vessels/main.htm>.
7. EaglePlastics. [cited 2009 14/03]; Available from: <http://www.indiamart.com/eagleplastic/plastic-products.html>.
8. Vacuum Infusion - The Equipment and Process of Resin Infusion. [cited 2006 05/11]; Available from: <http://www.fibreglast.com/documents/361.pdf>.
9. Applications and recent projects RTM-Worx and CVI technology. [cited 2006 25/04]; Available from: <http://www.polyworx.nl/apz/>.
10. LM Glasfiber: building on blade technology. Reinforced Plastics, 2000: p. 26-30.
11. Roving for filament Winding and pultrusion. 05/2003 [cited 2006 24/04]; Available from: [http://www.saint-gobain.com.cn/text/beijing\\_vetrotex/p192.pdf](http://www.saint-gobain.com.cn/text/beijing_vetrotex/p192.pdf).
12. DSM Product Data Sheet. 03/2005 [cited 2006 24/04]; Available from: [http://technicaldocuments.dsm.com/product\\_finder/technical\\_documents/DR/level10/DR\\_DRS\\_00000000006317\\_PDS\\_en\\_.pdf](http://technicaldocuments.dsm.com/product_finder/technical_documents/DR/level10/DR_DRS_00000000006317_PDS_en_.pdf).
13. The Newsletter from DSM Composite Resins. January 2004, Nr 1 [cited 2006 24/04]; Available from: [http://www.dsm.com/en\\_US/downloads/drs/gs\\_tpr\\_issue1.pdf](http://www.dsm.com/en_US/downloads/drs/gs_tpr_issue1.pdf).
14. DSM Product Data Sheet. 09/2000 [cited 2006 24/04]; Available from: <http://www.kemikaal.ee/failid/Atlac%20430%20vinylester%20PDS.pdf>.
15. ASTM International Standards World Wide. [cited 2006 05/01]; Available from: <http://www.astm.org/>.
16. ASTM D 3410/D 3410M - 03 "Standard Test Method for Compressive Properties of Polymer Matrix Composite Materials with Unsupported Gage Section by Shear Loading".
17. ASTM D 2344/D 2344M - 00e1 "Standard Test Method for Short-Beam Strength of Polymer Matrix Composite Materials and Their Laminates".
18. ASTM D 3039/D 3039M - 00e2 "Standard Test Method for Tensile Properties of Polymer Matrix Composite Materials".

19. ASTM D 3518/D 3518M - 94 (Reapproved 2001) "Standard Test Method for In-Plane Shear Response of Polymer Matrix Composite Materials by Tensile Test of a  $\pm 45^\circ$  Laminate".
20. ASTM D 2584 - 02 "Standard Test Method for Ignition Loss of Cured Reinforced Resins".
21. ASTM D 6272 - 02 "Standard Test Method for Flexural Properties of Unreinforced and Reinforced Plastics and Electrical Insulating Materials by Four-Point Bending".



## Chapter 5

### SELECTING SUITABLE LAMINATE LAY-UP WITH FINITE ELEMENT ANALYSIS

*In this chapter, the finite element calculations on the different point absorber shapes are discussed. First, the shapes that were defined before the project and at the start of the project are given. Later on, a so called ‘pencil’ shape was proposed and several calculations were done on it to assess bottom and breaking wave slamming. Finally, this has led to the proposal of a ‘cone/cylinder/cone’ shape which is, again according to several calculations, a suitable shape to withstand the slamming load. Additionally, a discussion about the influence of deformability on slamming peak pressures is raised.*

#### 5. 1. INITIAL SHAPES OF THE POINT ABSORBERS

##### 5. 1. 1. Introduction

At the start of the Seewec project, FOL delivered information to the partners. For WP4 an important issue was of course the shape of the point absorbers. In the pre-Seewec period (2005), the buoys mounted on ‘Buldra’ were scaled ‘egg’ shapes. This is how the short-name for all kinds of point absorbers, ‘eggs’, was introduced and was used during the whole project. Due to reasons of severe bottom slamming loads the tulip shape was considered to replace the egg since this shape goes more smoothly into the water. The tulip shape is shown in Figure 5-1. A central tube is present in all shapes to make the buoy water tight, note the right figure for a clear view. The egg shape is depicted in Figure 5-2. It has a height of 6 meter and a diameter of 5 meter.

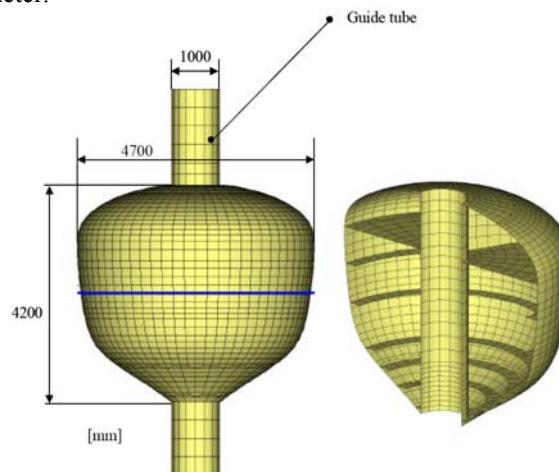


**Figure 5-1** The proposed tulip shape by FOL for the point absorber [1].

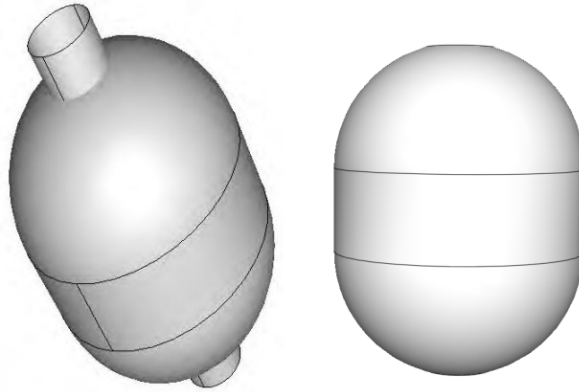


**Figure 5-2** The proposed egg shape by FOL for the point absorber.

Also, during the project, G. De Backer and M. Vantorre performed calculations about power output for a hemi-sphere, a cone and tulip which showed that there was not a lot of difference for these three shapes. There is a slight advantage for the cone shape compared to the egg and tulip shapes [2, 3]. Due to this finding and the ease of production, a shape with a simple conical bottom in transition to a cylinder; was proposed.

#### 5. 1. 2. Pencil

The dimensions of this pencil are 5.5 meter length and 4 meter diameter as is shown in Figure 5-3. Several finite element calculations were done on it to determine the lay-up of the laminate necessary to survive the slamming design conditions. Again, the buoy has a composite inner tube in it since it has to be watertight.

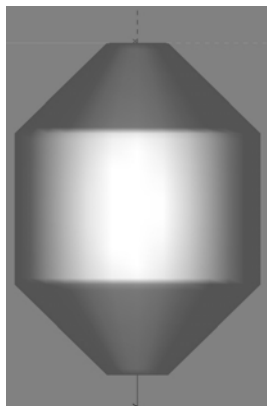


**Figure 5-3** The pencil shape; 5.5 meter length and 4 meter diameter.

## 5. 2. FINITE ELEMENT SOFTWARE

### 5. 2. 1. Introduction

Abaqus is the used finite element program. Of course, this software program will not be discussed in detail within this dissertation. But some relevant topics concerning the geometry, material orientations and the used failure criterion have to be mentioned.

First, since the point absorbers are probably hollow (with or without internal stiffeners) it seems logical to use shell elements for them. A shell element represents an object where one dimension is a lot smaller than the two other dimensions. In this case it is the thickness of the buoy which is a lot smaller than the height and the diameter. For the input in Abaqus of the material parameters this means that the E-modulus along the fibres ( $E_{11}$ ) and perpendicular to the fibres ( $E_{22}$ ), Poisson's ratio ( $\nu_{12}$ ) and the shear moduli ( $G_{12}$ ,  $G_{13}$  and  $G_{23}$ ) should be given [4].

Next, composite material is of course a non-isotropic material which means that properties are not the same in all material directions. Hence, the definition of material orientations within the finite element program is an important issue. For shell elements each layer is defined in a certain section with its thickness, number of integration points, material and angle relative to a defined orientation system. Within Abaqus this is quite straight forward. However, specific for filament winding modelling there is an additional problem, namely the calculation of the winding angles at each location on the structure. This is inherent to the production method. An easy solution is the commercially available software Cadwind discussed in paragraph 5. 3. With the help of this software, it is possible to translate the material orientations into an .INP file (ASCII text) which can be imported into Abaqus.

Finally, the output of the calculations gives an idea whether or not a structure breaks. For composites the Tsai Wu criterion is a common used fracture criterion. This criterion and how it is used within Abaqus is explained in following paragraph.

The boundary conditions for each point absorber were located on its top and bottom circle. The buoy was free to rotate about its axis and move up and down. All other movements are restricted. The material properties are the ones determined in Chapter 4 for SMC as well as for STY and can be used within the finite element calculations. For STY these properties are considered the same along the fibre and perpendicular to the fibre since the characterisation tests were done on 0/90 degrees textiles. It is very important to not that the average value of the properties is used

and not the characteristic value. The composite inner tube was made in all cases by filament winding. It consists out of several cross wound layers of 46 degrees until a thickness of about 10 mm is reached. For these winding calculations (inner tube and point absorber) a roving number of '60' - which is the amount of used fibre bundles - and a tex value of '2400' are used since this amount and kind of fibres was used in SMC.

### 5. 2. 2. Composite failure criterion

For composites the Von Mises or other isotropic failure criteria are not suitable. Hence, another criterion needs to be used. The Tsai Wu failure criterion is the most common one used for composite materials. It requires that  $I_F < 1$  with  $I_F$  defined in Equation 5-1. As soon as  $I_F$  equals one, fracture initiates [5].

$$I_F = F_1 \times \sigma_{11} + F_2 \times \sigma_{22} + F_{11} \times \sigma_{11}^2 + F_{22} \times \sigma_{22}^2 + F_{66} \times \sigma_{12}^2 + 2 \times F_{12} \times \sigma_{11} \times \sigma_{22}$$

**Equation 5-1 Definition of  $I_F$  for the Tsai Wu criterion.**

With

$\sigma_{11}$  = Normal stress in the fibre direction

$\sigma_{22}$  = Normal stress perpendicular to the fibre direction

$\sigma_{12}$  = Shear stress

and  $F_{i(j)}$  predefined coefficients. The definitions of these coefficients are given in Equation 5-2 and Equation 5-3.

$$F_1 = \frac{1}{X_T} - \frac{1}{|X_C|}; \quad F_2 = \frac{1}{Y_T} - \frac{1}{|Y_C|}; \quad F_{11} = \frac{1}{X_T \times |X_C|}; \quad F_{22} = \frac{1}{Y_T \times |Y_C|}; \quad F_{66} = \frac{1}{S^2}$$

**Equation 5-2 Definition of four coefficients of the Tsai Wu criterion.**

With

$X_T$  = Tensile strength in the fibre direction

$X_C$  = Compressive strength in the fibre direction

$Y_T$  = Tensile strength in the direction perpendicular to the fibre direction

$Y_C$  = Compressive strength in the direction perpendicular to the fibre direction

---

S = Shear strength

$$F_{12} = f^* \times \sqrt{F_{11} \times F_{22}}$$

**Equation 5-3 Definition of the  $F_{12}$  coefficient of the Tsai Wu criterion.**

In Equation 5-3  $f^*$  can be varied within the program between minus and plus one if desired. According to Tsai Wu this  $f^*$  could be taken equal to minus 0.5 as a good estimation. However, the default value of  $f^*$  is in Abaqus equal to zero. Since variations in the  $F_{12}$  do not have a lot of impact on the achieved results it was decided to leave it equal to zero within Abaqus. This means that the last term in Equation 5-1 is zero.

The Tsai Wu criterion (like other stress-based failure criteria such as Tsai Hill) defines a failure surface surrounding the origin in the 2D surface  $\{\sigma_{11}, \sigma_{22}\}$ . Failure occurs when a state of stress is either on or outside this surface. Now, within Abaqus, the failure index  $R$ , is used to measure the proximity to the failure surface.  $R$  is defined as a scaling factor so that for the given stress state  $\{\sigma_{11}, \sigma_{22}\}$ ,  $\{\sigma_{11}/R, \sigma_{22}/R\}$  results in  $I_F = 1$ . In other words '1/R' is the scaling factor which needs to be multiplied with all of the stress components simultaneously to lie on the failure surface.  $R < 1$  means that the state of stress is within the failure surface while  $R > 1$  indicates failure [5].

### 5. 3. DESCRIPTION OF CADWIND

#### 5. 3. 1. Introduction

Cadwind is a software program for filament winding applications. It is a useful tool to determine whether or not a given geometry can be wound. Hence, it is used to achieve realistic winding patterns. Additionally, within this doctoral thesis its purpose was dual. First, the program includes a module which translates the geometry properties to finite element programs such as Abaqus, Ansys, Nastran, Nisa and Lusas. Since Abaqus is the used finite element program within this research, the conversion of Cadwind to Abaqus is explained in the following paragraph [6]. Second, the Cadwind software has the possibility to generate the positions of all axes of a given winding machine to fulfil a certain winding pattern. This latter use is adopted in Chapter 6 since there this second purpose of this tool is explained.

#### 5. 3. 2. From Cadwind to Abaqus (and other programs for FEA)

All steps necessary to build up the .inp file (ASCII text) as an input file for Abaqus containing the material properties and orientations, are discussed within this paragraph with the help of an example of a silo. First, the desired shape has to be drawn within Cadwind or loaded into the program. Certain pre-made shapes exist already in the program such as cones and cylinders. Hence, for the silo example this is a possible way to proceed as is shown in Figure 5-4. However, even this straight forward shape can be made through loading of a mandrel file which contains ASCII text describing the necessary geometrical input data of the desired structure. This code needs to be written in a text file with the extension ‘.mdr’ added to its name. Again, this is shown for the silo example in Figure 5-5.

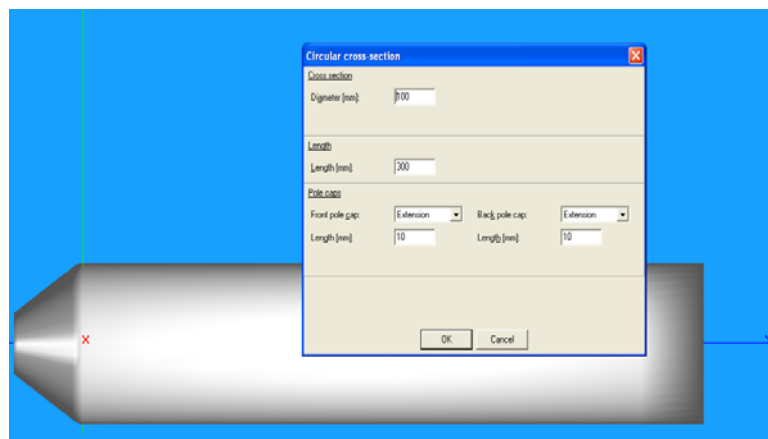


Figure 5-4 Example of the creation of a silo.

```

C:\Documents and Settings\chris\Desktop\ExampleSilo.mdr
CADWIND CONTOUR DATA FILE
MM
30
40
1
30
-2000.00 1500.00
-1894.12 1640.25
-1788.24 1780.49
-1682.35 1920.74
-1576.47 2060.99
-1470.59 2201.23
-1364.71 2341.48
-1258.82 2481.73
-1152.94 2621.98
-1047.06 2762.22
-941.18 2902.47
-835.29 3042.72
-729.41 3182.96
-623.53 3323.21
-517.65 3463.46
-411.76 3603.70
-305.88 3743.95
-200.00 3884.20
-100.00 3962.32
0.00 4000.00
1800.00 4000.00
3600.00 4000.00
5400.00 4000.00
7200.00 4000.00
9000.00 4000.00
10800.00 4000.00
12600.00 4000.00
14400.00 4000.00
16200.00 4000.00
18010.00 4000.00

```

**Figure 5-5 MDR code for the silo example.**

Row one and two contain standard code to start an mdr-file. Row three announces how many points will be given along the Y-axis. Row four gives the amount of sections that are desired later on for the mesh in tangential direction. For this example, forty sections are taken. For now, row five takes number one and row six the same number as row three. However, in reality the turning zones during filament winding occur further away from the edges. The values of row five and six still can be changed later on in the winding parameters. From row seven on there are two columns. The left one represents the values on the horizontal axis and the right column represents the corresponding diameter. The origin in such a file is always situated where the left column (Y-axis) reaches zero, here in row 26. The Z-axis is in the vertical direction on the figure and the X-axis is perpendicular to both.

This kind of method to create a mandrel has the advantage of granting control to the user concerning the distribution of points. This is important since this distribution determines the later mesh within the finite element program. The one given is quite a bad distribution since it contains a lot of points on the cone part of the silo

(translated by Cadwind into segments as is shown in Figure 5-6) and almost none on its cylindrical part.

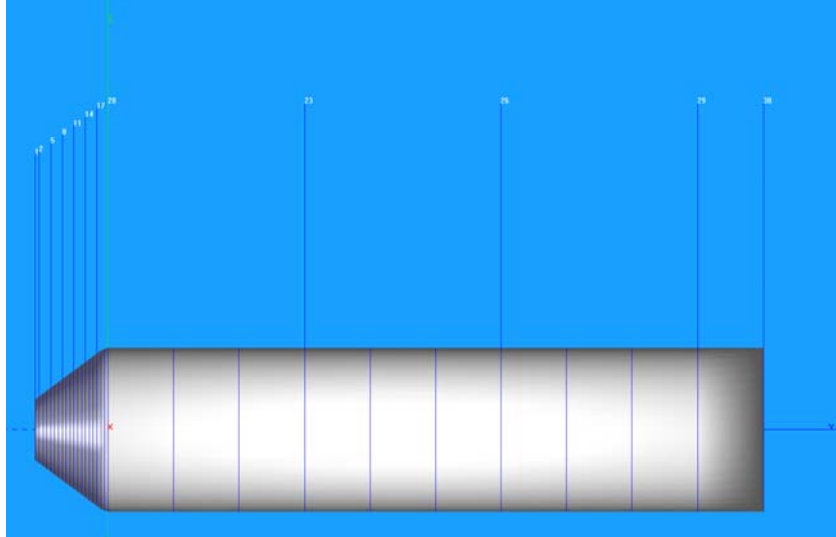


**Figure 5-6** Distribution (apparently non-uniform) of points or segments.

A code with fewer points on the cone and more on the cylinder was produced. In this way points are described along the Y-axis at about equal distances. For this example it is not completely equidistant, but it was enough to achieve a more uniform distribution which is shown in Figure 5-7. The corresponding code in the mdr-file is given in Figure 5-8.

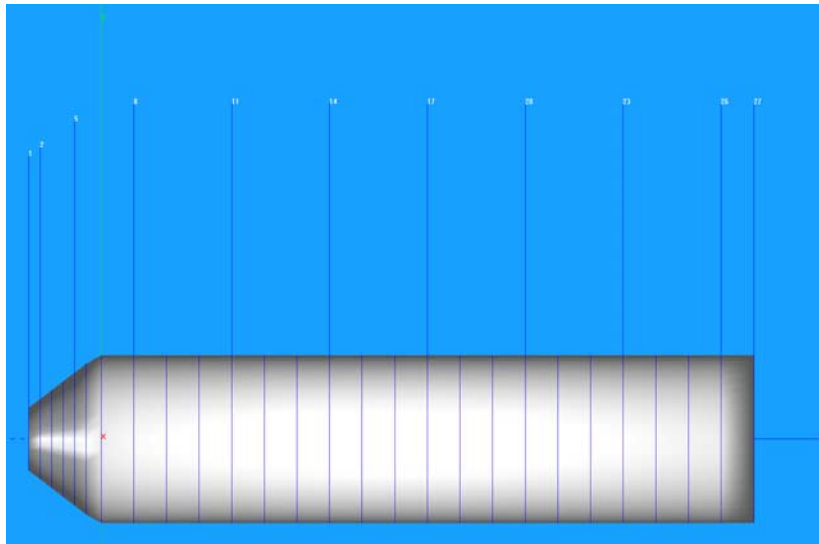


**Figure 5-7** More uniform distribution of points (or segments).

```

C:\Documents and Settings\chris\Desktop\ExampleSilo2.mdr
CADWIND CONTOUR DATA FILE
MM
27
40
1
27
-2000.00 1500.00
-1682.35 1920.74
-1364.71 2341.48
-1047.06 2762.22
-729.41 3182.96
-411.76 3603.70
0.00 4000.00
900.00 4000.00
1800.00 4000.00
2700.00 4000.00
3600.00 4000.00
4500.00 4000.00
5400.00 4000.00
6300.00 4000.00
7200.00 4000.00
8100.00 4000.00
9000.00 4000.00
9900.00 4000.00
10800.00 4000.00
11700.00 4000.00
12600.00 4000.00
13500.00 4000.00
14400.00 4000.00
15300.00 4000.00
16200.00 4000.00
17100.00 4000.00
18010.00 4000.00

```

**Figure 5-8** More uniform MDR code for the silo example.

Next, after the mandrel has been drawn or loaded into the software, the winding phase within this program is started. It is quite difficult to find suitable winding parameters to wind the part with one layer. Before doing this the material parameters should be filled in such as the amount of used fibre bundles, which is called 'the roving number'. This equals 60 at SMC and the tex value of the fibre which is 2400. Tex is the mass in grams per km. First, a winding pattern that covers the whole conical side and as much as possible of the cylindrical part as is shown in Figure 5-9, was chosen. Second, vice versa, a winding pattern that covered the full cylindrical part and as much as possible of the cone as is shown in Figure 5-10, was also chosen. The winding angle used as an input value is only correct locally at start of the winding, but changes along the position on the mandrel. This information is calculated in Cadwind while the layers are determined. In this case two layers are saved as .lam files. Next, those .lam files can be combined at will to produce a full laminate. Of course, the same layer can be used several times. In this case layer one is the first wound one in the combination. This combination of layers is seen by Abaqus as an .inp file and contains the node/element information about the mesh. Also, it includes the definition of the circular sections defined in the .mdr file.

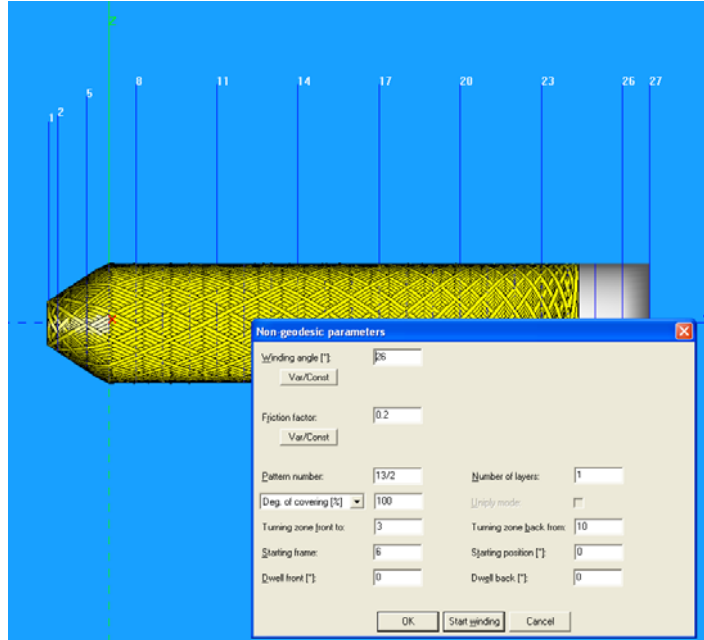


Figure 5-9 First winding layer for the example.

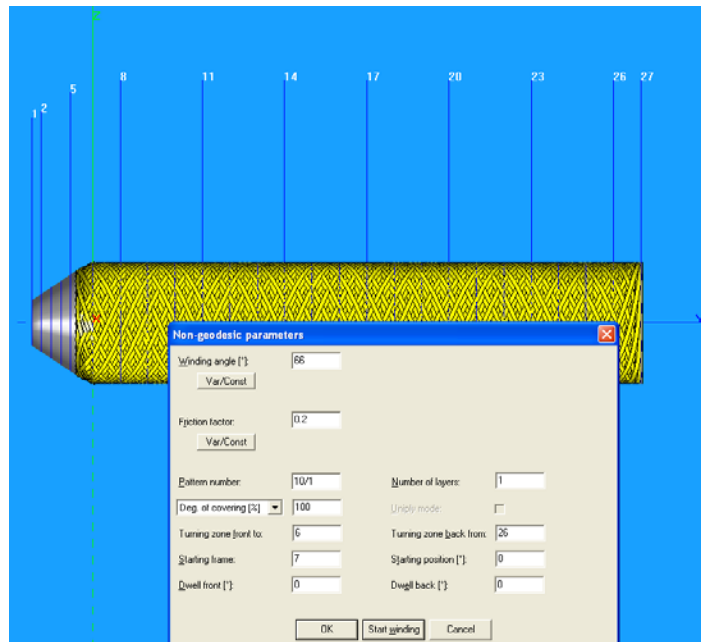
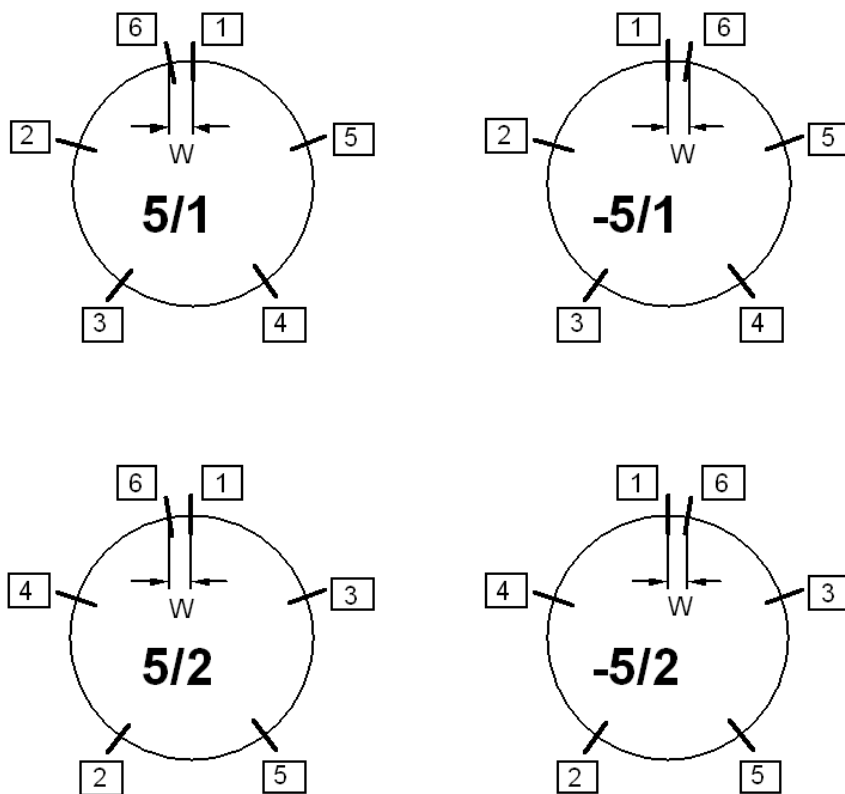


Figure 5-10 Second winding layer for the example.

The pattern number, here 13/2 for the first layer and 10/1 for the second, characterizes the winding pattern. This is the regularly recurring pattern of the filament path in a filament winding after a certain number of mandrel revolutions. It can be positive or negative; for a positive value the new starting point of a cycle is left of the previous one; for a negative value it is right of the previous one. The full traversing of the part from one end to the other and back is called a cycle. Besides the pattern number the skip index can be entered. Both values must be separated by a slash "/". The skip index is the number of bandwidths skipped between each circuit. A skip index of 1 means the band will move over (skip) one band position (i.e. next to the last circuit band). A skip index of 2 means that an empty band slot will be between the first and second circuit bands (this will be filled in by a subsequent circuit). And so on for higher skip indices. To fix thought four examples are given in Figure 5-11.



**Figure 5-11** Examples of four pattern numbers with skip indices 1 and 2.

Local orientations, calculated in Cadwind, are assigned per section as is shown in Figure 5-12 which depicts the sixth segment counted from left to right in Cadwind,

or in other words, from bottom to top in the input file (.inp) for Abaqus. There, two cross wound layers are shown hence per layer two code lines are introduced; one with a positive angle and one with a negative one. This conversion is done within Cadwind. It is not entirely correct because in reality the structure is cross wound, but the approximation is sufficient. The zero degrees axis is parallel to the axis of the silo.

```
*SHELL SECTION, ELSET=ELSET6, COMPOSITE, ORIENTATION=ORIS
1.050100, 5, MATERIAL1, 23.173000
1.050100, 5, MATERIAL1, -23.173000
1.336100, 5, MATERIAL1, 68.344000
1.336100, 5, MATERIAL1, -68.344000
```

**Figure 5-12** Code of the material orientations of the sixth circular section.

This inp-file has to be imported in Abaqus. For this example the result is shown in Figure 5-13. However, it has to be taken into account that this is not a geometrical part. Hence, it is not possible to redraw or re-mesh the part within Abaqus anymore. If changes are necessary this can be done in the inp-file or in the Cadwind software. This is why it is so important to choose the distribution of sections in the mdr-file well.

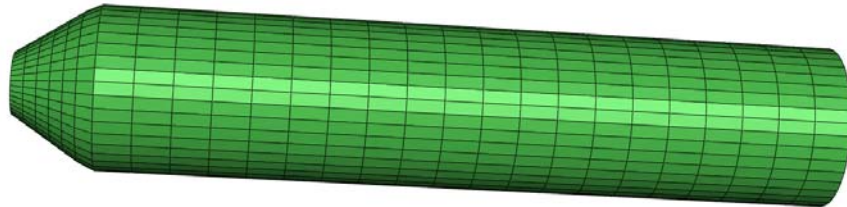


**Figure 5-13** Mesh part in Abaqus; Imported file out of Cadwind.

Another important remark is given about the refining of the grid. As mentioned above, it is not possible to change this mesh-file anymore *within* Abaqus. Hence, it has to be chosen well in Cadwind. However, when refining the grid (in Cadwind) several problems occur. First, several ascending sections do not differ anymore from each other. Second, and most severe, the .inp file in Abaqus gives irregularities in the mesh and material orientations. This is probably due to the fact that a lot of layers are used. For this, the grid of the simulated point absorbers is kept quite coarse and because of this there probably still is a numerical error in the performed simulations. Refining the mesh in some way could be an issue of improvement. However, since the translation of helical winding is also not entirely correct and has

in this way introduced a modelling error a consideration has to be made whether this refining effort would be worthwhile.

The mesh obtained out of Cadwind for a particular shape is re-used for the calculations with the vacuum infusion method. For these, the material orientations and constants were changed according to this production method in the respective .inp-code.

## 5. 4. FEA CALCULATIONS ON PENCIL SHAPE

### 5. 4. 1. Introduction

The mesh for the pencil shape was made with the Cadwind-Abaqus procedure as was explained in previous paragraph [6, 7]. This mesh was used for the materials of both companies. However, for the filament winding production method, additional work is necessary in the building up of separate layers. Due to this reason it was decided to start the preliminary calculations with the material properties and production method of SMC. The main design conditions for the buoy are bottom and breaking wave slamming. First, the pencil was designed according to bottom slamming conditions. A maximum stroke of 5 m was foreseen for the buoys. Hence, according to Equation 5-4 (also mentioned in Chapter 3) this is equal to a pressure of 0.316 MPa when a slamming factor of  $2\pi$  is used. It is opted to use this largest (and hence safest) proposed slamming factor in the DNV.

$$p_s = 0.5 \rho C_{pa} v^2$$

**Equation 5-4** Space average slamming pressure [8].

In consent with Seewec partner ‘Brevik’ this load was applied on a segment of 60 degrees and 1 meter height within the finite element calculations as is shown in Figure 5-14.

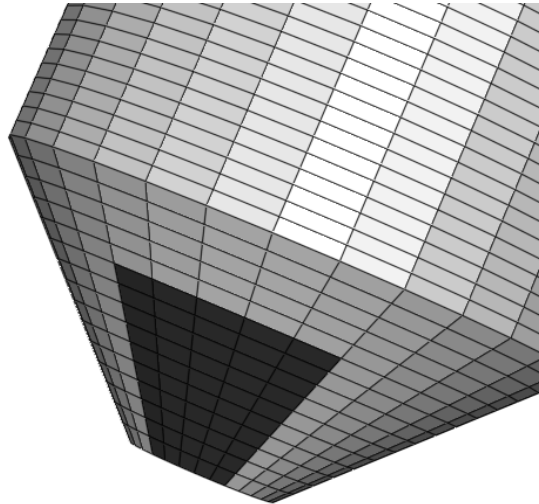


**Figure 5-14** Sector in Abaqus for applying the bottom slamming load; sector of 60 degrees, 1 meter height [1].

Also, some calculations were done on 360 degrees which is equal to the fall of the buoy on a smooth water surface. Of course, due to wave action, the surface is not always smooth. And a 60 degrees segment was proposed in consent with Brevik. Within this work only calculations on the latter are mentioned. Since the 60 degrees sector meant a more severe condition than the 360 degrees due to the axisymmetric shape of the buoys, it was decided to design the buoy to survive bottom slamming on a segment of 60 degrees.

Next, the pencil had to survive extreme breaking wave conditions as well. The same formula was used but now the wave celerity is taken for the velocity. In Chapter 3 the celerity was calculated for the return level of a storm occurring once in 25 years within a certain desired sea climate. This celerity is 12.1 m/s which results in a pressure of 0.472 MPa which was, in agreement with Brevik, applied on a circle segment of 60 degrees over the cylindrical part of the buoy (Figure 5-15).

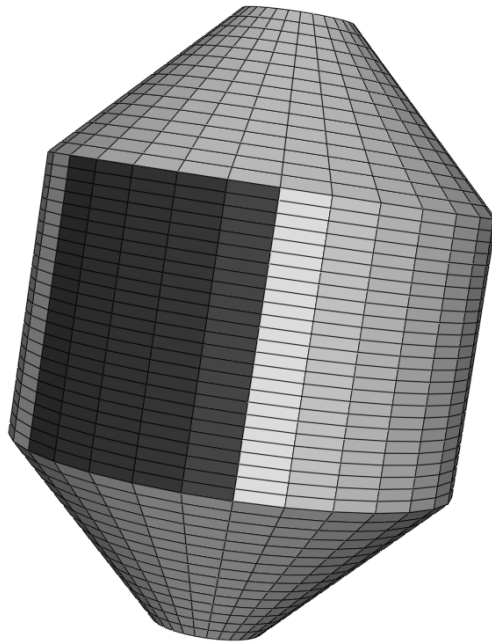


**Figure 5-15** Sector in Abaqus for applying the breaking wave slamming load; sector of 60 degrees, cylindrical part [1].

Discussion about the results of the finite element calculations on the pencil shape for both slamming phenomena is given in the following paragraph. However, first the inner composite tube needs to be mentioned. As explained in paragraph 5. 1. 2. in

each buoy an inner composite tube was mounted to keep it water tight. An additional advantage of this tube is that it provides extra stiffness to the buoy.

#### 5. 4. 2. Results for the pencil shape

The mandrel of the pencil shape was made in Cadwind. There, some suitable winding layers were sought and found. Four different layers were defined to combine in different lay-ups. These different layers are depicted in Figure 5-16 and were sought in a way to prevent a very high thickness on the turning zones which is inherent to the filament winding production method. The names are chosen as follows: ‘full’ (upper left), ‘symmetry 300 mm’ (upper right), ‘symmetry 600 mm’ (lower left) and ‘symmetry 900 mm’ (lower right). Full means that the buoy is fully covered, 300 mm means that there is 300 mm on each side left uncovered, etc.

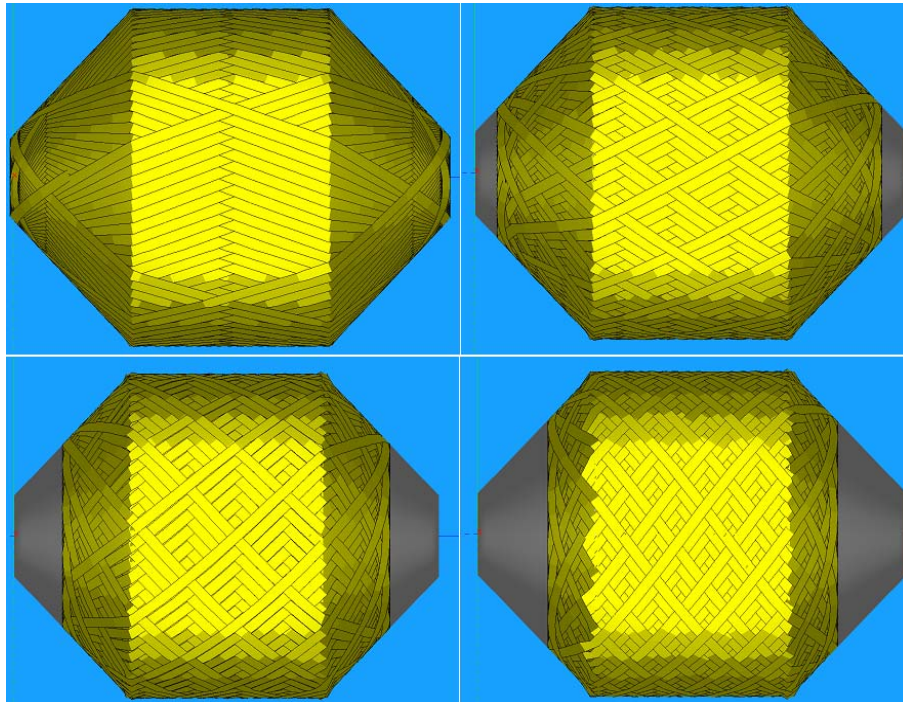


**Figure 5-16** Filament winding layers: full (upper left) with winding angle 20 degrees, pattern 5/1, turning zones 10-46, start 10; symmetry 300 (upper right) with winding angle 34 degrees, pattern 15/2, turning zones 6-50, start 6; symmetry 600 (lower left) with winding angle 46 degrees, pattern 11/1, turning zones 8-45, start 8; symmetry 900 (lower right) with winding angle 52 degrees, pattern 15/2, turning zones 16-43, start 16.

The determination of the lay-up was an iterative procedure. The use of only layers that covered the buoy fully resulted in an unrealistic thick laminate on the edges of the buoy. For these reasons other layers with parts uncovered were sought. Also, a layer called ‘extra bottom’ (winding angle 22, pattern 15/1, turning zones 2-38, start 3) was added. The last layer was chosen as reinforcement for the bottom slamming and to keep the Tsai Wu measure low enough for this kind of load. The buoy is not entirely symmetric inherent to the type of production method.

The following laminate combination seemed the optimum with these layers and it was made in Cadwind to import the code into Abaqus: full – extra bottom – symmetry 300 mm – symmetry 600 mm – symmetry 900 mm – extra bottom – full. Hence, a pencil of seven cross wound layers was created which were translated per layer in two angles of different signs in Abaqus. This is an estimation of the real filament winding structure as was explained in paragraph 5. 3. 2. The calculated mass of this buoy is 2850 kg.

The material parameters for this are the determined ones from SMC (Chapter 4) depicted in Figure 5-17. The first row shows the E-moduli, the Poisson coefficient and the G-moduli while the second row shows the allowable stresses.

E1	E2	Nu12	G12	G13	G23	
25770	6251.5	0.38	4200	4200	2500	
Ten Stress Fiber Dir	Com Stress Fiber Dir	Ten Stress Transv Dir	Com Stress Transv Dir	Shear Strength	Cross-Prod Term Coeff	Stress Limit
575.7	419	20.73	72	71.43	0	0

**Figure 5-17 SMC material properties in MPa except the dimensionless Poisson coefficient Nu12; input for Abaqus.**

The thickness of this proposed buoy is shown in Figure 5-18 as a distribution (upper) and from bottom to top along the length of the buoy (lower). It is clearly seen that the thickness varies over the length of the buoy. This is inherent to the filament winding production method. Each sector, defined as a different circle segment is modelled with a constant thickness. The calculated maximum measure for Tsai Wu on this buoy for bottom slamming is 0.73 as is shown in Figure 5-19. The most critical stress in this case, in other words the determining stress for the Tsai Wu measure, is the shear stress,  $\sigma_{12}$ . In Abaqus the symbol  $S_{12}$  is used.

This maximum Tsai Wu occurred in layer 1 at its bottom which is the inner side of the buoy. This calculation was done with a constant pressure of 0.316 MPa over a sector of 60 degrees and 1 meter height as explained in paragraph 5. 4. 1.

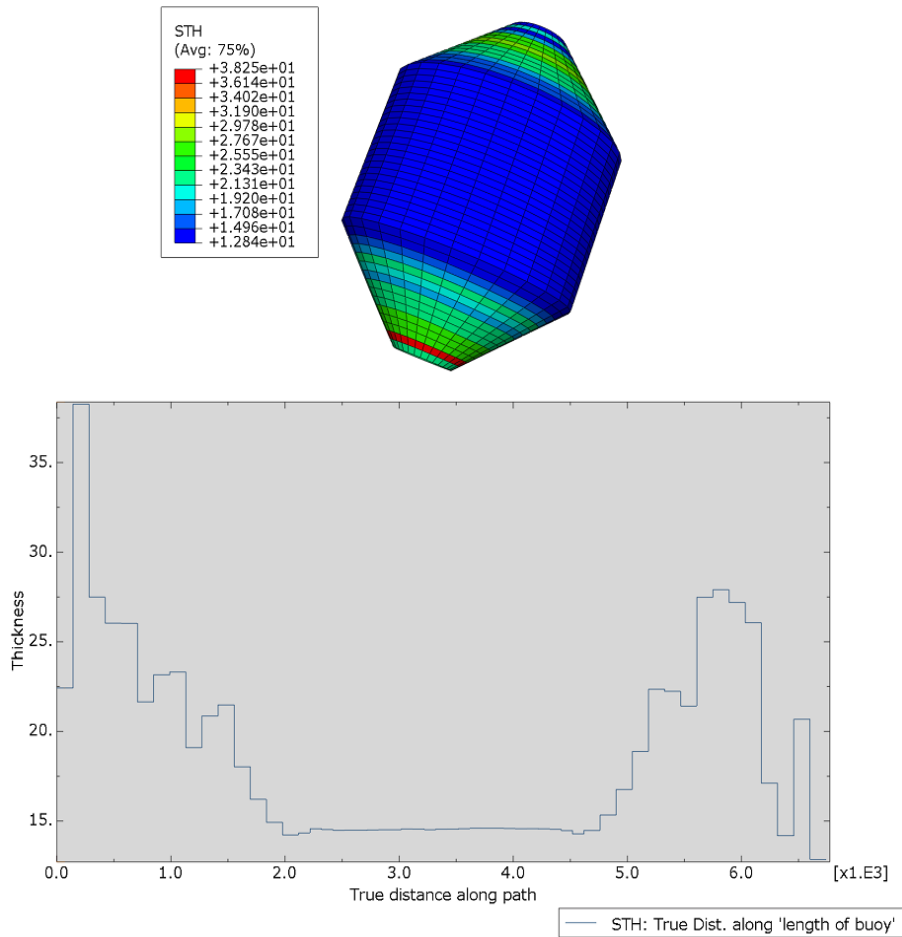


**Figure 5-18** Thickness of the buoy [mm]: distribution (upper) and along length [mm] of the buoy from bottom to top (right).

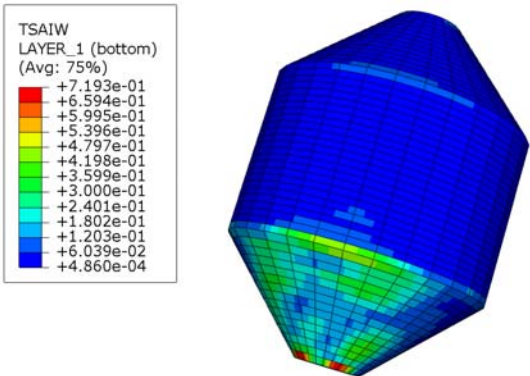


**Figure 5-19** Calculated distribution of the Tsai Wu measure in layer 1 for a constant bottom pressure of 0.316 MPa.

As mentioned in Chapter 3 the DNV norms suggests a smaller slamming factor for wedge shaped bodies. However, since this is a topped off cone it is not clear which factor is safe enough to use. Hence, the bottom calculation of 0.316 MPa is used. The peak pressure calculated with the cone formulae of S. Victor and G. De Backer, depicted in Equation 5-5, is 0.160 MPa peak.

$$P_{\max}(45^\circ) = \left(\frac{20}{\pi^2} + 1\right) * \frac{1}{2} \rho U^2$$

**Equation 5-5 Peak pressure for a cone of 45 degrees.**

In Figure 5-20 a first reflection is given on the use of DNV for cones of 45 degrees. The DNV constant pressure with an average pressure slamming coefficient of  $2\pi$  and of 2.5 (reduced factor for a cone of 45 degrees) is plotted in function of the impact velocity of the object. Next, also the 3D Wagner peak pressure calculated according to Equation 5-5 above is included. It is shown in the figure that the DNV with a  $2\pi$  slamming factor is very conservative. Additionally, the reduced slamming factor 2.5 is smaller but still in the same order of magnitude as the peak pressure predicted by the Wagner 3D model. For now, it could be concluded that the reduced slamming factor could be used for a cone of 45 degrees. Since DNV predicts a constant pressure this value is probably still conservative. In Chapter 7 a value lower than both theoretical pressures was measured for a particular impact velocity.

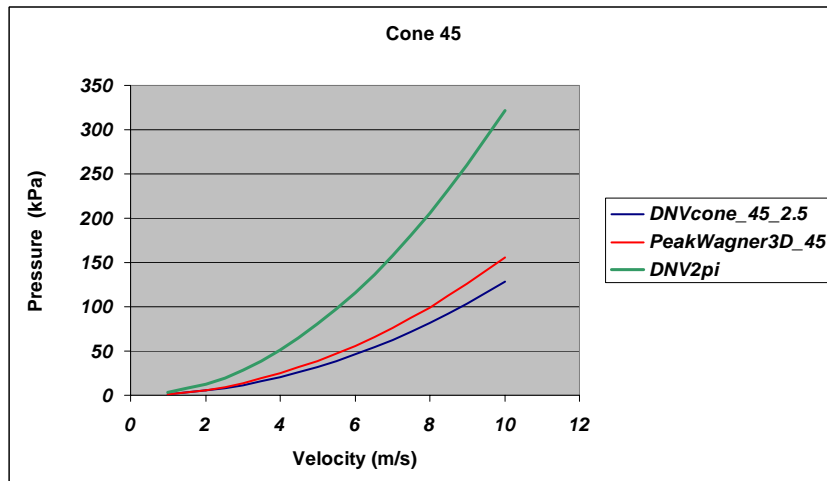


**Figure 5-20 Comparison between the DNV constant pressure in function of the impact velocity of the object with an average pressure slamming coefficient of  $2\pi$  and of 2.5 (cone 45 degrees) and the peak pressure according to Wagner for a 3D cone of 45 degrees.**

Next, several breaking wave calculations were performed on the buoy. First, a breaking wave calculation was done on the pencil buoy with inner composite tube. Next, two cases were calculated with added internal stiffeners. The main results of these calculations are summarised in Figure 5-1.

Pencil	Tsai Wu measure	$\sigma_{11}$	XT	$\sigma_{22}$	YT	$\sigma_{12}$	S
Stiffeners	(-)	(MPa)	(MPa)	(MPa)	(MPa)	(MPa)	(MPa)
0	2.77	165.6	575.7	43.2	20.73	85.1	71.43
1	2.42	104	575.7	40.8	20.73	79.2	71.43
3	1.53	65.8	575.7	25.5	20.73	75.8	71.43

**Table 5-1 Overview of the Tsai Wu measures and stresses for breaking wave calculations; comparison with allowable stresses.**

The first calculation resulted in a very high Tsai Wu (2.77) as is shown in Figure 5-21 (left). This maximum value occurs again in layer 1 hence at the inner side of the buoy. The main cause of this value is again, considering of course both the calculated and maximum stresses in all directions, the shear stress  $S_{12}$ . The radial displacement  $U_1$  is also shown on the same figure (right). The number of layers was increased, other filament winding combinations were tried, but still the maximum measure for Tsai Wu (buoy of 10 layers) was at its best 1.67. Additionally, adding more layers (up to 14) did not result in Tsai Wu measure lower than one. Already with 10 layers a lot of material would be used per buoy. Hence, another solution was sought. Within the calculated model of seven cross wound layers, the distribution of the radial displacements, as was shown in Figure 5-21 (right) shows that bending is the most critical aspect.

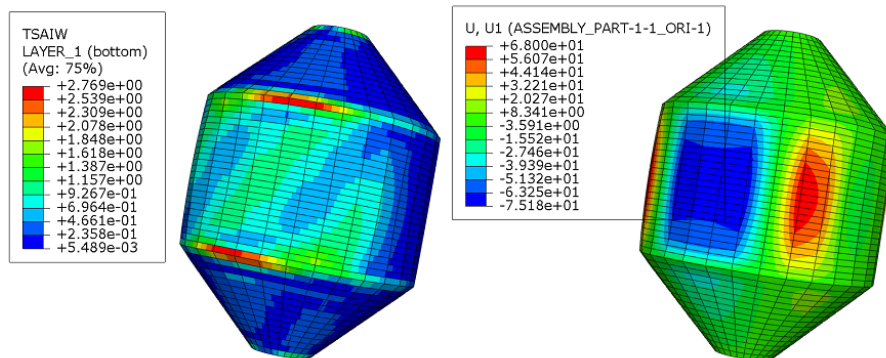


**Figure 5-21 Calculated distribution in Abaqus of the Tsai Wu measure for a constant breaking wave pressure of 0.472 MPa (left) and the radial displacement in mm (right).**

Internal stiffeners were simulated in the simplest way to confirm this diagnosis, namely they were modelled as restrained circles in the radial directions as is shown in Figure 5-22 for a stiffener in the middle at circle 13 (upper) and for three stiffeners in the cylinder at circles 13, 7 and 20 (lower). Circles are counted from the bottom to the top of the cylindrical part of the buoy.

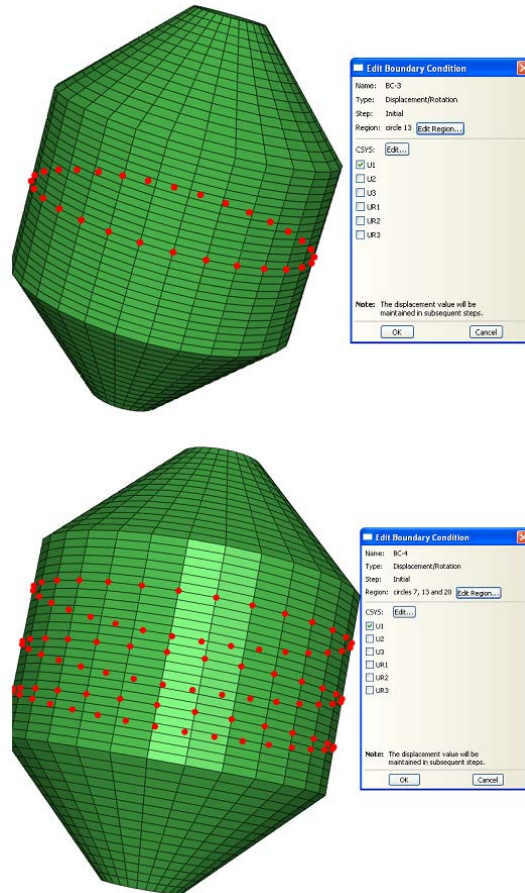


**Figure 5-22** Easy modelling of stiffeners: restraining the radial movement at one circle (upper) and at three circles (lower).

In this way the stresses  $S_{11}$ ,  $S_{22}$  and  $S_{12}$  decrease as is shown in Figure 5-23, Figure 5-24 and Figure 5-25. In each figure the stresses for the pencil without stiffeners (upper), with one stiffener (middle) and with three stiffeners (lower) are depicted. Stresses are always depicted in the local orientation system (the 1-axis is the fibre direction, the 2-axis is perpendicular to the fibre and the 3-axis is perpendicular to the shell). Due to this decrease in stresses the Tsai Wu measure decreases as well as is shown in Figure 5-26 for the pencil with one stiffener (upper) and with three stiffeners (lower) but is still not lower than one.

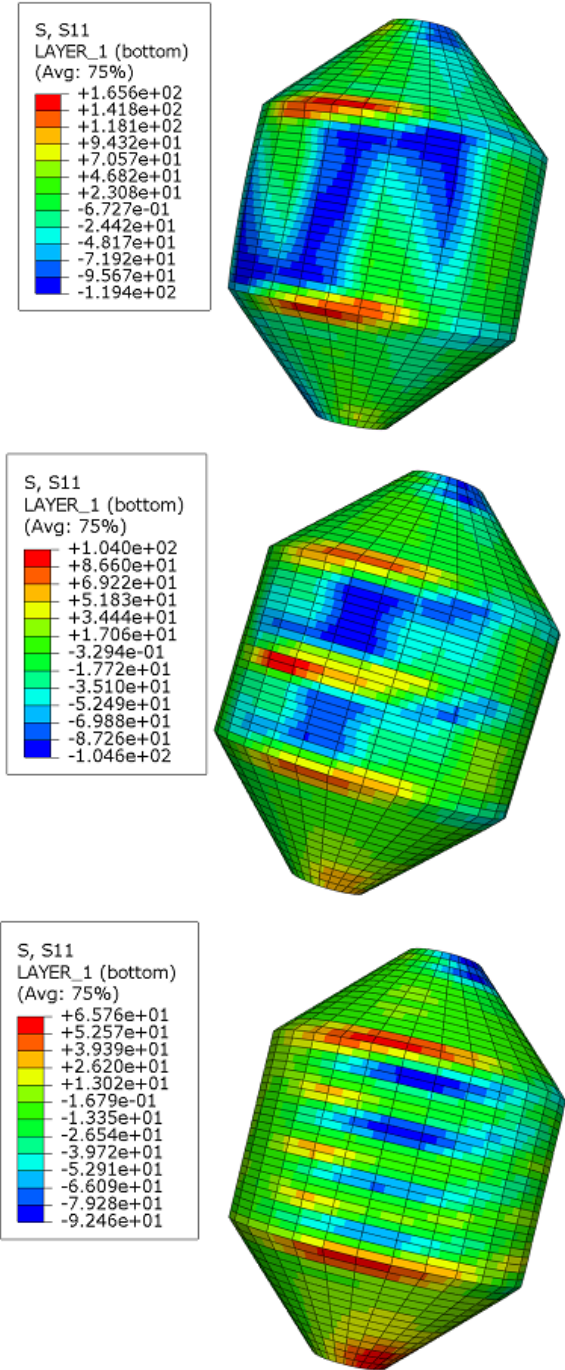


**Figure 5-23** Distribution of  $S_{11}$  ( $\sigma_{11}$ ) in layer 1 for the pencil without stiffeners (upper), with one stiffener (middle) and with three stiffeners (lower).

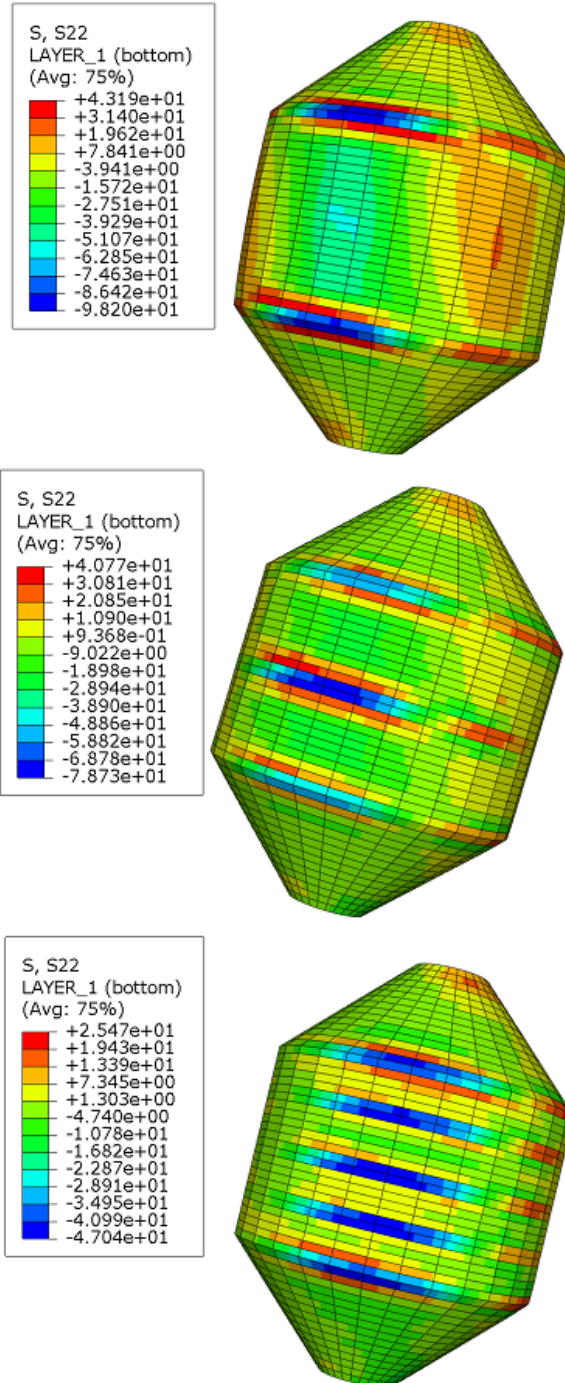


**Figure 5-24** Distribution of  $S_{22}$  ( $\sigma_{22}$ ) in layer 1 for the pencil without stiffeners (upper), with one stiffener (middle) and with three stiffeners (lower).

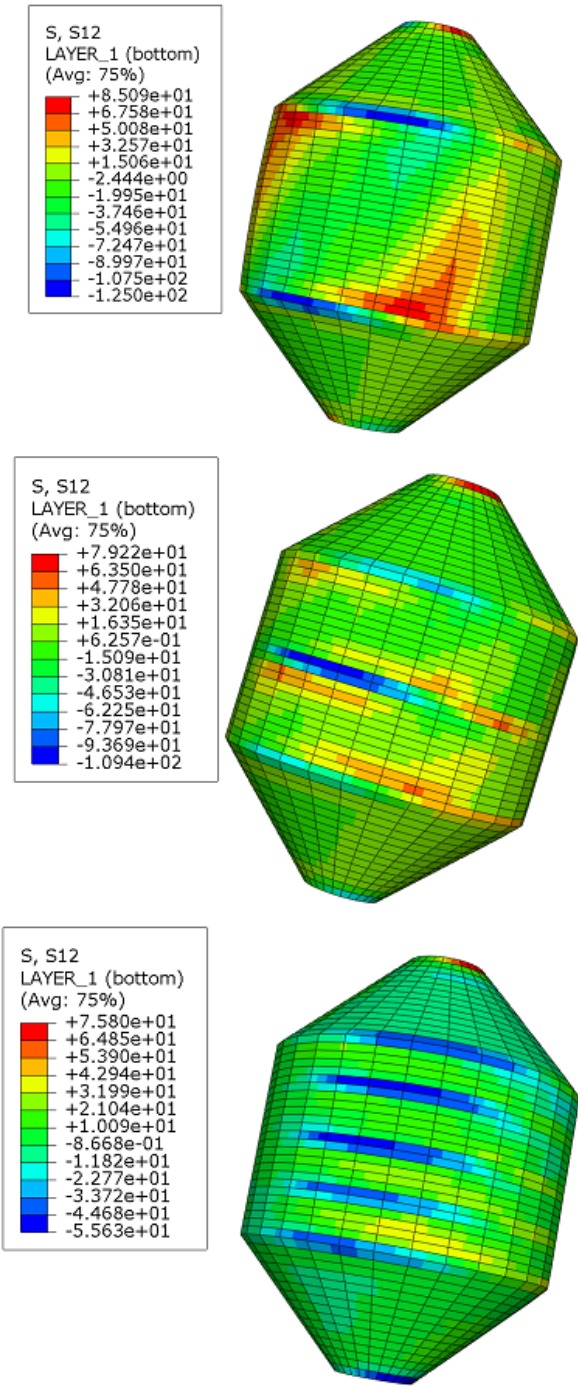
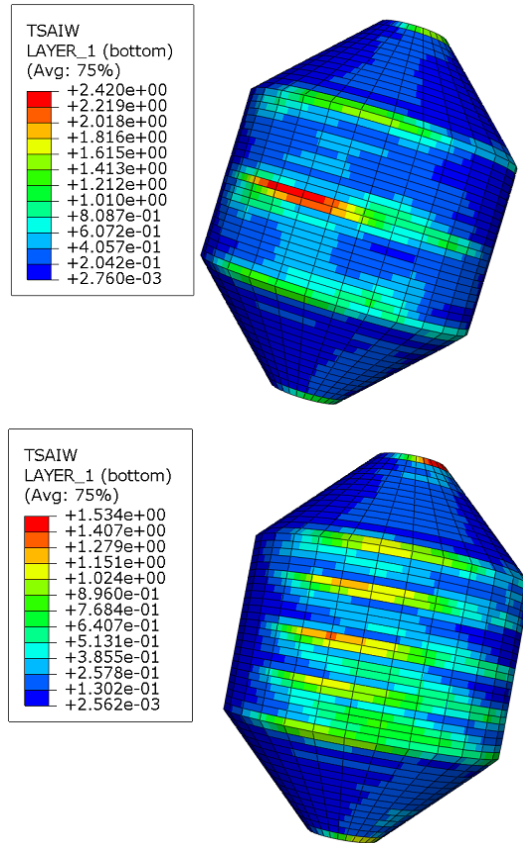


Figure 5-25 Distribution of  $S_{12}$  ( $\sigma_{12}$ ) in layer 1 for the pencil without stiffeners (upper), with one stiffener (middle) and with three stiffeners (lower).



**Figure 5-26** Distribution of Tsai Wu measure in layer 1 for the pencil with one stiffener (upper) and with three stiffeners (lower).

In conclusion, the pencil calculations showed that the bottom slamming criterion could be fulfilled for this shape. However, to fulfil the extreme breaking wave condition a lot of material have to be used which increases the cost. Additionally, it should be taken into account that only the cylindrical part was covered with the DNV slamming pressure and in reality also the edges could suffer from a (smaller) load, namely one comparable with the slamming on wedges or other angle-shaped objects. On the other hand DNV suggests using a slamming factor of 3 for smooth cylinders instead of  $2\pi$  for calculating the pressure [8]. This gives a constant pressure of 0.225 MPa and a maximum measure for Tsai Wu of 1.15 for one stiffener and of 0.74 for three stiffeners which is lower than one, but still needs a lot of material to achieve it. Hence, on the Project Technical Meeting (PTM) of Seewec at January 23<sup>rd</sup> and 24<sup>th</sup> 2007, it was decided to use a shape which uses less material in general and at the same time provides more resistance towards bending. A shorter ‘pencil’ was proposed as a new candidate shape as is explained in following paragraph.

## 5. 5. CONE-CYLINDER-CONE

### 5. 5. 1. Introduction

The final proposed shape within Seewec was only slightly different from the pencil. It was made shorter to limit the influences of the breaking wave slamming. However, since it could not be made too short for the bottom slamming, a fairly symmetrical shape (in dimensions) was proposed as is shown in Figure 5-27.

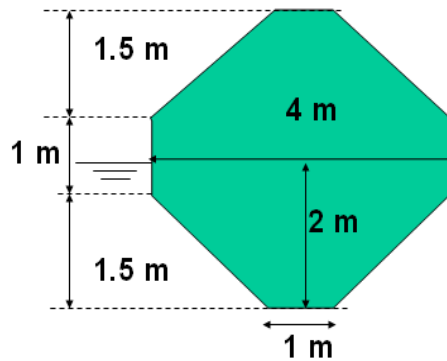


**Figure 5-27 Proposed cone-cylinder-cone shape.**

For the calculations at the cone-cylinder-cone shape a constant pressure is applied again at a circle segment of 60 degrees. The pressure along the height stays constant due to the fact that the behaviour of wave slamming was not known well enough to decrease pressures accordingly. For bottom slamming again 1 meter height was chosen but for the breaking wave slamming next to the cylindrical part also a small area of both conical parts is taken into account in a way that half of the height of the buoy is considered (2 m). The same load as for the cylinder was chosen, namely 0.316 MPa for bottom and 0.472 MPa for breaking wave slamming. The applied area for both is given in Figure 5-28. The calculations for the breaking wave slamming are discussed first because those were most critical for the pencil shape.

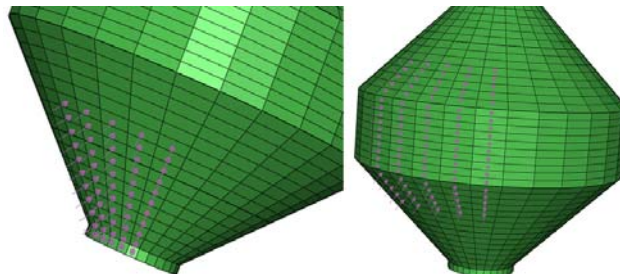


**Figure 5-28 Areas for pressure load of bottom slamming (left) and breaking wave slamming (right) [1].**

In Table 5-2 the Tsai Wu measures of several calculations on the cone/cylinder/cone shape are summarised. These results are discussed in detail in following paragraphs.

Cone/Cylinder/Cone		Tsai Wu measure	
		Breaking	Bottom
<b>Four layers SMC</b>	Without stiffeners	6.88	/
	With four internal stiffeners	3.45	/
<b>Six layers SMC</b>	Without stiffeners	4.96	/
	With four internal stiffeners	2.74	/
<b>Eight layers SMC</b>	Without stiffeners	3.74	0.71
	With four internal stiffeners	2.44	/
	Sandwich with 30 mm foam	0.822	0.57
<b>Glass fibre/epoxy STY</b>	15 mm thick	1.09	1.15
	20 mm thick	0.8	0.79
	10 mm/ 20 mm foam/ 10 mm	0.79	0.63

**Table 5-2 Overview of the Tsai Wu measures for several calculations on the cone/pencil/cone shape.**

### 5. 5. 2. Breaking wave slamming: assessing the influence of stiffeners

For this cone/cylinder/cone shape new Cadwind layer files were sought. Within this paragraph the influence of more realistic internal stiffeners are assessed. These calculations are done with the material and production method of SMC. Three different laminates are formed out of Cadwind with four, six and eight layers. The first one consists out of two different layers, one that fully covers the point absorber and one that leaves the edges uncovered as is shown in Figure 5-29. The full layer is used as the first one (internal layer) and the fourth one (external layer) while the other layer is used as layer two and three. Next, for the point absorber with six layers the same four layers were used with two extra layers added in the middle, i.e. as layer three and four in this laminate. A third type of layer was proposed because calculations with additional second layers showed that the thickness on the edges increased faster than the Tsai Wu measure decreased. Hence, the third layer, shown in Figure 5-30, was created and applied two times. Finally, for the point absorber with eight layers this same layer was again added two times in the middle.

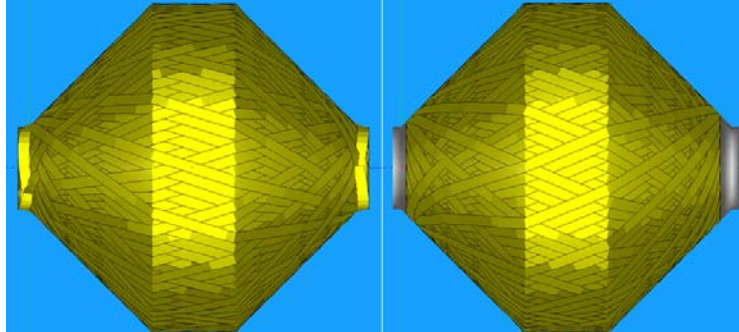


**Figure 5-29** Filament winding layers: layer 1 and 4 in four-layer buoy (left) with winding angle 18 degrees, pattern 17/11, turning zones 2-39, start 4; layer 2 and 3 in four-layer buoy (right) with winding angle 22 degrees, pattern 18/1, turning zones 8-34, start 8.

The calculated mass of the four layered buoy is 850 kg, for the six layered one it is 1330 kg and finally for the eight layered one it is 1800 kg. For the inner tube this is about 250 kg. This is an improvement in material cost (pencil 2850 kg). The FEA comparison for these three different laminates was done with the material constants of SMC for the buoy and inner tube. The four internal stiffeners were simulated as sandwich circular panels with skins of 2 mm thick consisting out of the chosen material of STY (glass fibre/epoxy) and a core of 20 mm PVC foam of 22 MPa, a Poisson coefficient of 0.32 and density of 70 kg/m<sup>3</sup>.

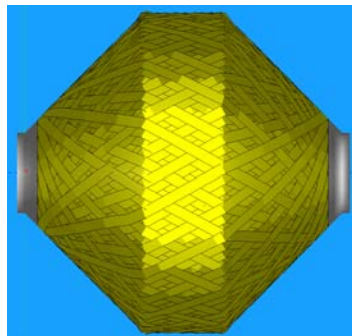


**Figure 5-30** Filament winding layer: middle layers for six- and eight-layer buoy with winding angle 29 degrees, pattern 29/2, turning zone 15-28, start 15.

An example with stiffeners and the inner tube are depicted in Figure 5-31 without the buoy around it. In this figure four stiffeners are applied. However, several calculations were done before: with one stiffener in the middle, with two, three and four. Finally this set-up seemed to give the best result.

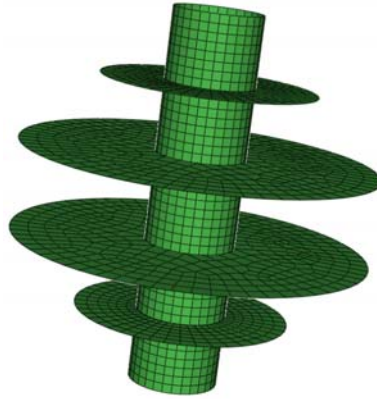


**Figure 5-31 Inner composite tube with four internal stiffeners.**

Now, on all three laminates of the buoy (four, six, eight layers) a lateral pressure of 0.472 MPa is applied on a sector of 60 degrees over the cylindrical part of the buoy and partly over the cones as explained in paragraph 5. 5. 1. The Tsai Wu measure for the four-layered buoy is shown without internal stiffeners (left) and with internal stiffeners (right) in Figure 5-32. The maximum Tsai Wu measure of 6.88 occur in cross wound layer four (outer layer) for the one without stiffeners and of 3.45 in the inner layer for the one with the four stiffeners. However, in the both cases, there is only a slight difference between the values of the inner and outer layer. Further, the Tsai Wu measures are depicted for the six and eight layered buoy in Figure 5-33 and Figure 5-34. There, the maxima are all located in the outer layer of the buoys. As is seen all measures for Tsai Wu improved a lot when using internal stiffeners. However, considering the additional production cost of the stiffeners, alternatives were sought as discussed in the following paragraph. No additional layers were added anymore since the thickness of the eight layered buoy is already pronounced as is shown in Figure 5-35.

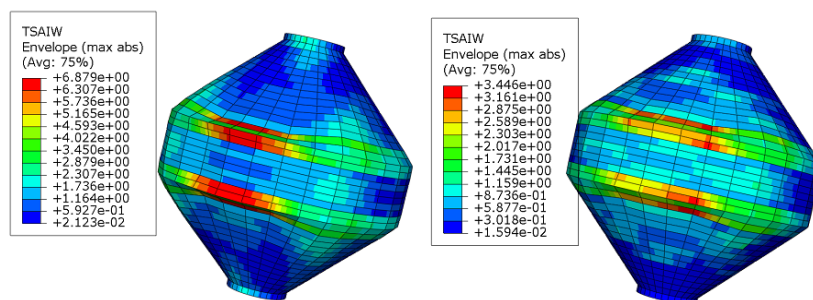


**Figure 5-32 Tsai Wu measure for the four-layered buoy; without stiffeners (left) and with four internal stiffeners (right).**

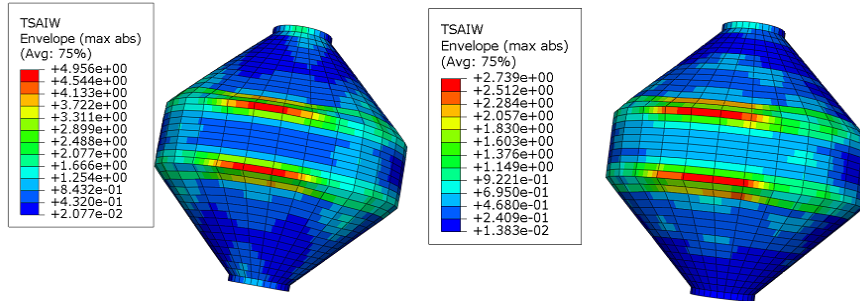


**Figure 5-33** Tsai Wu measure for the six-layered buoy; without stiffeners (left) and with four internal stiffeners (right).

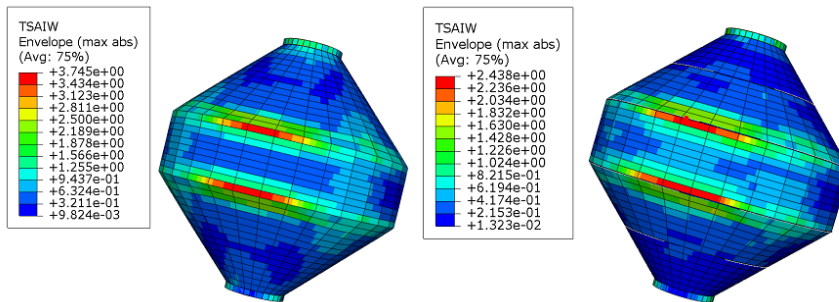


**Figure 5-34** Tsai Wu measure for the eight-layered buoy; without stiffeners (left) and with four internal stiffeners (right).

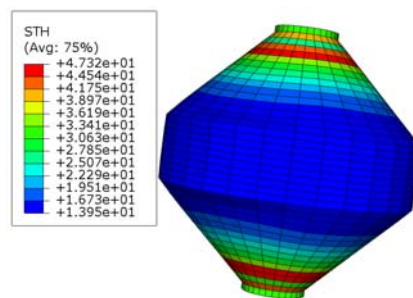


**Figure 5-35** Distributed thickness of the eight-layered buoy in mm.

All measures for Tsai Wu are still a lot larger than one. However, the purpose of this paragraph was to assess the effect of adding internal stiffeners.

### 5. 5. 3. Breaking wave slamming: assessing the use of foam

First, the foam used in the previous calculations for the stiffeners, was applied as the core material of 30 mm thickness in the eight layered buoy, so that the whole body of the buoy becomes a sandwich material. In the model of the shell a code line with the properties of the foam layer is added in between two skins each consisting of four filament wound layers.

The maximum measure for Tsai Wu measure for this case is 0.822 as is shown in Figure 5-36, which is a drastic improvement. The maximum value is situated in the third cross wound layer. This decrease is mainly due to the added stiffness that a sandwich material provides. In Figure 5-37 it is clear that the main improvement is due to a lower tensile stress  $\sigma_{22}$  in the direction perpendicular to the fibres.

Within WP4 of the Seewec project it was decided to propose a buoy with eight cross wound layers and 30 mm foam. Since the Tsai Wu measure for extreme conditions is below one, there was opted for such a buoy as ‘a proposal based on the calculations’ for the second generation point absorber. Next, as mentioned before, the slamming factor of  $2\pi$  can be replaced by 3 for smooth cylinders [8]. Then, the applied pressure decreases to 0.225 MPa and the Tsai Wu measure for the buoy with only eight cross wound layers without PVC foam is 1.78 as is shown in Figure 5-38 which is still larger than one but of course a lot better than before.

In the following paragraph the influence of changing the material and production method is assessed. For this, the selected material and production method of STY are used.

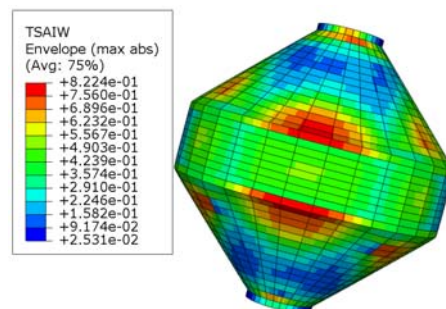


**Figure 5-36** Distribution of Tsai Wu measure for a buoy with a shell consisting out of eight cross wound layers with PVC foam.

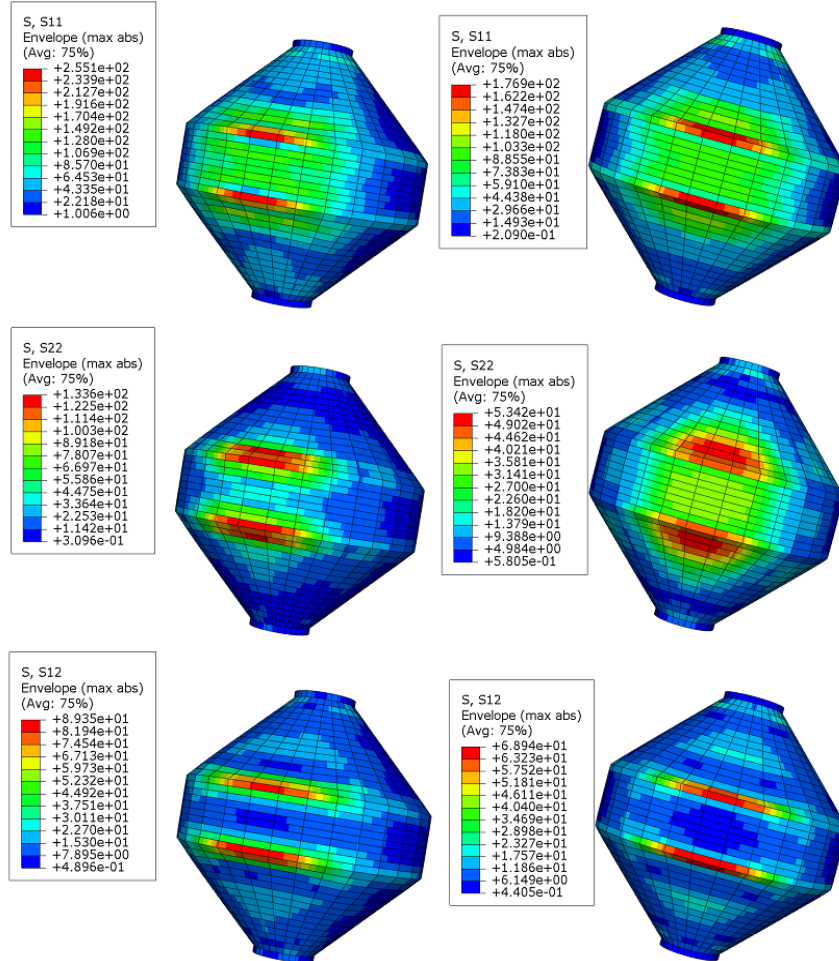


Figure 5-37 Distributions of stresses  $\sigma_{11}$ ,  $\sigma_{22}$  and  $\sigma_{12}$  of the eight layered buoy without foam (left) and with foam (right).

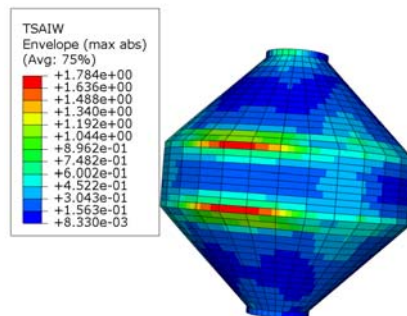


Figure 5-38 Distribution of the Tsai Wu measure for the cone/cylinder/cone shape at reduced DNV load.

#### 5. 5. 4. Breaking wave slamming: assessing the use of material and production method

The same breaking wave calculations (DNV norm which results in 0.472 MPa) is used on a buoy consisting out of 15 mm glass fibre epoxy, on one with 20 mm and on a sandwich buoy with 20 mm PVC foam and skins of 10 mm again out of glass fibre epoxy. The used input for the STY material properties are given in Figure 5-39. Again the first row gives the E-moduli, the Poisson coefficient and the G-moduli while the second row gives the allowable stresses.

E1	E2	Nu12	G12	G13	G23	
21550	21550	0.3	4200	4200	2500	
Ten Stress Fiber Dir	Com Stress Fiber Dir	Ten Stress Transv Dir	Com Stress Transv Dir	Shear Strength	Cross-Prod Term Coeff	Stress Limit
346.32	346.32	346.32	346.32	50	0	0

**Figure 5-39** STY material properties in MPa except the dimensionless Poisson coefficient Nu12; input for Abaqus.

Within Abaqus the same mandrel as for SMC was used, only the lay-up in the shell sections is different: for the sandwich buoy such a section contains three layers in all areas of the buoy, namely the two skins and the foam; for the buoy consisting solely out of glass fibre epoxy there is only one (and the same) layer in each area of the buoy. The material orientation for STY is zero since it concerns a 0/90 textile to start with. The Tsai Wu measure for the glass fibre epoxy buoy of 15 mm is given in Figure 5-40.

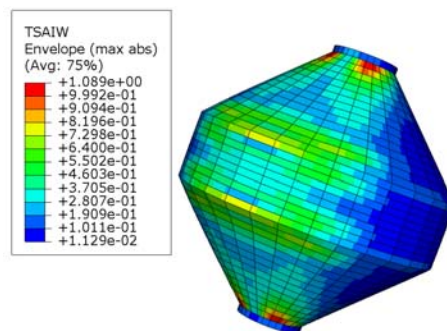


**Figure 5-40** Tsai Wu measure for the breaking wave slamming simulation (DNV) on a STY buoy consisting out of 15 mm glassfibre/epoxy.

And the STY buoy of 20 mm is given in Figure 5-41 (left) together with the sandwich buoy (right). It is seen clearly out of this last picture that the foam does not have a lot of influence in this case. Also, the critical zones for fracture are not the same as for the SMC buoy. Now, they are situated at the top and the bottom of the

buoy. Looking at the results in the left of Figure 5-41 for a buoy with an overall thickness of 20 mm it could be concluded that this STY buoy behaves better than the eight layered SMC buoy. However, the lay-up of the STY buoy is different from the SMC buoy. The thickness of the STY buoy is the same at every location while for the SMC buoy the thickness is variable along the axis which is inherent to the filament winding production technique. Second, for these calculations 0/90 degrees textiles have been used. This means that the STY buoy contains more glass fibres than the SMC buoy and hence is more expensive. In addition, also the vacuum infusion production method is more expensive than filament winding. For these reasons there was opted for the SMC buoy.

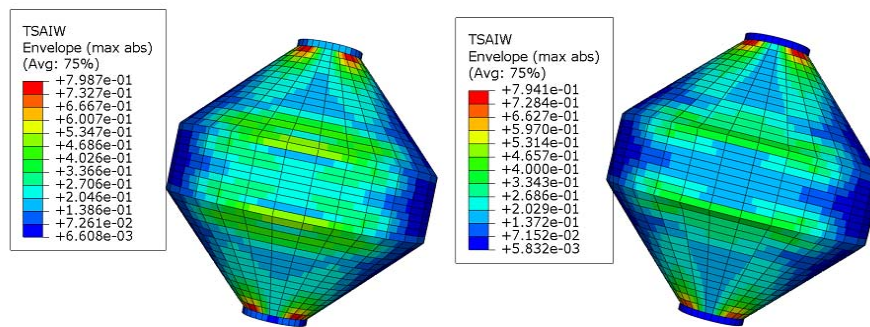


**Figure 5-41** Tsai Wu measure for the breaking wave slamming simulation (DNV) on a STY buoy consisting out of 20 mm glassfibre/epoxy (left) and of a sandwich buoy glassfibre/epoxy (10 mm) – PVC foam (20 mm) – glassfibre/epoxy (10 mm).

### 5. 5. 5. Bottom slamming

The results of bottom slamming (DNV value of 0.316 MPa over certain area as explained before) are given for both kinds of materials, SMC and STY to assess whether the buoys can also survive bottom slamming. The Tsai Wu measure is given in Figure 5-42 for the SMC eight layered buoy with 30 mm foam and for the same buoy without foam. For the one without foam the maximum Tsai Wu measure occurs in the outer layer and for the one with foam in the inner one. Figure 5-43 shows the same Tsai Wu measure for the STY buoys. Again, the result is given for a full glass fibre/epoxy buoy of 15 mm, 20 mm and for a sandwich buoy.

The Tsai Wu measure of the 20 mm STY buoy is worse than for the SMC buoy. The same can be concluded for both proposed sandwich buoys.

Within this Chapter several calculations were performed on the buoys. Finally, for the pencil shape a suitable SMC buoy was put forward. In Chapter 8 and 9 some

elaboration on the final proposal, based on experimental pressure measurements, can be found. First, in Chapter 6 and 7 a laboratory filament winding machine, with the making of some test samples, is discussed; and several slamming drop tests on a newly made laboratory slamming set-up are explained while their results are validated.

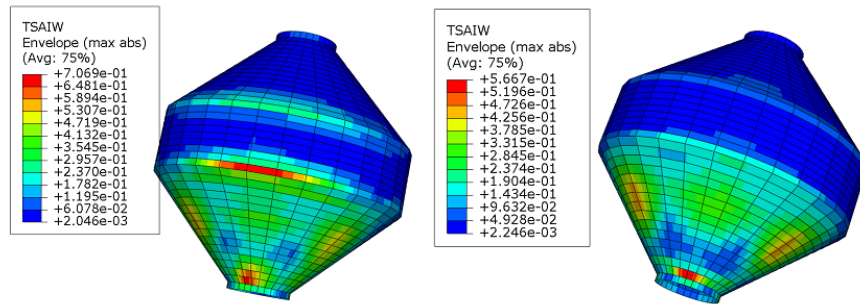


**Figure 5-42** Tsai Wu measure for the eight-layered SMC buoy with foam (left) and without foam (right).

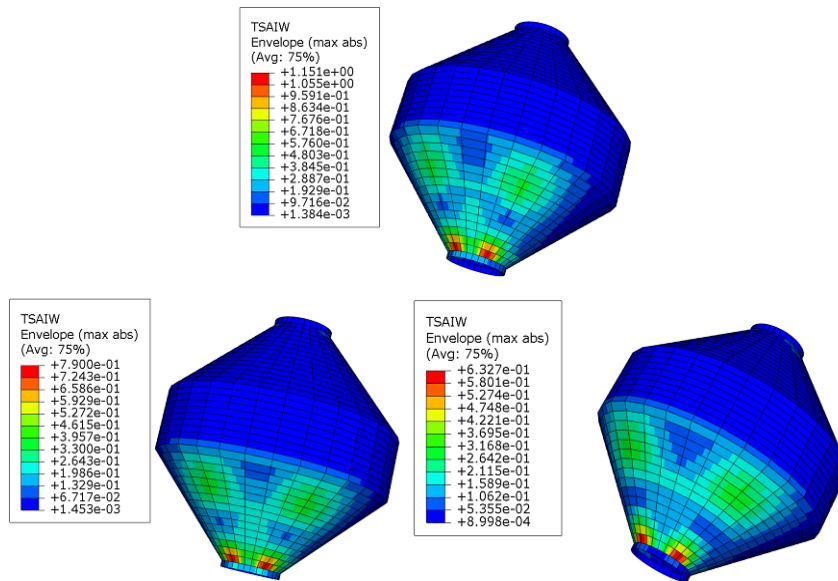


**Figure 5-43** Tsai Wu measure for the bottom slamming simulation (DNV) on a STY buoy consisting out of 15 mm glass fibre/epoxy (upper), one of 20 mm glass fibre/epoxy (left) and of a sandwich buoy with 10 mm glass fibre skins and 20 mm PVC foam core.

## 5. 6. REFERENCES

1. SEEWEC - Internal report from Brevik Engineering. FO3 - Prototype 1:1. Engineering and Construction. Section 3 Loads. 2006.
2. SEEWEC - Internal deliverable. WP5: D9bII – Part A, Power Absorption for a reference Point Absorber. 2009.
3. G. DeBacker, M. Vantorre et al., Numerical modelling of wave energy absorption by a floating point absorber system. Paper No. ISOPE-2007-JSC-259, 2008.
4. Abaqus Analysis User's Manual Version 6.7, Section 17.2.1 Linear elastic behavior - Defining orthotropic elasticity in plane stress.
5. Abaqus Analysis User's Manual Version 6.7, Section 17.2.3, Plane stress orthotropic failure measures.
6. CADWIND NG User Manual. p. 13-38.
7. Abaqus Analysis User's Manual Version 6.7.
8. Det Norske Veritas (DNV). Classification notes No. 30.5 “Environmental conditions and environmental loads”. Section 6 “Wave and current loads”. March 2000.

## Chapter 6

### FILAMENT WINDING MACHINE AND SLAMMING SET-UP AT LABORATORY SCALE

*In this chapter, the principle of the filament winding set-up in the laboratory is explained in detail. A first trial production, namely cylinders for external reinforcement of concrete, is given. Also, the production method of the cones for the proposed shape of the point absorber is explained. Finally, the design of the slamming set-up in the laboratory is discussed.*

#### 6. 1. FILAMENT WINDING SET-UP IN THE LABORATORY

##### 6. 1. 1. Introduction

At the Department of Materials Science and Engineering of Ghent University a small winding machine is available. It was designed and built in the late eighties and was last used in 2001 [1, 2] and by the end of 2005 it certainly did not work anymore as it should. Hence, in the framework of the master thesis of T. Derveaux and W. Baro [3], the machine was made operational again. The winding machine contains bobbin holders, a pre-tensioning mechanism, a resin bath, a winding robot and a controller. In the following paragraphs all these parts of the machine are discussed. In Figure 6-1 a schematic view of the winding machine is shown. From left to right: first, the pre-tensioning mechanism with the bobbin holders in a closet; second, the resin bath; and finally, the winding axes, are shown.

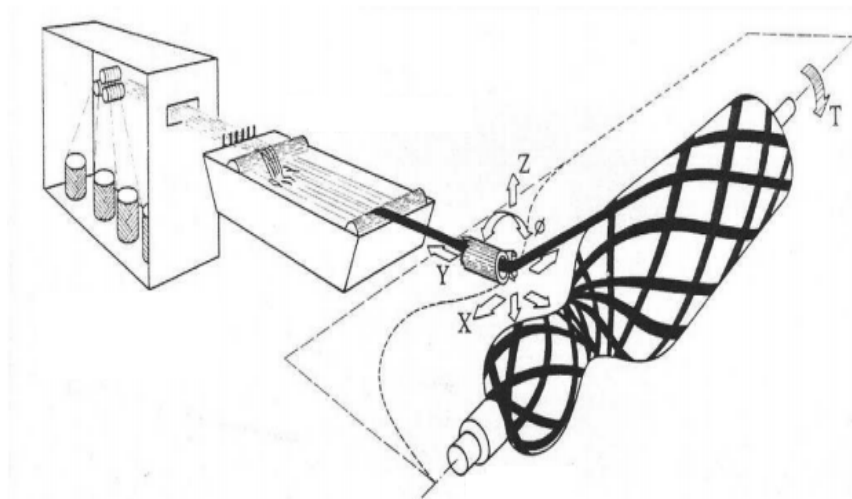


**Figure 6-1** Schematic view of the filament winding machine [1].

### 6. 1. 2. The bobbin holders

The dewinding of the bobbins can be done from the inner diameter or from the outer diameter of the bobbins. Both mechanisms are shown in Figure 6-2. In general the de-winding is external. Then, the bobbins are mounted on an electrical or mechanical brake axis which is used to regulate the pre-tension. In this machine the de-winding happens internally. As can be seen in Figure 6-1 the bobbins are mounted in a closet. The fibres go through a hole at one side. A picture of the closet with the bobbin holders is shown in Figure 6-3.

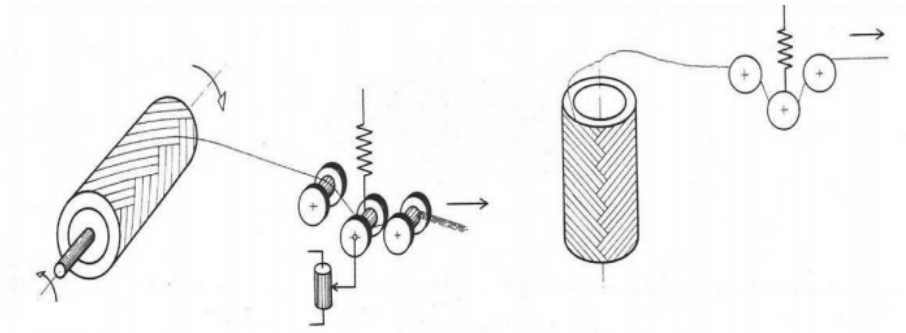


**Figure 6-2 De-winding: outer diameter (left) and inner diameter (right).**



**Figure 6-3 Closet with bobbin holders and pre-tension mechanism.**

The necessary pre-tension of the fibres is reached through the use of the ‘pre-tension mechanism’, discussed in following paragraph.

### 6. 1. 3. The pre-tension mechanism

In the pre-tension mechanism the fibres are guided between several rolls. The pre-tension is created by three rolls depicted in the upper left of Figure 6-4.

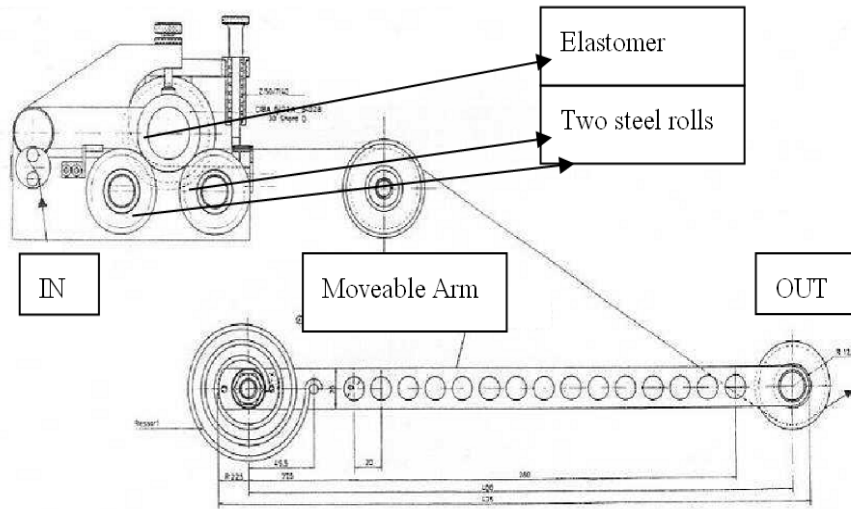


**Figure 6-4 Pre-tension mechanism for one bobbin.**

One of these rolls, the highest one, is made of an elastomeric material hence it can be pushed against the two steel ones. The fibre bundle, which is dewound internally out of the bobbin, is guided through these rolls. All rolls have bearings. In that way they are able to follow the desired velocity. One roll can be slowed down in a mechanical way. This tension is regulated by means of an adjustable spring which can be read out at a foreseen scale. Also, a moveable arm is foreseen to deal with velocity shifts.

In the closet, which was mentioned before, four of these pre-tension mechanisms are mounted. Hence, due to this, the filament winding machine can use a maximum of four fibre bundles coming out of four bobbins. The velocity of the fibres is determined by the filament winding process. The pre-tension mechanism is shown in Figure 6-5. By the movement of the rotating axis (C-axis; the axes of the machine are discussed in paragraph 6.1.5.) the fibre bundles are pulled through the complete pre-tension mechanism and brought together in the resin bath.

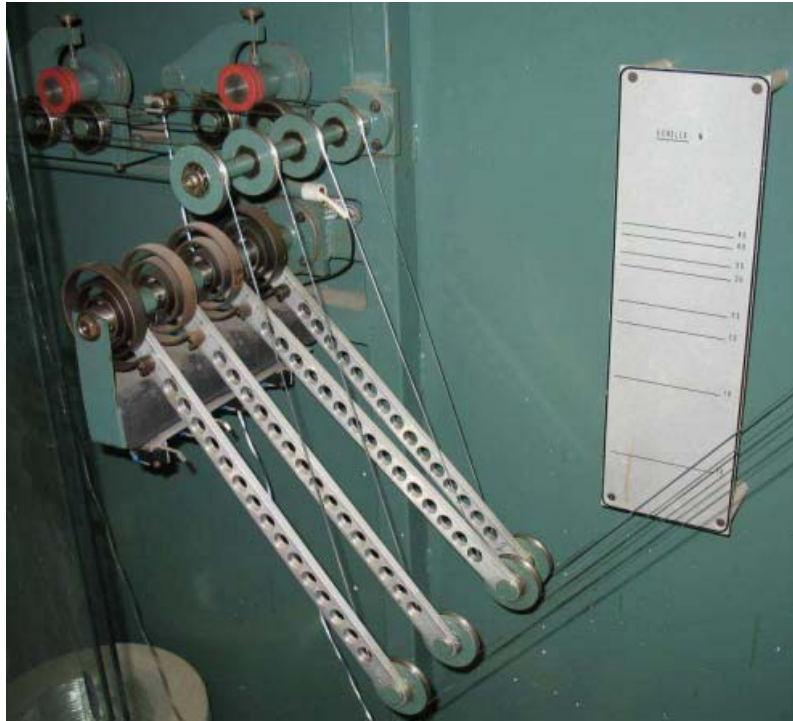


**Figure 6-5** Picture of the four pre-tension mechanisms.

#### 6. 1. 4. The Resin Bath

The technical drawing of the resin bath is shown in Figure 6-6. This resin bath is mounted in the X-arm of the robot and hence follows all its movements.

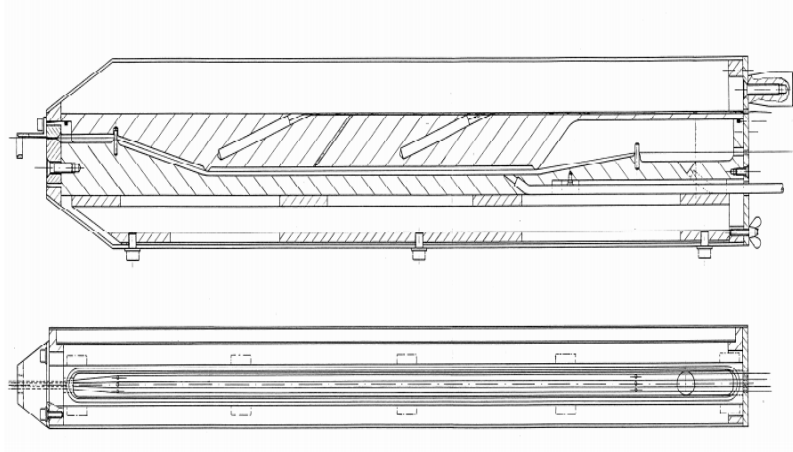


**Figure 6-6** Technical drawing of the resin bath.

The resin bath contains two aluminium parts. The lower part is the real bath where the resin is put in. The upper part can be clamped to it. Between the two parts there

is a seal. At the moment when both parts are put together, there is a very small area filled with resin where the fibres are pulled through. A warm curing resin should be used. This resin is pumped by a volumetric pump into the resin bath. The fibre bundles enter the resin bath through four small holes and are guided with the help of some small steel crests through the resin. On the other side of the resin bath they are pulled out again through a separate part with a calibrated hole. Within this doctoral thesis only cold curing (thermoset) resin was used (in consent with SMC) thus the resin bath was not used. Hence, the discussion of the resin bath stays limited to this paragraph.

#### 6. 1. 5. The winding robot

The CNC steered machine has four degrees of freedom. A sketch of the degrees of freedom for the winding machine in the laboratory is given in Figure 6-7.

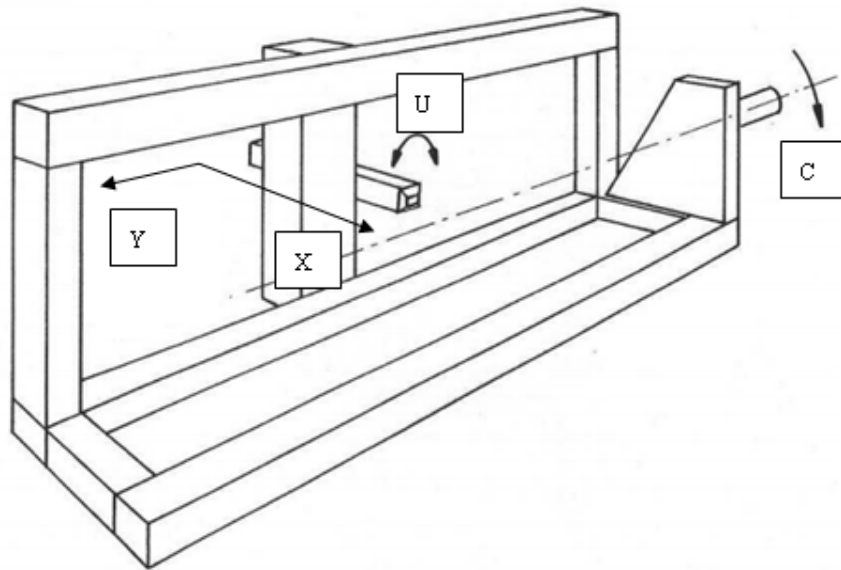


**Figure 6-7 Sketch of the degrees of freedom of the filament winding machine at laboratory scale.**

The first one is the rotation of the mandrel (C). This mandrel can be clamped between a centre point and claw. Also, two horizontal translation axes are available: one along the Y-axis which is parallel with the rotation axis and one along the X-axis which is perpendicular to the rotation axis. The last one is the free rotation of the winding eye (U). This moves freely due to the loads working on the fibre bundle. Hence, this degree of freedom falls automatically in the desired position. The two translations and the rotation of the mandrel are generated continuously by servo-

motors to achieve the desired winding path. The X-arm is made out of carbon epoxy material to achieve a very stiff and light part. In that way the arm does not suffer from a lot of inertia during the movement. The resin bath is mounted within that arm.

#### 6. 1. 6. Control: Labview and Cadwind

The commands for the machine come from a personal computer which controls all movements of the servo motors. They are the result of a pre-calculated winding path. To achieve a more modern and user friendly winding machine, it was decided to update the control. Previously this control was done with the help of a Baldor BPS-10 power supply unit, three separate Baldor BTS-10 servo drivers (one for each motor) and a PCAX3-card which allowed direct control of the three motors by a computer. The power supply, the three servo-drivers (shown in Figure 6-8) and the four end switches (to limit the translation movements of the X and Y axis) were preserved.



**Figure 6-8** Servo-drivers of the filament winding machine in the laboratory.

The PCAX3-kaart was removed inclusive all cables connecting with it. It was replaced with the Nextmove ESB controller of Baldor which is compact, flexible, user friendly and offers the possibility to control three servo-motors and four step-motors [4]. The installation of the controller was outsourced to Lernhout Engineering and the result is shown in Figure 6-9. Additionally, an emergency stop, pause button and velocity regulator were installed and are depicted in Figure 6-10.

The calculation of the winding path is done with the help of the software package Cadwind which was already introduced in Chapter 5. After a mandrel is created and the winding pattern is selected within Cadwind, still the machine parameters of the used winding machine are necessary inputs. For this laboratory filament winding machine these parameters are given in Table 6-1. A sketch is given in Figure 6-11.



**Figure 6-9** Installed Nextmove ESB controller of Baldor.



**Figure 6-10** Velocity regulator (upper left), pause button (lower left) and emergency button (right).

Machine parameters		
Carriage (Y-axis)	$Y_{max}$	770mm
	$Y_{ref}$	170mm
	$Y_{pos}$	dependent on position of the mandrel
	$V_{max}$	300mm/s
Cross Carriage (X-axis)	$A_{max}$	300mm/s <sup>2</sup>
	$X_{ref}$	310mm
	$V_{max}$	300mm/s
	$A_{max}$	300mm/s <sup>2</sup>
Mandrel (C-axis)	$V_{max}$	360°/s
	$A_{max}$	180°/s <sup>2</sup>

**Table 6-1** Machine parameters of the laboratory filament winding machine; necessary input for Cadwind [1].

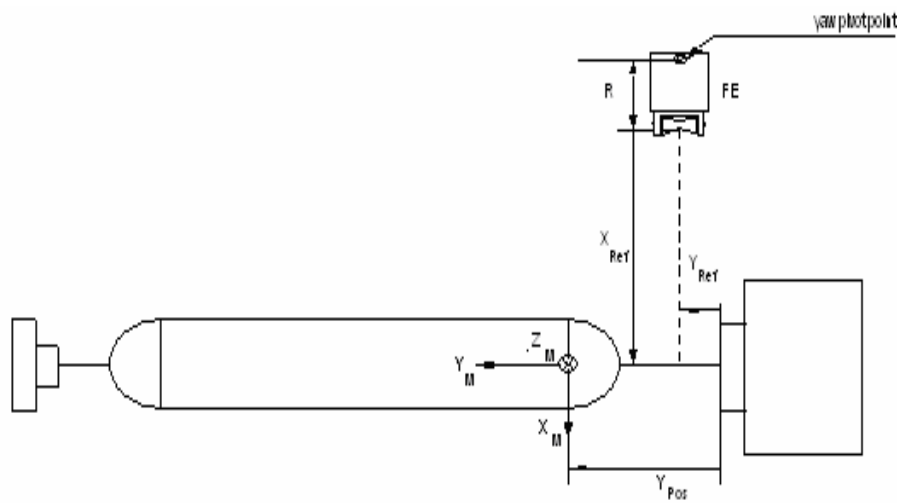


**Figure 6-11 Filament winding machine top view; machine parameters [1].**

Next, the winding path of the non-geodetic or geodetic curves is translated in rows, with positions for the three axes of the machine and for the time. A geodetic curve is a curve on a surface which connects two points with the minimum possible distance. However, not all bodies can be wound with these kind of curves and hence non-geodetic curves are introduced. This means that friction between fibre and surface is taken into account. An example is shown in Figure 6-12. Cadwind gives, in the last column, the fastest possible velocity i.e. the maximum velocity of the machine [5].

Labview programs are called Virtual Instruments or VI's. Labview contains several means to achieve, visualise, process and save data. By means of ActiveX it is possible to use all functions of MintMT for different platforms such as Labview. Through this program the MintMT start file can be loaded, the three axes homed and the Cadwind data file read. In this winding program a number of 0 to 10 should be given to vary the velocity. This number is multiplied with the numbers out of Cadwind and hence it is possible to adjust the winding velocity. Additionally, with the button of the velocity regulator (depicted in Figure 6-10 on the upper left) the velocity can be slightly adjusted during the winding. However, since this regulator does not change the velocity a lot it is better to test the velocity before actual production and hence choose an optimal number between 0 and 10. The most used number is seven. The other columns represent the movements of the axes of the filament winding machine. In this example, three columns are used while three others are zero since the machine of the laboratory only has three controlled axes. A spline is made of the positions given by Cadwind to produce the calculated winding path. MintMT is part of a so called 'workbench' and is the program language of Baldor to program the controller. Within this program the spline function is

available. The workbench is useful for direct commands such as direct movements of the axes. Also, MintMT is used for starting up the machine and homing of the axes which was also outsourced to Lernhout Engineering. Additionally, an automated user-friendly program was achieved by using Labview [6].

```

CADWIND CONTROL DATA FILE
MM
AXISYM: YES
REFERENCE POINT
0.000000 -230.000000 310.000000 0.000000 0.000000 0.000000
LAYER UNIT
93
1 0.000000 139.920105 95.943520 0.000000 0.000000 0.000000 0.000000
2 38.642876 174.699997 96.241211 0.000000 0.000000 0.000000 0.117104
3 95.755379 226.260910 97.118729 0.000000 0.000000 0.000000 0.290710
4 119.666801 247.988708 97.379463 0.000000 0.000000 0.000000 0.363867
5 143.639038 269.890594 97.723045 0.000000 0.000000 0.000000 0.437611
6 167.564865 291.809723 98.005318 0.000000 0.000000 0.000000 0.511413
7 191.530899 313.863403 98.326614 0.000000 0.000000 0.000000 0.585668
8 215.467392 335.973816 98.635284 0.000000 0.000000 0.000000 0.660114
9 239.410934 351.154999 98.823288 0.000000 0.000000 0.000000 0.727295
10 263.398621 363.692169 99.023872 0.000000 0.000000 0.000000 0.794601
11 287.388977 373.574219 99.181976 0.000000 0.000000 0.000000 0.861914
12 309.186920 379.289215 96.501541 0.000000 0.000000 0.000000 0.923075
13 331.059235 383.272736 94.159241 0.000000 0.000000 0.000000 0.984445
14 353.679932 385.638214 92.768341 0.000000 0.000000 0.000000 1.047915
15 377.427246 386.054993 92.523270 0.000000 0.000000 0.000000 1.114546
16 402.636780 384.012024 93.724548 0.000000 0.000000 0.000000 1.185280
17 429.426117 378.813416 96.781311 0.000000 0.000000 0.000000 1.260447
18 455.396851 370.343842 99.130302 0.000000 0.000000 0.000000 1.333316
19 479.404480 359.507294 98.956917 0.000000 0.000000 0.000000 1.400678
20 503.426453 345.973785 98.755295 0.000000 0.000000 0.000000 1.468079
21 527.488831 329.659973 98.559525 0.000000 0.000000 0.000000 1.535595
22 551.526794 310.552856 98.273643 0.000000 0.000000 0.000000 1.603041
23 575.582825 288.534393 97.966011 0.000000 0.000000 0.000000 1.677177
24 599.650269 263.520691 97.621124 0.000000 0.000000 0.000000 1.761399
25 623.702515 240.377823 97.288132 0.000000 0.000000 0.000000 1.839321
26 647.762085 218.592773 97.002281 0.000000 0.000000 0.000000 1.912671
27 671.799377 196.935577 96.666824 0.000000 0.000000 0.000000 1.985591
28 695.888428 175.284531 96.407013 0.000000 0.000000 0.000000 2.058490
29 719.977417 153.717667 96.148216 0.000000 0.000000 0.000000 2.131106
30 744.013123 132.310303 95.821762 0.000000 0.000000 0.000000 2.203184
31 768.066284 110.950623 95.535011 0.000000 0.000000 0.000000 2.275102
32 792.131958 89.670692 95.239532 0.000000 0.000000 0.000000 2.346752
33 816.174805 68.500099 94.925606 0.000000 0.000000 0.000000 2.418033
34 840.256470 47.357170 94.662514 0.000000 0.000000 0.000000 2.489222
35 864.267761 29.939795 94.383842 0.000000 0.000000 0.000000 2.556593
36 886.248291 20.483896 91.719749 0.000000 0.000000 0.000000 2.618267
37 906.778320 14.167573 87.854156 0.000000 0.000000 0.000000 2.675871
38 927.516357 9.164107 84.792030 0.000000 0.000000 0.000000 2.734059
39 948.817871 5.610533 82.617249 0.000000 0.000000 0.000000 2.793827
40 971.239624 3.753226 81.480576 0.000000 0.000000 0.000000 2.856739
41 995.518433 4.070061 81.674477 0.000000 0.000000 0.000000 2.924861
42 1022.229004 7.406956 83.716660 0.000000 0.000000 0.000000 2.999807
43 1051.223755 14.916768 88.312668 0.000000 0.000000 0.000000 3.081161
44 1080.274902 27.164055 94.339424 0.000000 0.000000 0.000000 3.162674
45 1104.258911 41.077744 94.562042 0.000000 0.000000 0.000000 3.229969
46 1128.213623 58.112598 94.800949 0.000000 0.000000 0.000000 3.297182
47 1152.139893 78.429947 95.059677 0.000000 0.000000 0.000000 3.365591
48 1176.115234 102.318016 95.431419 0.000000 0.000000 0.000000 3.446022
49 1200.014771 126.542496 95.729477 0.000000 0.000000 0.000000 3.527586
50 1215.483887 139.920105 95.943520 0.000000 0.000000 0.000000 3.572628

```

Figure 6-12 Example of a generated ‘winding path’ file out of Cadwind.

In Figure 6-13 the retrofitted filament winding machine of the laboratory is shown.



**Figure 6-13** The laboratory filament winding machine [3, 7, 8].

## 6. 2. FIRST TRIAL PRODUCTION: CYLINDERS FOR EXTERNAL REINFORCEMENT OF CONCRETE

### 6. 2. 1. Introduction

As a first trial it was agreed to cooperate with the Department of Civil engineering to provide them with a number of cylinders, namely seven with basalt fibres and five with glass fibres. These cylinders were used for a research project at that department about the reinforcement of concrete columns at laboratory scale. Concrete columns are used as supports for large buildings as is shown in Figure 6-14. Further on, in Chapter 7 several test objects for drop tests are discussed. Among those a full and hollow cylinder are present. Hence, this first experience with the winding machine was useful for the production of both of these test samples.



**Figure 6-14** Example of concrete columns used as support for this building (apartment complex ‘Monte Carlo’, De Royschans) [9].

The mentioned concrete columns are loaded in compression in the longitudinal direction. Failure has to be prevented because the whole structure could collapse when they fail. The winding of these columns supports them in their circumferential direction and hence they can bear a higher load. Additionally, when the concrete fails, the shape of these reinforced columns is preserved due to the composite cover.

### 6. 2. 2. Properties of the cylinders at laboratory scale

The desired dimensions of the cylinders were 300 mm length, 150 mm diameter. The used glass fibre is from ‘Owens Corning’. It has an average filament diameter of 17  $\mu\text{m}$  [10]. The used basalt fibre is called ‘Basaltex’ and has an average filament diameter of 13  $\mu\text{m}$  [11]. A roving is the fibre bundle wound on a bobbin. Both sorts of used roving (glass and basalt) have a linear density of 1200 tex. As mentioned in

Chapter 4, the unit tex is the amount of mass per unit length; 1 tex is  $10^{-6}$  kg/m. The thickness of the roving is about 2 mm. Note that the basalt roving has a close packing of spheres and hence the cross-section has a circular shape. The E-glass packing is flat hence the cross-section of the roving has a more rectangular shape. All cylinders are wound with one roving (i.e. one bobbin). The used resin is epoxy and contains two components, namely Tradecc PC 5800 A and B [12]. As soon as both components are mixed, there are thirty minutes left before the curing reaction starts. A cold curing resin was chosen since there was experience available at SMC for such a resin. However, with a cold resin, the resin bath could certainly not be used because after thirty minutes it would be very difficult to remove the resin out of it. With an identical winding process, the composite with basalt fibre should have a higher stiffness than the one with E-glass and especially higher material properties. However, the research of the reinforced concrete columns is not within the scope of this work.

### 6. 2. 3. The mandrel

Before production of the cylinders could start, a mandrel had to be made. The main design conditions for this mandrel were the ease of winding and the ease of loosing the cylinder from the mandrel. To achieve this, there was opted for a polyethylene tube which was made slightly conical on the lathe. It is seen in Figure 6-15 (upper). Wooden plates were clamped in the tube. A rod goes through the wooden plates as is also shown in Figure 6-15 (lower).



**Figure 6-15** Parts of the mandrel used for the winding of cylinders [3].

In this way it was very easy to mount the mandrel on the lathe as well as on the winding machine. Additionally, after the plates and rod are removed (when the cylinder is wound on the tube) the cylinder and the mandrel can be separated quite easily. A picture of the total 'cylinder mandrel' is given in Figure 6-16.



**Figure 6-16** Cylindrical mandrel [3].

#### 6. 2. 4. The winding patterns for the cylinders

The theoretical desired pattern for the cylinders was a winding angle of 90 degrees relative to its axis. However, the highest possible angle in Cadwind was 88 degrees as is shown in Figure 6-17. A hollow cylinder made like this – even with two or three layers – would easily fall apart. Hence, it was decided to include one cross wound layer with a smaller angle (56 degrees). The theoretical winding of such a layer is depicted in Figure 6-18.

To achieve a winding pattern as close as possible to the desired one (i.e. circumferential), it was decided to use the 88 degrees layer as the first one, the 56 degrees cross wound layer as the second one to keep the fibres from falling apart and finally a third layer equal to the first one (i.e. again 88 degrees). As explained these Cadwind files are able to control the filament winding machine. The mandrel in Cadwind is 400 mm length where 25 mm from each side should not be wound. Hence, a cylinder of 350 mm is achieved. At location 0 mm on the mandrel (i.e. where the conical part of the cylinder starts) the diameter is 148 mm. At location 400 the diameter is 159 mm. On the edges the cylinder is thicker inherent to this production method (turning zones fibres). For this, 25 mm is cut off at each edge and hence cylinders of 300 mm were obtained.

Before starting the winding, the mandrel is cleaned with acetone. Next, a thin layer of resin is brushed on the mandrel. As soon as the mandrel is completely covered with resin, the starting fibre bundle is glued to it and the winding program for the

first layer is started. Since the used resin starts curing after thirty minutes, resin is added gradually and the wound fibres are impregnated with the resin through the use of a brush as is shown in Figure 6-19. As mentioned, the resin should start curing after thirty minutes according to its data sheet. In reality it does ‘start’ at that moment but it lasts quite some time. The first cylinder was separated from the mandrel after two hours. However, this was not as easy as expected. For the second cylinder the time for curing was increased by leaving it overnight. This method worked; hence the other cylinders were released from the mandrel the morning after they were wound. A picture of all cylinders is shown in Figure 6-20.

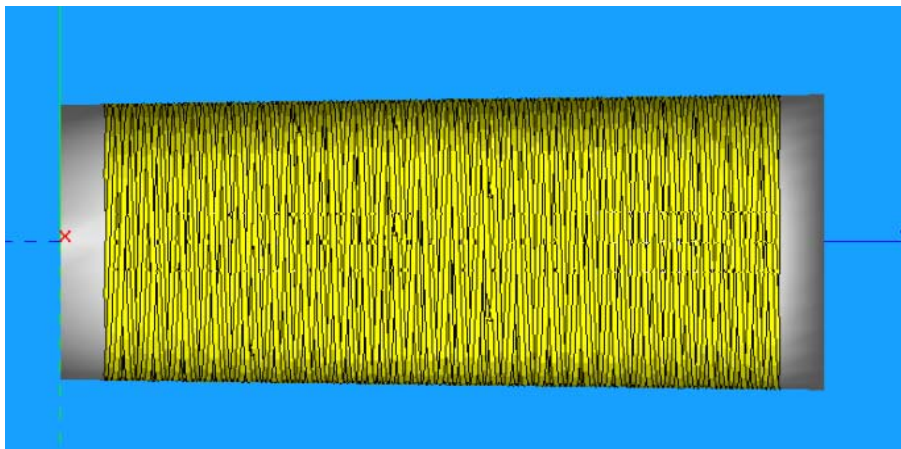


**Figure 6-17** Cadwind: winding angle of 88 degrees.

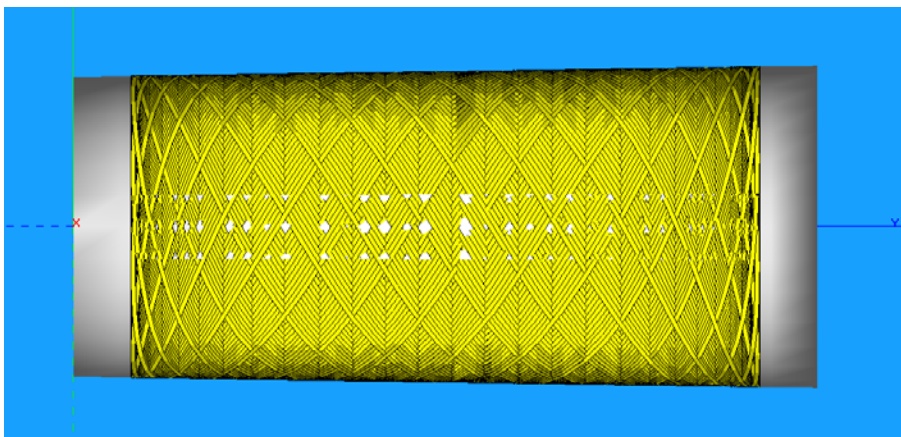


**Figure 6-18** Cadwind: winding angle of 56 degrees.

In the next paragraph, a second trial was performed, namely the production of a scaled shape of the cone/cylinder/cone point absorber. As mentioned, in Chapter 7, a

hollow and full cylinder test sample were made. However, another kind of mandrel was sought since these objects could not be conical at all.



**Figure 6-19** Winding of a cylinder; Gradually adding of resin [3].



**Figure 6-20** Twelve wound cylinders: five made with glass fibre and seven with basalt fibre [3].

In Figure 6-21 a tested basalt cylinder is shown.



**Figure 6-21** One of the tested basalt cylinders filled with concrete [3].

### 6. 3. LABORATORY SCALE PRODUCTION OF A POINT ABSORBER

#### 6. 3. 1. Introduction

The production of the cylinders succeeded as was explained in detail in the previous paragraph. However, a cylinder is by far the easiest shape to wind on the machine. Next, the challenge was producing a point absorber at laboratory scale. The shape of this point absorber is the last one used within the Seewec project, namely the cone-cylinder-cone as was mentioned in Chapter 5. The scale factor is 1:10 which gives the dimensions shown in Figure 6-22.

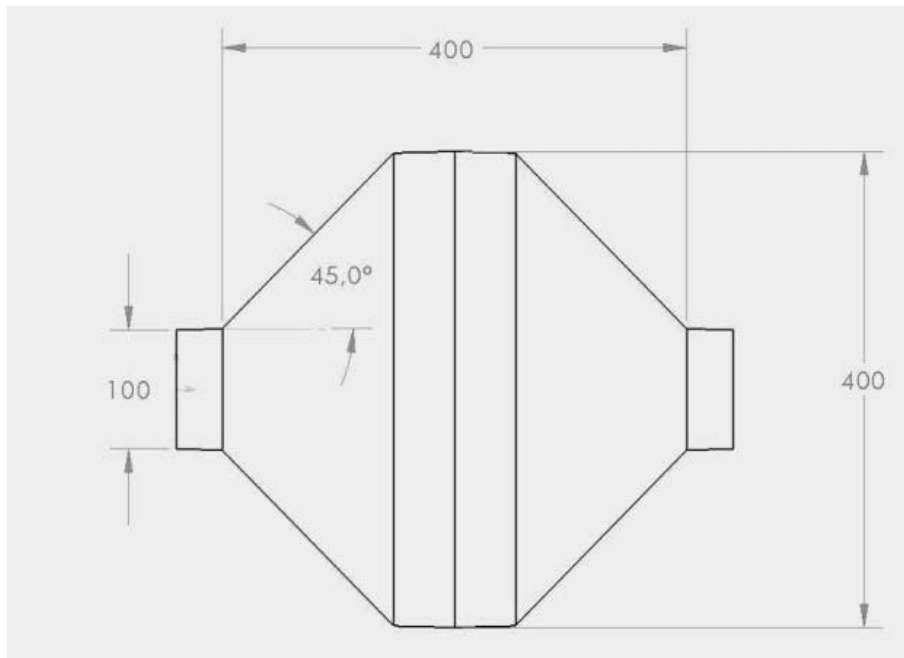


**Figure 6-22** Technical drawing of the point absorber at laboratory scale 1:10.

#### 6. 3. 2. The mandrel

A first possibility for the mandrel of the point absorber was pouring white plaster around a rod. The desired shape of this plaster structure could be formed on a lathe. After winding the point absorber and the curing of the resin, the plaster can be removed with a solvent and a high pressure sprayer. A disadvantage of this method is that for each object a new mandrel has to be made. Also, the production of a plaster mould and the removal out of the absorber are intensive, uneasy and messy. For these reasons a second option was taken into account, looking to methods with a

re-usable mandrel. However, the shape of the point absorber makes it very difficult to remove the mandrel.

Additionally, this method should be suitable for large scale buoys as well. In consent with SMC an option was proposed which was called ‘the method of the cones’ and this production method is explained in the following paragraph.

### 6.3.3. Method of the cones

The name of the method was chosen because two separate cones, which were made first, were put together over a tube as shown in Figure 6-23. Next, this structure was over wound on the winding machine.

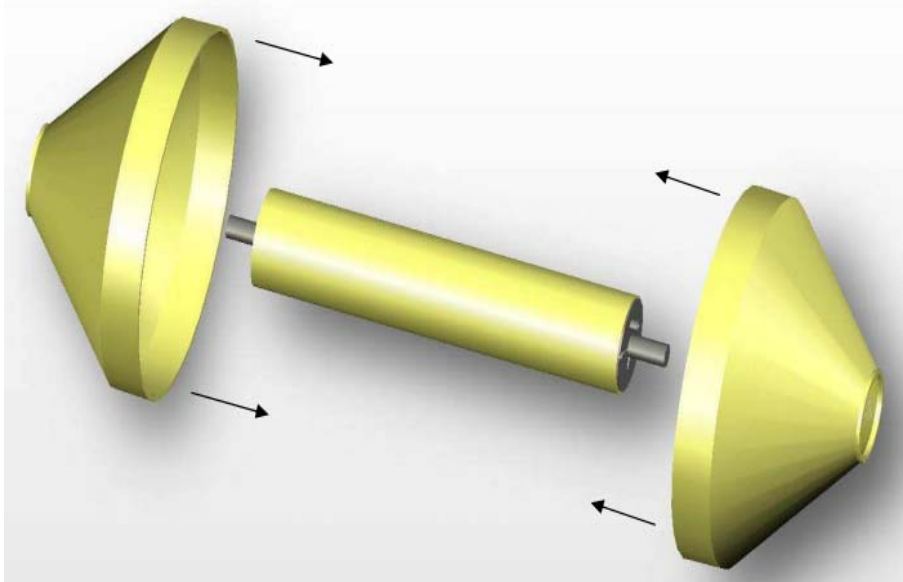


**Figure 6-23** Schematic view of the first phases in the ‘Method of the cones’.

For the production of the cones a mandrel, shown in Figure 6-24, was made out of polyethylene. The cylindrical parts have a small inclination because the removal of the composite cone of the mandrel would be easier. Also, at both sides of the mandrel there is a removable plate connected to a rod to mount the mandrel in the winding machine. The cone mandrel was mounted in the filament winding machine for the ease of working. The two cones were made by hand lay-up with a brush, resin and chopped fibres as is shown in Figure 6-25. One of the finished cones is shown in Figure 6-26.

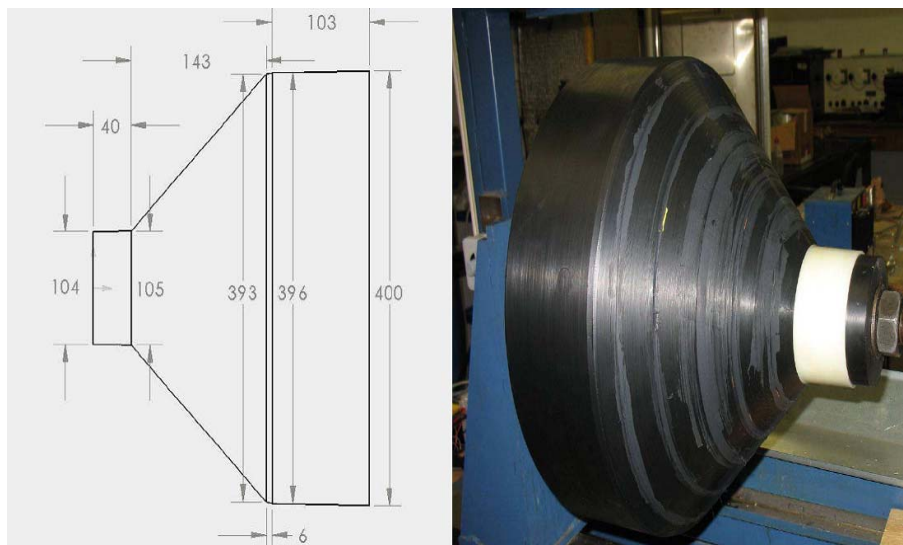


**Figure 6-24** Technical drawing of the cone mandrel (left) and the finished mandrel (right) [3].



**Figure 6-25** Production of a cone with chopped fibres [3].



**Figure 6-26** One of the two cones made with chopped fibres and resin [3].

Next, the inner central tube had to be made or provided. For the finite element calculations a cross wound tube of 46 degrees was used because it is a commonly used value at SMC for tubes. However, in SMC a mandrel for tubes is available but in the laboratory there is none. Hence, for the laboratory point absorber it was decided to use a PVC tube with the dimensions shown in Figure 6-27. Again, both ends of the PVC tube were foreseen of removable plates with a rod so that it could be mounted easily on the winding machine as is seen in Figure 6-28.

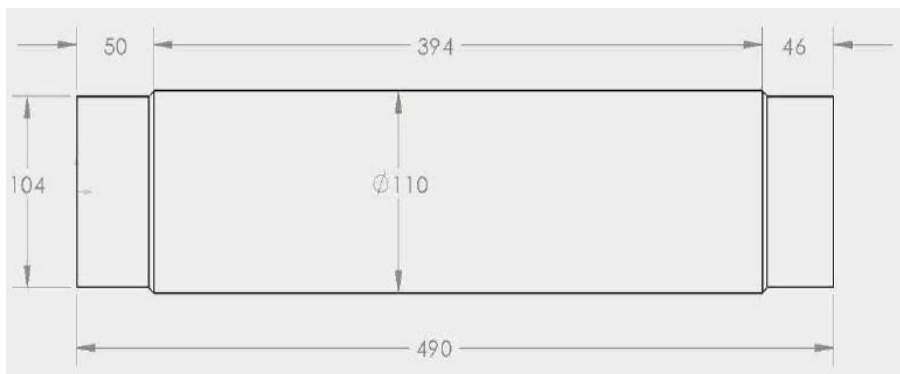


**Figure 6-27** Technical drawing of the inner PVC tube.



**Figure 6-28** PVC tube mounted on the filament winding machine [3].

Then, the cones were mounted on the winding machine. This mounting is shown in steps (one cone on the left, the second on the right) in Figure 6-29. A bit of resin was used to fix the cones together.

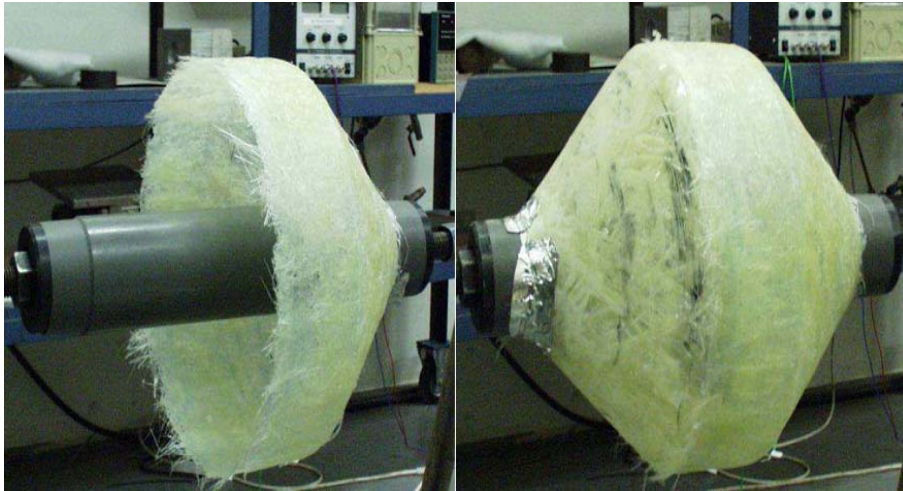


**Figure 6-29** Mounting of the two cones over the PVC tube on the filament winding machine [3].

At this stage the base structure was overwound. The used winding pattern is generated by Cadwind. It has a winding angle of 22 degrees. The winding pattern is shown in Figure 6-30. For this point absorber the layer was wound two times. The used fibres are again glass fibres supplied by 'Owens Corning' (Scandinavian Glasfiber AB, Falkenberg, Sweden). These fibres have an average filament diameter of 17  $\mu\text{m}$  and a linear density of 600 tex [10]. Four roving bundles were used. The resin is the same epoxy resin as the one used for the cylinders [12].

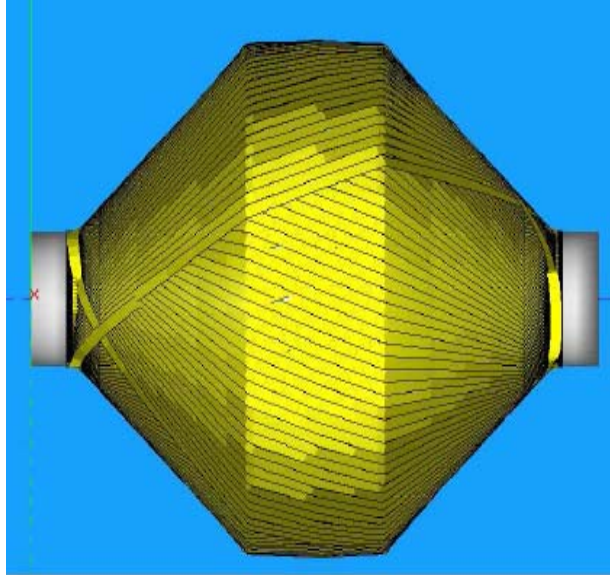


**Figure 6-30** Used winding pattern on the produced point absorber at laboratory scale.

The minimal distance between winding eye and mandrel was taken as 40 mm within Cadwind. Figure 6-31 shows a picture during the winding phase and in Figure 6-32 the final result is given. In this way experience was gained with the production method on laboratory scale.



**Figure 6-31** Over winding of the two cones [3].



**Figure 6-32** Result of the first produced laboratory point absorber on the filament winding machine[3].

#### 6. 3. 4. Possible improvement

In the full scale calculations no PVC tube is used but a filament cross wound tube of 46 degrees. Hence, for future work at the department, an easy way to produce cylinders would be an improvement for the process. A possible solution is a very similar mandrel to the one that SMC uses for making tubes and the small scale proposal is shown in Figure 6-33.

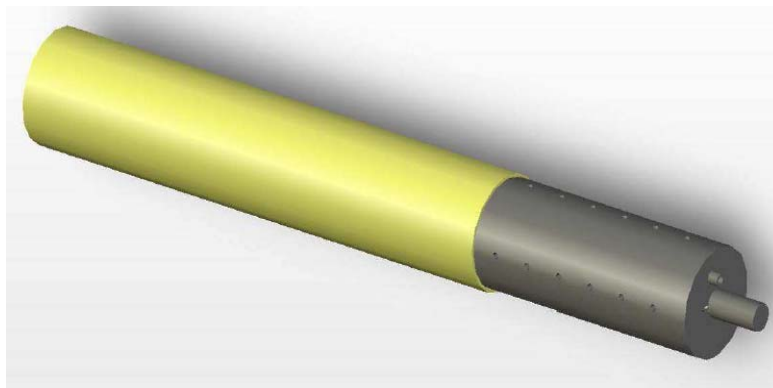


**Figure 6-33** Mandrel for making tubes; pressure holes which enables an easy separation of the composite tube and the mandrel [3, 13]

### Composite floating point absorbers for wave energy converters

---

The idea consists out of a hollow tube with a number of small holes on its surface. At one of the ends of the mandrel there should be a fitting to connect the high pressure of a compressor. Before winding, all holes are closed with a tape to prevent the leakage of resin into the mandrel. After the resin is cured, the compressor increases the pressure within the mandrel and hence the composite expands a bit and makes no longer contact with it. In this way it is quite easy to remove the composite tube from the mandrel.

## 6. 4. LABORATORY SLAMMING SET-UP

### 6. 4. 1. Introduction

It seemed useful to have a slamming set-up available for laboratory tests. It is important to gain experimental knowledge about the behaviour of certain composite shapes under slamming loads (pressure, acceleration, strain). Now that the filament winding machine is up to date it is possible to provide wound test samples for a slamming set-up. Unlike the filament winding machine, where a lot of the equipment already existed and still was in a good condition, for the slamming set-up the design and built-up started from zero. It had to fulfil several design conditions. It had to be able to simulate both straight and lateral slamming. In other words structures can fall down from different sides to the water. Next, it is more useful if the set-up can be used for several shapes besides the point absorber. Finally, the possibility of simulating repeated slamming should already be taken into consideration for future research. Of course, the location was also important. Since there was a room available with a large well in the ground the design is based with this boundary condition in mind as can be seen in Figure 6-34 which shows the finally chosen design. This design was achieved in the framework of the master theses of T. Derveaux, W. Baro, J. Himpe and D. Van Nuffel [3, 7, 8, 14, 15].

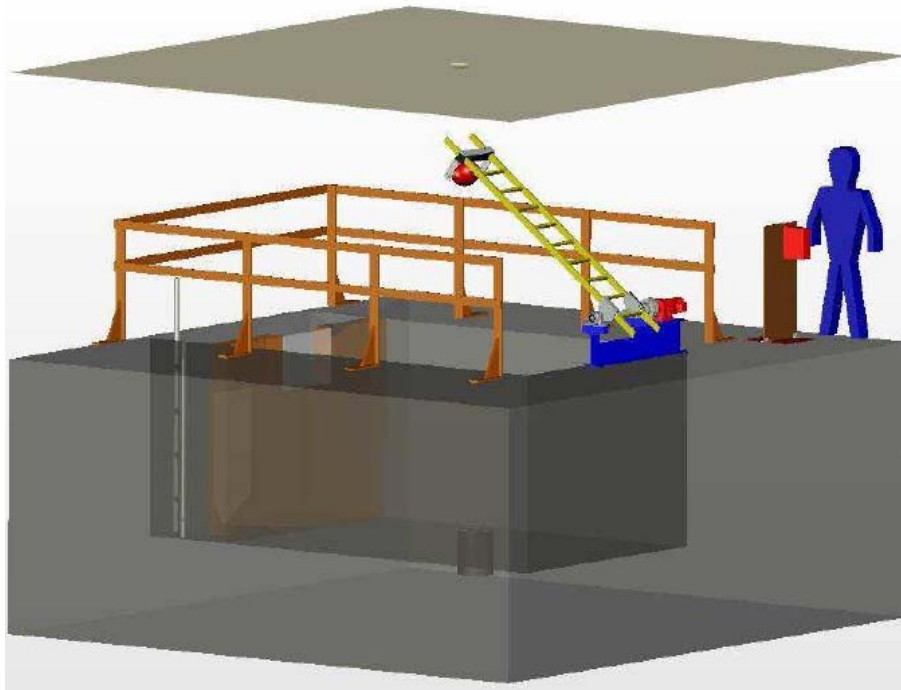


**Figure 6-34** Sketch of the slamming set-up.

Here, the egg (or any object) is mounted on the end of a ladder. The other end of the ladder is mounted on a shaft with bearings. For repeated tests, this shaft is coupled to a motor. A major advantage of the set-up is that the shape and size of the test object is quite free to choose of course keeping in mind the size of the water bath.

#### 6. 4. 2. Realisation of the set-up

The several parts that were made for the mechanical construction outside the well are shown in Figure 6-35.

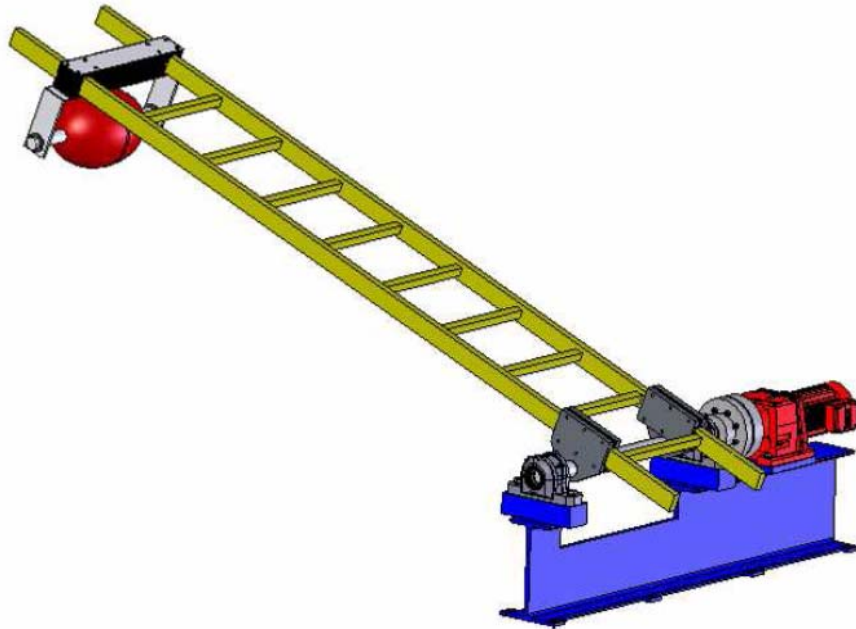


**Figure 6-35** Part of the slamming set-up outside the well.

In following paragraphs all the parts are discussed separately. Of course the construction of the water bath is discussed as well. However, the connection of an object (in the figure a shape of an egg) to the ladder is not treated within this chapter but in Chapter 7, where several test samples including their connections to the ladder were made.

#### 6. 4. 3. Ladder

There was opted for a ladder because this was an easy and cheap solution. Both aluminium and composite (glass fibre) were considered since the two materials have good resistance to water and are very light. An additional advantage is the fact that a

ladder normally should be able to carry a person hence the strength of the ladder is quite good. The calculations done in [3] with a mass of 10 kg showed that the composite ladder results in a larger displacement than the aluminium one due to its smaller E-modulus [3]. However, the fatigue resistance of aluminium is not so good. Since fatigue plays a major role in the repeated tests, it was decided to choose for the composite ladder. The dimensions of the ladder were selected so that the point absorber (or other object) should fall about in the middle of the well. On demand, the supplier included some reinforcements between the two last ladder rungs near the connection of the ladder to the shaft and near the last rungs where the test object should be mounted on the ladder. These reinforcements are achieved through fillings in the bars. The locations are shown in Figure 6-36.

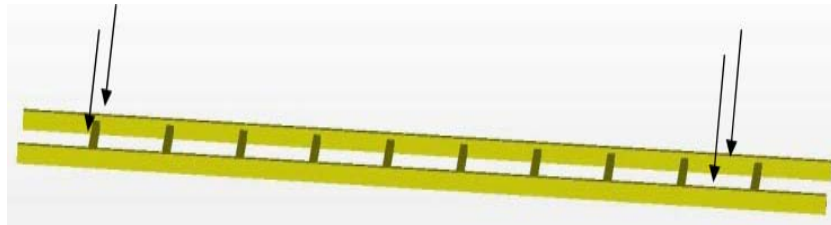


**Figure 6-36 Reinforced locations on the composite ladder.**

#### 6. 4. 4. Shaft

The shaft was calculated for necessary strength and stiffness to determine its thickness. Additionally the maximum angle rotation of the shaft during torsion was taken into account. These calculations showed that the minimal diameter of the rod had to be 0.04 m [3]. However, there was opted for a rod of 0.055 m since this larger diameter was easier to mount the ladder on.

#### 6. 4. 5. Connection between shaft and ladder

Two flanges were welded on the shaft. Also, these flanges are fixed to the ladder with the help of two plates and bolts. Locally some rubber is glued on the bars to prevent shifting of the ladder. The final design is seen in Figure 6-37.

#### 6. 4. 6. Bearings

The shaft has two supporting bearings which were calculated to withstand a static and dynamic load with a certain lifespan. Since the bearings have to work in a water environment there was opted for water resistant bearings that were lubricated for their whole lifespan [3]. They are depicted, mounted on the rod, in Figure 6-38. The bearing closest to the torque moment is taken as the fixed bearing. The other bearing is loose and the shaft can expand in this way at will.

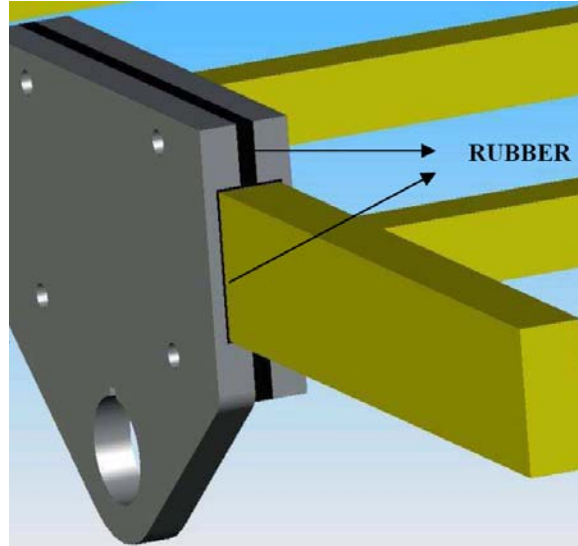


**Figure 6-37** Connection rod/ladder.



**Figure 6-38** Bearings mounted on the rod.

#### 6. 4. 7. Support

The chosen support for the motor and bearing housings was a standard I-profile (height = 300 mm, width = 150 mm, length = 1600 mm). The width of it was slightly too small hence a plate and two blocks were welded on the profile for the mounting of the bearing housings and the motor. An advantage of the use of the I-profile was the easy alignment of the bearings with the motor. On the bottom of the I-profile eight plates with holes were welded and with some expansion bolts the whole set-up could be fixed very well in the ground. A part of the I-profile was

burnt out so that the ladder would not be hindered in its movement. This can be seen in Figure 6-39 where the final I-profile is given.



**Figure 6-39 Adjusted I-profile.**

#### 6. 4. 8. Water container and well

The first option was to fill the whole well with water and drop the objects in it. However, since it is useful to make movies with the high speed camera at the water level this was not done. There was opted for a container (provided with windows) that should be installed in the well. The easiest solution was to choose an existing container that has served to keep fish. It has dimensions of 1800 mm height, 1740 mm length and 1400 mm width hence a volume of about 1500 litres. In the bottom of the container is a hole where a PVC tube is connected. This was useful later on for the floater installation which is explained in paragraph 6. 4. 9.

The position of the bath in the well is chosen so that the test object falls at about the same distance from three of the four walls as is shown in Figure 6-40 (right). The distance to the fourth wall can not be the same since the surface of the container is rectangular. However, since slamming has a very short duration, it initiates locally very high pressures and the distance until that wall is quite large, the possible wave reflections occur too late to cause important disturbances. Also, on Figure 6-40 (left) two installed windows, to allow measurements with the high speed camera, are seen. The design of these windows was done with as little stiffness and strength loss of the container as possible. Nevertheless, they should not be too small because that would make the recording with the high speed camera more difficult. At the outer side of the container a steel L-profile frame was foreseen. And on the inner side a flat frame was bolted. This was made water tight with silicone. One of the windows is shown in Figure 6-41. At the side of the container, there were reinforcements present hence the height of that particular window was limited. This results in two slightly different windows; the one on the long side of the container is smaller than the other one. The windows are made in polyacetal and have a thickness of 10 mm. To

prevent calcification on the windows and walls of the container, demineralised water was used.

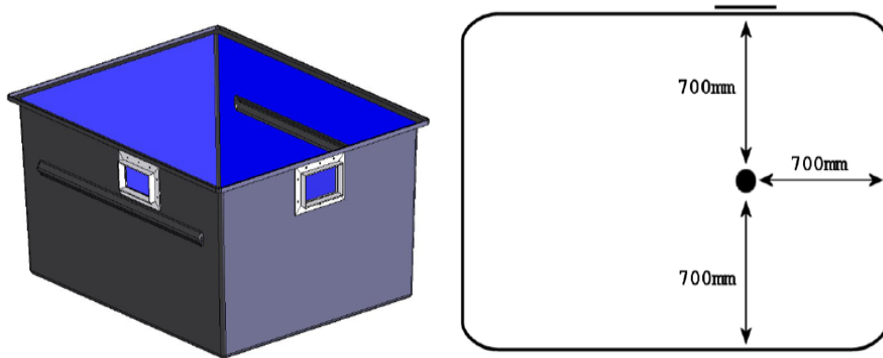


**Figure 6-40** Model of the used container with two windows (left). The test object falls at a position about equidistant to three of the four walls of the container (right) [14].



**Figure 6-41** One of the windows in the container [14].

Each time a test object falls in the water, a large quantity would be splashing over the edges of the container. Hence, it was decided to extend the walls of the container. The chosen material for this additional frame is concreteplex which is a wooden multiplex with an epoxy top layer. It is water tight which is a necessary requirement for its use on the container. The final construction is shown in Figure

6-42. At the front side of the wooden construction a hole was foreseen to allow the movement of the ladder.



**Figure 6-42** Container with added wooden frame to prevent large quantities of water splashing over the edges [14].

The ‘dry part’ (motor, bearings, ladder, etc.) was installed so that the water surface was situated about 100 mm under the edge of the well. Now, the container has a height of 800 mm and the well a depth of 1800 mm. The easiest solution was to fill the well partly with sand. This was outsourced to a firm which pumped the sand into the well as is shown in Figure 6-43. An advantage is that it is now possible to walk in the area around the container. Also, it increases the safety of the set-up since the well is less deep than before.



**Figure 6-43** Filling the well with sand near start (left) and end (right) [14].

The container that was bought is designed for static loads. However, during the slamming experiments also dynamic pressures are present on the walls. Hence, a supporting rectangular steel construction was built around the container for additional lateral support. Two steel profiles are welded to the rectangle. The vertical U-profile bars have a small angle (3 degrees) to provide more support. Between this supporting structure and the container there is 3 mm foreseen to place rubber in between. The final support construction is shown in Figure 6-44. As can be seen two wooden plates were put in place under the construction.



**Figure 6-44 Reinforcement construction [14].**

Also, these dynamic loads cause pressure waves present on the walls of the container. Hence, it was decided to mount a polyether foam layer of 20 mm against the walls to protect them and to damp the reflection of the waves. The mounted foam was polyether because it has good damping properties. The used density is  $35 \text{ kg/m}^3$ .

Next, the amount of water that splashes over the edges of the wooden frame is kept quite small but it would still make the sand wet and dirty. It was decided to cover the sand surface with building plastic which is non permeable for water. Most types are made out of polyethylene. There was opted for one of 0.4 mm thickness to prevent fast failure. It was already depicted in Figure 6-42 applied over the sand bottom.

#### 6. 4. 9. Floater system

As was mentioned in the previous paragraph there is still some water splashing over the edges. Of course a constant water level is desired to perform good experiments.

The solution for this is a reservoir with a floater in it that keeps the water level constant. This reservoir (volume of 210 litres) is installed near the well and is connected with a floater in a PVC tube of 11 mm which is at its turn connected to the bottom of the water container. A toilet floater was chosen due to its cheap price and easy mounting. It is not installed in the container itself because the local high peak pressures, during slamming tests, could break it. A schematic overview of the used system is shown in Figure 6-45.

Before the installation of the building plastic in the well, this system of PVC tubes was installed. Between the two wooden fibreboard plates, a ditch was dug for the PVC tubes. Hence, the container does not lean on the tubes but on the sand. The vertical part of the PVC tube was fixed to the wall of the well. The head of the floater is screwed in a hole to the tube. From there a flexible cable is connected to the valve of the water reservoir. An auxiliary attachment was made so that this connection was without leaks.

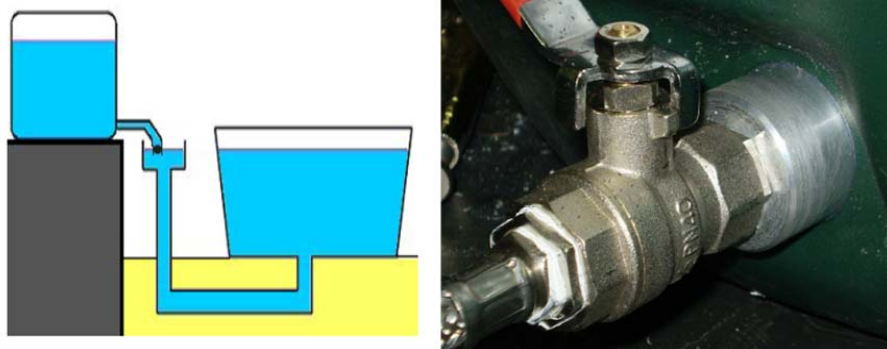


**Figure 6-45** Used principle of communicating vessels (left) and the auxiliary attachment at the water reservoir [14].

#### 6. 4. 10. Motor, control and torque moment

The motor that was needed consisted out of an AC motor, a reductor and a velocity regulator. Additional, a possibility to put the motor in neutral should be included. There was opted for a heavier motor (0.55 kW) to increase the possibilities for future work. Its maximum velocity is 18.5 rotations per minute and this delivers a torque of 283.9 Nm. When the velocity is lower, the torque increases.

The maximum occurring torque moment was calculated for a connected mass (test object plus connection) of about 10 kg in [3]. There, Equation 6-1 was calculated. However, in the motor control the motor velocity and its acceleration can be given. Also, counter weights can help to decrease the torque.

$$146\ddot{\theta} + 325 \cos(\theta) = M(\theta)$$

**Equation 6-1 Dynamic torque equation.**

The necessary torque may not be higher than the available one. Also a safety factor of 1.5 was taken into account. The relation between the torque moment and the power is given in Equation 6-2.

$$M_{mot} = \frac{P_{mot}}{\frac{2\pi n}{60}}$$

**Equation 6-2 Relation between torque moment and power.**

Considering Equation 6-2 and that  $\theta$  equals zero (maximum torque), the following condition has to be fulfilled:

$$1,5 \left( 146 \ddot{\theta} + 325 \right) \frac{2\pi n}{60} \leq P_{mot}$$

The control of the motor can be done with the application regulator 'Movidrive MDX61B' [16]. The steering is from SEW and is shown in Figure 6-46.



**Figure 6-46 Movidrive application regulator.**

Movitools is the software interface. The computer is connected with a serial RS-232 interface to the regulator. Movitools is a software environment consisting of different tools to provide a user-friendly program manner.

For the choice of the clutch three demands were put forward. First, it has to be able to disconnect the ladder-motor connection before impact of the test object on the water surface to prevent damage of motor and reductor. The switching time is not critical here. Second, it also should have the possibility to re-establish this connection just after impact of the test object on the water surface to slow down the object through the brake resistor of the motor. In this way, impact of the ladder on the edge of the container (location shown in Figure 6-47) and possible damage to it should be prevented. A short switching time is necessary. Finally, low cost is an important issue.

A first option was an electro-magnetic torque from Warner (type E220 Var 05) of which the drawing is shown in Figure 6-48. This clutch consists out of two parts: an electro-magnetic part and an elastic one. It has a very high performance with low switch times and it is suitable for a torque up to 800 Nm. However, it is very expensive and a cheaper variant was chosen. This was also an electro-magnetic clutch, now from Mayr and it is depicted in Figure 6-49. It has the same working principle as the expensive one but does not contain an internal bearing or elastic torque anymore. A direct consequence of this is that the switching time decreases. Hence, an additional external damper should be mounted on the edge of the wooden frame. For this, air cushion foil on a rectangular plate is used [15].



**Figure 6-47** Location of the ladder impact [15].

Within this Chapter it was shown that the filament winding machine was updated and ready for use. Also, a new slamming set-up was designed and built. Further, a first set of drop tests on chosen test objects will be discussed in the following Chapter.

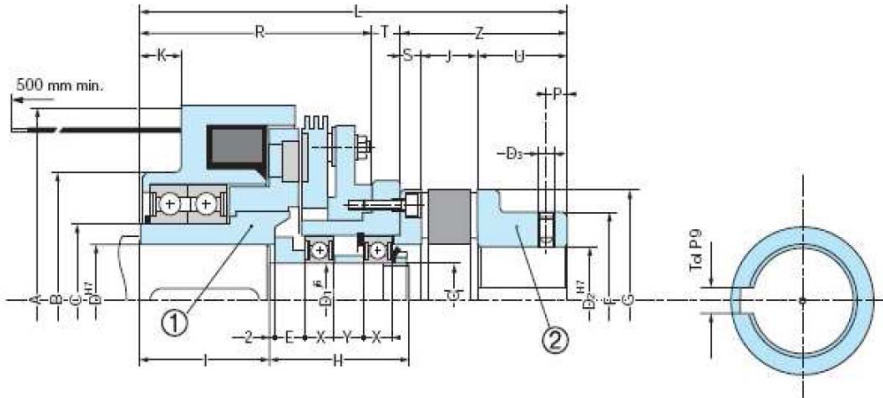


Figure 6-48 Electro-magnetic clutch, Warner.

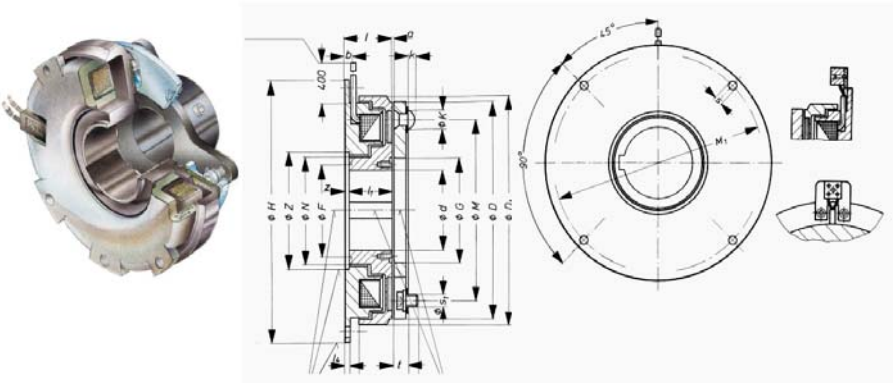


Figure 6-49 Electro-magnetic clutch, Mayr.

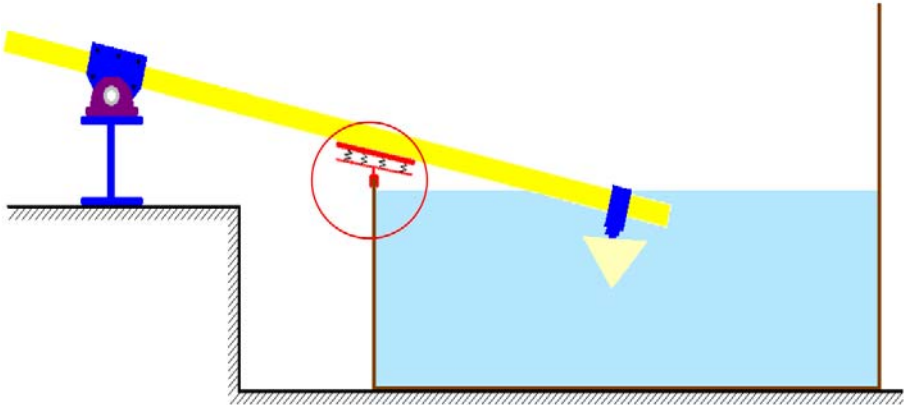


Figure 6-50 Damping system to prevent severe impact on the ladder.

## 6. 5. REFERENCES

1. P. Martin, Shape optimisation of thin anisotropic shells applied on filament wound pressure vessels. 1991, Ghent University. Doctoral thesis 1991.
2. W. DeWaele, Structural monitoring of composite elements using optical fibres with Bragg-sensors, Ghent University. Faculty of Engineering, PhD thesis 2001.
3. W. Baro and T. Derveaux, Ontwerp, realisatie en beproeving van een composiet vlotter voor golfenergie-conversie, Ghent University. Faculty of Engineering, Master thesis academic year 2006-2007.
4. Motion Controller NextMove ESB-2. Available from: <http://www.baldor.com/products/motioncontrol/nmesb2.asp>.
5. CADWIND NG User Manual. p. 13-38.
6. National Instruments - Labview. Available from: <http://www.ni.com/labview/>.
7. C. Blommaert, J. Degrieck et al. Design of composite material for cost effective large scale production of components for floating offshore structures. in Proceedings of the 13th European Conference on Composite Materials (ECCM-13). 2-5 June, 2008. Stockholm, Sweden.
8. C. Blommaert, W. Van Paepegem et al., Design of Composite Material for Cost Effective Large Scale Production of Components for Floating Offshore Structures. Accepted for Special Issue of Plastics, Rubber and Composites: Macromolecular Engineering, 2009.
9. Apartment complex 'Monte Carlo', De Royschans. [cited 2009 01/04]; Available from: <http://www.zoetermeer.nl/index.php?simaction=content&mediumid=18&pagid=1121&stukid=5756>.
10. Product Data Sheet - Glassfibre SE 1200 type 30 roving [cited 2007 20/01]; Available from: <http://www.owenscorningchina.com/upload/File/476696193.pdf>.
11. Basaltex. [cited 2007 20/01]; Available from: [www.basaltex.com](http://www.basaltex.com).
12. Product Data Sheet. 22/02/2007 [cited 2007 20/03]; Available from: [http://www.ecc-belgium.be/images/upload/File/technischefiches/TF\\_ECC/Slijtvasteenchemischresistentebedrijfsvloeren/Primers/PC%205800%20TF.pdf](http://www.ecc-belgium.be/images/upload/File/technischefiches/TF_ECC/Slijtvasteenchemischresistentebedrijfsvloeren/Primers/PC%205800%20TF.pdf).
13. Spiromatic. [cited 2006 25/04]; Available from: [www.spiromatic.com](http://www.spiromatic.com).
14. J. Himpe, Optimalisatie en validatie van een experimentele slamming set-up, Ghent University. Faculty of Engineering, Master thesis academic year 2007-2008.
15. D. VanNuffel, Slammingexperimenten van composiet-'eieren' op laboschaal, Ghent University. Faculty of Engineering, Master thesis academic year 2008-2009.
16. Movidrive MDX61B. [cited 2007 20/03]; Available from: <http://www.sew-eurodrive.de/download/pdf/11252626.pdf>.



## Chapter 7

### LABORATORY SCALE TEST SAMPLES: PRODUCTION, EXPERIMENTS AND VALIDATION

*In this chapter, the experiments on the new laboratory slamming set-up are explained. First, the chosen test objects are discussed. Second, the used instrumentation is mentioned. Next, the production of all samples including the integration of some of the sensors is treated. Finally, an overview is given of the test set-up for each object.*

#### 7. 1. TEST SAMPLES FOR LABORATORY SLAMMING

##### 7. 1. 1. Introduction

The slamming set-up was ready for testing as was explained in Chapter 6 [1-3]. At start experiments (without motor) were done. In a later stage, also repetitive tests can be done due to the design of the slamming set-up.

The test objects had to be chosen first. A cone seemed the most obvious choice, since its 2D equivalent – a wedge – was studied quite extensively [4-9]. Hence, this cone test case was considered as a reference test case to confirm the proper working of our machine with the literature. A cone of 45 degrees was chosen since the last proposed point absorber shape was conical with that angle. Second, it seemed useful to perform tests on cylinders [10-13]. A comparison was made between a quite rigid (full) cylinder and a more deformable (hollow) cylinder.

Finally, a point absorber in the cone/cylinder/cone shape (the final chosen shape within Seewec) was chosen as a test object for laboratory slamming. The detailed results can be found in [2, 3].

##### 7. 1. 2. Instrumentation

Several sensors were used during the slamming tests like strain gauges, pressure sensors and a high speed camera. The used strain gauges (distributed by Akron) were of the same type as the ones used in Chapter 4 for the characterisation tests (type CEA-06-250UN-350). Each test object at laboratory scale had at least two strain gauges; one longitudinal and one perpendicular as depicted in Figure 7-1. Next, the pressure sensors were dynamic ones from PCB Piezotronics. The used types are 102B06, 102A07 and 112A23. The first type has a range of 3450 kPa, while both others have a range of 730 kPa.

These sensors are shown in Figure 7-2. This kind of sensor is used in hydraulic and pneumatic environments of relative low pressure in presence of shocks and vibrations. Examples of some of its applications are jet engines, compressors, and turbines. Hence, the measurement of slamming pressures is within the scope of these sensors. The relevant properties of the respective used sensor are explained for each test set-up in the following paragraphs. The high speed camera (type fastcam-ultima-APXRS of Photron) can take 10000 frames per second at a resolution of 512 by 512 pixels. A picture of this high speed camera (HSC) is given in Figure 7-3. By determining the displacement, the velocity at impact can be calculated of the camera images.

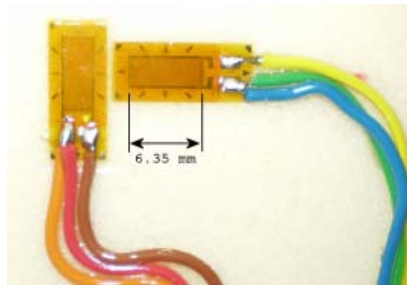


**Figure 7-1** Strain gauges.



**Figure 7-2** Pressure sensors: 102B06 (left), 102A07 (middle) and 112A23 (right).



**Figure 7-3** High speed camera (HSC).

## 7.2. TEST CASE ‘CONE’

### 7.2.1. Introduction

The rigid cone, or its 2D equivalent ‘the wedge’, is studied quite extensively in literature. Hence, it was a straight forward choice to start with this shape for the slamming experiments. A cone of 45 degrees was chosen and was compared with the extended 3D formulation of Wagner [7] and the results of Peseux [5]. The test case of the cone should assess the designed and built slamming set-up. The height of the cone is not so important for the experiments since the shape stays the same no matter what height the cone has. A cone of 300 mm maximum diameter was proposed. Since slamming is a very short phenomenon this size was more than sufficient. The reason for limiting the cone to 300 mm is on the one hand the suitability for testing in the slamming set-up and on the other hand this size was still producible on the lathe. The dimensions of the produced cone are shown in Figure 7-4.

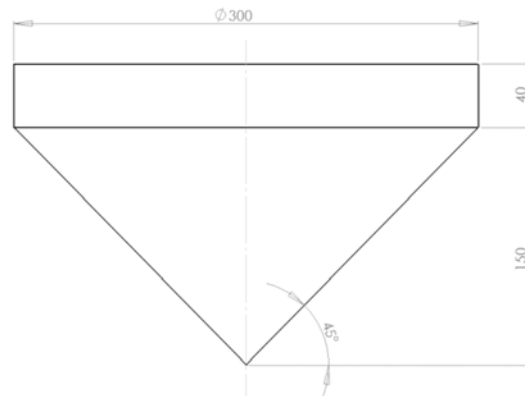


**Figure 7-4** Dimensions of the produced cone.

### 7.2.2. Production

The cone should be as rigid as possible. However, the motor was calculated to lift 10 kg hence it should weigh as light as possible. These two design conditions are opposing each other. Polyurethane (PU) exists in several densities and this allows choosing one according to the applications (e.g. light but still rigid enough). A PU object can be made by spraying. However, the density of the object is difficult to control in that way. Additionally, a mandrel would have to be made. Hence, it was decided to buy finished rectangular quantities of this foam with a density of 100 kg/m<sup>3</sup> and dimensions of 400 mm length, 400 mm width and 100 mm height. Polyurethane (PU) foam is machinable so these rectangular foams could be shaped in the lathe to flat cylinders of 300 mm diameter and 100 mm thickness. The conical test object was made on the lathe out of two such plates. The final result is shown in

Figure 7-5. PU foam is a material that absorbs water hence an epoxy coating was put on. It is again the epoxy resin Tradecc PC 5800 A and B that was used in paragraph 6.2 for making the first cylinders on the filament winding machine in the laboratory [14].



**Figure 7-5 Produced cone in polyurethane (PU).**

### 7.2.3. Instrumentation

For the tests on the rigid cone, two strain gauges, one pressure sensor and the HSC were used for instrumentation. The location of the pressure sensor is shown in Figure 7-9. It is a sensor of type A23. At the same circle sector diametric to the pressure sensor two strain gauges were glued with M-bond 200: one in the longitudinal direction ( $0^\circ$ ) and one in the perpendicular direction ( $90^\circ$ ) as is shown in Figure 7-6. Next, an additional epoxy resin coating was mounted on the cone to protect the strain gauges against water.

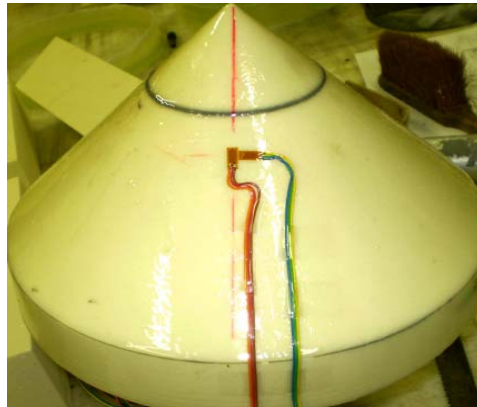


**Figure 7-6 Cone with two strain gauges [2, 15, 16].**

The pressure sensor looks like a rod with a thickening. In general, the sensor is mounted in a hole foreseen of screw thread, made to fit. Hence, the probe is fixed between the clamp bolt (which can freely slide over the sensor) and the wall due to

the built-in thickening as is shown schematically in Figure 7-7. However, for the cone (and the other test objects) it is not possible to mount the sensor as explained above. In this case the sensor can not be mounted backwards into the hole because the polyurethane is too thick. Additionally, tapping screw thread in the PU is not without danger for crumbling of the material. The final design consists out of two parts: a small metal tube (depicted most right on Figure 7-8) and a metal guiding tube (depicted most left on Figure 7-8). The metal tube is glued into a hole in the test object and it is foreseen of inner screw thread. A hole was drilled from the upper surface of the cone to the backside of this tube. The sensor and the cable are pulled through until they come out of the tube. In the metal guiding tube the sensor was mounted backwards according to its design. However, this whole part (metal guiding tube plus sensor plus clamp) was mounted from the front into the object. First, the sensor was connected to the cable with help of the connector and next, the metal guiding tube was screwed into the tube.

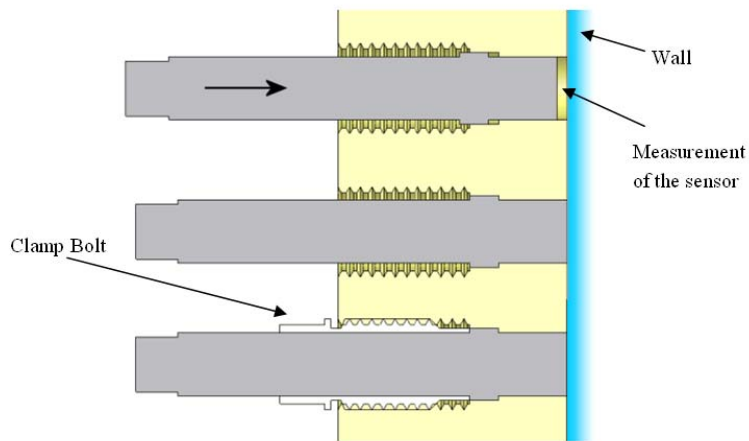


**Figure 7-7 Method for the probe connection.**

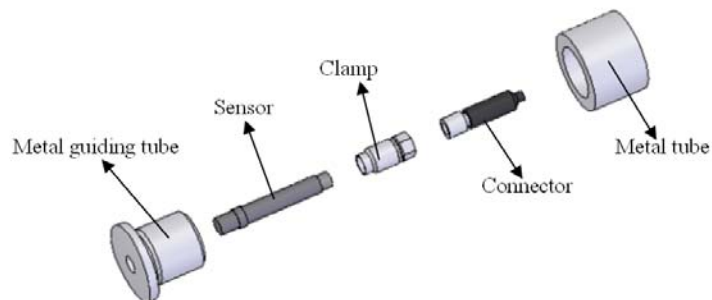


**Figure 7-8 Mounting of the sensor.**

The sensor was mounted in the cone at a height of 67.2 mm (counted from its top) as is shown in Figure 7-9.



**Figure 7-9** Position of the pressure sensor.

#### 7. 2. 4. Test set-up

To mount the cone on the ladder, four holes are made in the upper side of the cone. In each hole a screwed rod was glued. Additionally, resin was put into the holes to make the area near the screwed rods stronger. The resin was partially absorbed by the PU foam. However, during the design of this connection it has to be kept in mind that the ladder performs a rotating movement. Hence, the upper surface of the cone, during falling, is only at a certain moment horizontal. The cone is attached to the ladder so that it makes an angle of  $1.5^\circ$  at impact and of  $2.5^\circ$  at the moment the upper surface of the cone impacts the water as is shown in Figure 7-10. The influence of this choice could be part of future research.

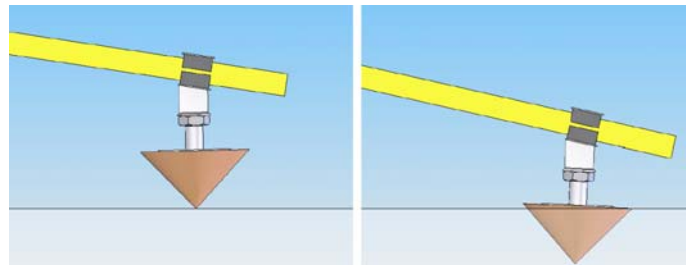


**Figure 7-10** Impact of the cone at start ( $1.5^\circ$ ) and at end ( $2.5^\circ$ ).

Other demands for the connection to the ladder are low weight (with a total maximum of 10 kg), stiff construction and as user friendly as possible. Hence, cold rolled steel plates of 2 mm thickness were shaped in U-profiles which result in a very stiff construction without drastically increasing the weight. The construction consists out of three main parts: the clamping to the ladder, the frame and the connection for the cone. The whole construction is shown in Figure 7-11. The clamping on the ladder consists of two small and one large U-profile. To prevent loads on the ladder, four rubber blocks are mounted between these profiles. The

small U-profiles and the rubbers were re-used for the rigid cylinder as is discussed in paragraph 7.3.4.

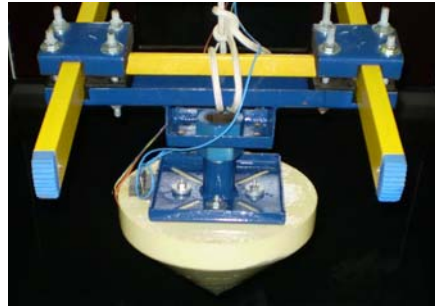


**Figure 7-11 Connection of the cone to the ladder [2, 15, 16].**

The frame is welded on the long U-profile of the clamping. It was shaped into an open part with a skew upper surface to allow a quite horizontal impact (1.5 degrees) of the cone in the water. The connection for the cone consists out of a tube and a plate welded together. Four holes are foreseen in the plate for the screw rods hence the PU could be fixed against the plate. Additionally, four long holes are foreseen for the cable(s) of the pressure sensor(s). In this way, the amount of sensors can vary at will. The frame could be used for the hollow cylinder as is explained in paragraph 7.3.7. The total mass of the cone and its connection is 7.5 kg.

#### 7.2.5. Results and validation

As was mentioned in paragraph 7.2.3, the pressure sensor is mounted on a height of 67.2 mm, hence along the surface starting from the top of the cone this is 95 mm. The drop tests were done six times at a drop height of 1000 mm which equals a drop velocity of 4.43 m/s, without motor and at a measuring sample rate of 30 kHz. A representative plot of the measured pressure signal is given in Figure 7-12. All pressure signals are given in Appendix. The pressure increases very fast until a peak value is reached. This peak value occurs during impact and for these seven drop tests the average was about 22.6 kPa with a standard deviation of 3.9 kPa. The signal smoothly decreases after this peak. Figure 7-13 shows the calculated value for a cone with a deadrise angle of 45 degrees according to S. Victor, as discussed in Chapter 3 [17, 18]. The measured signal decreases faster after impact which is logical due to the deceleration of the object in reality. In the theory the velocity is assumed as constant. Additionally, the duration of the peak pressure is larger than expected. This could be due to the rotational movement of the slamming set up or due to a non flush mounted pressure sensor. The theoretical 3D Wagner peak value is about 30 kPa which is higher than the measured value. Using DNV with a reduced average pressure slamming coefficient of 2.5 (for the 45 degrees cone) the constant pressure would be 25.1 kPa which is still higher than measured. However, the same

was the case for the results of Peseux and for the cone simulations of Stoop & Vermeulen in [5, 19]. The decrease in pressure is lot slower than measured. This is due to the assumption of a theoretical constant velocity, which decreases in reality, and the assumption of incompressible water. Hence, it was decided that the new laboratory slamming set-up was suitable for further slamming measurements. However, in a later stage more cone experiments are recommended (e.g. assess influence of chosen entry angle; check influence flush mounted sensors, etc.)

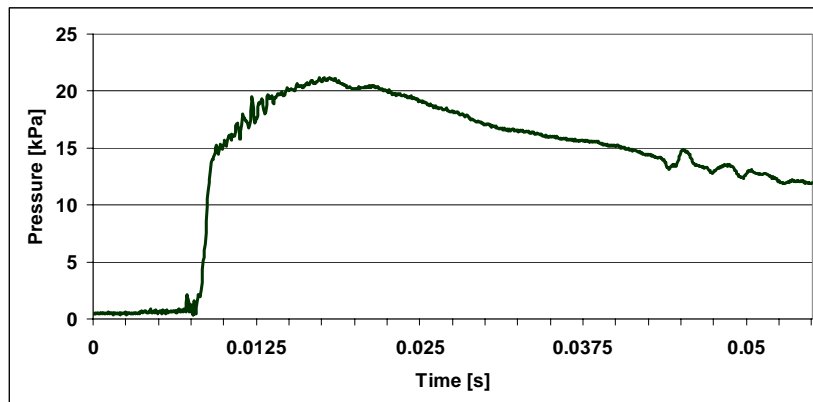


**Figure 7-12** Representative result of the pressure sensor in the cone at a drop height of 1000 mm [2, 15, 16].

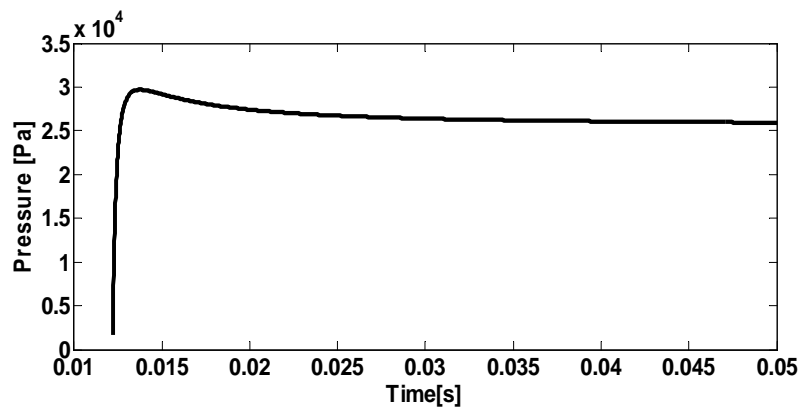


**Figure 7-13** Calculation of the pressure in time for a cone of 45 degrees at fixed radius of 0.0672 m; based on formulae of Wagner 2D; extended for 3D by S.Victor [17, 18].

The two strain gauges measured very low strain values as is shown in Figure 7-14. These results were expected since the cone was designed to be as rigid as possible. Figure 7-15 shows images taken with the HSC during a drop test. Especially the upper row in the figure is important. There the cone penetrates the water surface

smoothly which causes a rising up of the water along the edges of the cone. This uprising of the water causes very high local pressures. As the cone penetrates the water these pressures move along its surface. Finally, separation of the water drops occurs.

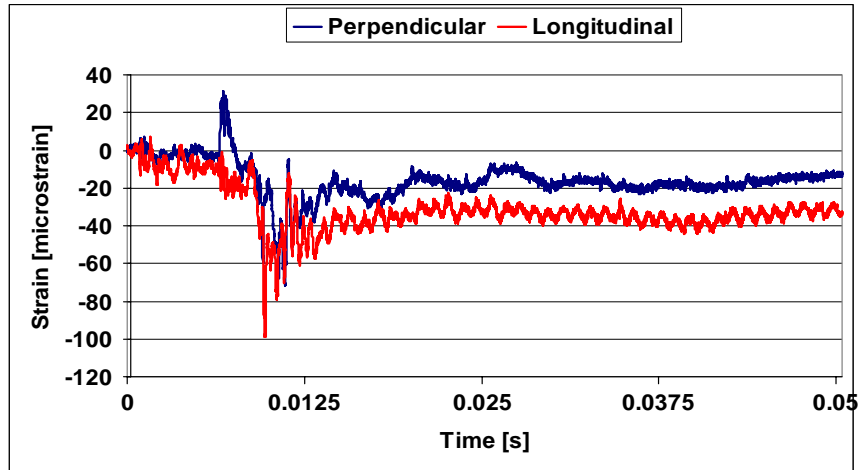


Figure 7-14 Measurements of the two strain gauges for the laboratory cone test sample [2, 15, 16].

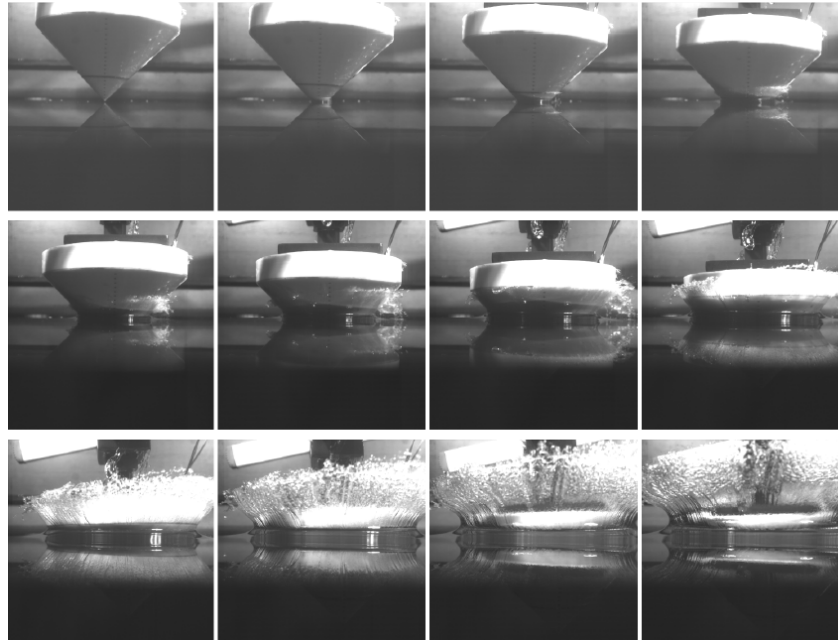


Figure 7-15 Images from the HSC for the cone [2, 15, 16].

### 7. 3. TEST CASE ‘FULL AND HOLLOW CYLINDER’

#### 7. 3. 1. Introduction

Testing a rigid cylinder and a more deformable one seemed very useful to make a comparison between both occurring peak pressures. For the rigid cylinder there is opted for a PU full cylinder reinforced with wound composite layers (glass fibre/epoxy). For the deformable cylinder a hollow cylinder was chosen consisting of a spray-up layer and two filament-wound layers, again out of glass fibre/epoxy. Also, a validation with literature was done.

Additionally, computational fluid dynamics (CFD) calculations were done and explained within this Chapter [19]. The diameter of the cylinders was 300 mm and their length 400 mm because these dimensions were suitable on the filament winding machine for production of the cylinder and for drop tests on the slamming set-up.

#### 7. 3. 2. Production of the full cylinder

The full and hollow cylinders are produced in quite a similar way. Within this paragraph the production of the full cylinder is explained while the difference in the production method for the hollow one is given in paragraph 7. 3. 6.

Both test objects are made from flat PU cylinders with diameter 300 mm and height 100 mm. Five such blocks per cylinder (this equals a length of 500 mm instead of 400 mm) were foreseen of a centre hole for an aluminium tube of 48.3 mm and glued together (Seal & Bond Sealtrans). The used centre tube was a standard one available in the laboratory. Aluminium was chosen because it is lighter and it has a better corrosion resistance than steel. The edges of the wound objects are always a bit thicker due to the turning zones.

For this reason, five blocks of 100 mm were mounted together instead of four. Also, the mandrel in Cadwind is 500 mm. As is shown in Figure 7-16 this mandrel is totally wound. Hence, the resulting cylinders are 500 mm long. After the cylinders are wound the thicker edges were sawn off and two smooth cylinders of 400 mm were made. The cylinder was wound with glass fibre/epoxy. For the full cylinder this increased its rigidity. Two identical layers with a winding angle of 70 degrees were wound using all four rovings. Such a cross wound layer is 1.2 mm thick. A file was made in Cadwind, which is necessary to wind a certain shape (as was explained in Chapter 6).

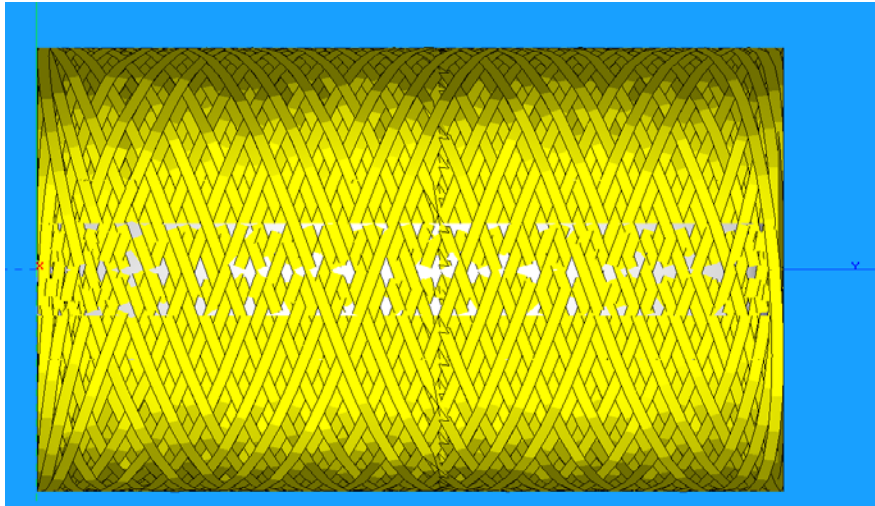


**Figure 7-16** Cadwind file for the two cylinders.

The used glass fibre was one of 600 tex from Owens Corning [20]. Both cylinders were wound with 3 rovings. The used resin was the same epoxy resin as used for the coating of the cone and for the first trial samples on the machine (Chapter 6) [14]. A picture of the cylinder during the winding phase is shown in Figure 7-17 where all five parts and also the winding pattern can be seen. The mandrel is fixed on the laboratory scale winding machine and automatically winds the fibres in the desired winding pattern. The epoxy resin is manually put on the mandrel by means of a brush because the curing time of the resin is only 30 minutes.



**Figure 7-17** Winding phase on the full cylinder [2, 15, 16].

### 7.3.3. Instrumentation of the full cylinder

The full cylinder was equipped with a pressure sensor and two strain gauges. The pressure sensor was mounted in the same way as for the cone. In the middle of the cylinder a hole was made of 40 mm depth and 25 mm diameter. Again, a fitting small aluminium tube was fixed with glue (fix-all). The cable went through a smaller hole towards the aluminium tube. The strain gauges were again fixed with M-Bond 200. Both strain gauges, a perpendicular and longitudinal one, were located next to the pressure sensor as is shown in Figure 7-18.



**Figure 7-18 Full cylinder with two strain gauges and its preparation for one pressure sensor [2, 15, 16].**

### 7.3.4. Test set-up full cylinder

For the connection of the cylinder, the same design conditions as for the cone apply. The drawing of the connection is shown in Figure 7-19. Again, cold rolled steel plates were used. The construction consists out of a grip where the aluminium tube (in the cylinder) can be clamped. On top of the grip there are some holes drilled so that it can be fixed at the ladder together with the rubber blocks and small U-profiles that were used for the cone. The grip can be re-used for the connection of the small point absorber as is shown in paragraph 7.4.3. The total mass of the full cylinder and its connection is 9.34 kg.

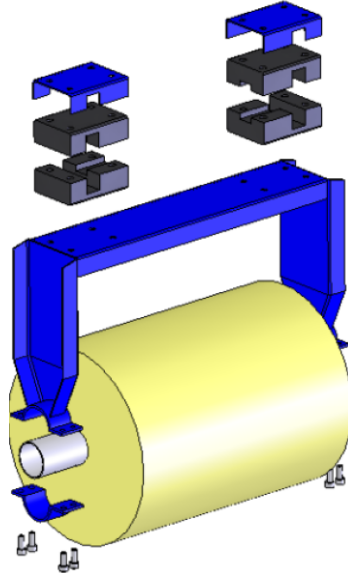


**Figure 7-19 Connection of the full cylinder [2, 15, 16].**

### 7.3.5. Full cylinder: results and validation

The experiments with the full cone were done six times with the pressure sensors down (called 0 degrees), six times with the pressure sensor over 20 degrees and six times with the pressure sensor over 40 degrees, all from a drop height of 1000 mm. This equals a drop velocity of about 4.43 m/s. A representative pressure signal for the drop tests at 0 degrees is shown in Figure 7-20. The peak pressure occurs in a time interval smaller than 3 milliseconds and decreases very fast. Additional oscillations/peaks can be noticed which could be due to disturbances of the water surface. The signals of the six tests are given in Appendix.

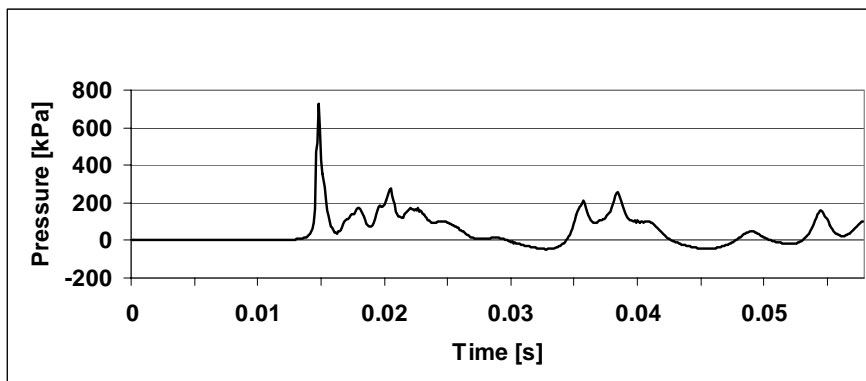


**Figure 7-20 Pressure signal for the full cylinder at zero degrees; drop height 1000 mm [2, 15, 16].**

In the first measurements for this object the pressure sensor A23 was used. There, over six tests at a sample frequency of 100 kHz the maximum was reached, namely 727.28 kPa which equals a dimensionless pressure coefficient of 74.1. Additional measurements were carried out with the A06 which has a higher range. However, there the average was only 517 kPa over six new tests but with a maximum value of 830 kPa and a minimum of 235 kPa. This lower average peak value and large deviation could be due to the lower sample frequency of 51.2 kHz which was the highest possible sampling frequency with the used card.

In literature Lin and Shieh (1997) calculated a dimensionless pressure coefficient out of experiments. Their main findings are shown again in Figure 7-21 [11]. The dimensionless pressure coefficient at zero degrees,  $C_p(0)$ , peaks at about 110 to 120 which are shown in Figure 7-21. This is an estimation and can be used instead of the infinite  $C_p$  according to the Wagner model. However, there is a quite large deviation for these experiments. Lin and Shieh do not think that the sample frequency is the cause since they measured already at 200 kHz but propose as probable cause compressible enclosed air between the sensor and the water surface. For the experiments at 30 degrees (horizontal axis value 0.5, the sinus of 30) the values are almost the same for all impact velocities, namely a  $C_p$  of about 7.5.

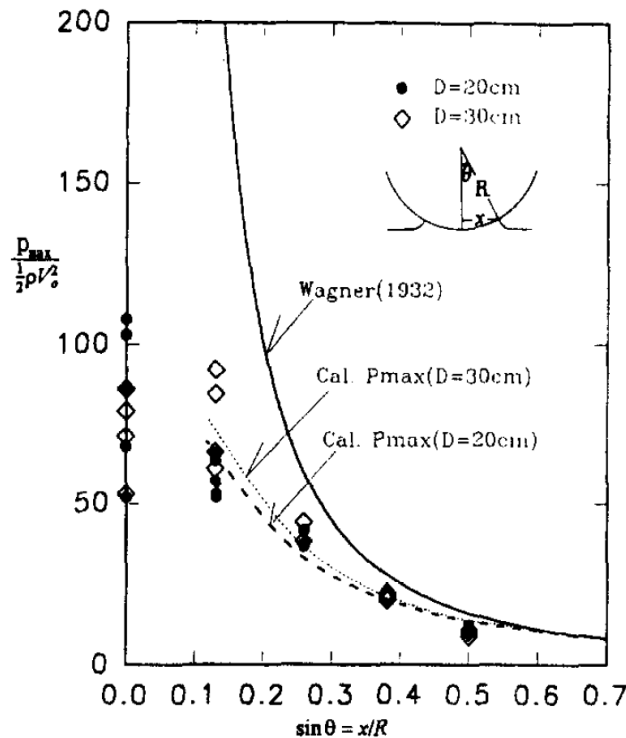


Figure 7-21 Dimensionless pressure coefficient out of Lin and Shieh [11].

The two strain gauges signals (for a representative test) are depicted in Figure 7-22. The longitudinal strain gauge has a cyclic ‘tensile-compressive’ pattern. The average maximum strain is about 100 microstrain. The perpendicular strain gauge signal has a clear peak and decreases afterwards. The value is higher (average 190 microstrain) which was expected due to the tendency towards an elliptic deformation. Since the full cylinder was made quite rigid this deformation stays limited.

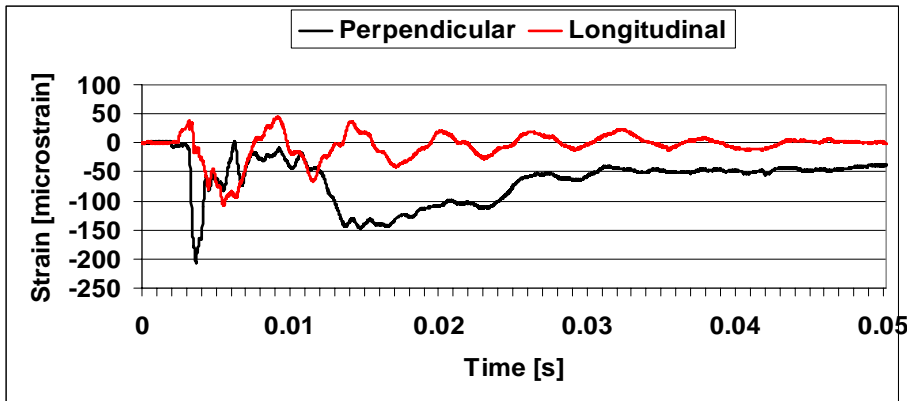


Figure 7-22 Strain gauge signal for the full cylinder; drop height 1000 mm [2, 15, 16].

The pressure signals at 20 and 40 degrees are shown in a representative example in Figure 7-23 and Figure 7-24.

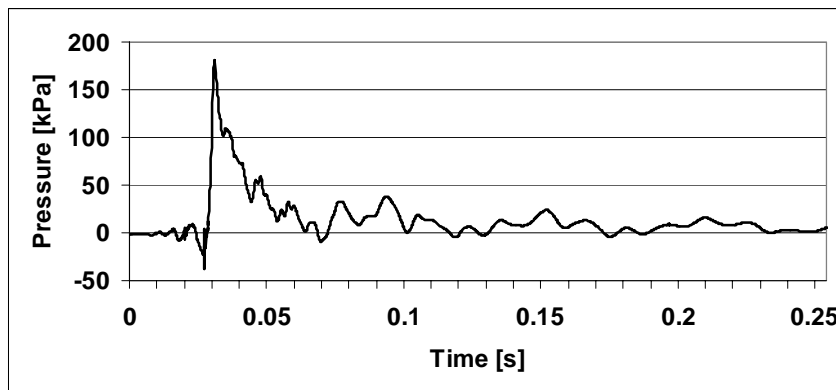
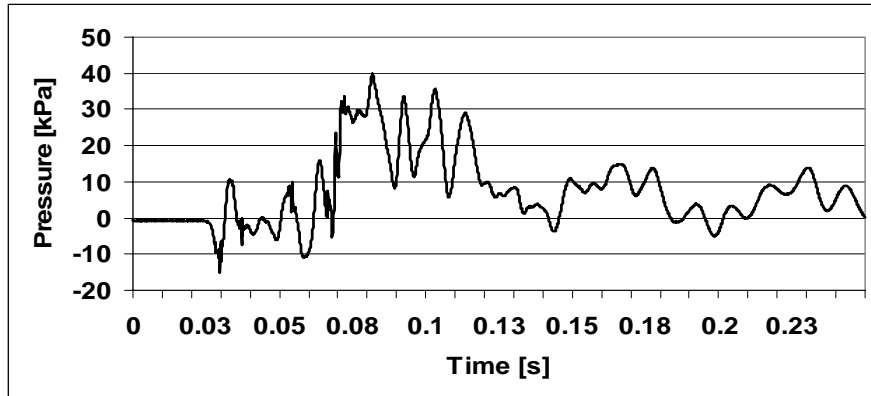


Figure 7-23 Pressure signal for the full cylinder at 20 degrees; drop height 1000 mm [2, 15, 16].

For the 20 degrees test the shape of the signal shows also a peak value but the resemblance with the signal of the zero degrees stays limited. The peak value is 177 kPa (with a standard deviation of 4.1 kPa) which is a lot lower than for the zero

degrees. Also, just before the pressure peak, pressure oscillations occur due to the earlier slamming on the lower side of the cylinder. The  $C_p$  of these experiments is 18.



**Figure 7-24** Pressure signal for the full cylinder at 40 degrees; drop height 1000 mm [2, 15, 16].

For the 40 degrees signal the peak is even lower ( $38 \pm 2.3$  kPa) and the oscillations are more pronounced. For these experiments the  $C_p$  is 4. This seems equal to the values of Lin and Shieh. Also, the earlier mentioned value of 7.5 of Lin and Shieh for the experiments at 30 degrees is in between our measured  $C_p$ 's at 20 and 40 degrees as it should be. Lin and Shieh divided the impact of a cylinder in the water in three phases: the splashing phase, the rising-up phase and the separation phase. These three phases are depicted in Figure 7-25. During the splashing phase very high pressures occur because the bottom of the cylinder is locally equal to a flat surface (deadrise angle of 0 degrees). Next, the cylinder goes deeper with an increasing deadrise angle which results in a fast uprising of the water. On the spots where separation occurs, no pressure peak is present any more [11]. The three phases were also noticed during the laboratory scale tests. Figure 7-26 shows images taken with the HSC during a drop test.

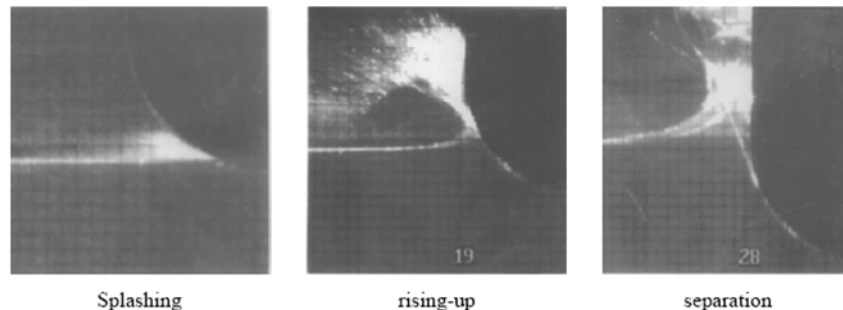


**Figure 7-25** Phases during impact of a cylinder on a water surface [11].

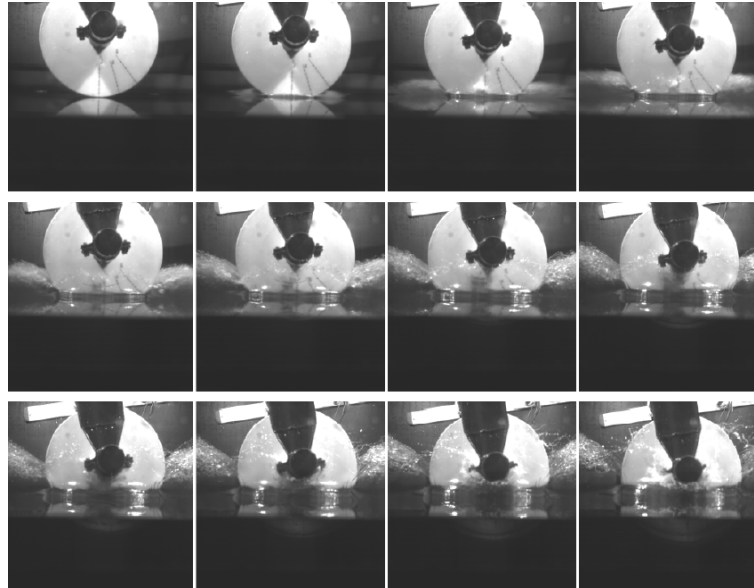


**Figure 7-26** Images from the HSC for the rigid cylinder with the splashing phase (upper), rising-up phase (middle) and separations phase (lower) [2, 15, 16].

### 7.3.6. Production and instrumentation of the hollow cylinder

The production of the hollow cylinder is quite similar to the one of the full cylinder. However, there are some differences. The main one is the mounting of the pressure sensor: for the full cylinder this could happen after the production as explained in paragraph 7.3.3. but for the hollow cylinder this should happen during production. The same principle as for the rigid objects was used with the help of an aluminium tube with screw thread. However, for the rigid objects the tubes were glued to the PU while this is of course not possible for the hollow cylinder due to the small thickness of its composite shell. The metal tube is soldered on a plate which is curved in the same way as the cylinder itself. This plate should be fixed between two layers of the hollow cylinder. The first layer was not a wound one but an isotropic chopped fibres mat of 0.6 mm. There is opted for such a layer because it is possible to impregnate the mat rather fast with resin. This is important since the mounting of the sensor connection (tube and plate) takes some time and the resin starts curing after 30 minutes. A second advantage is the structure of the mat: the fibres are quite loose which makes it easier to place the tube and plate.

The production of the cylinder was done in following order. First, the shape of the sensor connection is cut out of the PU (Figure 7-27) to achieve a smooth outer surface of the cylinder despite this sensor guidance.



**Figure 7-27** PU cylinder: preparation of the location for the pressure sensor [2, 15, 16].

Next, a household foil was wrapped around the PU cylinder for allowing easy removal of the PU foam mandrel once the fibre mat and winding layers are done. The isotropic mat is wrapped around the cylinder with a small overlap area of 10 mm situated diametrical to the location of the pressure sensor to reinforce the object for the connection to the ladder. The mat is held tight with the help of two glass fibres which are put around the cylinder and tied together as is shown in Figure 7-28.



**Figure 7-28** PU cylinder with chopped fibre layer and curved plate for the pressure sensor [2, 15, 16].

Next, the tube and plate for the sensor are put in place. The tube is foreseen of inner screw thread. However, since it is mounted before winding some measures are necessary to prevent the resin of flowing in. Before mounting the sensor connection on the mandrel, a dummy was made in polyethylene and was put in the tube. Top and bottom are sealed with candle-grease to keep out the resin as well as possible. The dummy and the sealing of candle-grease are seen in Figure 7-29. Next, the same two layers as for the full cylinder are wound. Again the two edges of the cylinder are thicker due to the winding process. For this test object, only the composite layers were cut on the lathe since the foam had to be removed entirely with drill, hammer and chisel. Due to the use of the household foil the inner surface of the hollow cylinder is very smooth. Pictures are shown in Figure 7-30 and Figure 7-31.

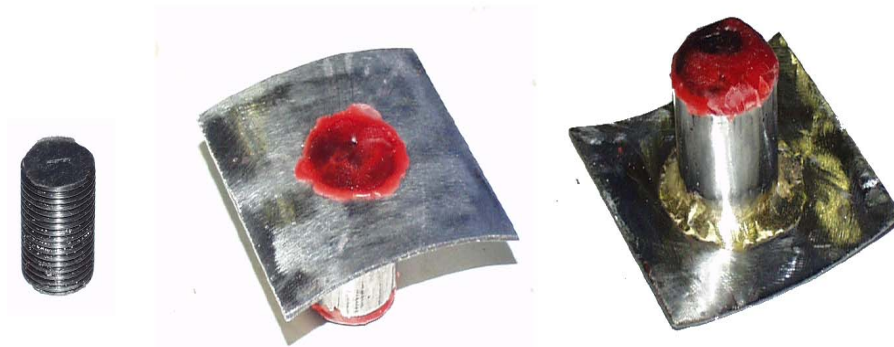


**Figure 7-29** A polyethylene dummy (left) and sealing of the sensor connection with candle-grease (middle and right).



**Figure 7-30** Removal of thick edges of the cylinder (results in cylinder of 400 mm length) and start of the removal of the internal PU foam [2, 15, 16].

The used pressure sensor was again the A23 since lower peak pressures were expected. Also, four strain gauges and the HSC camera were used besides the pressure sensor. Two of the strain gauges were mounted in the same way as for the full cylinder, namely a perpendicular and a longitudinal one on the same meridian as the pressure sensor (Figure 7-32). The two extra strain gauges were glued on the same spot but on the inner side of the hollow cylinder to assess a possible difference between outer and inner strain gauges.



**Figure 7-31** Finished hollow cylinder [2, 15, 16].



**Figure 7-32** Two outer strain gauges on the hollow cylinder [2, 15, 16].

### 7.3.7. Test set-up hollow cylinder

The connection of the hollow cylinder to the ladder is based on the one of the cone. Hence, most parts of that connection are re-used as is seen in the drawing in Figure 7-33.

The two lower parts are new. The first is a small flat bar on the inner side of the cylinder and the second one is a U-profile just above the cylinder. In the flat bar some holes are drilled where the bolts are welded. This bar is mounted on the inner side of the cylinder with some rubber in between and is fixed to the U-profile. Also, a rubber is present between the outer side and the U-profile. This profile is 2 mm thick and four screwed rods are welded to it to fit in the frame that was also used for the cone.

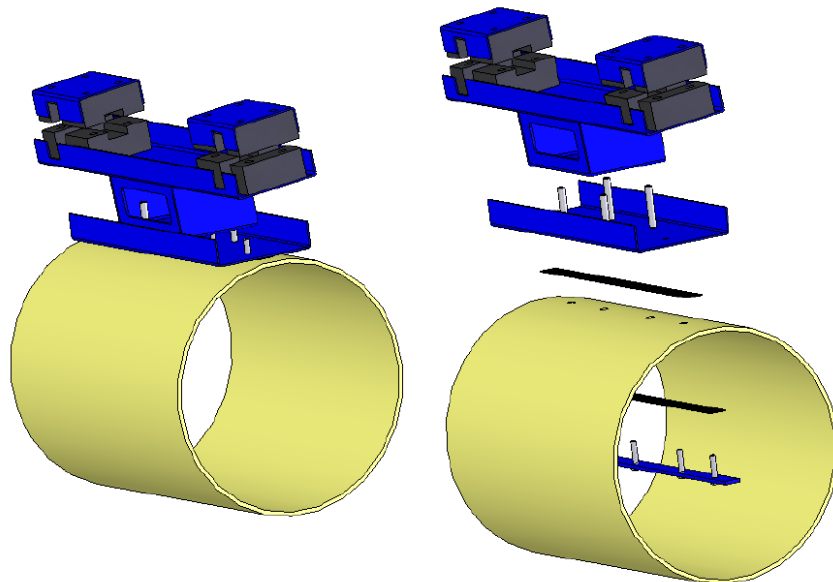


**Figure 7-33 Connection of the hollow cylinder and the ladder [2, 15, 16].**

### 7.3.8. Hollow cylinder: results and validation

The first tests on the hollow cylinder measured the pressure only at zero degrees. It is not possible to rotate this cylinder as it was done for the full one because no inner tube is present. Six of these tests were done. In the measured signals it became clear that the pressure peak was a lot lower for the deformable cylinder than for the rigid cylinder. The average, measured at 100 kHz, is  $335 \pm 68$  kPa which is almost a factor two smaller. A representative curve is given in Figure 7-34. The peak pressure occurs again in some milliseconds. After the peak pressure the signal oscillates out.

The signals of the six tests are given in Appendix. This result is compared with CFD calculations in Fluent further in this Chapter in paragraph 7. 5.

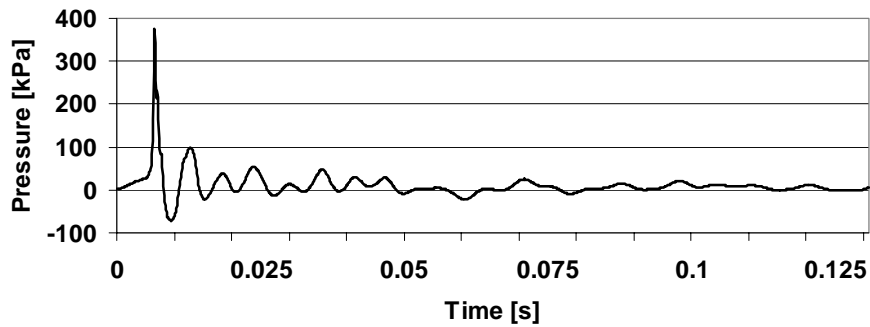


**Figure 7-34** Pressure signal for the hollow cylinder zero degrees; drop height 1000 mm [2, 15, 16].

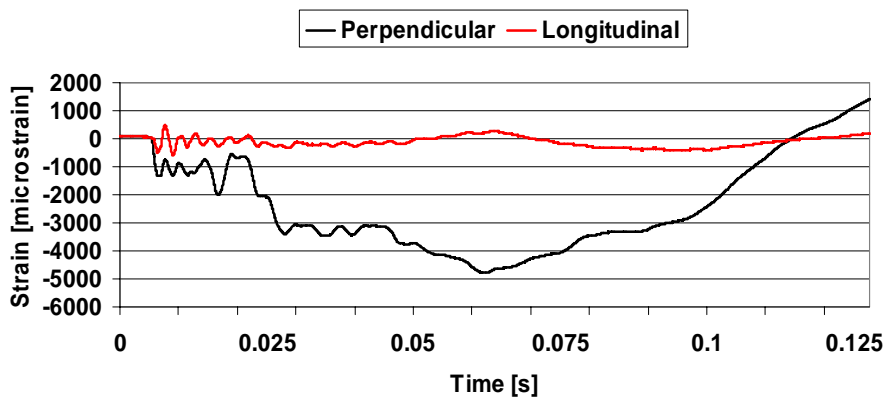


**Figure 7-35** Outer strain gauges for the hollow cylinder zero degrees; drop height 1000 mm [2, 15, 16].

Next, some signals of all strain gauges are given in Figure 7-35 for the outer ones and Figure 7-36 for the inner ones. For the perpendicular inner strain gauge the average is about 4350 microstrain, for the outer one minus 4900 microstrain. The pattern of these both strain gauges is about mirrored about the time axis. The structure is bend hence compressive behaviour at the inner side equals tensile behaviour at the outer side and vice versa. For the longitudinal strain gauges the values are a lot lower but still an average of 680 microstrain is measured for the outer one and an average of minus 490 microstrain for the inner one. Figure 7-37 shows the images taken with the HSC during a drop test. The three phases – splashing, rising-up and separation phase – are noticed.

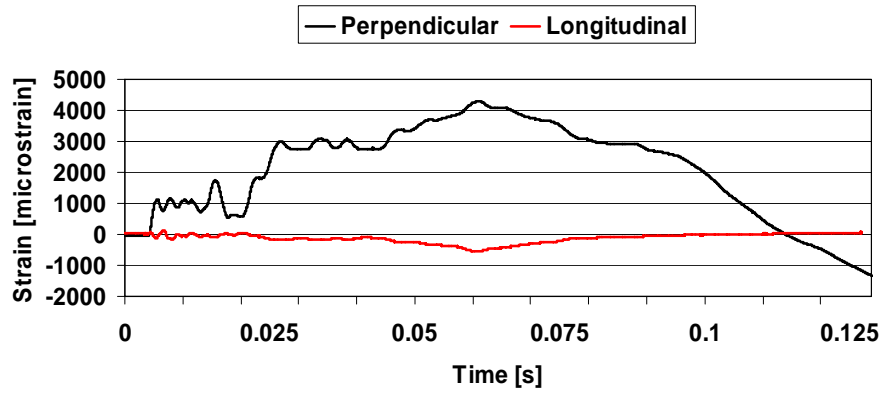


Figure 7-36 Inner strain gauges for the hollow cylinder zero degrees; drop height 1000 mm [2, 15, 16].

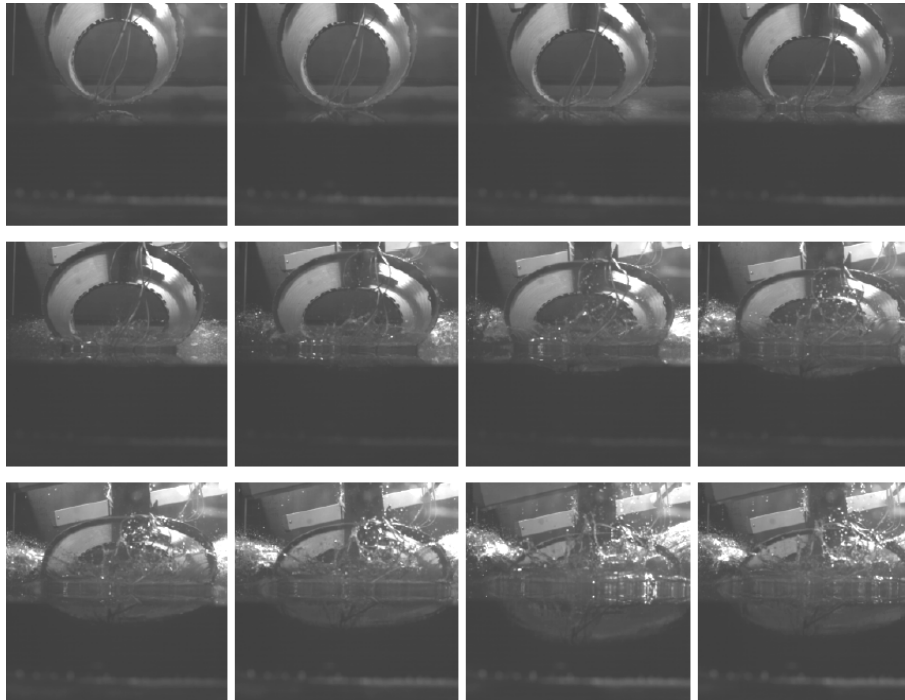
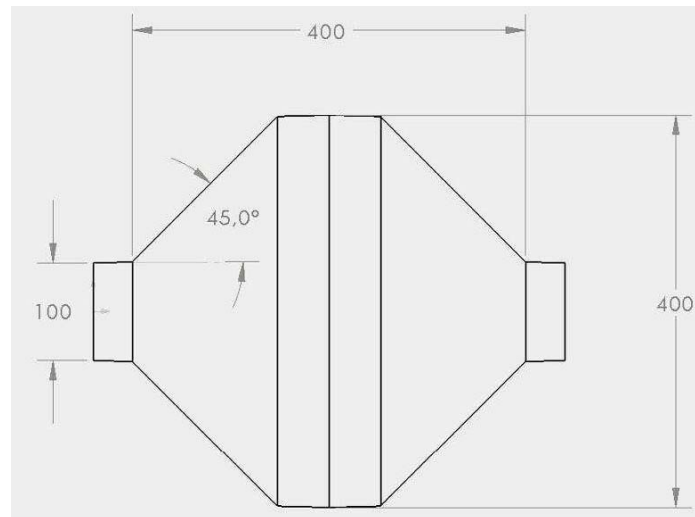


Figure 7-37 Images from the HSC for the hollow cylinder; the splashing phase (upper), the rising-up phase (middle) and the separation phase (lower) [2, 15, 16].

## 7. 4. TEST CASE ‘POINT ABSORBER’

### 7. 4. 1. Introduction

The last test object considered within this work was a small scale point absorber. There was opted for the cone/cylinder/cone shape at 1:10 scale as is shown in Figure 7-38. However, the shape is at 1:10 scale but the winding pattern is not. As became clear with the first made point absorber in Chapter 6, even two layers resulted already in a quite rigid point absorber. Hence, it was decided to make a slamming test buoy with only one wound layer.



**Figure 7-38** Point absorber ‘cone/cylinder/cone’.

### 7. 4. 2. Production and instrumentation of the laboratory scale point absorber

As mentioned in the previous paragraph, this new point absorber was made thinner. Also, within the design, the connection of the pressure sensor was foreseen. The point absorber was tested in breaking wave slamming (dropped in the vertical direction of Figure 7-38) because it seemed a more critical load than the bottom slamming as was shown in Chapter 5. However, this does not mean that it would not be useful to do (repetitive) bottom slamming tests in the future. Nevertheless, for now, breaking slamming was chosen.

First, two cones were made as is shown again in Figure 7-39 to fix thoughts. The pressure sensor connection was the same as for the hollow cylinder, namely a small tube with inner screw thread and a curved plate. A hole was drilled into the inner cone. Next, the size of the plate was cut out of the second (outer) halve to prevent

irregularities in the surface of the object. From here on the same procedure was followed as for the hollow cylinder (i.e. polyethylene dummy and candle grease). On the inner side of one cone two strain gauges were mounted, again a perpendicular and a longitudinal one on the same meridian as the pressure sensor and near the middle of the point absorber. Then, the winding phase could start. This time the layer with a winding angle of 22 degrees was wound only one time because the first made one was very thick at that scale.



**Figure 7-39** Two cones made with chopped fibres.

#### 7. 4. 3. Test set-up

As was mentioned, the point absorber was tested laterally. Hence, the connection grip of the rigid cylinder was re-used for it. However, the diameter of the PVC tube in the point absorber was too large to fit. Additionally, parts were cut out of available tubes in the lab: two out of a polyethylene tube and also two out of a polypropylene tube.



**Figure 7-40** Aluminium tube with polyethylene and polypropylene parts.

These are put over an aluminium tube of the same size as the one for the rigid cylinder as is shown in Figure 7-40. This is clamped in the inner PVC tube in the point absorber. The final structure is seen in Figure 7-41.



**Figure 7-41** Laboratory scale point absorber with connection for the ladder [2, 15, 16].

#### 7. 4. 4. Laboratory scale ‘point absorber’: results and validation

The point absorber was dropped six times with the sensors at zero degrees. Since there is a small cylindrical part, the pressure signals are compared to that of the cylinder. Again, as for the full cylinder, six tests at a sample rate of 100 kHz with the A23 sensor gave 727.28 kPa which is the maximum value this sensor can measure. A typical signal is shown in Figure 7-42. The signals of the six tests are given in Appendix. Also, a new series of six tests were done with the A06 (but only at 51.2 kHz). As for the full cylinder the average value is again lower but with a large standard deviation possible due to the lower sample frequency.

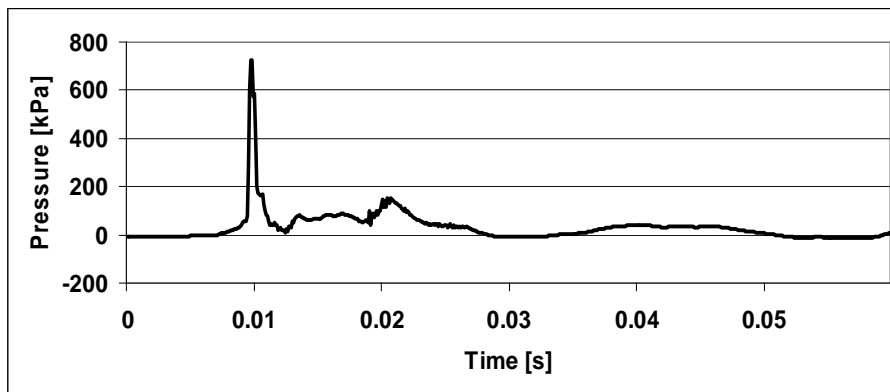


**Figure 7-42** Pressure signal for the laboratory point absorber; drop height 1000 mm [2, 15, 16].

It was expected that the point absorber would show a peak pressure lower than the rigid cylinder but higher than the deformable one. However, since the pressure sensor was limited to 727.28 kPa the rigid cylinder and the point absorber gave the

same peak pressure. The average value of the longitudinal strain gauge is about 875 microstrain and of the perpendicular strain gauge is about 170 microstrain. These strain gauge signals are shown in Figure 7-43. For this object the deformation is higher for the longitudinal strain gauge which is different than the behaviour of the other objects. This is probably due to the specific geometry of the point absorber.

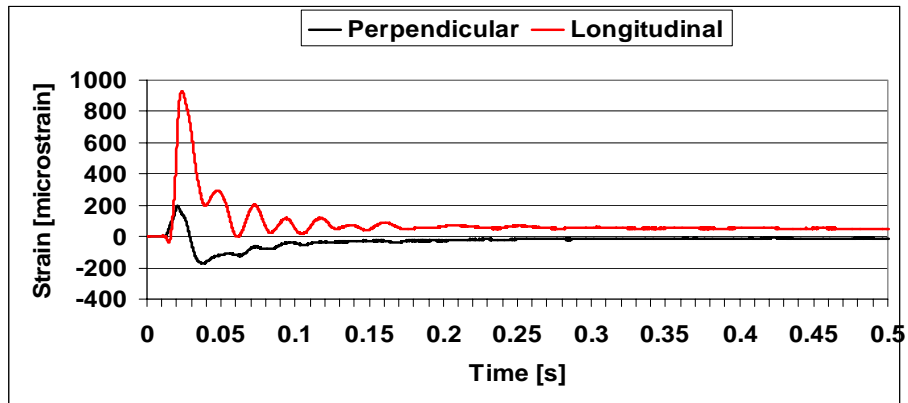


**Figure 7-43** Strain gauges for the laboratory point absorber; drop height 1000 mm [2, 15, 16].

The images of the HSC showed again a clear splashing phase and a rising up phase as can be seen in Figure 7-44. The separation phase is also noticed but looks different than for the cylinder. The separation spots are situated on the cone surface. These images are shown in Figure 7-45.

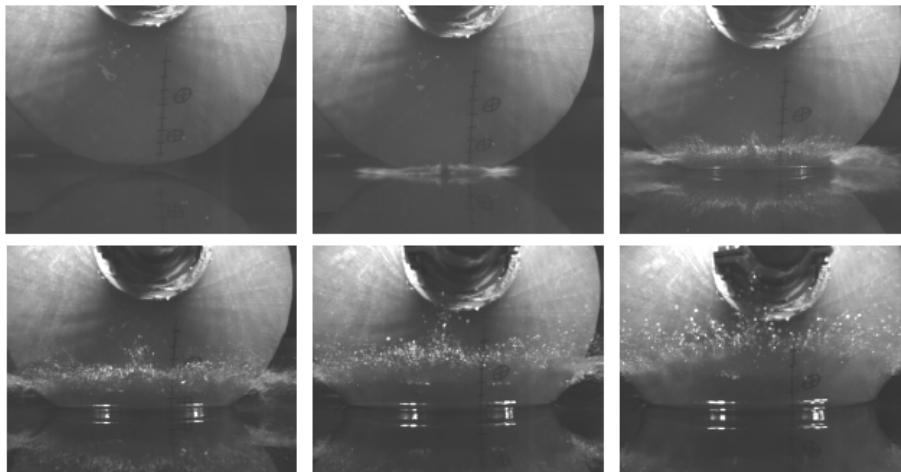


**Figure 7-44** Images from the HSC for the laboratory scale point absorber during the splashing phase (upper) and rising up (lower) [2, 15, 16].

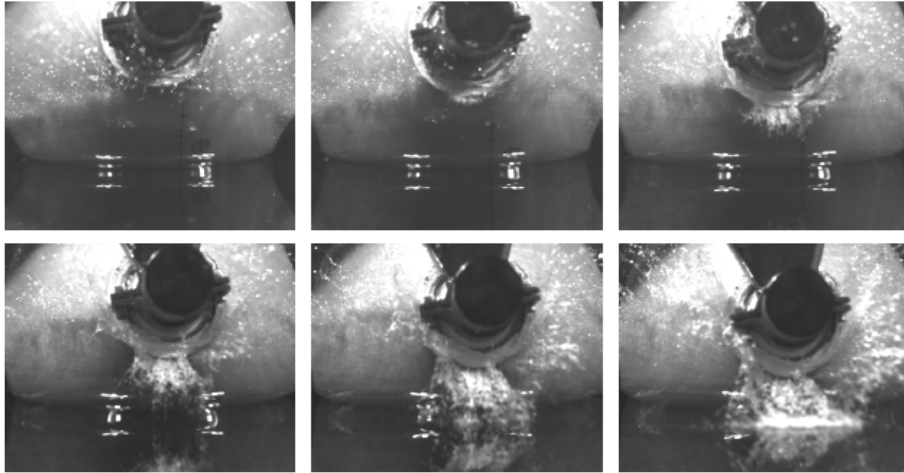


**Figure 7-45** Images from the HSC for the laboratory scale point absorber during the separation phase [2, 15, 16].

## 7. 5. COMPUTATIONAL FLUID DYNAMICS (CFD)

### 7. 5. 1. Introduction

As was mentioned in Chapter 3, the hydrodynamic slamming pressures only last some fractions of a second, but they can locally cause severe damage to the objects. A numerical method for estimating hydrodynamic impact pressures was obtained with the aid of the Department of Fluid Mechanics at Ghent University which is explained within this paragraph. The detailed results can be found in [16, 19, 21]. As a fluid solver the commercial CFD software package Fluent 6.3 and as structural package Abaqus 6.7 is used. To model the multiple phases, the Volume of Fluid model, included in Fluent, is used for all the simulations. The simulations were performed in 2D with a laminar scheme and both the water and air phases are defined as incompressible.

### 7. 5. 2. Volume of Fluid

The Volume of Fluid model (VOF) is a moving grid method where the grid can be linked to a moving object in the domain. This model was designed for insoluble phases. In this case, air and water were modelled as two phases. The model follows the interface between both. It solves a set of momentum-equations for each cell. Next, a parameter  $\alpha_q$  per cell, with  $0 < \alpha_q < 1$ , is assigned. It is the volume fraction of phase q in that particular cell. Since the work is done in 2D, 'surface fraction' seems a more correct name. However, 'volume fraction' is commonly used. In general, the VOF algorithm solves the velocity field first and adjusts the values of  $\alpha_q$  next. The main difficulty is the reconstruction of the interface.

The simplest method is the Simple Line Interface Calculation (SLIC) or the Solution Algorithm (SOLA-VOF). Both methods are first order methods for reconstructing the interface. The grid is reconstructed out of some segments aligned with the edges of the cells. This method is quite rough as can be seen in Figure 7-46 (left).

A more accurate VOF technique uses Piecewise Linear Interface Calculation (PLIC) of the interface. For this a cell is divided in as many areas as there are phases, hence for a two phase system (air and water) the cells are divided in two. This partitioning is done by a line which has a slope depending on the curvature of the interface. The PLIC algorithm allows discontinuities and does not construct a smooth interface with all lines, as is shown in Figure 7-46 (right). When the curvature is small (i.e. large radius in comparison with the size of the cells) this method is very accurate, namely of order  $O(\kappa, h)$  with  $\kappa$  the curvature and  $h$  is the size of the cells. For a high curvature all details smaller than the cell size  $h$  are lost. Next, once the interface

is reconstructed its movement should be modelled by the flow field by means of an advection algorithm i.e. calculating the phase fluxes through the cell edges. Then, the fractional step method or operational split recalculates the volume fraction  $\alpha_q$  by applying advection along the interface at one spatial direction. The values of  $\alpha_q$  are adjusted immediately. However, the slope of the interface is not yet adjusted in this step. The final volume fractions are achieved as soon as advection is applied in all spatial directions.

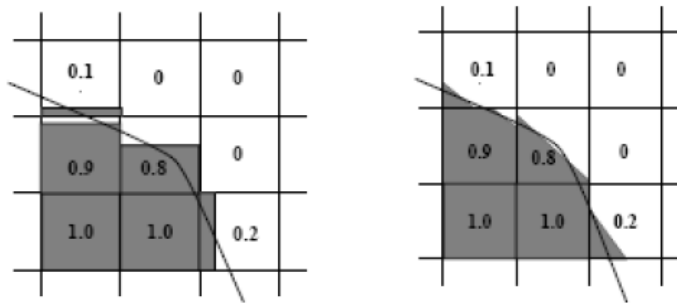


**Figure 7-46 The Simple Line Interface Calculation or SLIC (left) and the Piecewise Linear Interface Calculation or PLIC (right).**

However, the VOF has two important drawbacks. First, at the interface, ‘flotsam’ could occur which is the releasing of small drops of a free water surface. Second, it is possible that the quantity of water increases or decreases due to a rounding error, in other words the conservation of mass is not fulfilled. For this, the VOF model is improved (iVOF) by Wemmenhove et al. and Kleefsman et al. with the ‘local height function’ which improves the shape of the free surface [22, 23]. For each cell of the interface locally a function is defined that contains the height of the water column over three vertical cells as is seen in Figure 7-47. After the calculation of the phase fluxes through the cell edges the volume fractions are not calculated, as would be the case for normal VOF. The local height function is calculated instead and from the height of the fluid in the column, the volume fractions of the three cells are determined.

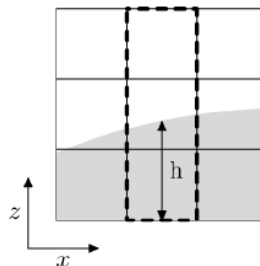


**Figure 7-47 Local height function.**

The VOF method is present as an ‘Euler-Euler approach’ in the commercially available code ‘Fluent’ which is used at the Department of Fluid Mechanics at Ghent University. Previously, research about slamming with VOF in Fluent was done by Fairlie-Clarke and Tveitnes [24]. However, instead of a falling object a rising water surface was used.

In this research a cone was simulated to compare the new numerical model with literature. Also, a cylinder of the size of our used test sample (paragraph 7. 3. ) was calculated. Both are described in the following paragraphs.

### 7. 5. 3. Cone simulation versus literature

Before simulations could start, a convergence study was necessary. This means that the same test case is run over and over again with smaller cells and/or time steps until the results are independent of the chosen time step and cell size. An important parameter is the dimensionless Courant number defined in Equation 7-1. It is the ratio of the physical velocity  $v_{fluid}$  to the grid velocity  $\Delta x/\Delta t$

$$C = \frac{\Delta t \times v_{fluid}}{\Delta x}$$

**Equation 7-1 Courant number [-].**

When the Courant number is ‘c’, the displacement of the interface in one time step is the product of ‘c’ and  $\Delta x$ . At high Courant numbers convergence problems occur frequently. Hence, it is important to use low Courant numbers. Here, it was decided to use a Courant number lower than 1 which means that it will certainly last more than one time step before a cell near the interface changes entirely of phase. The impact of a rigid body with fixed velocity has been simulated and the results have been compared with data from the literature. All calculations are performed in two dimensions. The test case is one from Peseux et al. for which numerical and experimental data is available. This test case is the impact of a rigid cone with a deadrise angle of 14 degrees and a fixed velocity of 5.2 m/s [5]. The geometry and boundary conditions are shown in Figure 7-48. The lower and side edges of the mesh are defined as walls. The upper edge is defined as a pressure outlet where the air phase can flow in and out. For water this is not done, since in normal conditions, the water will not reach up to this edge. As mentioned, the simulations were performed in 2D with a laminar scheme and both the water and air phases are defined as incompressible. The zone ‘moving-fluid’ Figure 7-48 moves undeformable with the cone and the zone ‘fluid’ deforms during simulation and is re-meshed. In the ‘moving-fluid’ zone the hydrodynamic load is calculated hence here an accurate mesh (i.e. a fine mesh) is desired. Also, a transition pattern for the

mesh is used. In this way the mesh is coarser further away from the cone by gradually decreasing the number of cells. The peak pressure predicted by the numerical model of Peseux et al. is 0.35 MPa and the results in Table 7-1 for  $\Delta x \leq 0.50$  mm correspond well with this value [5]. The used  $\Delta x$  is the size of the fine grid of the moving-fluid zone near the cone.

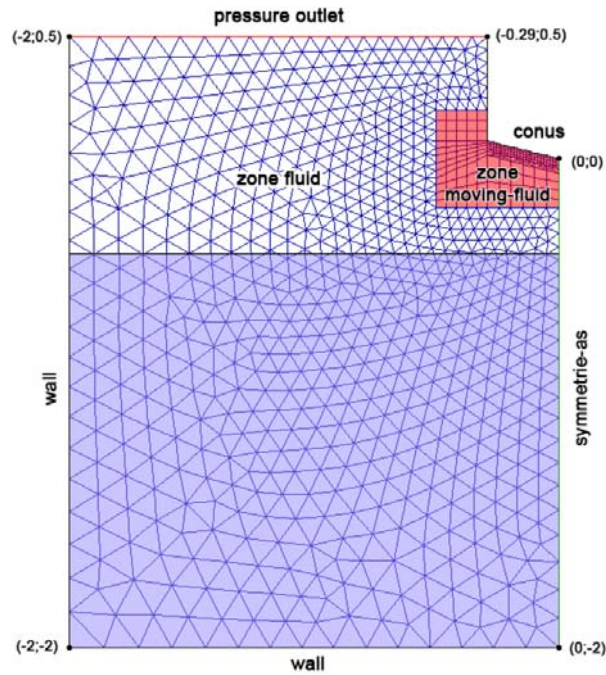


**Figure 7-48** Grid for a cone (distances in meter) [19, 21].

$\Delta t \downarrow$	$\Delta x \rightarrow$	1.00	0.50	0.25
10		$2.74 \cdot 10^5$	-	-
5		$2.83 \cdot 10^5$	$3.49 \cdot 10^5$	-
2.5		$2.70 \cdot 10^5$	$3.49 \cdot 10^5$	$3.60 \cdot 10^5$

**Table 7-1** Peak pressure [Pa] on a rigid cone with deadrise angle of 14 degrees and fixed drop velocity of 5.2 m/s as a function of the grid size  $\Delta x$  [mm] and time step  $\Delta t$  [ $\mu$ s].

Considering the computational cost (due to a smaller time step) and the small difference in peak pressure between  $\Delta x = 0.50$  mm and  $\Delta x = 0.25$  mm, a grid size of 0.50 mm is chosen for all subsequent calculations. The resulting peak pressure for a mesh with  $\Delta x = 0.25$  mm and  $\Delta t = 2.5 \mu$ s remains stable. Numerically, Peseux et al. found a peak pressure of about 0.35 MPa. However, experimentally, they found a peak pressure of only 0.27 MPa as even a stiff cone deforms and the impact velocity is never completely constant, the simulation was done in 2D and the water was

assumed incompressible. Hence, the model is quite conservative and predicts a pressure of 30 % too high. This deviation is more pronounced for cones with a smaller deadrise angle [5]. The results are summarised in Table 7-2.

	Peak pressure [MPa)
VOF simulation	0.349
Peseux simulation	0.350
Peseux experiments	0.27

**Table 7-2 Comparison of VOF simulations with numerical and experimental results from Peseux [5].**

7. 5. 4. Rigid cylinder simulation versus experiments

The impact of a cylinder with diameter 0.3 m is simulated. Again, only half of the domain is modelled since it is a symmetrical problem and the plain strain assumption is valid. The convergence study has shown that a cell size of 0.5 mm is small enough to capture the pressure peak. This peak is higher than for the cone because the lower surface is almost flat. However, these peaks decrease quite fast due to the increasing deadrise angle. The geometry and boundary conditions are shown in Figure 7-49.

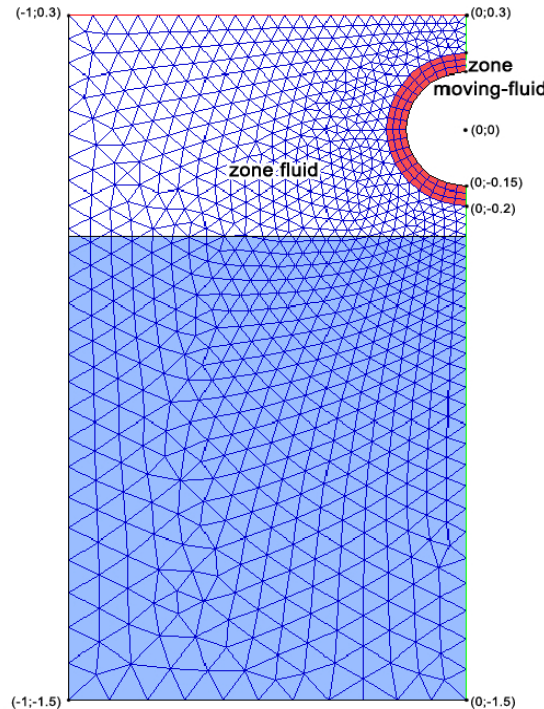


**Figure 7-49 Grid of a hollow cylinder (distances in meter) [19, 21].**

Again, the zone ‘moving-fluid’ moves in an undeformable way with the cylinder and the zone ‘fluid’ deforms during simulation and is re-meshed. The dimensionless pressure in function of time after impact is shown in Figure 7-50. It can be seen that at  $z/R = 0.01$  the maximum pressure is already decreased a lot in comparison with the initial peak.

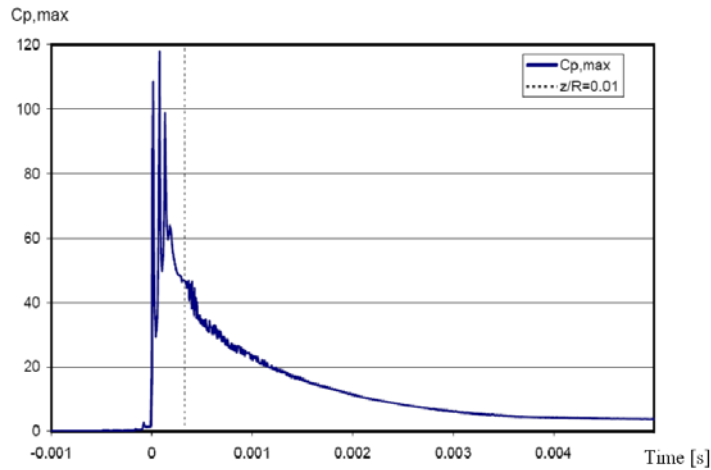


**Figure 7-50 Maximum Cp in function of time [19].**

The maximum Cp is 118 hence the experimental results on the rigid cylinder for zero degrees was lower, namely a Cp of at least 73.4. The results are summarised in Table 7-3.

Full cylinder	Dimensionless pressure coefficient $C_p$
VOF simulation	118
Drop test	> 73.4

**Table 7-3 Comparison of the dimensionless pressure coefficient at zero degrees for the VOF simulation and experiments on the full cylinder.**

### 7. 5. 5. Coupled hollow cylinder simulation versus experiments

The impact of an object on a water surface is a fluid structure interaction problem. Until now this has not been considered within this work. However, the hydrodynamic pressures that occur at water entry of the body, lead to deformations of that body. Additionally, these deformations influence the pressures. As mentioned earlier, Fluent 6.3 was used for the simulation of the flow problems and Abaqus 6.7 for the calculation of the deformations of the material. The pressures, calculated with Fluent should be given as a boundary condition to Abaqus and the deformation

of the structure, calculated in the latter, should be given as a boundary condition to Fluent. Since it is not straight forward to exchange information between the two programs, a coupling-algorithm was used as proposed by Vierendeels et al [25]. Per time step different iterations are performed between Abaqus and Fluent. Starting at time step  $n$ , first a prediction is made of the position of the interface, based on the velocity of the interface in time step  $n$ . Next, with this new position the fluid domain is solved which results in the forces on the interface. With these forces the structure calculations are done and this results in a new position of the interface which is used for a new calculation of the fluid. This loop is repeated until convergence is reached. Next, the algorithm moves forward to the next time step ( $n + 1$ ) and the loop runs again. In conclusion, the purpose is to achieve convergence per time step in the fluid domain as well as in the structure domain. The initial version of the coupling software was made user friendly by Joris Degroote from the Department of Fluid Mechanics at Ghent University, and was called ‘Tango’ [26]. This version uses

- i) Gambit for the construction of the mesh used in Fluent and Abaqus
- ii) Fluent to calculate the 2D fluid problem
- iii) Abaqus to perform the structure calculations
- iv) the Intel C++ compiler for the User-Defined Functions (UDF) in Fluent
- v) the Intel Fortran compiler for the User-Defined Subroutines in Abaqus

For validation purposes, the same geometry as the hollow cylinder with a diameter of 0.3 m is chosen, consisting out of three layers (chopped fibre layer and two wound layers) as was discussed in paragraph 7.3.6. Tango is written for 2D as well as for 3D calculations. The cell size is taken small enough to capture the peak pressure; hence the time step should be small enough to limit the Courant number for reasons of stability. Additionally, per time step a number of iterations between Fluent and Abaqus are necessary thus the calculation time increases quite fast. Hence, a 2D simulation in Fluent is desired to achieve accurate results in combination with limited calculation time. However, to simulate the material orientations of a composite tube in Abaqus a 3D shell structure is needed. Since the pressures are calculated in 2D in Fluent, the influence of a 3D structure can not be correctly modelled. Hence, the cylinder is modelled as infinite in Abaqus and the load out of Fluent is applied for the whole cylinder. In reality the cylinder is of course not infinite but limited with edges but these are not taken into account. The infinite cylinder was modelled as a half ring as is shown in Figure 7-51 with necessary boundary conditions depicted in Figure 7-52. Left, the symmetry in the yz-surface, which allows only a vertical movement, is depicted; in the middle the symmetry in the xy-surface, which only allows rotation and translation in the xy-

surface, is shown; and finally, the initial velocity of the cylinder is given with a ‘Predefined Field’ on the right.

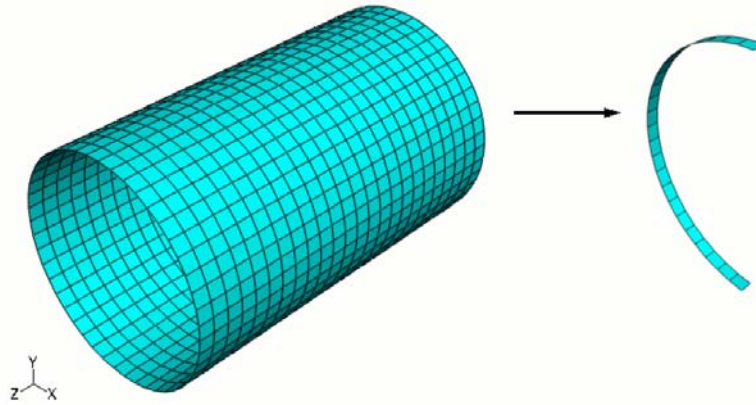


**Figure 7-51** Full geometry of cylinder, reduced to half ring; considered infinite [19, 21].

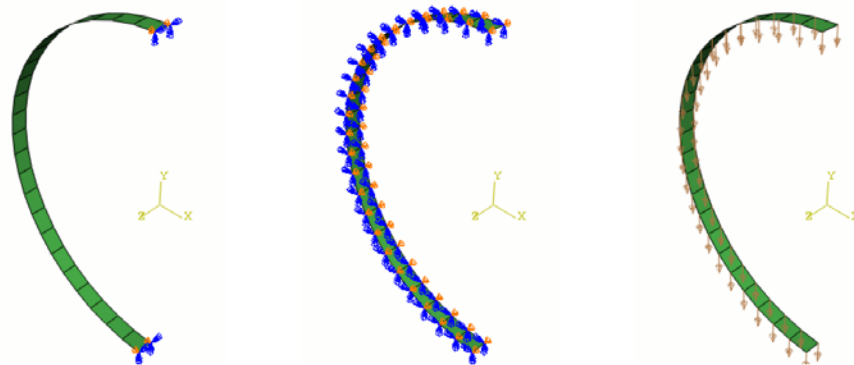


**Figure 7-52** Boundary conditions in Abaqus: symmetry in the yz-surface (left), symmetry in the xy-surface (middle) and initial velocity (right) [19, 21].

The shell elements S4R are taken in Abaqus. The same material constants as for the SMC material which was characterised in Chapter 3 and used for several calculations on the full scale buoys in Chapter 5 are used. The structural calculation is implicit and dynamic. As mentioned, the calculations in Fluent are done in 2D. These pressures should be applied in Abaqus at the 3D surface. The mesh for Fluent is created in Gambit. Next, in Fluent an Abaqus input file is created which contains the xy-coordinates of a half circle. A 3D model was achieved by means of a C++ program that adds a z-coordinate to the half circle and forms the necessary elements as is shown schematically in Figure 7-53. Also, within this program another file is loaded with the data of the material properties.

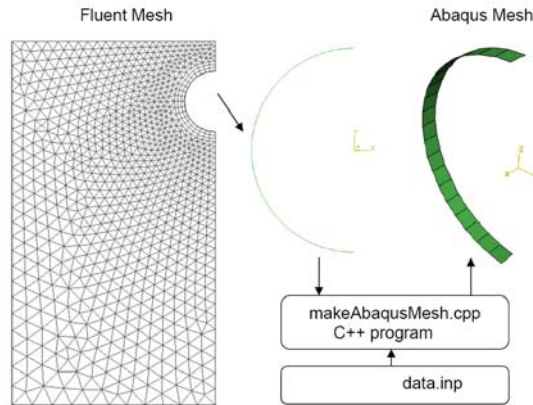


**Figure 7-53 Adding z-coordinates for the process of changing the 2D Fluent mesh into a 3D shell mesh in Abaqus [19, 21].**

The influence of the deformation on the peak pressures was investigated. This was done by performing a coupled calculation of the cylinder with the elastic properties of the composite material. The dimensionless pressure ( $C_p$ ) in function of time is given in Figure 7-54. The peak pressure coefficient for the coupled calculation of the deformable composite cylinder is quite a lot lower, namely 40-45. For the experimental test case of the hollow cylinder the measured value of 335 kPa which means a peak pressure coefficient of 34. This small difference between calculation and experiment could be caused by a theoretical constant velocity which, in reality, decreases. A second peak and even a third peak are clearly noticed for the simulation. They are probably caused by a non-flat surface at the moment of impact. The results are summarised in Table 7-4.

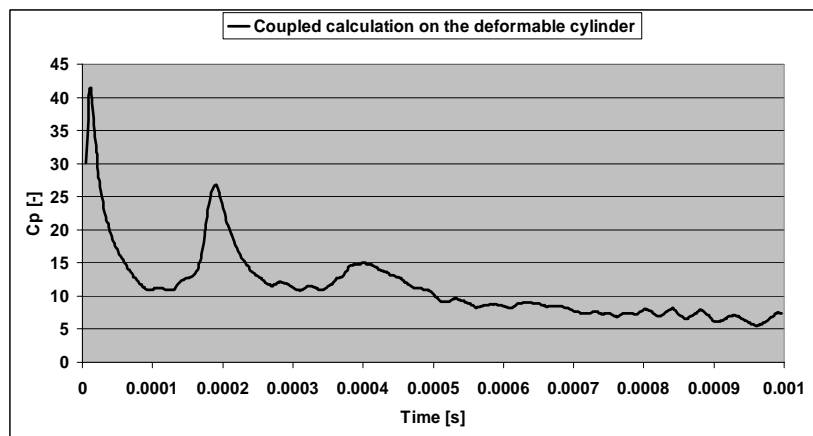


**Figure 7-54 The dimensionless pressure coefficient in time during a coupled calculation on a composite cylinder [19, 21].**

Hollow cylinder	Dimensionless pressure coefficient Cp
VOF simulation	40-45
Drop test	34

**Table 7-4 Comparison of the dimensionless pressure coefficient at zero degrees for the VOF simulation and experiments on the hollow cylinder.**

An overview of several pressures in function of the impact velocity is given in Figure 7-55. First, two curves were generated for the VOF peak pressures in function of the impact velocities for both cylinders. This was done by means of the simulated (VOF) Cp value for one velocity. The same was done for the experimental peak pressures for both cylinders. Also, the DNV constant pressure with average pressure slamming coefficient equal to  $2\pi$  is drawn in function of the impact velocity. It is shown that the value of the VOF and the experimental value for the deformable cylinder do match with a slight over prediction. For the rigid cylinder the difference is higher which is probably due to the range of the pressure sensor. Now, the DNV constant pressure (the lowest curve) is not in the same order of magnitude as the measured and calculated peak pressures. Of course their respective interpretation should be kept in mind: on the one hand peak pressures (VOF and experiments) and on the other hand constant DNV pressure. Still, since the difference is very large for higher impact pressures it would be advisable to design a cylinder against high local pressures.

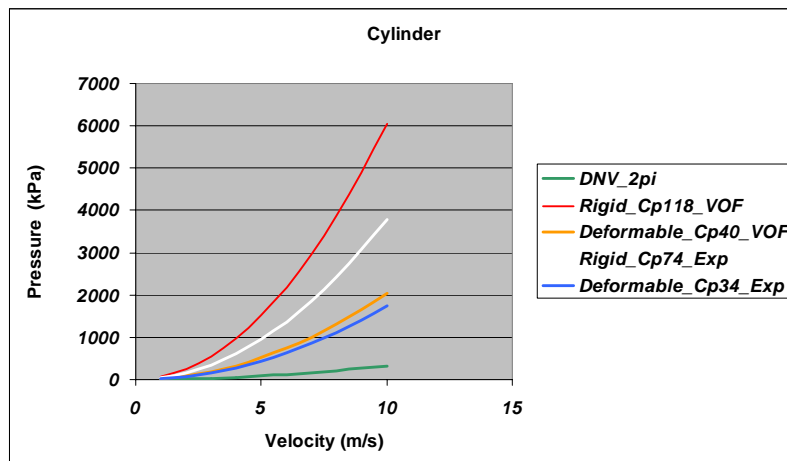


**Figure 7-55 Comparison between the VOF peak pressures for the two cylinders, the experimental peak pressures for the two cylinders and the DNV constant pressure (coefficient  $2\pi$ ) in function of impact velocity.**

## 7. 6. REFERENCES

1. W. Baro and T. Derveaux, Ontwerp, realisatie en beproeving van een composiet vlotter voor golfenergie-conversie, Ghent University. Faculty of Engineering, Master thesis academic year 2006-2007.
2. J. Himpe, Optimalisatie en validatie van een experimentele slamming setup, Ghent University. Faculty of Engineering, Master thesis academic year 2007-2008.
3. D. VanNuffel, Slammingexperimenten van composiet-'eieren' op laboschaal, Ghent University. Faculty of Engineering, Master thesis academic year 2008-2009.
4. X. M. Mei, Y. M. Liu et al., On the water impact of general two-dimensional sections. *Applied Ocean Research*, 1998. 21(1): p. 1-15.
5. B. Peseux, L. Gornet et al., Hydrodynamic impact: numerical and experimental investigations. *Journal of Fluids and Structures*, 2005. 21: p. 277-303.
6. vonKarman, The impact on seaplane floats during landing. 1929: p. 321.
7. H. Wagner, Uber Stoss- und Gleitvorgänge an der Oberfläche von Flüssigkeiten. *Zeitschrift für Angewandte Mathematik und Mechanik*, 1932. 12(4): p. 193-235.
8. Yettou, Desrochers et al., Experimental study on the water impact of a symmetrical wedge. *Fluid Dynamics Research*, 2006. 38: p. 47-66.
9. R. Zhao and O. M. Faltinsen, Water entry of two-dimensional bodies. *Journal of Fluid Mechanics*, 1993. 264: p. 593-612.
10. D. Battistin and A. Iafrati, Hydrodynamic loads during water entry of two-dimensional and axisymmetric bodies. *Journal of Fluid and Structures*, 2003. 17: p. 643-664.
11. M.-C. Lin and L.-D. Shieh, Flow visualization and pressure characteristics of a cylinder for water impact. *Applied Ocean Research*, 1997. 19: p. 101-112.
12. J. Wienke, Druckschlagbelastung auf schlanke zylindrische bauwerke durch brechende wellen - theoretische und großmaßstäbliche Laboruntersuchungen, in *Technischen Universität Carolo-Wilhelmina zu Braunschweig*. PhD thesis. 2001.
13. J. Wienke and H. Oumeraci, Breaking wave impact force on a vertical and inclined slender pile - theoretical and large-scale model investigations. *Coastal Engineering*, 2005. 52: p. 435-462.
14. Product Data Sheet. 22/02/2007 [cited 2007 20/03]; Available from: [http://www.ecc-belgium.be/images/upload/File/technischefiches/TF\\_ECC/Slijtvasteenchemischresistentebedrijfsvloeren/Primers/PC%205800%20TF.pdf](http://www.ecc-belgium.be/images/upload/File/technischefiches/TF_ECC/Slijtvasteenchemischresistentebedrijfsvloeren/Primers/PC%205800%20TF.pdf).
15. C. Blommaert, J. Degrieck et al. Design of composite material for cost effective large scale production of components for floating offshore structures. in *Proceedings of the 13th European Conference on Composite Materials (ECCM-13)*. 2-5 June, 2008. Stockholm, Sweden.

16. C. Blommaert, W. Van Paepegem et al., Design of Composite Material for Cost Effective Large Scale Production of Components for Floating Offshore Structures. Accepted for Special Issue of *Plastics, Rubber and Composites: Macromolecular Engineering*, 2009.
17. S. Victor, Onderzoek naar slammingsverschijnselen bij point absorbers: experimenteel en literatuurstudie, Ghent University. Faculty of Engineering, Master thesis academic year 2006-2007.
18. G. DeBacker, M. Vantorre et al., Experimental Investigation of Water Impact on Axisymmetric Bodies. 2008.
19. K. Stoop and S. Vermeulen, Numerieke simulatie van de vloeistof-structuur interactie bij hydrodynamische impact, Ghent University. Faculty of Engineering, Master thesis academic year 2007-2008.
20. Product Data Sheet - Glassfibre SE 1200 type 30 roving [cited 2007 20/01]; Available from: <http://www.owenscorningchina.com/upload/File/476696193.pdf>.
21. J. Degroote, C. Blommaert et al., Partitioned simulation of the impact of a deformable composite cylinder on a water surface in *International Conference on Computational Methods for Coupled Problems in Science and Engineering*. June 2009: Italy.
22. K. M. T. Kleefsman, G. Fekken et al., A volume-of-fluid based simulation method for wave impact problems. *Journal of Computational Physics*, 2005. 206(1): p. 363-393.
23. R. Wemmenhove, G. E. Loots et al., Numerical simulation of hydrodynamic wave loading by a compressible two-phase model, in *European Conference on Computational Fluid Dynamics*. 2006.
24. A. C. Fairlie-Clarke and T. Tveitnes, Momentum and gravity effects during the constant velocity water entry of wedge-shaped sections. *Ocean Engineering*, 2006.
25. J. Vierendeels, L. Lanoye et al., Implicit coupling of partitioned fluid-structure interaction problems with reduced order models. *Computers and Structures*, 2007. 85: p. 970-976.
26. J. Degroote, K.-J. Bathe et al., Performance of a new partitioned procedure versus a monolithic procedure in fluid-structure interaction. *Computers and Structures*, 2009. doi:10.1016/j.compstruc.2008.11.013.

## Chapter 8

### PRODUCTION OF LARGE SCALE BUOYS

*In this chapter, the production of large scale components is discussed. First, the choice of the representative demonstrator is treated. Also, some explanation about the scaling of a filament wound structure is given. Second, two possible production processes are treated. Third, a test program including indoor and outdoor tests was planned and prepared with respective instrumentation.*

#### 8. 1. DISCUSSION OF A REPRESENTATIVE DEMONSTRATOR

##### 8. 1. 1. Buoy

Within the Seewec project, it was foreseen that SMC and STY, as production partners within WP4 of the Seewec project, would each make a representative demonstrator [1].

First, it had to be decided which representative demonstrators would be made. It was quite a straight forward choice to go for a buoy or part of a buoy as they are the main concern of WP4. However, as mentioned in Chapter 5 it became clear during the project that the filament winding was the best production method. Hence, it was decided that it would be more useful to use the available money in the production and testing of a buoy made by SMC. Because of this it seemed useless to make only part of a buoy because the whole concept of assessing the filament winding would serve to no purpose in that way.

Second, as a consequence of the decision of making a full buoy, discussion started about a possible scale factor for the buoy. Making a full size buoy seemed of course spectacular. However, the costs of production for such a stand alone demonstrator are very high.

Next, it seemed useful to choose the size fitting on 'Buldra'. In this way the diameter of the vertical rod should be 298.5 mm. It was decided that the inner composite tube would have a diameter of 315 mm because SMC made tubes like this before. Hence, no additional preparations were needed. With this in mind the 4 m by 4 m buoy was re-scaled to 'Buldra' scale. During the project it was called the '1:3 scale' (or 'large scale'). However, this is not entirely correct. The real scale factor is about 1:2.29. Hence, a buoy of 1.75 m by 1.75 m was proposed. Figure 8-1 shows the technical drawing of such a 'Buldra' scaled point absorber. The lay-up of the laminate of the full buoy is also used for this scale model i.e. four wound layers

of glass fibre/polyester material, one foam layer and again in reversed order the same four wound composite layers. The foam is a PVC foam with an E-modulus of 22 MPa and a density of  $70 \text{ kg/m}^3$ , the resin is the same one as proposed in Chapter 4 [2] but the glass fibre is Advantex instead of the proposed Vetrotex fibre [3]. This deviation of the original proposal of SMC was done due to contacts with the company 3B Fibreglass (former ‘Owens Corning’), a glass fibre producer. They are no partner within Seewec but nevertheless they proposed to try-out their Advantex glass fibre (which is commercially available since 2005) as a test sample for the buoys. This kind of fibre seemed worthwhile. Its basic mechanical properties and price are comparable to E-glass. There is no boron present (which is good for environmental issues). Additionally, the stress corrosion properties are very good, at 40% of UTS up to 50 years in a sea environment (3 months for E-glass).

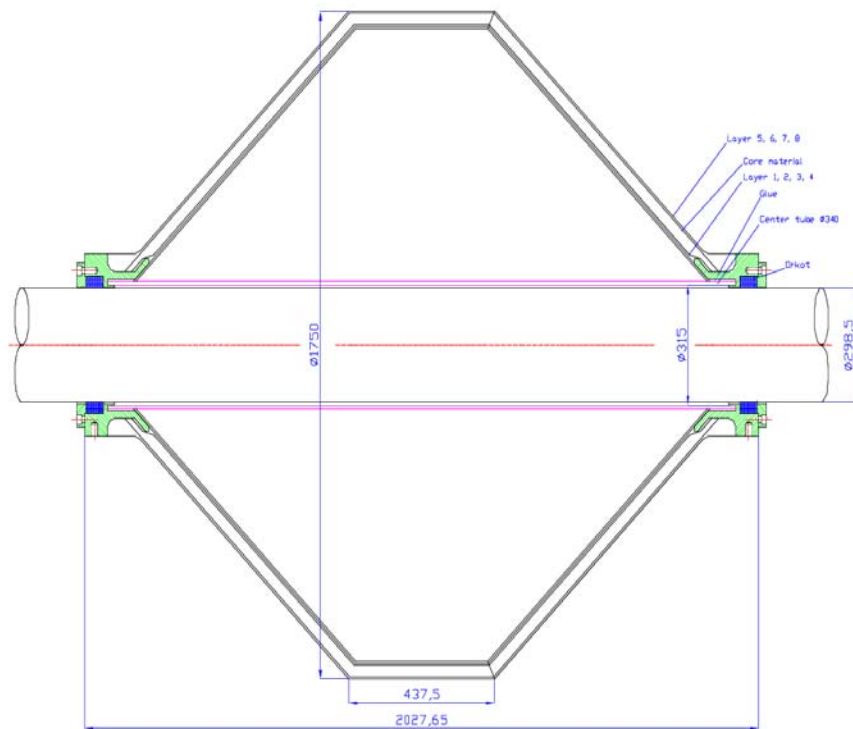


**Figure 8-1** Technical drawing of the ‘Buldra’ scale buoy.

### 8. 1. 2. Filament winding method and scaling

In Chapter 4 it was explained that glass fibres used for winding are available in standardised measures of ‘tex’. Next, inherent to the production method it is quite impossible to perform a perfect scaling of all the different layers. It was decided that the stacking of the scaled buoy had to resemble as good as possible the stacking of the full buoy. Hence, first, the winding angle of each layer was kept. Second, it was

decided to use glassfibre of 1200 tex instead of 2400 tex. Finally, the buoy had to be recalculated with FEA and checked whether or not the Tsai Wu measure at survival condition (25 year storm, DNV norm) for breaking wave slamming was further away from fracture than was the case for the full version. In Figure 8-2 it is shown that this measure is about 0.35 for the scaled buoy. For the full scale buoy with foam at the same load this was 0.822. Hence, for the same load the small buoy has a larger reserve to failure. However, no layers were added or removed anymore because the winding lay-up of the full scale buoy was followed as good as possible. As was mentioned in Chapter 5 the maximum for the Tsai Wu measure occurred in cross wound layer 3 for the full scale. For this scaled buoy it occurred both in cross wound layer 3 and in the outer layer (0.35). The inner composite tube was also made in 1200 tex instead of 2400 tex but it has not changed in winding angle. Also, four layers were wound.

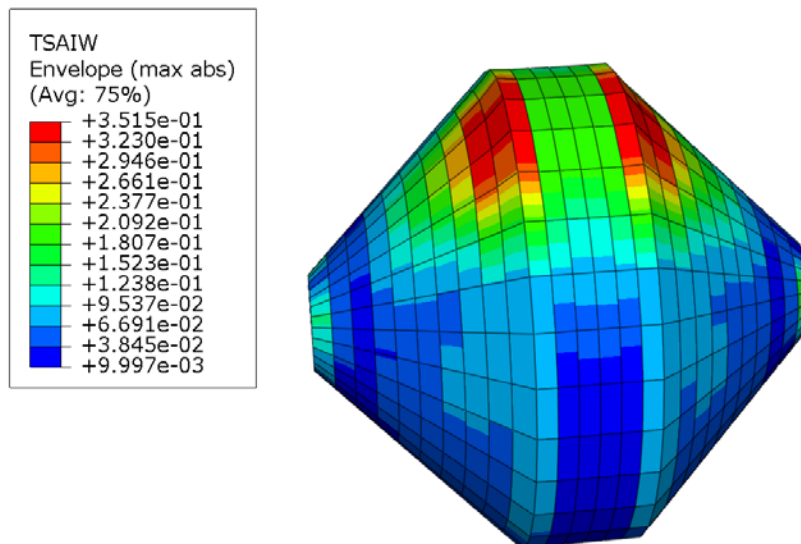


**Figure 8-2 Measure for Tsai Wu for the scaled buoy.**

### 8. 1. 3. Choice of Second buoy

At first, as was mentioned in paragraph 8. 1. 1. , the goal was that both production partners made a representative demonstrator. However, since filament winding was a more suitable method considering the cost, it seemed more interesting to use the remaining funding for production and testing of the filament wound buoy. A testing program was proposed and the costs for it had to be counted in before production could start. This testing program included fatigue tests, several drop tests and fracture tests. An estimated cost calculation showed that it was possible to fabricate and test two such scaled buoys instead of one. Next, it was decided to make a more

deformable second buoy to assess the difference in occurring peak pressures. No foam was included hence no sandwich material was obtained. Instead of only dismissing the foam, additional calculations were used to determine the amount of layers on the second buoy. In Chapter 7 it was shown that the maximum pressure for a rigid cylinder was more than twice as high as the one for a more deformable cylinder [4, 5]. Of course, it is difficult to compare this experiment with the laboratory cylinder experiments but in any case a lower maximum pressure was expected for a more deformable structure. The Tsai Wu measure for the first buoy was about 1 at 1320 kN as is shown in Figure 8-3. This maximum value occurs again in the outer layer and in cross wound layer 3. The thickness of the second buoy was designed in such a way that a load of 660 kN (half the load of the first buoy) should give a Tsai Wu measure of about one and second, the stacking of the layers of the second buoy should resemble those of the first one as well as possible.

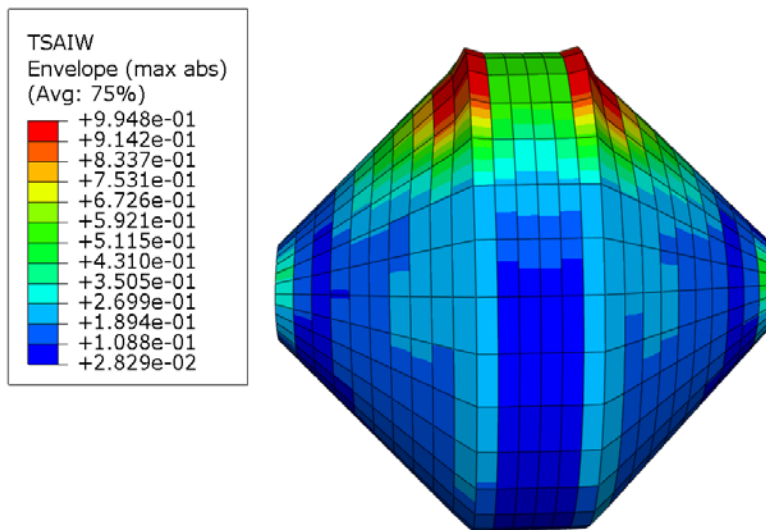


**Figure 8-3 Tsai Wu measure equals one for a load of 1320 kN.**

Through trial and error the amount of layers of the second buoy was determined. A first calculation was done on a buoy consisting of the eight layers without the foam with a load of 660 kN. However, the measure for Tsai Wu for such a buoy, given in Figure 8-4, is about 0.9 (occurring in the outer layer) so still a bit lower than one.

Hence, it had to be checked whether or not the thickness of the buoy could be further decreased. The next calculation was done with the same load applied on a buoy with seven layers where one of the four identical middle layers was removed. In Figure 8-5 it is shown that the measure for Tsai Wu is about one (again occurring

in the outer layer) for this buoy. Hence, the design of the second buoy was determined. The ‘buoy with foam’ is abbreviated as BWF while the ‘buoy without foam’ is called the BWOF.

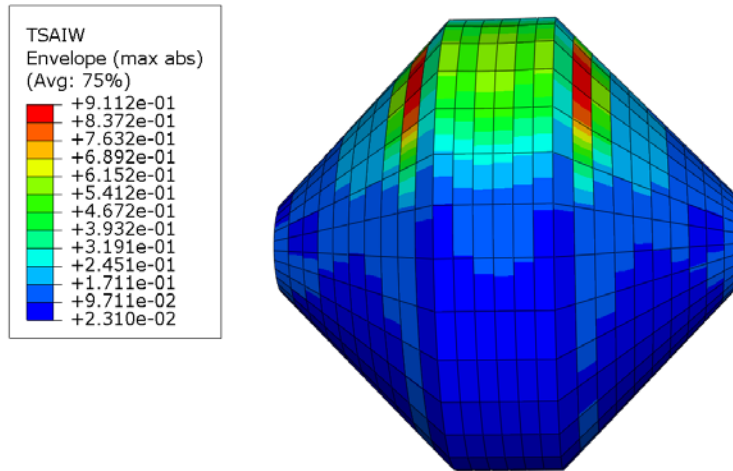


**Figure 8-4** Tsai Wu measure; Buoy with eight layers without foam.

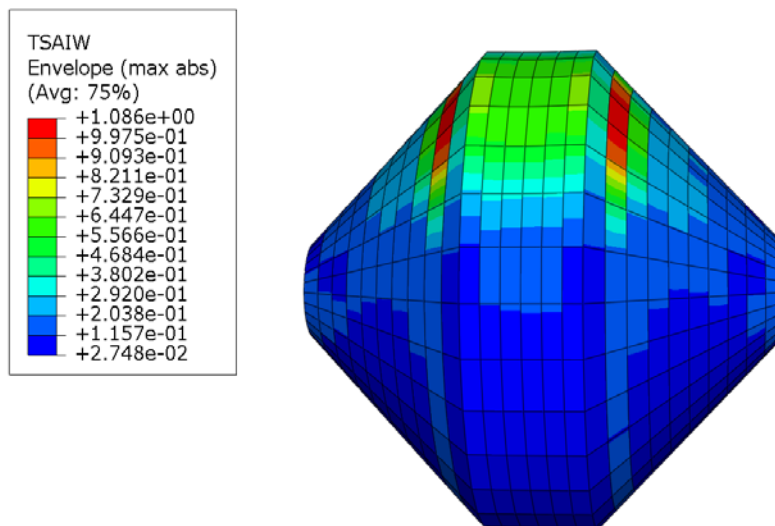


**Figure 8-5** Tsai Wu measure; Buoy with seven layers.

The calculated thicknesses of these buoys are shown in Figure 8-6 for the BWF and in Figure 8-7 for the BWOF.

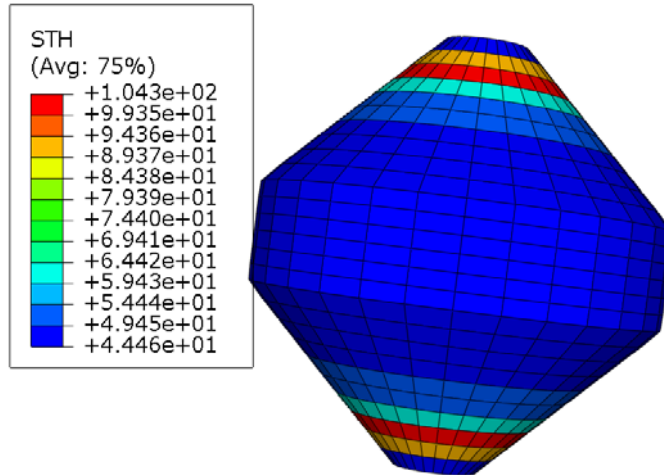


**Figure 8-6** Thickness of the BWF over the length.

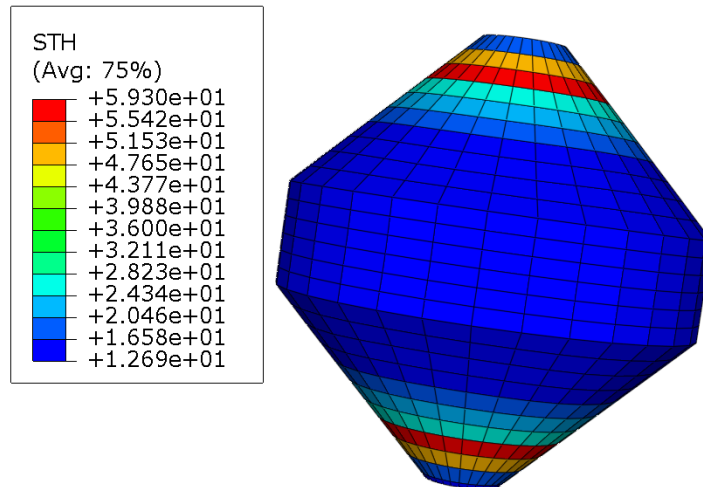


**Figure 8-7** Thickness of the BWF over the length.

In the following paragraph a short overview is given of the test program on both buoys to improve the comprehensiveness of the remaining of this chapter. However, all detailed results and measurements are only discussed in Chapter 9.

## 8. 2. TESTING PROGRAM

### 8. 2. 1. Fatigue test

In the first test, the point absorber is loaded in fatigue at the set-up in the laboratory Magnel of Ghent University. The buoy is loaded on its side, over a sector segment of 60 degrees. This test is an experimental simulation of the repeated breaking wave slamming. A picture of the set up is given in Figure 8-8. All preparations for this test are discussed further in this chapter.



**Figure 8-8** Picture of a buoy in the fatigue set up.

### 8. 2. 2. Drop test

Two kinds of drop tests were carried out on a canal in Ghent, namely one called the lateral (or breaking wave) and the straight (or bottom) slamming. This means that the buoy was dropped from a different side into the water.

First, for the lateral slamming tests the buoy was dropped at its side into the water as is shown in Figure 8-10 to simulate breaking wave of one year. As mentioned in Chapter 3, for the considered sea state, the celerity for the '1 year storm' ( $H_s = 6.6$  m) is 9.75 m/s which equals the drop velocity in the experiments. Hence, this celerity equals a drop height of about 4.85 m. Per buoy 10 drop tests were planned with the W0 meridian (strain gauges) down and 10 with the P0 meridian (pressure sensors), which is 30 degrees relative to W0 meridian, down. A schematic sketch of the location of all four 'strain-gauge-meridians' (W0, W20, M0, M20) and the 'pressure-sensor-meridian' (P0) is shown in Figure 8-9.

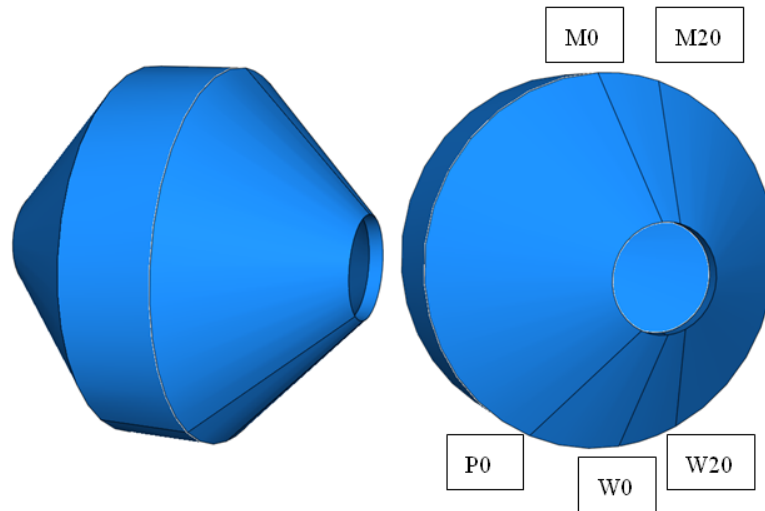


**Figure 8-9** 3D sketch of the location of the four ‘strain-gauge-meridians’ (W0, W20, M0, M20) and the P0 ‘pressure-sensor-meridian’.

The detailed location of all these sensors is given in paragraph 8. 6. which is the ‘instrumentation’ section.



**Figure 8-10** Picture of a lateral slamming drop test.

Second, for the straight tests the buoy was dropped ‘straight-up’ as is seen in Figure 8-11. Forty bottom tests were done and should be explained in more detail in the doctoral thesis of G. De Backer, foreseen for the end of 2009 [6]. They are not treated here since the calculations (Chapter 5) showed that bottom slamming is less important than breaking wave slamming for survival for these kinds of buoys.



**Figure 8-11** Picture of straight slamming drop test.

### 8. 2. 3. Fracture test

As for the fatigue test, the buoy is tested on its side over a segment of 60 degrees to simulate breaking wave slamming. However, this time the purpose is the determination of the maximum load that the buoy can resist. The set-up is quite the same as for the fatigue test, but another load cell with a higher range (2000 kN) was used since the predicted failure load for the BWF (strongest buoy) was about 1320 kN. A building-up load program was applied.

Now the testing program is situated, the production and instrumentation of the buoys is discussed in detail in following paragraphs.

### 8. 3. DISCUSSION OF THE PRODUCTION PROCESS

#### 8. 3. 1. Introduction

The major topic of consideration was the mandrel that would be used for winding upon. For the current storage silos, SMC uses a special steel mandrel that was designed and built in-house. Yet, it takes time to mount and dismount the mandrel for each silo. Since the production method of the buoys has to be suitable for series production, other options had to be studied.

#### 8. 3. 2. Blow up mandrels

SMC has some experience with the use of a so-called blow-up mandrel. Pictures are shown in Figure 8-12. It can typically be used for up to 100 production runs (i.e. 100 buoys). Also, it can be put in place and removed very fast by inflating and deflating. However, another method explained in the following paragraph, allowed infinite re-use of the mandrel hence there was opted for that one.

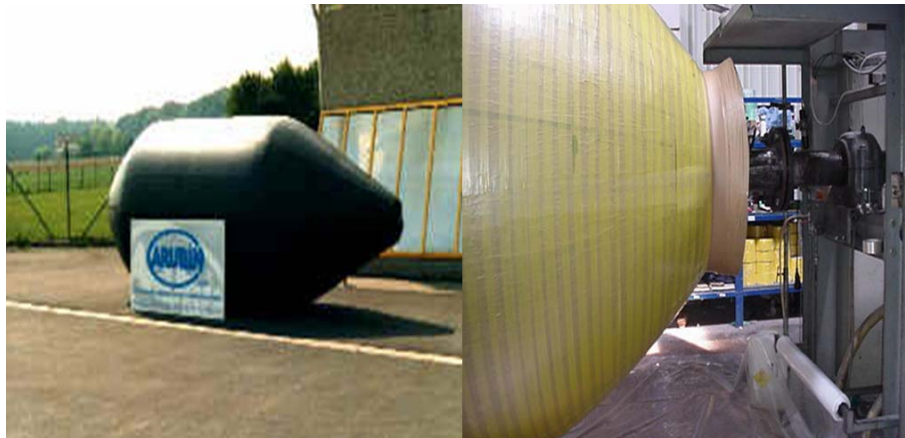


**Figure 8-12** Pictures of a blow-up mandrel.

#### 8. 3. 3. Method of the cones

This method was also used for the production of the laboratory point absorbers as was explained in Chapter 6. It was then called 'the method of the cones' because first two spray-up cones were made on a cone mandrel. Next, to make a buoy, two such cones served as a built-in mandrel for the filament winding process. This is the method of the cones. It was chosen for the production of the two Buldra-scale buoys since the first experience for the production of the small scale point absorbers, was successful. Additionally, once the cone mandrel is made it can be used almost infinitely. The use of the blow-up mandrel stays restricted to about 100 production runs.

## 8. 4. PREPARATION OF TESTING PROGRAM

### 8. 4. 1. Introduction

The planned testing program on the buoys was quite extensive. First, a fatigue test in the laboratory ‘Magnet’ of Ghent University, was done on both buoys. Second, outdoor drop tests were done at the “*Watersportbaan*” in Ghent. Finally, the point absorbers were tested up to fracture, again in the laboratory Magnet of Ghent University.

A preliminary sketch of the indoor support system is shown in Figure 8-13. The buoy needs to be mounted over a steel tube and two supports are holding the structure. A shell (purple in Figure 8-13) was made. Also, a rubber was mounted between the shell and the point absorber to transfer the load to the buoy as uniformly as possible. For these tests the strain gauges on the M0 and M20 meridian were measured.

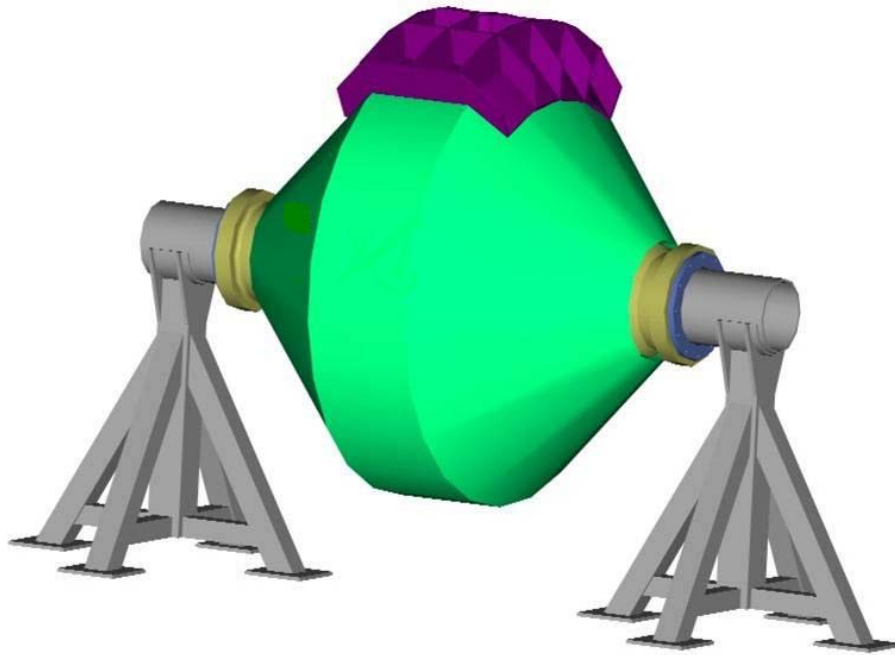


**Figure 8-13** Preliminary sketch of the indoor support setup.

The drop tests were done on the water surface of a canal in Ghent. For these tests the pressure sensors were measured and the strain gauges on the W0 and W20 meridian. A picture of the location of the tests is shown in Figure 8-14. Ghent University has

asked permission to the city administration to perform drop tests at this water leisure park in the south of Ghent. As is seen in Figure 8-14 the area included a road hence was made traffic free. An application form needed to be submitted and some administrative procedures fulfilled but after a relative short time the approval was achieved. This meant that the process for the outdoor tests was officially started.



**Figure 8-14** Location of the outdoor drop tests.

Since the buoys were tested several times in water environment they were designed watertight. Otherwise they would be quite heavy to lift up again. Hence, for these tests two additional ‘closing flanges’ were made to assure this. One side of the buoy is shown in Figure 8-15 (the flange is depicted in red). Two per buoy (one for each edge) are necessary. However, only two of them were made since they were re-used for the second buoy. To have the ability to mount these ‘closing flanges’, two additional ‘fixed flanges’ per buoy were necessary.

Again, one is shown in Figure 8-15. Since those ones were mounted on the buoy during production four had to be made. The ‘when’ and ‘how’ of this mounting is explained in paragraph 8.5.2. Also, a crane was rent to lift the point absorbers above the water at a height that is feasible and corresponding to a certain breaking wave (lateral) or bottom (straight) slamming. Thus, during the production of the flanges it was taken into account that holes should be foreseen for the mounting of lifting eye bolts.

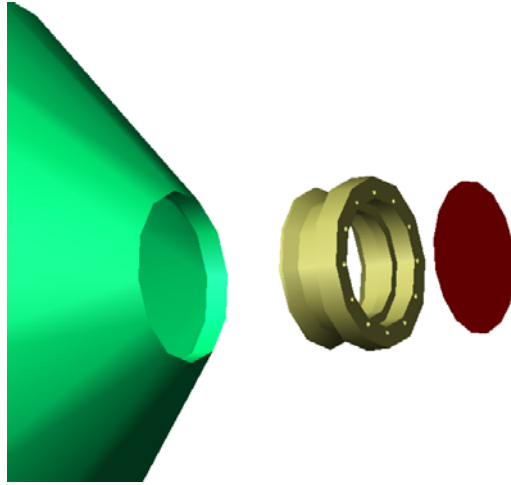


**Figure 8-15** Sketch of a ‘closing flange’ (red) and a ‘fixed flange’ (yellow) to make buoys watertight.

Further, the two buoys were to be dropped several times in water, it was of course preferable that they would float. Watertight buoys are less heavy to lift than buoys filled with water, but nevertheless it is a lot easier to lift a floating buoy than one that has sunk to the bottom. The law of Archimedes (Equation 8-1) states that if the gravity force of an object is smaller or equal to the buoyancy, the object will float.

$$F_g \leq F_b \Rightarrow \text{object floats}$$

**Equation 8-1** Archimedes Law.

With

$F_b$  = Buoyancy

$F_g$  = Gravity force

The buoyancy is the upward force on an object produced by the surrounding liquid or gas in which it is fully or partially immersed. In Equation 8-2 the formula of the buoyancy is given,  $\rho$  is the density of the water which is  $1000 \text{ kg/m}^3$ ,  $g$  refers to the gravitational constant which is  $9.81 \text{ m/s}^2$  and  $V$  is the volume of the buoy.

$$F_b = \rho \times g \times V$$

**Equation 8-2** Buoyancy.

Here, the volumes of both buoys are considered the same since first, the actual difference is small. Second, the value of this difference was not known exactly

before production. And finally, this calculation only serves to know whether or not the buoys will float, in other words an order of magnitude is sufficient. In this case  $V$  is  $2.43 \text{ m}^3$ . The buoyancy is thus  $23.86 \text{ kN}$ .

Next, the mass of the BWF is of course larger than the BWOF. Hence, if the BWF floats the BWOF floats as well. An estimation of the mass of the BWF was about  $500 \text{ kg}$ . To take into account several assets (e.g. closing and fixed flanges) a safety factor 2 is used in this calculation. This means that the gravity force for a buoy of  $1000 \text{ kg}$  equals almost  $10 \text{ kN}$  which is still a lot smaller than the buoyancy. The conclusion of this rapid calculation is that both buoys – once they are dropped on the water – will float.

The preparation for all additional assets follows in the next paragraphs, 8. 4. 2. - 8. 4. 5.

#### 8. 4. 2. Steel support tube

As mentioned in paragraph 8. 4. 1. a steel tube was used as a support for the indoor tests. A sketch of this set up was given in Figure 8-13. The tube should be able to carry the maximum load of the fracture test which was estimated at  $1320 \text{ kN}$ . In Abaqus a steel tube was calculated so that it fulfilled the desired strength. In the model, the material properties of standard steel (st37) were used, which means an E-modulus equal to  $210\,000 \text{ MPa}$  and a Poisson ratio of  $0.3$  [7]. The input dimensions of the steel tube are a length of  $3000 \text{ mm}$  and an outer diameter of  $298.5 \text{ mm}$ . The calculation gives an idea of which thickness was needed for the tube to be able to withhold  $1320 \text{ kN}$ . Standard thicknesses of  $10, 11, 12.5, 16, 18$  or  $20 \text{ mm}$  were available. The model was made as a shell since the thickness of the tube is very small in comparison with its length and diameter. This had the advantage that it was easy to re-calculate the model for several thicknesses. The areas of the red markers are constrained in the X and Z direction and rotation around the Y-axis was also prevented. These supporting areas were modelled as a short half cylinder as is seen clearly in Figure 8-16. The load of  $1320 \text{ kN}$  was simulated as half the load ( $660 \text{ kN}$ ) on each of the two loaded areas of the tube shown in Figure 8-17. The width of the areas was chosen the same size as the (orkot) bearing would have had which is  $50 \text{ mm}$ . The surface is calculated by means of Equation 8-3 which gives half the surface of an open cylinder.

$$S = \frac{1}{2} \times 2 \times \pi \times R \times H$$

**Equation 8-3    Formula for halve the surface of an open cylinder.**

With

$R = \text{radius} = 149.25 \text{ mm}$

$H = \text{height} = 50 \text{ mm}$

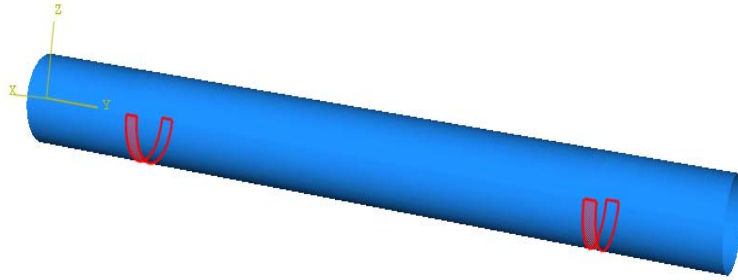


**Figure 8-16** Boundary condition in the steel tube model.

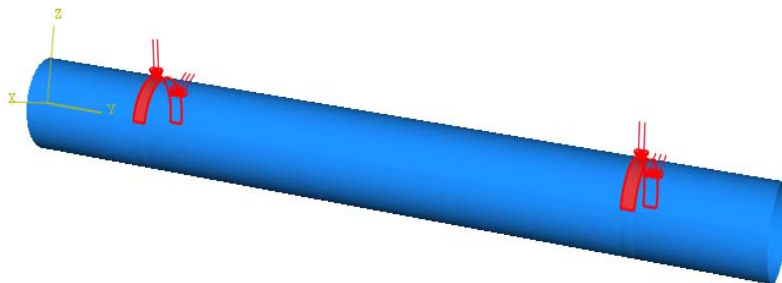


**Figure 8-17** Applied load in the steel tube model.

The surface of one area is  $23\,444 \text{ mm}^2$ . Hence, a pressure was applied on each of those areas of  $28 \text{ MPa}$ . A first FEA calculation was done with a thickness of  $10 \text{ mm}$ . However, the result showed that this kind of tube would be insufficient to carry such a load. For this kind of tube and load, a maximum stress of more than  $300 \text{ MPa}$  ( $336 \text{ MPa}$  as is shown in Figure 8-18) would occur. Since the yield stress of steel is only  $200\text{--}210 \text{ MPa}$ , this tube is insufficient to withhold the foreseen fracture load. Next, a

steel tube of 16 mm was considered. In Figure 8-19 the stress distribution shows that this tube for the estimated maximum load is sufficient.

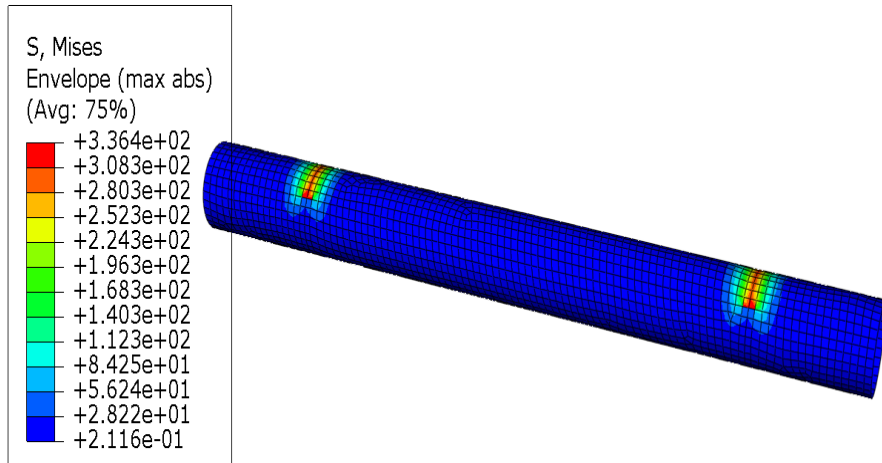


**Figure 8-18** Von Mises stress for a steel tube of 10mm thickness.

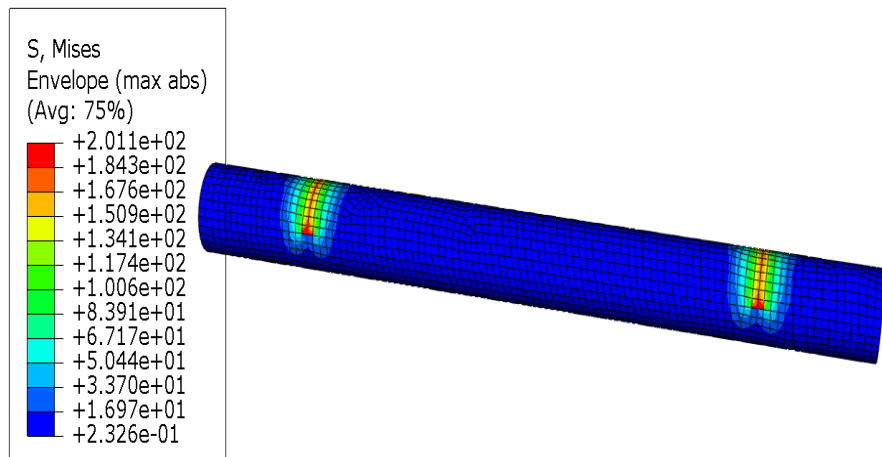


**Figure 8-19** Von Mises stress results for a steel tube of 16mm.

It was decided to order a standard tube of 16 mm. Of course, this calculation gives only an estimation of the expected behaviour during tests of the tube. However, it is sufficient since its purpose is to prevent fracture of the tube.

### 8. 4. 3. Supports

As shown in Figure 8-13, two supports for the steel tube were present. However, in consent with the responsible person from the laboratory Magnel it was decided to deviate slightly from the first sketch. He preferred two large rectangular blocks of

concrete fixed at the ground. In this way, only some smaller supports for the tube had to be delivered by SMC and put on the concrete rectangular blocks. In Figure 8-20 the technical drawing of one of these smaller steel supports is shown. The front plate is shown on the upper left. Two of those plates are used per support for its front and back. On the upper right the side view of one support is given. The top plate is made from a flat plate with dimensions of 1000 x 260 x 20 mm. Next, it had to be curved into the shape of a half circle to fit in the upper part of the support. On the lower left of the figure the ground plate is shown (top view). This plate has a thickness of 20 mm. These plates each have a thickness of 20 mm. The dimensions of a side plate (two of those per buoy) are 290 x 200 x 20 mm.

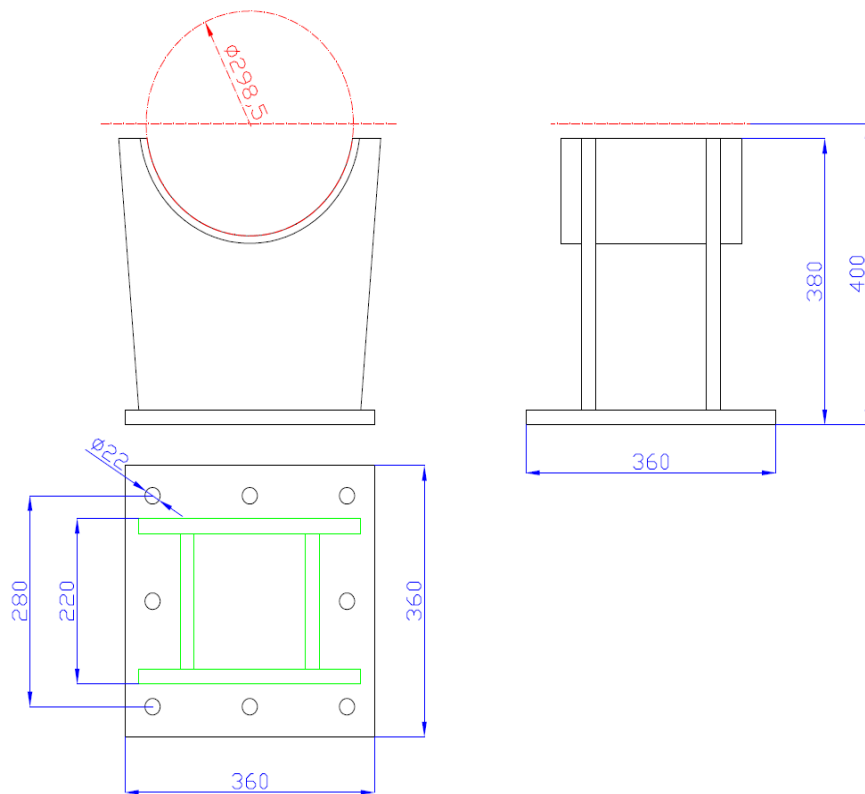


**Figure 8-20** Technical drawing of one support; the ground plate (lower left), front or back plate (upper left) and the side view (upper right).

Again, as for the steel tube, a simplified simulation was done in Abaqus. There, the boundary condition was applied on the ground plate as is shown in Figure 8-21 (left) and does not allow any movement. Again the maximum load is 1320 kN, hence 660 kN for one support. In Abaqus this was applied as a load on the upper surface of the

support as is shown in Figure 8-21 (right). The magnitude of the pressure is achieved by the use of Equation 8-3 (surface of a half open cylinder). In this way the pressure applied on one support is equal to 6.4 MPa. The proposed material was again standard steel (st37) due to reasons of cost. The mechanical characteristics of that isotropic material are an E modulus of 210 000 MPa and a Poisson coefficient of 0.3. The welded joint is of the type SG3, in other words, it has a higher load resistance than the base material itself. Hence, in the model the characteristics of steel were considered. Figure 8-22 shows the calculated distribution of the stresses. The yield stress of steel (200-210 MPa) is higher than the calculated maximum (165 MPa).

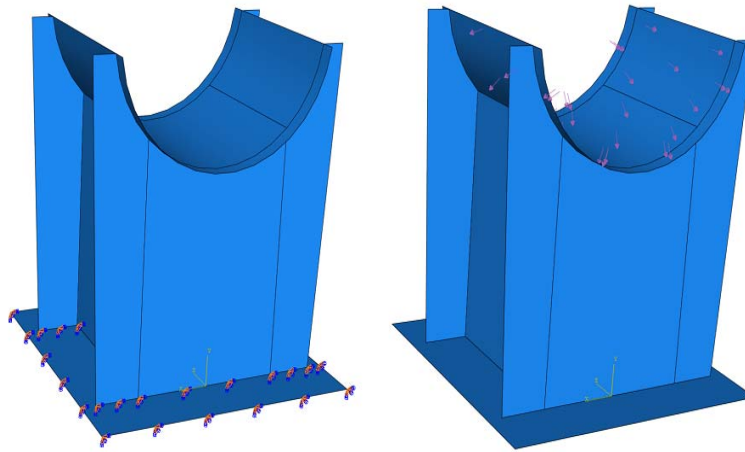


**Figure 8-21** Model in Abaqus displaying the area of the boundary condition (left) and the load (right).

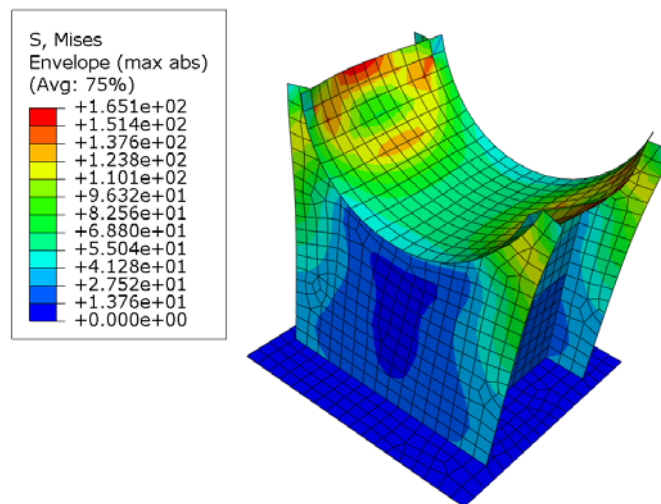


**Figure 8-22** Distribution of Von Mises stresses in a support.

The concrete supports dimensions are  $1 \times 1 \times 0.6 \text{ m}^3$ . Again, the load considered in the FEA calculation is 660 kN. The surface where it is applied is the area where the ground plate of the small support would be situated as is shown in Figure 8-23. This area is  $129600 \text{ mm}^2$  hence the pressure on it is 5.1 MPa. The compressive strength for the used kind of reinforced concrete is 51 MPa after a curing time of 28 days. This is determined by destructive compressive tests in the laboratory Magnel on a cubicle of 150 by 150 mm in the same concrete. The material properties of concrete are an E modulus of 200 MPa and a Poisson coefficient of 0.2. The S11 stresses (downward direction) are given in Figure 8-25 and the maximum is about 2 MPa. The stresses in the other directions are even smaller. As a boundary condition it is chosen to make the ground plane of the concrete block fixed as is seen in Figure 8-24.

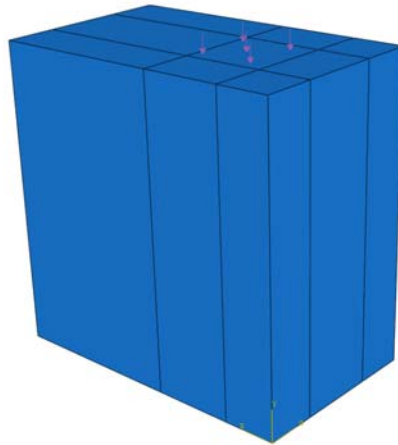


**Figure 8-23** Sketch in Abaqus of the concrete block and the load.

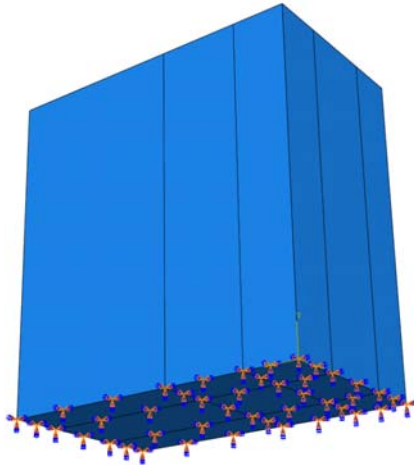


**Figure 8-24** Sketch in Abaqus of the concrete block and the boundary condition.

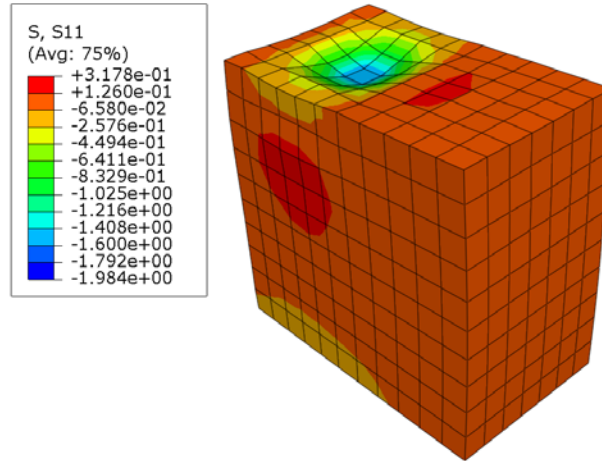


**Figure 8-25** Stresses  $\sigma_{11}$  along the downward direction of the block.

Some pictures of this support system, a concrete block as well as a small support (green) and part of the steel tube, are shown in Figure 8-26.



**Figure 8-26** Rectangular concrete block and small support (green).

#### 8. 4. 4. Shell with rubber

The machine did not have a suitable tool to transfer the load from the actuator of the testing machine to the buoy. It had to transfer this load into a quasi-homogeneous pressure on the desired sector segment of the point absorber to simulate breaking wave slamming. Such a fixture was made and was called ‘shell’ due to its shape. In Figure 8-27 a sketch of the shell is given. The dimensions are similar to the circle segment and length used for simulating breaking wave slamming.

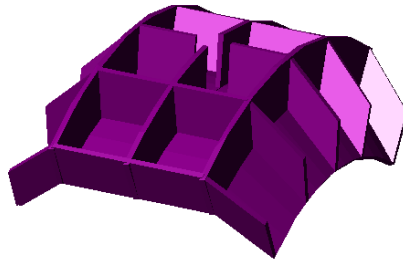


**Figure 8-27** Sketch of the shell.

This fixture should be very rigid. Hence, the shell was made in standard steel (st37). However, to distribute the pressure as homogeneous as possible, an air cushion or a rubber layer should be used between the fixture and the point absorber radius. Existing air cushions were not able to handle the maximum load. And, even more crucial, in the shape that was desired no supplier would guarantee even lower working conditions. Hence, it was decided to choose for a rubber layer of 30 mm. It had a fracture resistance of 3.5 MPa. Enough rubber was foreseen for the two buoys. A picture of the set up (with part of the buoy, rubber, shell and actuator) is given in Figure 8-28.



**Figure 8-28** Shell in real set-up in laboratory Magnel.

For validation purposes the rubber and the shell were taken into account in a new finite element model. The whole model is depicted in Figure 8-29. The shell is depicted in blue and is simulated as a rigid structure. There, a vertical force of 300 kN was applied for the comparison with the fatigue tests. For the fracture tests a load of 1320 kN was applied when comparing fracture of the BWF and 880 kN when comparing fracture of the BWOF.

The rubber is depicted in orange. Special about rubber is that it shows a hyper elastic behaviour. Within Abaqus it is possible to use the Arruda-Boyce model for this where values of nominal strain and stress can be given. Within Abaqus it is necessary to use a hybrid mesh for this kind of material. For this model, test results on an 8% sulphur rubber, previously done at the department, were used. This biaxial data can be found in [8]. There the initial E modulus is about 2.2 MPa. For the used rubber this was 5.2 MPa. Still, there was decided to perform the calculations with the known biaxial data since this data was not available for the used rubber. The thickness of the rubber was determined by applying the 1320 kN. There, the occurring stresses had to be lower than the fracture resistance of the rubber; 20 mm seemed sufficient but for safety matters three pieces of 10 mm rubber were used per buoy.

The buoy is shown in grey. Also, the two red circles mark the locations of the boundary conditions. One side of the buoy is kept fixed while the other side allows an axial movement.

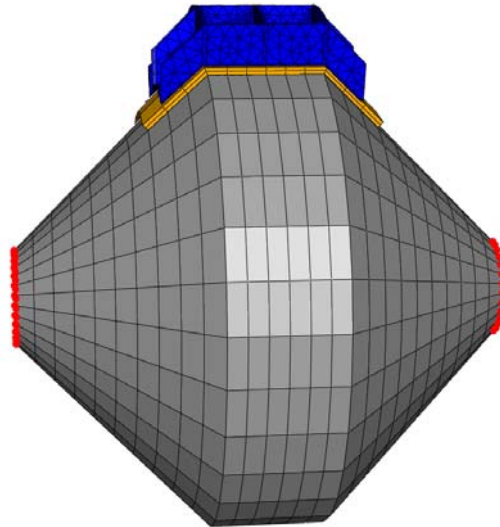


**Figure 8-29** Finite element model of the buoy with shell and rubber.

In this model there are two contact conditions applied: one between the shell and the rubber, and one between the rubber and the buoy. For both the contact condition ‘surface to surface’ in Abaqus was applied. Also for both, the rubber was the slave surface and respectively the shell or the buoy the master surface. The friction coefficient used for the contact condition between the steel shell and the rubber mat

was 0.5, the one used for the contact condition between the rubber and the composite buoy was 0.2.

#### 8. 4. 5. Flanges

Two kinds of flanges had to be made: the ‘fixed flanges’ and the ‘closing flanges’. Figure 8-1 showed the full technical drawing of the BWF. Now, in Figure 8-30 the location of the bearings is magnified. Also, holes were foreseen in the flanges for lifting eyebolts as was explained in paragraph 8. 4. 1. It is seen on the technical drawing of the side view in Figure 8-31 that this has been taken into account. The outer holes were meant for lifting eye bolts during tests. In paragraph 8. 6. 3. it is explained how these holes were also used as a means to know the location of the inner strain gauges *after* the buoy was fully produced. The inner holes served to fix the closing flanges on the buoy.

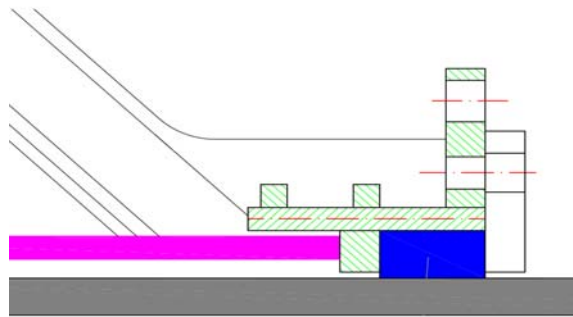


**Figure 8-30** Location of a ‘fixed flange’.

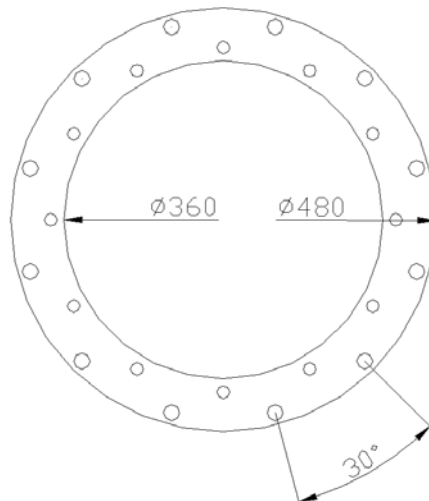


**Figure 8-31** Technical drawing of the front view of the fixed flange.

As was shown in Figure 8-30 the fixed flanges serve as a bearing housing for the orkot material. Bearings in general need a very accurate finishing (for tolerances and surface roughness). First, for the real wave energy converter, it was proposed to use flanges out of stainless steel with a turning machine. Hence, it is possible to achieve tolerances of some hundreds of mms. Of course these are very expensive pieces since the dimensions are quite large.

Within the testing program, the focus was the buoy and no sea experiments were done. Thus, it seemed logical to accept lower quality for the flanges in this case. Hence, the flanges used for the 'Buldra-scale' buoys were fabricated in a cheaper manner, namely a combination of welded and rolled plates of stainless steel 304 was applied. In this way, the flanges had almost the same strength but the finishing is insufficient for a bearing that has to last for a large amount of working hours.

## 8. 5. PRODUCTION OF THE BULDRA-SCALE BUOYS

### 8. 5. 1. Introduction

In this paragraph, the actual production of the buoys is discussed and pictured. The discussion starts from the making of the cones on a new conical mandrel, moves via the mounting of all separate assets to the buoy, the winding, the inclusion of the foam for one of the buoys and finally concludes with the end result of both coated and marked buoys.

### 8. 5. 2. Spray-up cones

The actual production of the two point absorbers was started with the fabrication of four cones. First, a mandrel suitable for this fabrication was made. This mandrel is shown in Figure 8-32 and was made out of standard steel (st37) from a plate which is rolled and then welded together.



**Figure 8-32** Mandrel for spray up cones.

Second, with the use of this mandrel four spray-up cones (of chopped glass fibres) with a thickness of 4 mm were produced. A picture of such a cone is shown in Figure 8-33. Next, in this stage of the production, the four ‘fixed flanges’ were fixed to the spray-up cones with glue (Plexus MA422 [9]) as is shown in Figure 8-34.

Composite floating point absorbers for wave energy converters



**Figure 8-33** One of the four spray up cones.

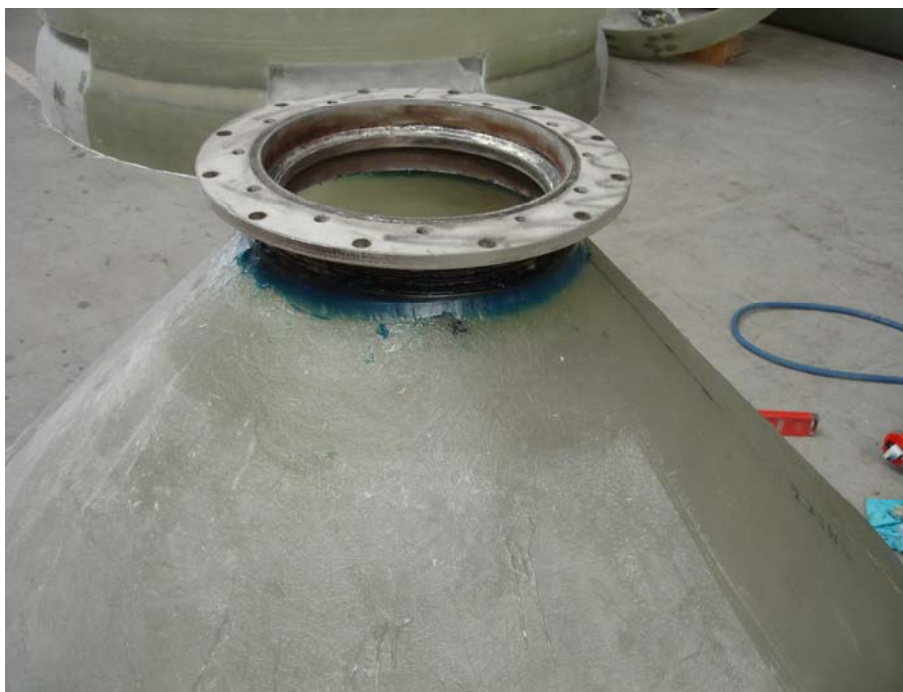


**Figure 8-34** 'Fixed flange' glued on a spray up cone.

### 8. 5. 3. Inner composite tubes

The making of composite tubes is a standard procedure at SMC [10]. Two tubes were made, one for each buoy. As explained in paragraph 8. 1. 2. they have four cross wound layers of 46/-46 degrees. This results in tubes of about 10 mm thickness. In Figure 8-35 (left) the production of such a tube on the winding machine is shown. Also, the finalised tube is given in Figure 8-35 (right).



**Figure 8-35** Production of composite tube (left) and finalised tube (right).

### 8. 5. 4. First winding phase

At this stage the four cones were ready. Next, the inner strain gauges were mounted as will be explained in paragraph 8. 6. 3. Each cone was connected with a fixed flange. Also, two inner composite tubes were ready for use. Finally, the steel tube - which was meant to be used during the indoor tests - also had another purpose. As is shown in Figure 8-36 two of the cones are glued together (with Plexus MA422) and formed one part.

Next, this part is mounted over the steel tube and fixed to it with the aid of a lifting eye bolt on each side. This assembly was mounted on the winding machine in SMC. Then the winding of the buoy could start. The first four layers of the BWF and of the BWOF were produced in exactly the same way. Figure 8-37 gives an action picture of the buoy on the winding machine.

In paragraphs 8. 5. 5. and 8. 5. 6. the next steps in the production of the BWF (and BWOF) are discussed. However, the reader should keep in mind that the BWOF does neither contain any foam nor composite layer five. Hence, these steps are not executed for that buoy. All the other steps are similar for both.



**Figure 8-36** Assembly of two cones, one inner tube and the steel tube.



**Figure 8-37** Action picture of the winding of the point absorber.

#### 8. 5. 5. Foam

For the BWF a foam layer of 30 mm had to be added after four layers were wound. The buoy was dismantled of the winding machine because it was easier in this way to glue (with 1152PA from Scott Bader) the foam onto the buoy. A picture of the situation half way this task is shown in Figure 8-38.



**Figure 8-38** Fixing the foam to the BWF.

#### 8. 5. 6. Second winding phase

After the foam was fixed to the BWF, the buoy was again mounted over the steel tube on the winding machine. A second phase of winding could start immediately. Now, the same four layers (named layer 5 up to layer 8) as in the first phase were wound but in reverse order. A picture of the BWF in the second winding phase is given in Figure 8-39. Note that for the BWOF the buoy does not need to be dismantled since the foam phase does not exist for this one. Also, layer five is skipped there and after the first four winding layers that buoy continuously goes on with its (second) winding phase which only consists out of three more layers, namely layer six up to layer eight.



**Figure 8-39** Second winding phase on BWF.

### 8. 5. 7. Coating and markers for the high speed camera

It was decided to give a white top coat (isophthalic polyester gel coat ral 9010 [11]) and black markers (aerosol paint) to the buoy as is seen in Figure 8-40. These colours give a very good contrast in movies made by the HSC.



**Figure 8-40** Buoy with white coating (left) and black markers (right).

### 8. 5. 8. Feedback of production towards FEA

The BWOFF and the BWF were the first buoys to be made in this way. Since no experience was available it seemed useful to measure the thicknesses of each buoy for feedback towards the FEA calculations. However, due to the fact that the winding production method was used, the thickness varies along the axis of the structure. In other words the nearer towards the top side of the cones the thicker the buoy is. Nevertheless it was decided to measure only the thickness of the cylindrical part of the buoy after each layer since that larger region is the most crucial one for failure.

It became clear that the BWOFF was made a bit thicker in reality than in the simulations. Hence, some additional FEA calculations had to be done for the BWOFF. The adjusted thickness is shown in Figure 8-41 and is a more correct estimation. Through trial and error the new estimated fracture was reached at a load of 880 kN placed on the shell.

For the BWF the total difference between the real buoy and simulations was smaller than 2 mm. The difference per layer was not measurable. Since even the total measured difference is very small no additional calculations for that buoy were done.

The real mass of the BWF was 520 kg and 390 kg for the BWOF.

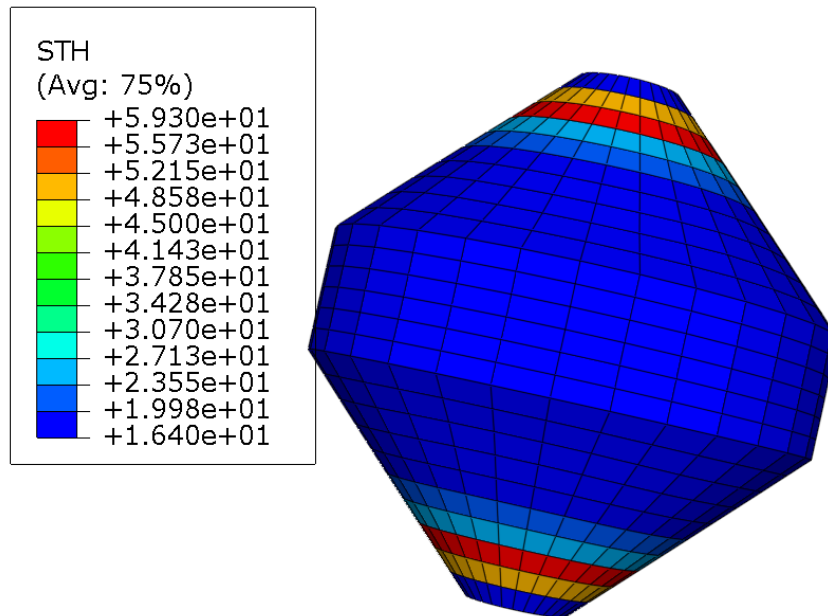


**Figure 8-41** More correct estimation of the real thickness of the BWOF.

## 8. 6. INSTRUMENTATION OF THE LARGE SCALE BUOYS

### 8. 6. 1. Introduction

The instrumentation of the buoys is strongly dependent on the kind of experiments done. For the fatigue and fracture tests ‘Linear Variable Differential Transducers’ (LVDT sensors) and strain gauges were mounted. The LVDT sensors were used to measure the displacements and the strain gauges to measure the deformations. The force was measured through the use of a load cell. For the outdoor drop tests, strain gauges, pressure sensors, a shock accelerometer and a HSC were used. The strain gauges used for the drop tests were not the same ones as those used for the indoor tests again to increase their survivability as is explained in paragraph 8. 6. 3. The two buoys are instrumented in exactly the same way. An overview of all used sensors for the indoor (fatigue and fracture) and outdoor (drop tests) experiments per buoy is given in Table 8-1.

	Fatigue & fracture test	Drop tests
<b>LVDT sensors</b>	5	0
<b>Strain gauges</b>	14	24
<b>Pressure sensors</b>	0	5
<b>Accelerometers</b>	0	1
<b>HSC</b>	0	1

**Table 8-1 Overview of used sensors for indoor and outdoor tests for one buoy.**

### 8. 6. 2. LVDT sensors

The LVDT sensors (of the brand ‘Solar’) were used for the indoor tests. Five of them were installed and this was done after the buoy was mounted in the testing machine as is shown in Figure 8-42.

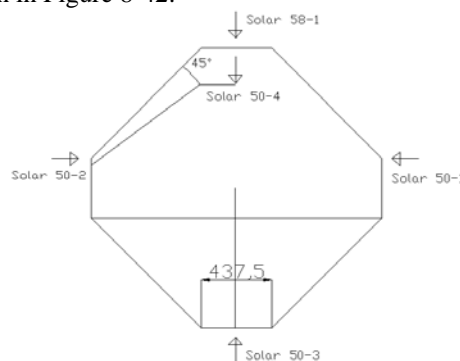


**Figure 8-42 Position of the LVDT sensors.**

The two horizontal ones were mounted for safety reasons: as soon as large displacements should occur there, it could be an indication that the flanges were loosening.

Some differences in this configuration occurred during the four (two fatigue and two fracture) indoor tests. However, this is explained further when the results of the LVDT sensors are discussed in Chapter 9.

### 8. 6. 3. Strain gauges

During all tests, strain gauges were measured. However, it is possible to make a distinction between the indoor and outdoor tests.

For the indoor fatigue and fracture tests there were twenty channels available for reading out measurements. This was a fixed number since those tests were outsourced to another department of Ghent University. One channel was used for the measurement of the force as a check up. Additionally, at least four channels were used for LVDT sensors. Two of those were included especially for safety reasons as was explained in paragraph 8. 6. 2.

In respect to this, fifteen channels were left for the measurement of strain gauges. It was desirable to measure both a longitudinal strain gauge and a perpendicular one at the same position. Hence, an even number was chosen, namely fourteen. Those strain gauges were mounted on the inner side of the point absorbers to increase the chances of survival during the outdoor drop tests. After all, the indoor fracture test still had to be done as a final test, preferably with at least quite some working strain gauges. Since they were mounted on the inner side, this was done during production after the four spray-up cones for the two buoys were made. Figure 8-43 shows such a spray-up cone with mounted strain gauges.



**Figure 8-43** Pictures of the mounted inner strain gauges.

At all positions, which are shown in Figure 8-44, a longitudinal (along the axis of the buoy, labelled with 'L') and a perpendicular one (perpendicular to the longitudinal, labelled 'D') were mounted. For the outdoor tests, another fourteen inner strain gauges were mounted, this time on the 'lower' side of the point absorber in this position. Also, it was decided to position them within the other cone-end as is seen in Figure 8-45 to prevent disorder of cables.

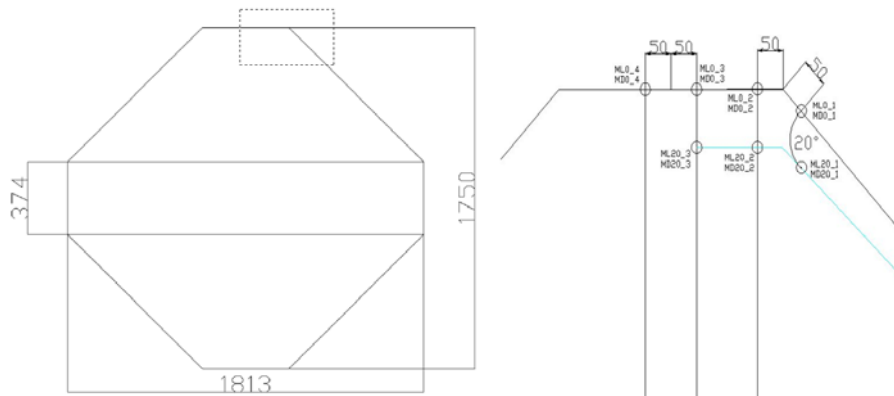


**Figure 8-44** Position of the strain gauges for the indoor tests.

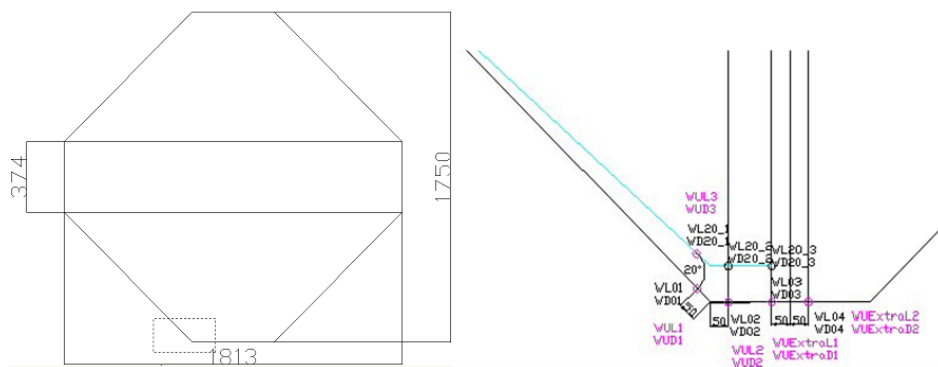


**Figure 8-45** Position of strain gauges (inner and outer) for outdoor tests.

The positions of the strain gauges were chosen near to the transition cone-cylinder due to the fact that this is one of the most critical zones. Once the 'fixed flanges' were mounted to the cones, the meridians of 0 and 20 degrees (upper for Magnel hence M and lower for Watersportbaan hence W) were marked on those flanges as is shown in Figure 8-46.



**Figure 8-46** Marked meridians on flange.

As mentioned in paragraph 8. 4. 5. those flanges were mounted on the cone in this way that one of the outer holes of the flange falls on the 0 meridian. The marking was done because otherwise the position of the strain gauges would be unknown as soon as the point absorbers were wound.

For the outdoor tests, twenty measurements channels were available for the reading out the strain gauges, so more were mounted on the outer side of the buoys once they were produced. Again, as for the indoor tests, all strain gauges were mounted in pairs (a longitudinal and a perpendicular one). A picture of the five pairs of outer strain gauges is shown in Figure 8-47.



**Figure 8-47** Buoy with the five pairs of outer strain gauges.

They were already given in Figure 8-45 and marked with a 'U'. As such, instead of six (together with the fourteen inner ones this would make twenty) ten strain gauges were mounted on the outer side of each buoy. In this way four 'extra' strain gauges were available for use as soon as one of the others should fail during tests. The used cables for all strain gauges are of the type 7-2-36-C. A picture is shown in Figure 8-48.

These cables were fixed on the inner side of the point absorber to prevent rotating during winding. Next, for the fatigue test they were guided outside through a hole in the point absorber near the flanges. This hole was made water tight again during the outdoor drop tests with 'Power Fix', two components glue.

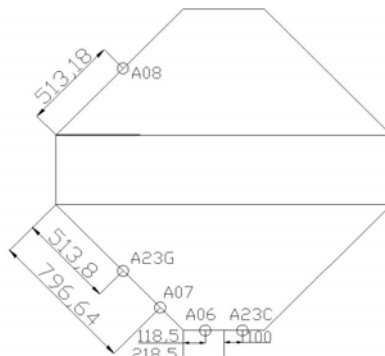
### Type 7-2-xxC



**Figure 8-48** Used cables to mount strain gauges.

#### 8. 6. 4. Pressure sensors

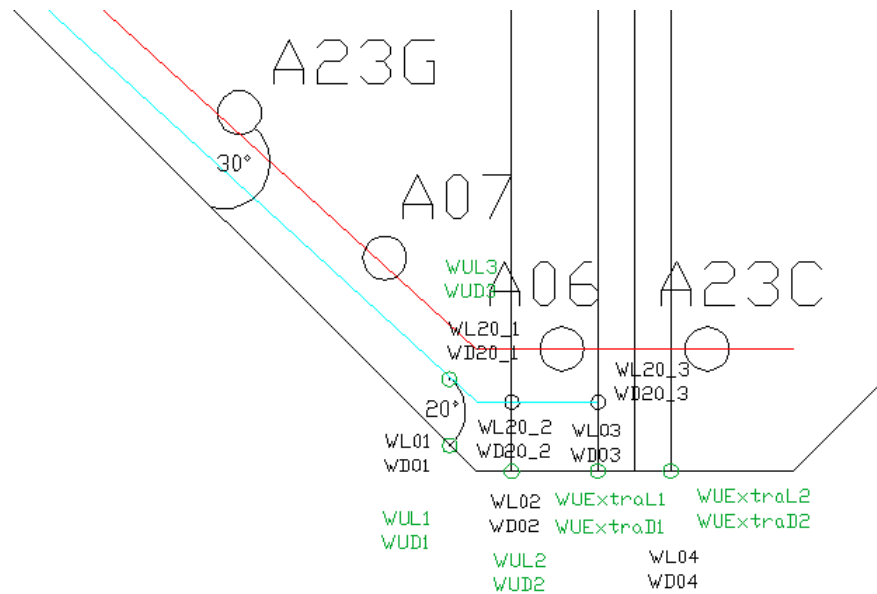
Five pressure sensors were used during the outdoor test on each buoy. The position of those sensors with their respective name is shown in Figure 8-49.



**Figure 8-49** Positions of the pressure sensors.

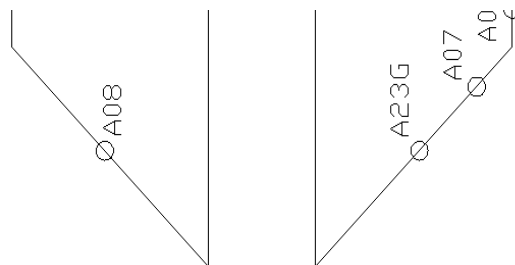
The buoy in Figure 8-49 is turned 30 degrees to the front in comparison with the one for the strain gauges. This can be noticed more clearly in Figure 8-50 where the buoy is pictured with again the W0 meridian at the lower side. In comparison with

Figure 8-45 the meridian of the pressure sensors is added. It is shown that four of the pressure sensors are positioned on a meridian 30 degrees *in front* of the W0 line while the strain gauge 20-meridian was 20 degrees *after* the W0 line. To fix thoughts, look at Figure 8-9 again. For the lateral slamming the A07, A06 and A23C were used. The different properties for these sensors were explained in Chapter 7.



**Figure 8-50** Relative position of pressure sensors to the W0 meridian.

The fifth pressure sensor A08 is used only for the bottom drop test. Hence, the buoy falls straight into the water as is shown in Figure 8-51. Sensor A08 is positioned 180 degrees of the sensor A23G. For the bottom drop tests the A08, A23G and the A07 were installed.



**Figure 8-51** Position of the pressure sensors used for bottom drop tests.

The mounting of the sensors was the same as for the laboratory tests, namely with tubes foreseen of inner screw thread. The cables are also guided together with the cables of the strain gauges. For the tests on the Watersportbaan that hole is filled up with glue to prevent entry of water.

#### 8. 6. 5. Accelerometers

A shock accelerometer of 500g was used. This is sufficient for this application and it is depicted in Figure 8-52.



**Figure 8-52 Shock accelerometer 500g.**

A small cubicle of PVC was made and the accelerometer was mounted on it so that it could be used in lateral and bottom slamming tests with very few necessary changes for each set up.

#### 8. 6. 6. HSC

With the HSC high speed movies were made during all tests. The impact velocity is calculated with the help of a Labview program (made by T. Versluys from the Department of Coastal Engineering). Within the program, the resolution of the movie, namely the number of mm per pixel is necessary input. Next, a marker is followed: its displacement is measured in time and the velocity at impact is calculated. Since the view angle of the camera is not always the same, these measurements are only used as a validation of the shock accelerometer.

---

## 8. 7. REFERENCES

1. SEEWEC - Sustainable Economically Efficient Wave Energy Converter. Sixth Framework Program (FP6), Specific Targeted Research Project (STREP), Priority 6-1: Sustainable Energy Systems, 2005-2008(contract nr. SES6-CT2005-019969).
2. DSM Product Data Sheet. 03/2005 [cited 2006 24/04]; Available from: [http://technicaldocuments.dsm.com/product\\_finder/technical\\_documents/DR/level10/DR\\_DRS\\_00000000006317\\_PDS\\_en\\_.pdf](http://technicaldocuments.dsm.com/product_finder/technical_documents/DR/level10/DR_DRS_00000000006317_PDS_en_.pdf).
3. 3B the fibre glass company - Product Data Sheet: Advantex, R25H Direct Roving for Filament Winding and Pultrusion Operations. Available from: [http://www.3b-fibreglass.com/files/docs/R25H\\_Dec\\_2008.pdf](http://www.3b-fibreglass.com/files/docs/R25H_Dec_2008.pdf).
4. K. Stoop and S. Vermeulen, Numerieke simulatie van de vloeistof-structuur interactie bij hydrodynamische impact, Ghent University. Faculty of Engineering, Master thesis academic year 2007-2008.
5. J. Degroote, C. Blommaert et al., Partitioned simulation of the impact of a deformable composite cylinder on a water surface in International Conference on Computational Methods for Coupled Problems in Science and Engineering. June 2009: Italy.
6. G. DeBacker, PhD in preparation, Ghent University, Faculty of Engineering, foreseen for end 2009, Optimisation of a wave energy converter for south Nordsea conditions.
7. J. Degrieck, Composieten, Course at Ghent University, Faculty of Engineering. 2006-2007.
8. D. Standaert and J. Goethals, Ontwikkeling van een crash-platform voor extreme impactbelastingen, Ghent University. Faculty of Engineering, Master thesis academic year 2006-2007.
9. Product Data Sheet - Plexus MA422. Available from: <http://www.plexusiasia.com/TDS/MA422%20TDS.pdf>.
10. Spiromatic. [cited 2006 25/04]; Available from: [www.spiromatic.com](http://www.spiromatic.com).
11. Polyprocess GEL COAT Type GCIM series W. Available from: <http://www.polyprocess.fr/>.



## Chapter 9

### LARGE SCALE BUOYS: EXPERIMENTS

*In this chapter, relevant results of all large scale tests are discussed in the following order: fatigue, lateral slamming, bottom slamming and fracture test. Within this doctoral thesis the focus lays on the lateral slamming, hence also the testing program had its focus on that kind of experiment. This is due to the fact that from the material and production point of view the lateral slamming is a more critical load. Still, within the test program, a number of outdoor bottom slamming tests were included.*

#### 9. 1. FATIGUE

##### 9. 1. 1. Introduction

In this test, the point absorber is loaded in fatigue at the set-up in the laboratory Magnel of Ghent University. As mentioned in Chapter 8, the buoy is loaded on its side, over a sector segment of 60 degrees which is an experimental simulation of the repeated breaking wave slamming. A picture of the set up is given in Figure 9-1.



**Figure 9-1** Picture of a buoy in the fatigue set up.

The yearly storm (defined in Chapter 3) was considered to have a period of 6 seconds, duration of 24 hours per year and the buoy should have a lifetime of 25 years. This results in an amount of 360000 cycles. A load of 340 kN on the surface of a made rigid shell was used to simulate the pressure of the yearly storm in that sea climate (according to the DNV standard as explained in Chapter 3). This load was transferred as uniformly as possible via the shell and the rubber onto the buoy. The machine was able to perform a little faster than 1/3 Hz. This means that one fatigue test lasted somewhat less than 1080000 s which is equal to 300 hours or 12.5 days.

For this test the load was measured, fourteen strain gauges were read out and also five LVDT sensors. From previous experience at our department it is known that signals of strain gauges have the tendency to drift under fatigue load. This was known due to previous experience with measurements of strain gauges in fatigue in the research group [1]. However, it seemed useful to measure them anyway, to compare the measurements at start with finite element simulations and to assess the measurements near half and ending time in terms of their amplitude. In this paragraph the results of those three kinds of sensors are discussed. As was explained in Chapter 8, for the experiments at Magnel a more extensive finite element model was made inclusive the shell and the rubber. The measurements were compared with that simulation. Hence, for fatigue, a force of 340 kN was applied in that model.

### 9. 1. 2. Load

In Figure 9-2 a typical load signal is given with duration of more than one hour. At first sight this signal seems quite strange since there are parts containing lots of data and parts containing apparently none. However, the explanation for this is straight forward. It was foreseen to have this type of signal. The whole fatigue test was considered as a very long test (about 12.5 days) and the measurement of the signals was done at 10 Hz hence the data would build up quite fast. Therefore it was decided to measure periodically only part of the whole testing time. This was done in the following way: for five minutes long everything was registered at 10Hz, next ten minutes nothing was registered, etc. In this way, only one third of the experiment was measured. Within Figure 9-2 this sequence is clearly seen. In Figure 9-3 a magnified part of five minutes measurement of the fatigue test at 1/3 Hz with  $F_{\min}$  equal to 100 kN and  $F_{\max}$  equal to 340 kN is shown. As explained before, this maximum load simulates the DNV breaking wave slamming load for the 1 year storm condition in the proposed sea climate. The signal of 1/3 Hz is accelerated in comparison with the reality. However, taken the experience of our research group with fatigue 1/3 Hz should not have any influence on this kind of composite material.

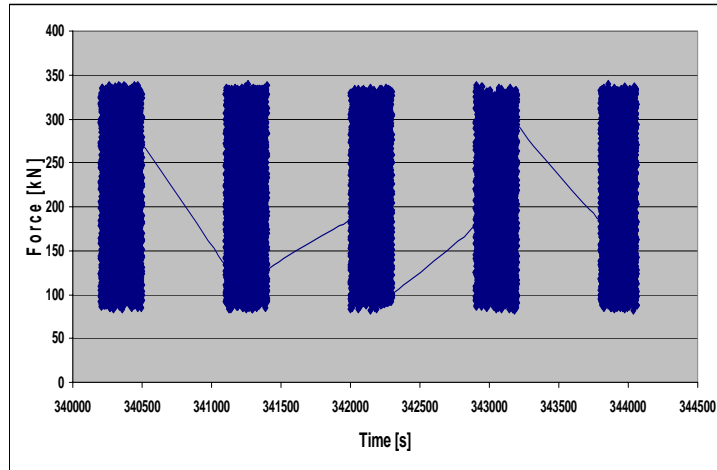


**Figure 9-2** Fatigue test; Measured force signal over more than one hour.

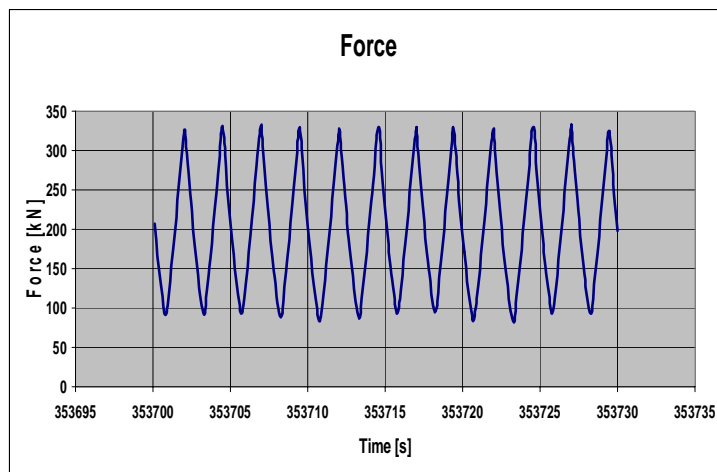


**Figure 9-3** Force fatigue signal at 1/3 Hz with  $F_{\min} = 100$  kN and  $F_{\max} = 340$  kN.

### 9. 1. 3. Strain Gauges

Second, the signals of the fourteen Magnel strain gauges, labelled 'M' are discussed. To simplify the results of those signals they are divided in three groups as is shown in Figure 9-4. The first two groups are the strain gauges of the zero degrees meridian: one with the strain gauges on or near the cone and one with the strain gauges on the cylinder. The third group is the one of the 20 meridian strain gauges. These groups are chosen because the difference between the signals and the finite element calculations show the same trend. Each group of signals is given for the BWF and the BWOE. However, even though there are only measurements for one third of the full duration of the experiment there is still a lot of data available. This is

solved by giving the results at three different times during the test. In that way it is possible to notice whether or not there is a significant difference in strain during the fatigue test. The chosen times are situated in the beginning (first hour), somewhere before the middle (5.5 days) and somewhere near the end of the test (maximum 12.5 days depending of the testing speed that the machine could handle which is a little faster than 1/3 Hz). As mentioned, the measurements at start (first hour) are used for comparison with finite element analysis. Those are the values entered in Table 9-1 for the BWF and in Table 9-2 for the BWOE which are the peak strains with their respective sign (+ for tensile, - for compressive strain) near start.

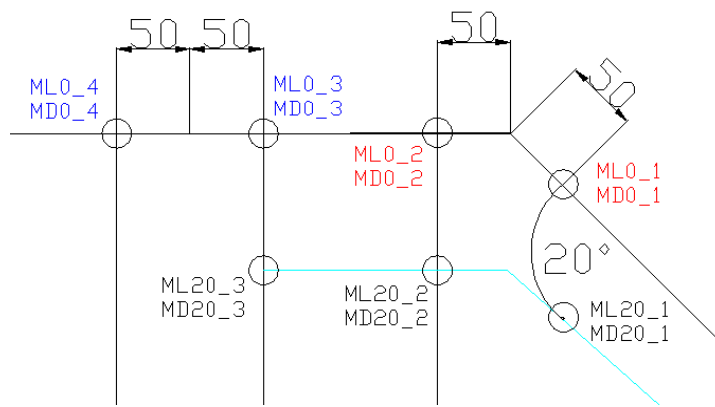


Figure 9-4 The inner ‘Magnel’ strain gauges divided in three groups.

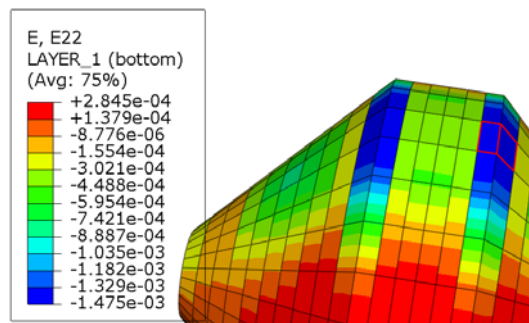
	BWF (experimental; microstrain)	BWF (calculations; microstrain)	BWF (percentage)
ML0_1	-800	-1500	87
MD0_1	800	1700	112
ML0_2	-800	-1500	87
MD0_2	550	1700	209
ML0_3	-2100	-600	-71
MD0_3	-1600	-700	-56
ML0_4	-1300	-600	-54
MD0_4	-2000	-700	-65
ML20_1	-900	-1300	44
MD20_1	900	1500	67
ML20_2	-700	-1300	86
MD20_2	1400	1500	7
ML20_3	-700	-600	-14
MD20_3	-600	-500	-17

Table 9-1 Summarised results of the BWF in microstrain of strain gauges during fatigue test; ‘percentage’ is defined as 100\* (value\_calculations – value\_experiments)/value\_experiments.

	BWOF (experimental; microstrain)	BWOF (calculations; microstrain)	BWOF (percentage)
ML0_1	-1000	-2600	160
MD0_1	800	900	12
ML0_2	-1400	-2600	86
MD0_2	800	900	12
ML0_3	3300	450	-86
MD0_3	-900	-600	-33
ML0_4	1300	450	-65
MD0_4	-900	-600	-33
ML20_1	-1100	-1800	64
MD20_1	1200	750	-37
ML20_2	-1300	-1800	38
MD20_2	1000	750	-25
ML20_3	300	450	50
MD20_3	-500	-500	0

**Table 9-2 Summarised results of the BWOF in microstrain of strain gauges during fatigue test.**

There it is seen that some of the strain gauges measure higher strains than calculated and vice versa. Nevertheless it has to be kept in mind that the simulated rubber differed from the used one (due to few availability of rubber data) while the shell was assumed as rigid. Hence the order of magnitude is in agreement with FEA. The signs are correct in all zones while the over/under estimation is consistent per zone of the buoy. Within this paragraph a more detailed discussion is given per zone for the two buoys. In Figure 9-5 the simulated longitudinal strain distribution is given for the BWF and in Figure 9-6 the transverse strain. These distributions are always (unless mentioned) given in the cylindrical axes system where the longitudinal direction is axial and the transverse direction tangential. The red squares mark the location of the first group.



**Figure 9-5 Longitudinal strain distribution of the BWF; the red squares are the location of group one.**

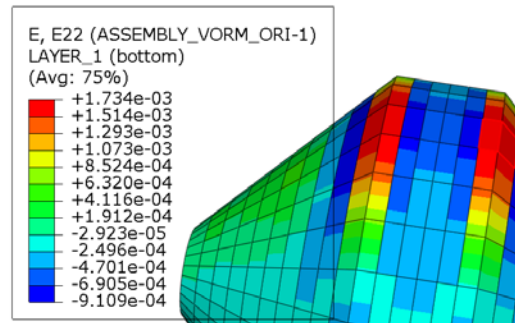


**Figure 9-6** Transverse strain distribution of the BWF; the red squares are the location of group one.

For the longitudinal strain gauges mounted on the cone part of the buoy it is better to use a local axes system along the cone. However, the result for the ML0\_1, which is about -1500 microstrain and which is depicted within the red square in Figure 9-7, does not differ a lot from the one depicted in the cylindrical axes system, also about -1500 microstrain, of Figure 9-5.

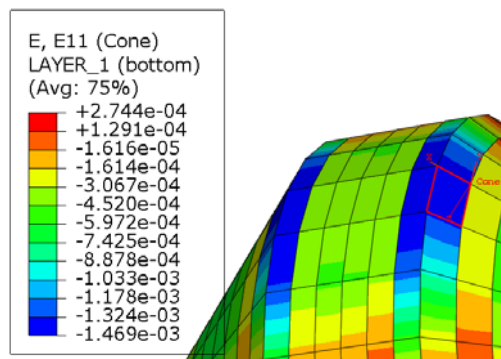


**Figure 9-7** More correct ML0\_1 value in the local axis system along the cone.

The BWF signals of the first group of strain gauges (ML0\_1, MD0\_1, ML0\_2 and MD0\_2) are given at three different times in Figure 9-8 (near the start of the test), Figure 9-9 (middle) and Figure 9-10 (end). The signals near starting time match with the trends in the finite element calculations; however the latter over predicted the values with about a factor two (100 %). In the signals near half and ending time there seems to be drift as was expected. This was expected due to previous experience with measurements of strain gauges in fatigue in the research group [1]. However, out of the measurements it can still be concluded that some amplitudes increase (ML0\_2 and MD0\_2) which means more deformation and others decrease (ML0\_1 and MD0\_1) which means less deformation.

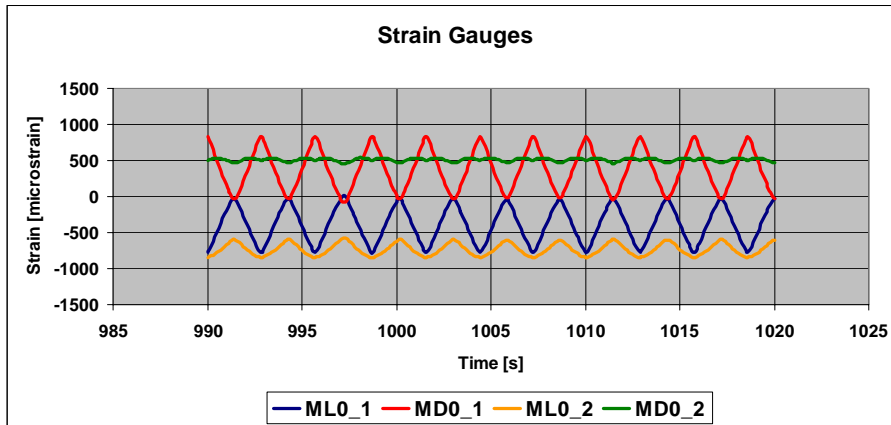


Figure 9-8 BWF fatigue; signals of four strain gauges at start; ML0\_1, MD0\_1, ML0\_2 and MD0\_2.

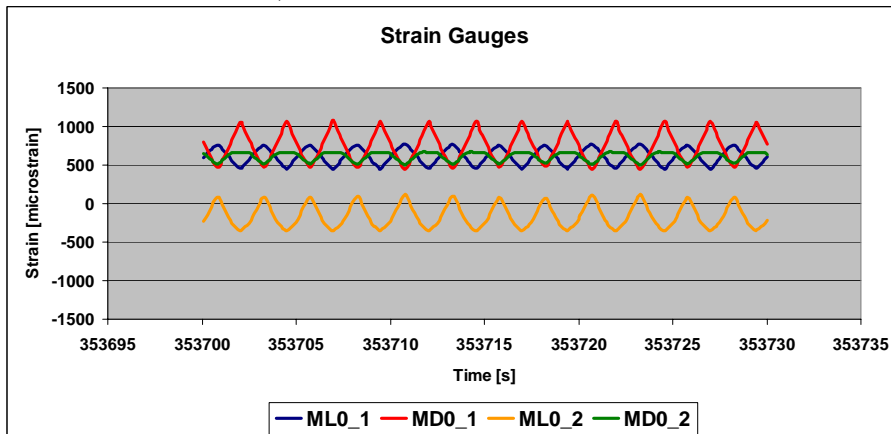


Figure 9-9 BWF fatigue; signals of four strain gauges just before half-time; ML0\_1, MD0\_1, ML0\_2 and MD0\_2.

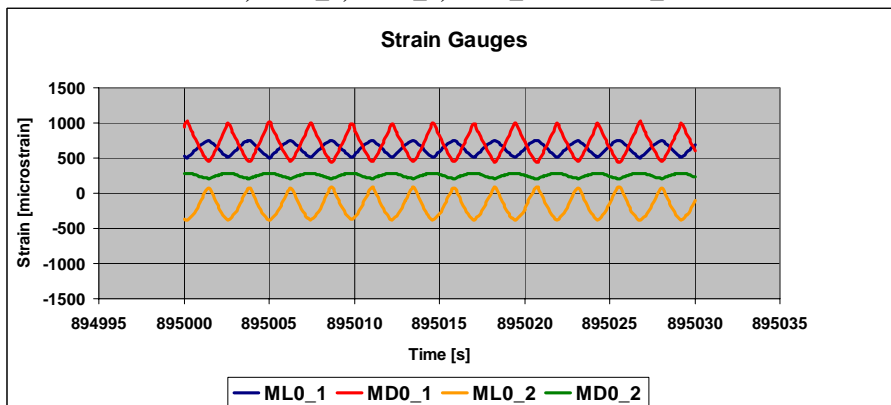
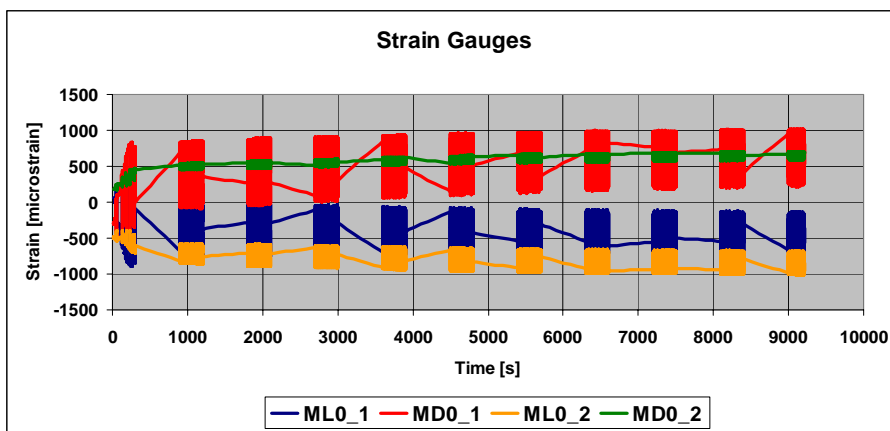
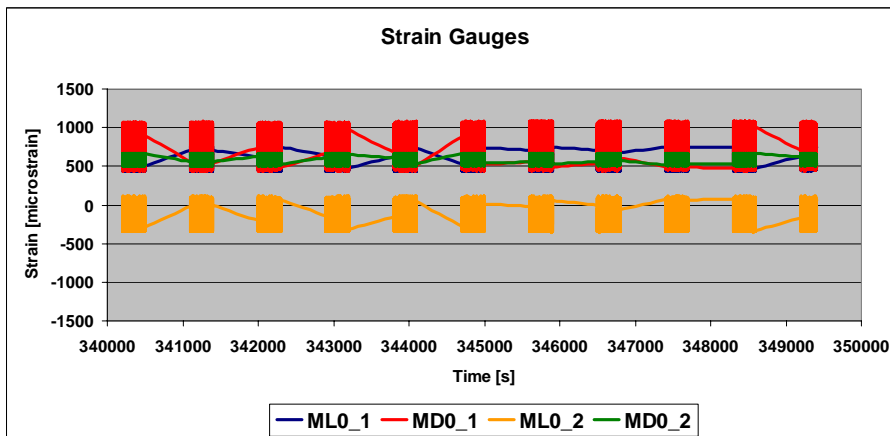


Figure 9-10 BWF fatigue; signals of four strain gauges near ending time; ML0\_1, MD0\_1, ML0\_2 and MD0\_2.

Since the drift is variable for different signals no useful detrend could be done. To illustrate this, more extensive signals of the ML0\_1, ML0\_2, MD0\_1 and the MD0\_2 of the BWF are shown in Figure 9-11 (first 10000 seconds) and Figure 9-12 (340000 up to 350000 seconds). The MD0\_1 signal (red) and the MD0\_2 (green) show an upwards drift at first. Later on the MD0\_1 signals stays about constant while the MD0\_2 signal moves down again. The ML0\_1 (blue) and the ML0\_2 (yellow) decrease at first but later on they drift upwards. Note that the blue signal is hidden after the red one in Figure 9-12.



**Figure 9-11** Signals of the ML0\_1, ML0\_2, MD0\_1 and the MD0\_2 of the BWF during the first 10000 seconds; this is about the first 3 hours of the fatigue test.



**Figure 9-12** Signals of the ML0\_1, ML0\_2, MD0\_1 and the MD0\_2 of the BWF at 340000 up to 350000 seconds; this is about the first 3 hours of the fourth day of the fatigue test.

Next, the simulations for this first group of strain gauges for the other buoy, the BWO, are marked with red squares in Figure 9-13 (longitudinal distribution) and in Figure 9-14 (transverse distribution). As for the BWF, the ML0\_1 which is mounted on the cone should be depicted in a more local axis system as is shown in Figure 9-15. There, the value of the ML0\_1 is about -2600 which is almost equal to the value in the cylindrical axis system in Figure 9-13.

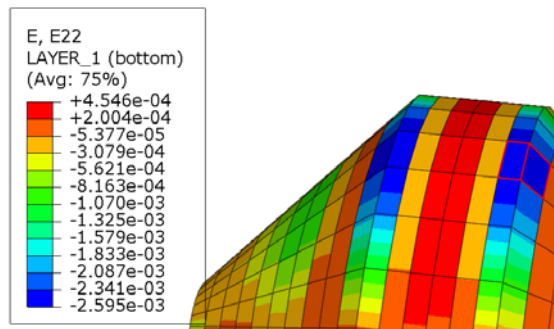


**Figure 9-13** Longitudinal strain distribution of the BWO; the red squares are the location of group one.

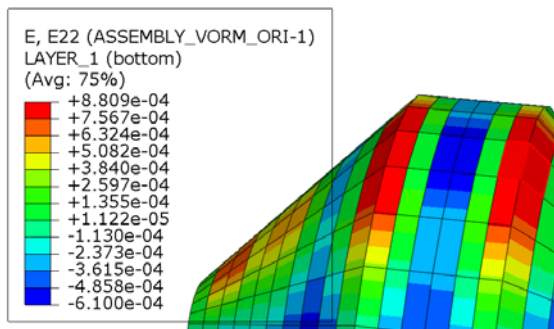


**Figure 9-14** Transverse strain distribution of the BWO; the red squares are the location of group one.

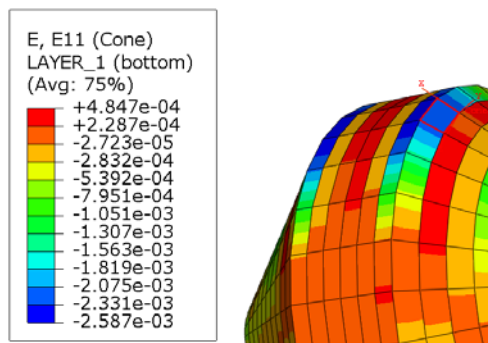


**Figure 9-15** ML0\_1 value in the local axis system along the cone.

Also, the same strain gauge signals for the BWOFF are now shown in Figure 9-16 (start), Figure 9-17 (middle) and Figure 9-18 (end).

The perpendicular signals near starting time match very well with the finite element calculations (12 % over prediction) for the BWOFF. For the longitudinal ones, the simulations over predicted the values a lot more, namely an over prediction of about a factor two as for the BWF. In the signals near half and ending time there seems to be drift as was expected. Here, the amplitudes do not show such a clear trend as with the BWF. Those of the perpendicular ones first increase near half time but near ending time one of those goes down again. The amplitudes of the longitudinal ones stay more or less the same (MD0\_2).

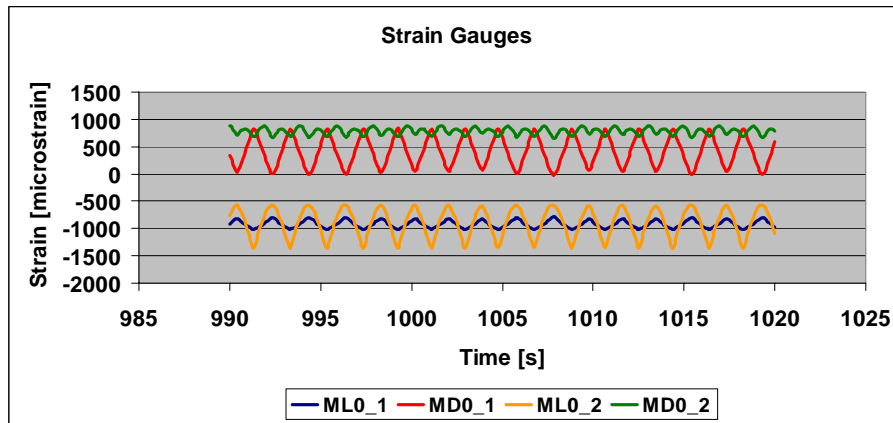


Figure 9-16 BWOFF fatigue; signals of four strain gauges at start; ML0\_1, MD0\_1, ML0\_2 and MD0\_2.

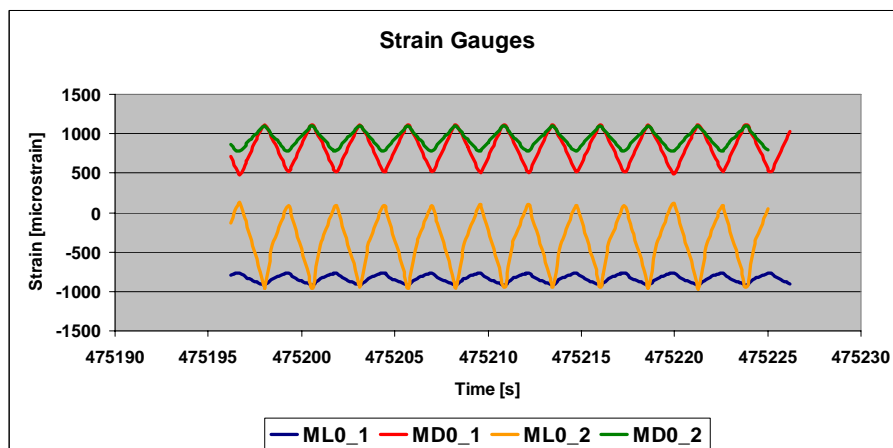
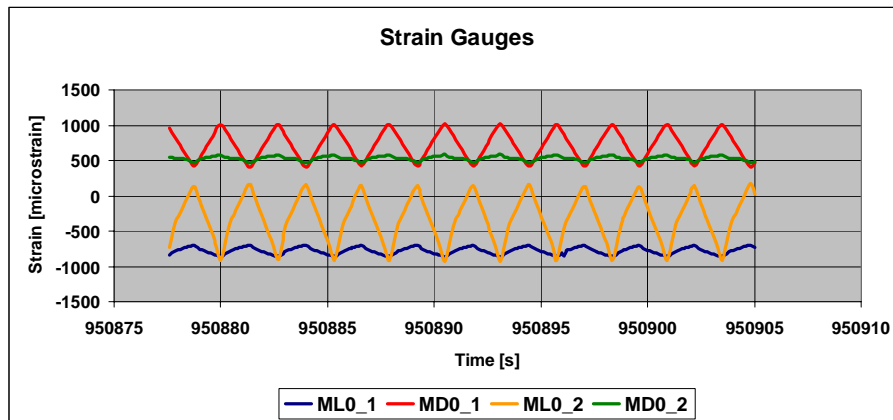
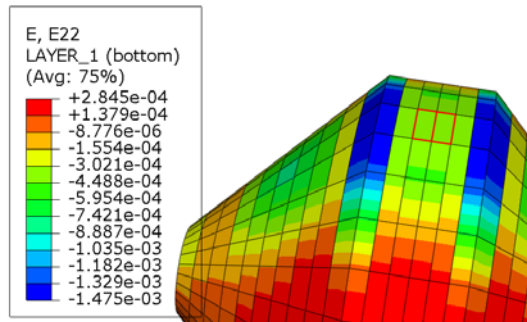


Figure 9-17 BWOFF fatigue; signals of four strain gauges just before half-time; ML0\_1, MD0\_1, ML0\_2 and MD0\_2.



**Figure 9-18** BWF fatigue; signals of four strain gauges near ending time; ML0\_1, MD0\_1, ML0\_2 and MD0\_2.

Now, the strain gauges of the second group are given for both buoys. The BWF longitudinal and transverse strain distributions are shown respectively in Figure 9-19 and Figure 9-20.



**Figure 9-19** Longitudinal strain distribution of the BWF; the red squares are the location of group two.

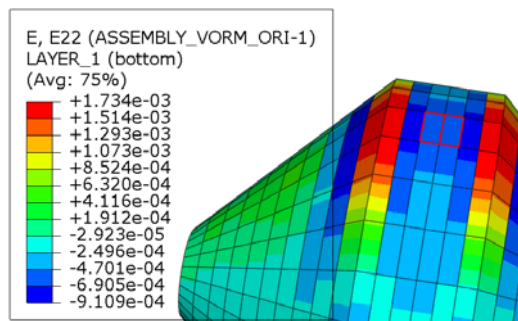


**Figure 9-20** Transverse strain distribution of the BWF; the red squares are the location of group one.

Next, the measured signals of the second group of strain gauges (ML0\_3, MD0\_3, ML0\_4 and MD0\_4) of the BWF are again given at three different times in Figure 9-21 (start), Figure 9-22 (middle) and Figure 9-23 (end).

For the BWF, the signals of the second group near starting time match with the trends in the finite element calculations. Now, the simulations under predicted the values (50-70 %). In the signals near half and ending time there seems to be drift as was expected. All amplitudes stay more or less the same but still they show a small decrease in time.

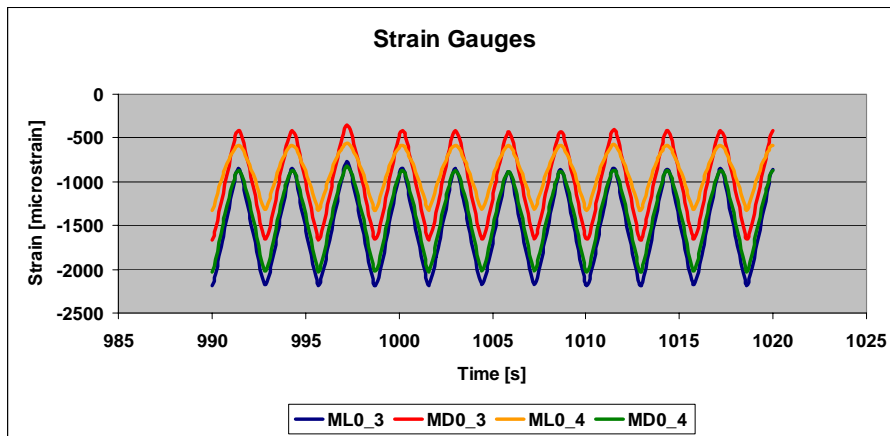


**Figure 9-21** BWF fatigue; signals of four strain gauges at start; ML0\_3, MD0\_3, ML0\_4 and MD0\_4.

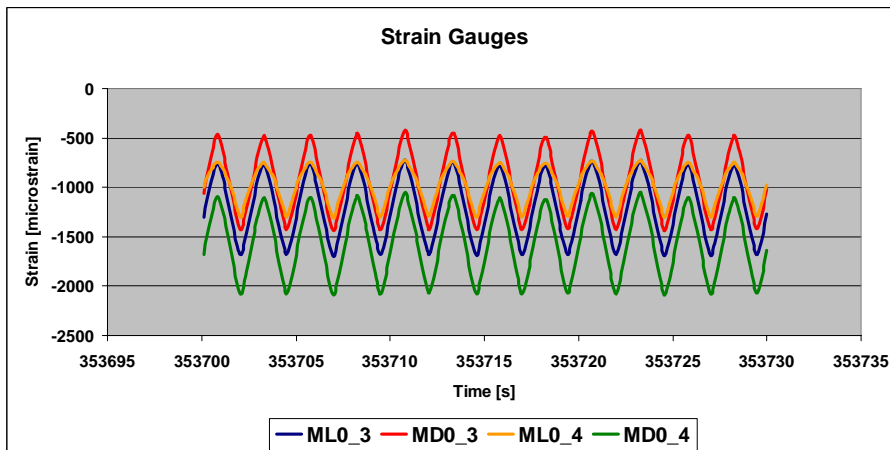


**Figure 9-22** BWF fatigue; signals of four strain gauges just before half-time; ML0\_3, MD0\_3, ML0\_4 and MD0\_4.

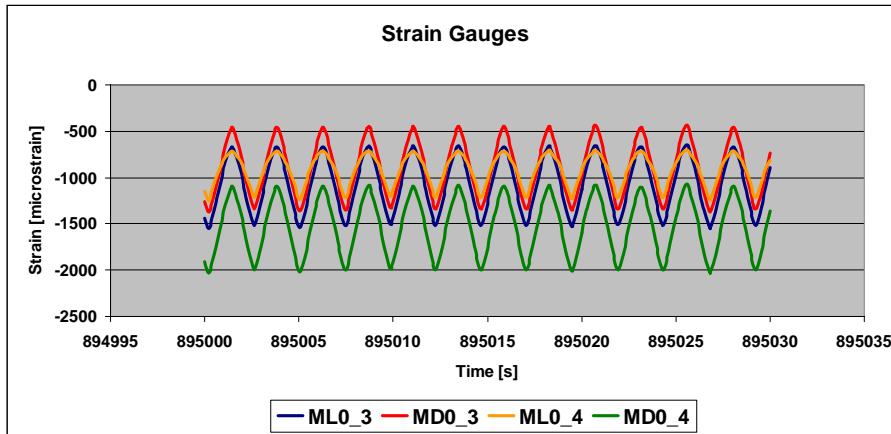


**Figure 9-23** BWF fatigue; signals of four strain gauges near the ending time; ML0\_3, MD0\_3, ML0\_4 and MD0\_4.

The simulations of the same strain gauges of the BWOFF are now given in Figure 9-24 for the longitudinal distribution and in Figure 9-25 for the transverse distribution.

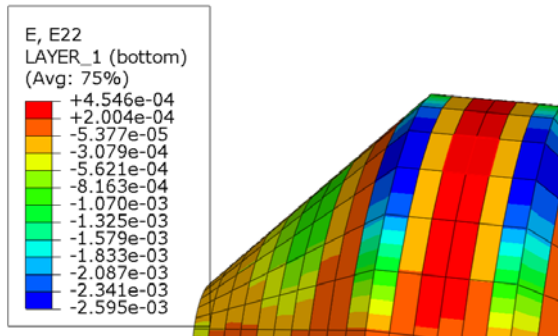


**Figure 9-24** Longitudinal strain distribution of the BWOFF; the red squares give the location of group two.

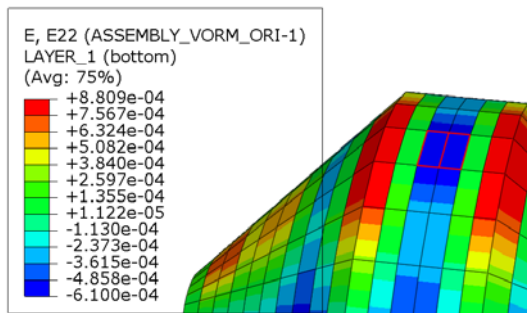


**Figure 9-25** Transverse strain distribution of the BWOFF; the red squares are the location of group two.

The measured signals are shown in Figure 9-26 (start), Figure 9-27 (middle) and Figure 9-28 (end).

For the BWOFF, the perpendicular peak values of the second group near starting time (-900 microstrain) have the same order of magnitude as the finite element calculations (-600 microstrain). As for the BWF, the simulations under predicted the values for the longitudinal ones more than for the perpendicular ones (65-90 %). In the signals near half and ending time there seems to be drift as was expected. The amplitudes of the perpendicular strain gauges increase and the amplitude of the remaining longitudinal strain gauge stays about the same in time.

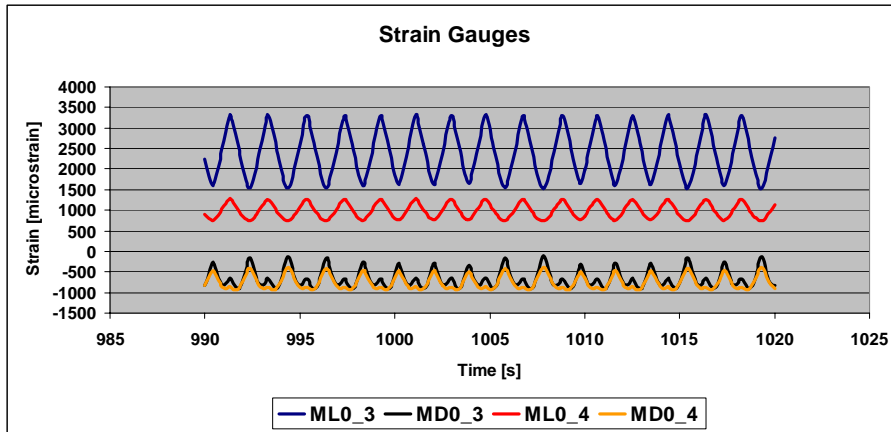


**Figure 9-26** BWOFF fatigue; signals of four strain gauges at start; ML0\_3, MD0\_3, ML0\_4 and MD0\_4.

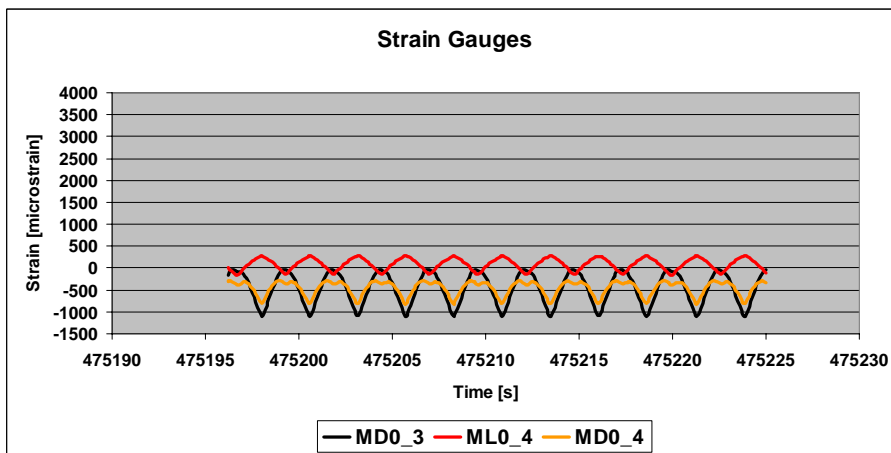


**Figure 9-27** BWOFF fatigue; signals of four strain gauges just before half-time; ML0\_3, MD0\_3, ML0\_4 and MD0\_4.

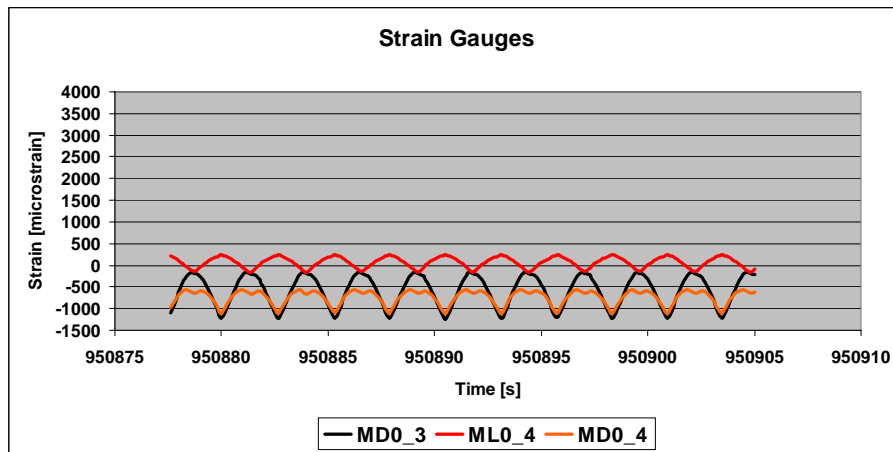


**Figure 9-28** BWOFF fatigue; signals of four strain gauges near the ending time; ML0\_2, MD0\_2, M and MD20\_2.

The longitudinal and transverse strain distributions of the BWF are respectively shown in Figure 9-29 and Figure 9-30. The red squares mark the locations of group three.

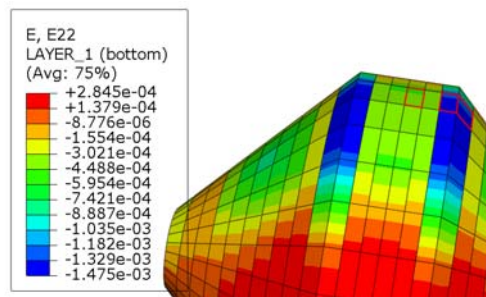


**Figure 9-29** Longitudinal strain distribution of the BWF; the red squares are the location of group three.

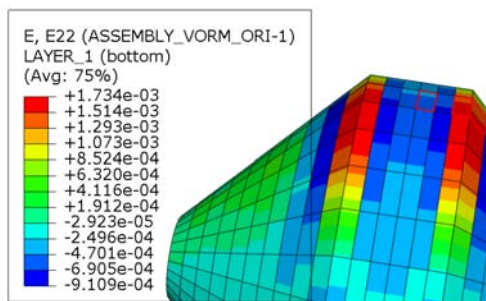


**Figure 9-30** Transverse strain distribution of the BWOFF; the red squares are the location of group three.

As for the ML0\_1 in strain group one, here for the ML20\_1 mounted on the cone part of the buoy it is better to use a local axes system along the cone. However, the result for the ML20\_1, which is about -1300 microstrain and which is depicted within the red square in Figure 9-31, does not differ a lot from the one depicted in the cylindrical axes system, also about -1300 microstrain, of Figure 9-31.

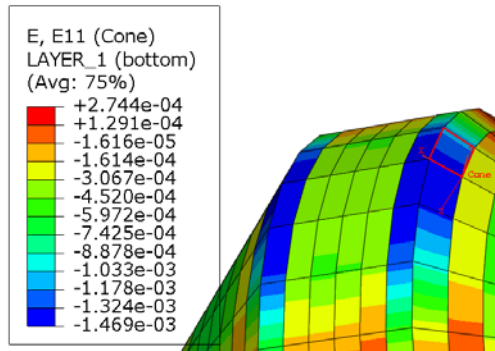


**Figure 9-31** More correct ML20\_1 value in the local axis system along the cone.

Next, the BWF signals of this group of strain gauges (ML0\_3, MD0\_3, ML0\_4, MD0\_4, ML20\_3 and MD20\_3) are given at three different times in Figure 9-32 (start), Figure 9-33 (middle) and Figure 9-34 (end).

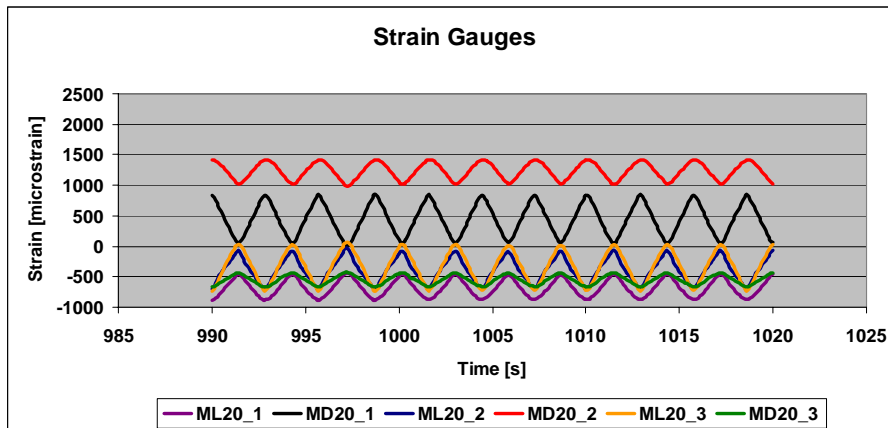


**Figure 9-32** BWF fatigue; signals of six strain gauges at start; ML20\_1, MD20\_1, ML20\_2, MD20\_2, ML20\_3 and MD20\_3.

The signals for the BWF of the third group near starting time have the same order of magnitude as the finite element calculations. The ML020\_1, ML20\_2, MD20\_1 and

the MD20\_2 were over predicted (from 7 up to 86 %) while the ML20\_3 and the MD20\_3 were slightly under predicted (14-17%). In the signals near half and ending time there seems to be drift as was expected. Again, the amplitude of some strain gauges decreases (MD20\_1, MD20\_2 and ML20\_3) and of others increases (ML20\_1 and MD20\_3).

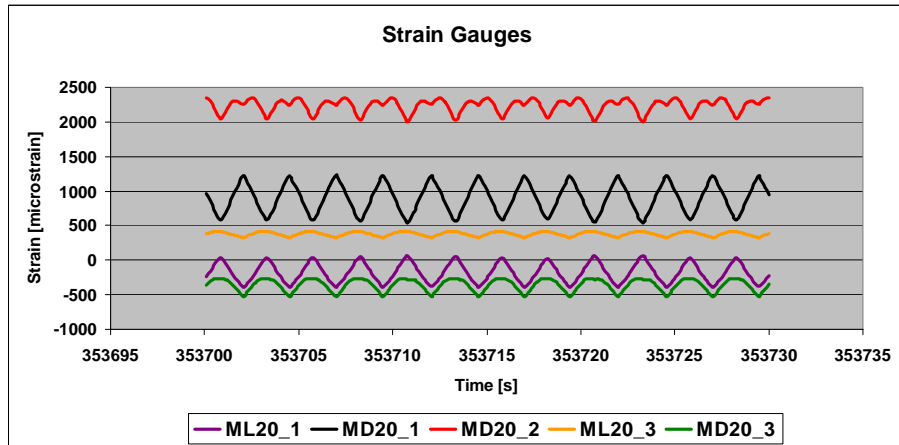


**Figure 9-33** BWF fatigue; signals of six strain gauges just before half-time; ML20\_1, MD20\_1, ML20\_2, MD20\_2, ML20\_3 and MD20\_3.

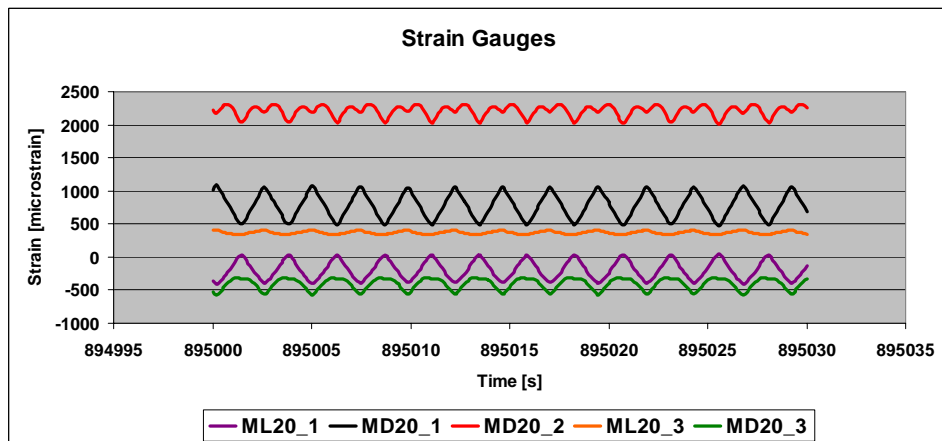


**Figure 9-34** BWF fatigue; signals of five strain gauges near the ending time; ML20\_1, MD20\_1, ML20\_2, MD20\_2, ML20\_3 and MD20\_3.

The simulations of the same strain gauges of the BWOF are given in Figure 9-35 for the longitudinal distribution and in Figure 9-36 for the transverse distribution.

As for the BWF, the ML20\_1 is mounted on the cone for the BWOFF and should be read out of the simulations in a local axis system. This value is depicted in Figure 9-37 (-1800 microstrain) and is about the same as in the cylindrical axis system depicted in Figure 9-35.

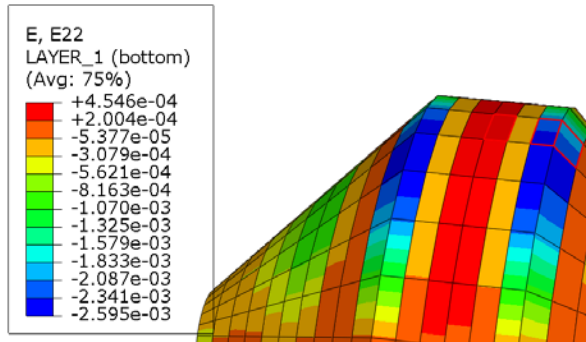


**Figure 9-35** Longitudinal strain distribution of the BWOFF; the red squares are the location of group three.

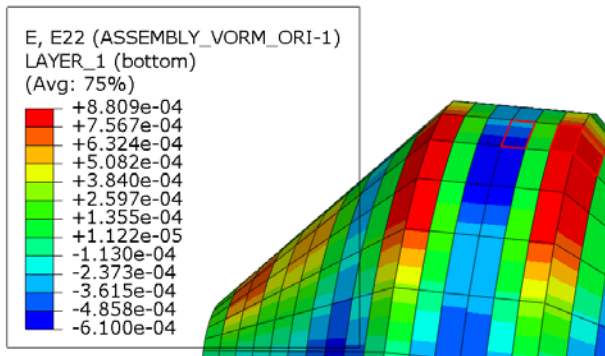


**Figure 9-36** Transverse strain distribution of the BWOFF; the red squares are the location of group two.

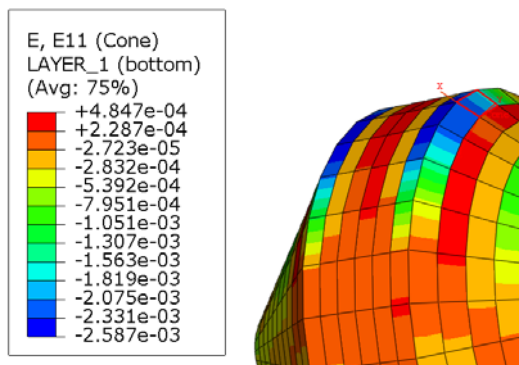


**Figure 9-37** ML20\_1 value in the local axis system along the cone.

The measured signals of the BWOFF for the third group of strain gauges are now shown in Figure 9-38 (start), Figure 9-39 (middle) and Figure 9-40 (end). The signals for the BWOFF of the third group near starting time match very well with order of magnitude of the finite element calculations. In this zone over and under prediction occur. The highest one is an over prediction of 64% for one strain gauge. In the signals near half and ending time there seems to be drift as was expected. Again, the amplitude of some strain gauges decreases (ML20\_2, MD20\_1) and of others increases (ML20\_1, MD20\_2 and MD20\_3). The amplitude of the ML20\_3 stays more or less the same in time.

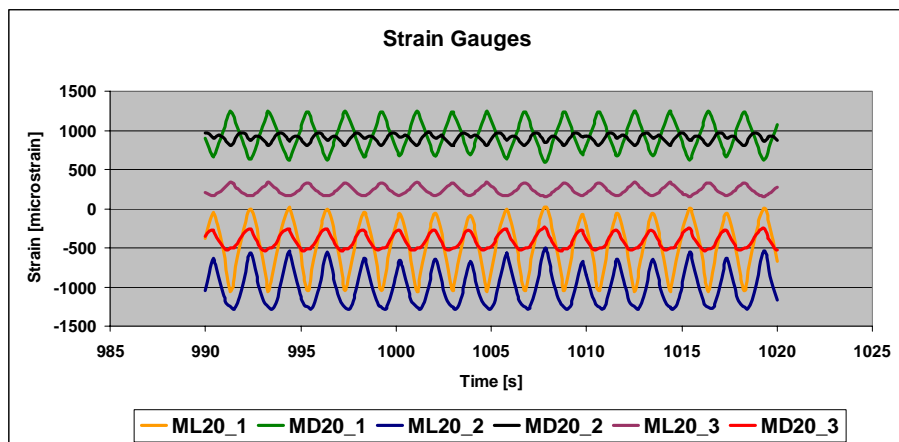


**Figure 9-38** BWOFF fatigue; signals of six strain gauges at start; ML20\_1, MD20\_1, ML20\_2, MD20\_2, ML20\_3 and MD20\_3.

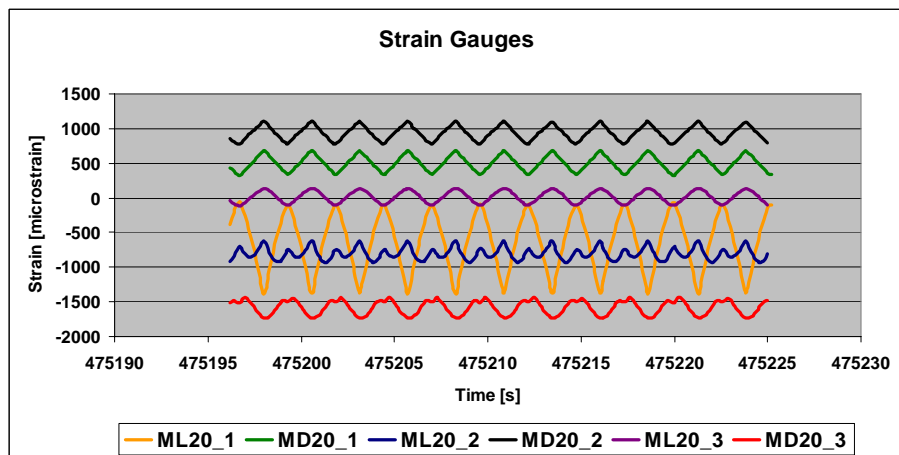


**Figure 9-39** BWOFF fatigue; signals of five strain gauges just before half-time; ML20\_1, MD20\_1, ML20\_2, MD20\_2, ML20\_3 and MD20\_3.

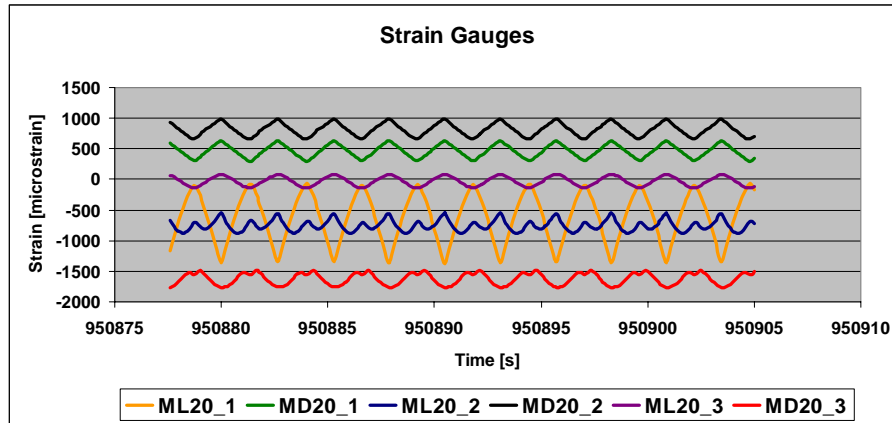


**Figure 9-40** BWOFF fatigue; signals of five strain gauges near the ending time; ML20\_1, MD20\_1, ML20\_2, MD20\_2, ML20\_3 and MD20\_3.

In general, the peak values at start of all 14 measured strain gauges show the same trend as was predicted in the finite element calculations per zone. The signs are for all zones correct while the over/under prediction stays consistent. Hence, taken into account the made assumptions (rigid shell, used rubber) the measurements were considered as corresponding well with the finite element calculations.

#### 9. 1. 4. LVDT sensors

Third, the measurements of the LVDT sensors are given and explained. Again, as for the strain gauges, those signals are given at three different times during the fatigue test. The first experiment was on the BWOFF. For this buoy five LVDT sensors were used. Their positions are depicted in Figure 9-41. For the BWF the sensor Solar 58-1 in the tube was moved and used to measure the vertical displacement on top of the buoy. The new location is shown in Figure 9-42.

The displacement is a relative signal hence here an increase in signal is a positive displacement and a decrease a negative one. The experiments of the first hour are used for comparison with the finite element simulations just as for the strain gauges. The distribution of the vertical displacement out of Abaqus for the BWOFF is given in Figure 9-43 where two red squares mark the position of the solar 50-3. The simulated value is -1 mm while the measured value is about -2 mm. Next, since in the simulation one side of the buoy is fixed, the calculated axial displacement on the other side should equal the subtraction of the solar 50-1 and the solar 50-2. This simulated value is 0.8 mm while the subtraction of both measured signals gives a displacement of less than one mm. It seems that for the fatigue measurements of the

BWOF no drift occurred as can be seen in Figure 9-45 (near half time) and in Figure 9-46 (near ending time). This is also as was expected since the LVDT sensors do not measure in the same way as the strain gauges do. They work by means of a moving magnet while with strain gauges a change in electrical resistance is measured. The figure shows that the signals do not change a lot in time.

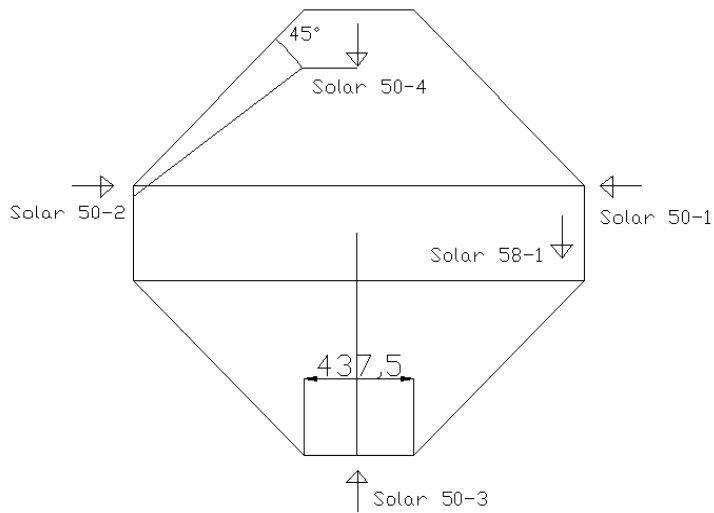


**Figure 9-41** Positions of the LVDT sensors for the BWOF fatigue test.

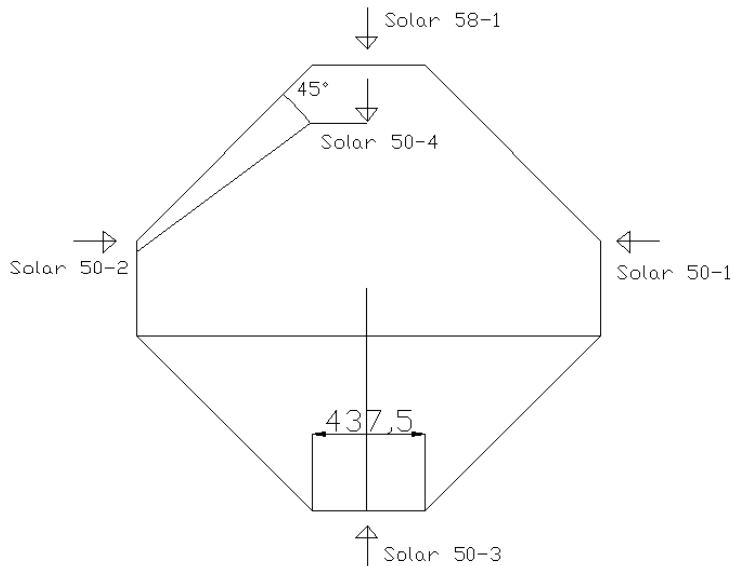


**Figure 9-42** Positions of the LVDT sensors for the BWF fatigue test.

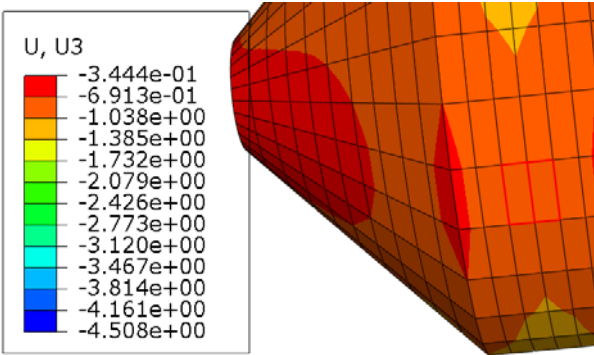


**Figure 9-43** Distribution of the vertical displacement of the BWO; the red squares mark the bottom of the buoy where the solar 50-3 is situated.

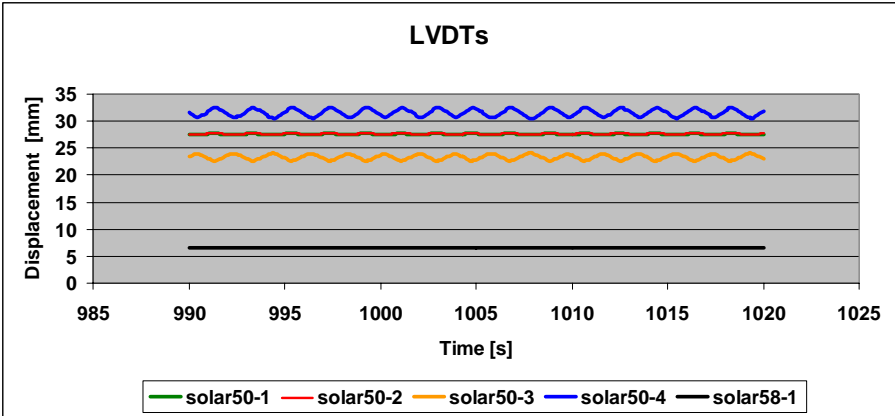


**Figure 9-44** BWO; fatigue; signals of the five LVDT sensors at start.

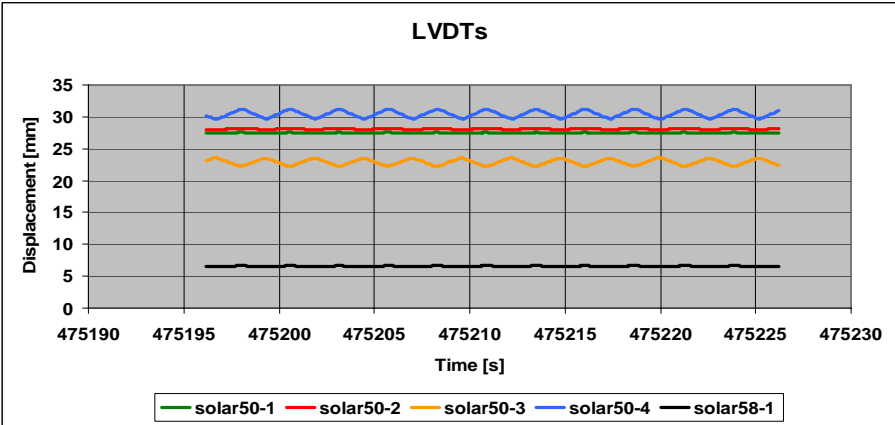


**Figure 9-45** BWO; fatigue; signals of the five LVDT sensors just before half-time.

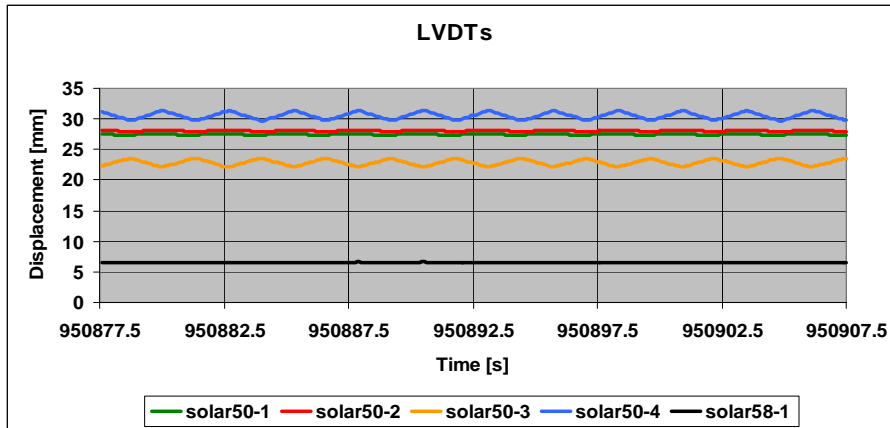


**Figure 9-46** BWOFF fatigue; signals of the five LVDT sensors near ending time.

The distribution of the vertical displacement out of Abaqus for the BWF is given in Figure 9-47 where two red squares mark the position of the solar 50-3. The simulated value is  $-0.6$  mm while the measured value is about  $-2$  mm. Next, since in the simulation one side of the buoy is fixed, the calculated axial displacement on the other side should equal the subtraction of the solar 50-1 and the solar 50-2. This simulated value is about  $0.8$  mm while the subtraction of both measured signals gives a very small displacement of about one mm. Again, as for the BWOFF, it seems that for the fatigue measurements of the BWF no drift occurred as can be seen in Figure 9-49 (near half time) and in Figure 9-50 (near ending time) with a possible exception of the solar 58-1.

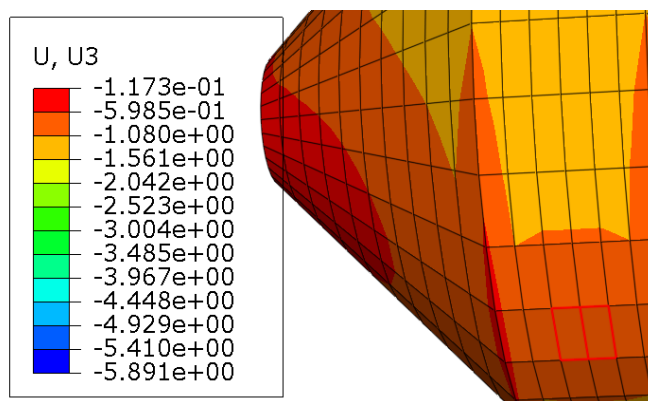


**Figure 9-47** Distribution of the vertical displacement of the BWF; the red squares mark the bottom of the buoy where the solar 50-3 is situated.

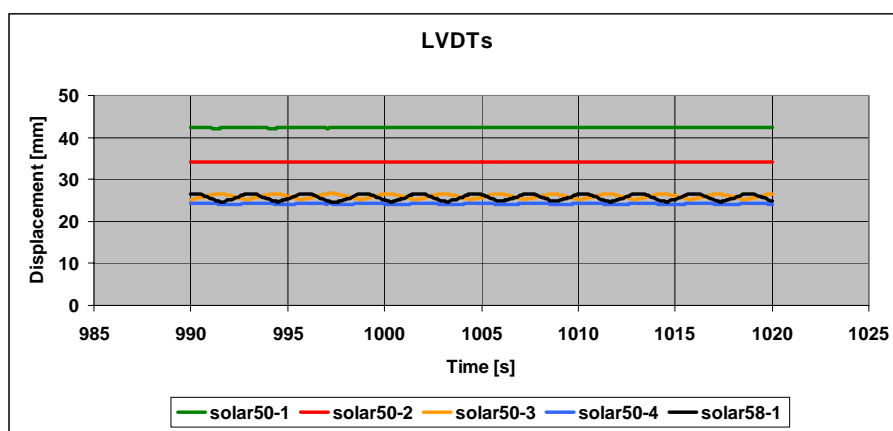


**Figure 9-48** BWF fatigue; signals of the five LVDT sensors at start.

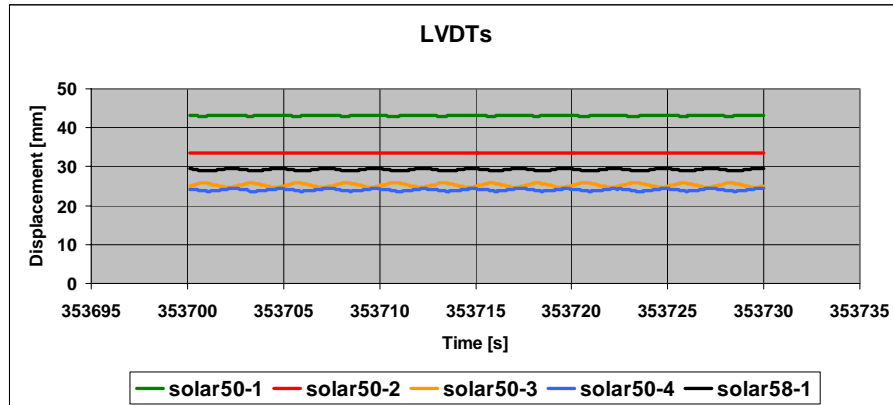


**Figure 9-49** BWF fatigue; signals of the five LVDT sensors just before half-time.

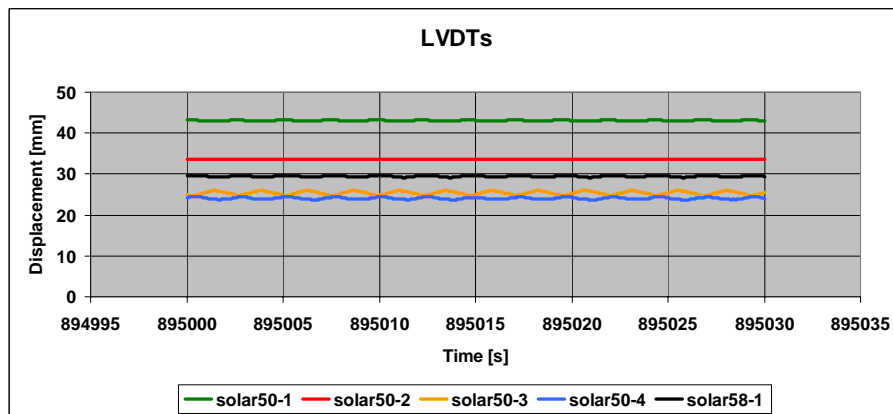


**Figure 9-50** BWF fatigue; signals of the five LVDT sensors near ending time.

## 9. 2. DROP TESTS FOR LATERAL SLAMMING

### 9. 2. 1. Introduction

Two kinds of drop tests were carried out, namely one called the lateral (or breaking wave) and the straight (or bottom) slamming. This means that the buoy was dropped from a different side into the water. The description of the lateral slamming tests is given next. For these tests, the buoy was dropped at its side into the water as is shown in Figure 9-51.



**Figure 9-51** Picture of a lateral slamming drop test.

Again, as discussed in Chapter 7 (lab scale tests) this sort of test resembles a breaking wave hitting the buoy on its side. As mentioned in Chapter 3, for the considered sea state, the celerity for the ‘25 year storm’ ( $H_s = 9.6$  m) is 12.1 m/s and the celerity for the ‘1 year storm’ ( $H_s = 6.6$  m) is 9.75 m/s. The drop speed is considered to be equal to the celerity of a particular wave. Hence, the celerity can be translated into drop height in the outdoor experiment. Celerity of 12.1 m/s equals a drop height of 7.46 m and celerity of 9.75 m/s equals a drop height of about 4.85 m. For several reasons (safety factor for the buoy and instrumentation including connections, an acceptable length of the cables, risk of hitting the bottom of the “*Watersportbaan*”) it was decided to perform drop tests for the ‘1 year storm’ which means drop tests at a height of about 4.85 m. Per buoy there were 10 such tests planned with the W0 meridian (strain gauges) down and 10 tests with the P0 meridian (pressure sensors), which is 30 degrees relative to W0 meridian, down.

Hence, P30 is equal to W0. The 3D sketch of the location of the four meridians of the strain gauges and one of the pressure sensors was shown in Chapter 8 and, to fix thoughts, again in Figure 9-52.

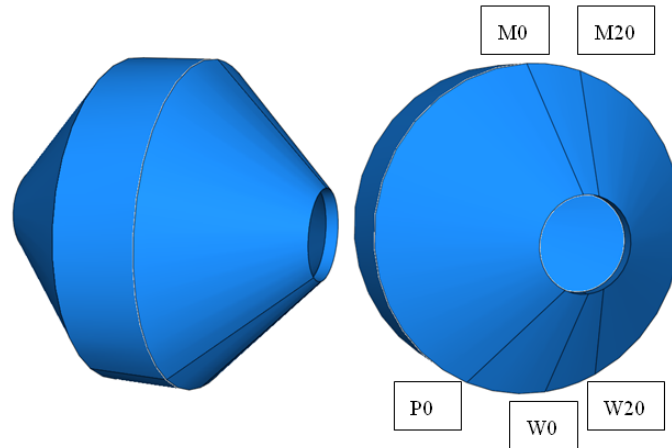


**Figure 9-52** 3D sketch of the location of the four ‘strain-gauge-meridians’ (W0, W20, M0, M20) and the P0 ‘pressure-sensor-meridian’.

Next, on the final test day there was time left to perform some additional experiments. Three experiments were done on the BWO (pressure sensors down) from a drop height of 7.2 m. The test matrix for the lateral slamming experiments is given in Table 9-3.

			BWF	BWO
Height [m]	Theoretical velocity at impact [m/s]	Angle [degrees]	Number of tests [-]	
4.8	9.7	0	10	10
4.8	9.7	30	10	10
7.2	11.9	0	/	3

**Table 9-3** Test matrix of the lateral drop tests.

Second, for the straight tests the buoy was dropped ‘straight-up’ as is seen in Figure 9-53. Forty bottom tests were done and should be explained in more detail in the doctoral thesis of G. De Backer, foreseen for the end of 2009 [2]. They are not treated here since the calculations (Chapter 5) showed that bottom slamming is less important than breaking wave slamming for survival for these kinds of buoys.

Figure 9-54 shows some pictures of the scene during tests. The crane is mounted on the shore which is seen on the upper left. The instrumentation for reading out the

HSC, strain gauges, an accelerometer and pressure sensors was mounted on the river shore as is shown on the upper right. On the lower left a picture is given after a drop test and the buoy is prepared to be lifted again. On the lower right picture the buoy rests still on solid ground and is prepared to be lifted over the water.



**Figure 9-53** Picture of straight slamming drop test.

The crane had to lift the point absorber in two different ways, straight and lateral. For both sorts of tests two elastic cables were attached to the flanges on the edges of the buoy. In Figure 9-55 (left) a picture is shown of the buoy to be lifted laterally with the help of the two elastic cables. A magnified view of the attachment of an elastic cable to a lifting eye bolt on a flange is given in Figure 9-55 (right).

A simple mechanical system, shown in Figure 9-56, held the other side of the two elastic cables and allowed releasing the point absorber without needing a guiding system, because a guiding system would be very expensive and very difficult to construct at that location. Action pictures of a lateral drop tests are given in Figure 9-57. In this figure a disruption of the water surface can be noticed due to the cables. This should be kept in mind when interpreting the peak pressures. In this way air could be included which would mean that the real peak pressures are even higher than the ones measured. The real drop height was 4.8 m since it was measured through an internal measuring system in the crane. The accuracy of the system is 0.1 m. It measures an end point at the horizontal water surface by bringing the buoy just above it. Next, the buoy is lifted until the crane's internal system measures the start point (i.e. the desired drop height).



**Figure 9-54** Pictures of the surroundings during experiments on the “Watersportbaan”.



**Figure 9-55** Two elastic cables used to lift the buoy (left) and detailed picture of elastic cable to a lifting eye bolt (right).



**Figure 9-56** Picture of the used mechanical releasing system.



**Figure 9-57** Action pictures of a lateral drop test.

The accelerometer and pressure sensors were measured with the data acquisition card NI-USB-6251 from National Instruments at 75 kHz. The strain gauges were measured with the strain smart software at 10 kHz which was the highest possible sample rate. For the lateral drop tests twenty strain gauges channels were measured. Three pressure signals (A23C, A06 and A07) and a shock accelerometer were useful for these tests. Also, the complete event was registered with a HSC with high accuracy.

### 9. 2. 2. Accelerometer

It was mentioned in Chapter 8 a shock accelerometer of 500 g was used. A representative measurement of the shock accelerometer for an experiment with the BWOF at a drop height of 4.8 m is given in Figure 9-58. The sample rate is 75 000 Hz. From this signal the velocity at impact is determined. In Matlab the velocity was calculated with the help of an integration program. Again, a representative graph of the velocity for the same drop height is shown in Figure 9-59. Both the accelerometer signal and the calculated velocity graph have the same shape for both buoys. The theoretical drop speed at 4.8 m is 9.7 m/s. This is calculated through the use of Equation 9-1.

$$v = \sqrt{2 \times g \times h}$$

**Equation 9-1     Formula for the drop speed at a certain height.**

With

$g$  = gravitational constant = 9.81 m/s<sup>2</sup>

$h$  = drop height [m]

The average of the impact speed for the BWF is 9.61 m/s with a standard deviation of 0.46 m/s. The same average for the BWOF is 9.65 m/s with a standard deviation of 0.56 m/s. As explained, the measurement of the height is not very accurate with the crane which explains the large standard deviation for these tests.

Next, three such drop tests were done at a height of 7.2 m for the BWOF. Representative graphs of the acceleration signal and of the integrated velocity are shown respectively in Figure 9-60 and Figure 9-61. For this experiment the theoretical impact velocity was about 11.9 m/s. Again, an average of the experimental impact velocity was made for the three breaking wave test at a drop height of 7.2 m. This average is 12 m/s. Also, the standard deviation was calculated and is 0.2 m/s. Here, the standard deviation is smaller than for the 4.8 meter tests but this is probably due to the fact that at this higher height only three tests were done.

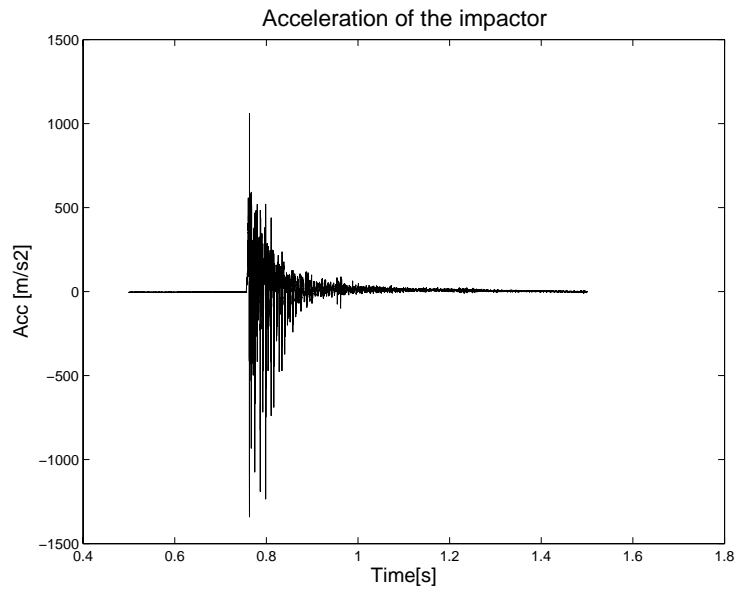


**Figure 9-58** Signal of the shock accelerometer during lateral impact of the BWOFF for a drop test at 4.8 m.

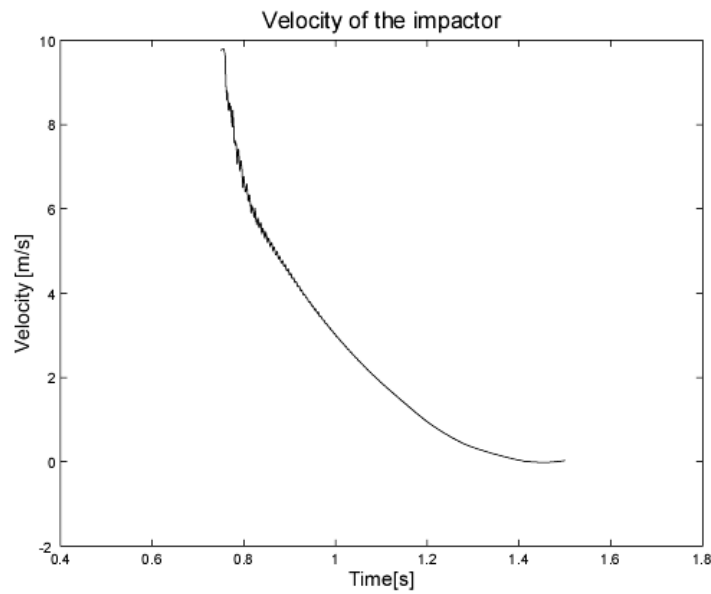


**Figure 9-59** Integrated signal of the accelerometer; velocity at lateral impact of the BWOFF for a drop test at 4.8 m.

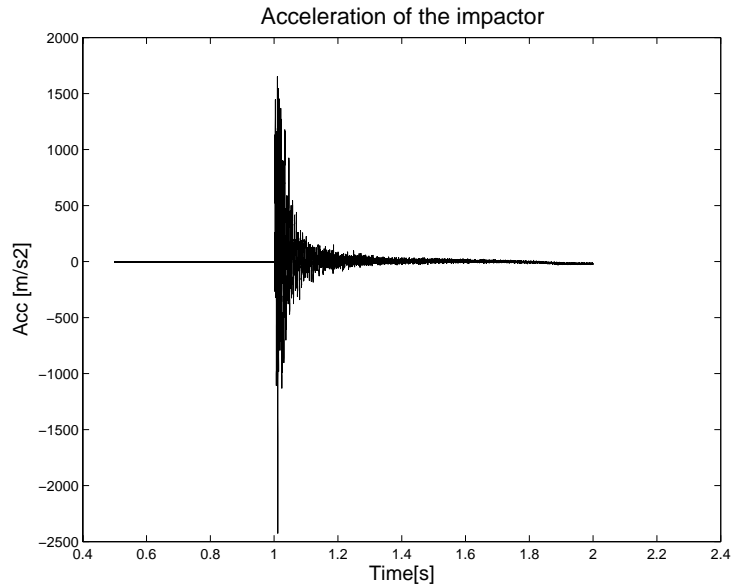


**Figure 9-60** Signal of the shock accelerometer during lateral impact of the BWOFF for a drop test at 7.2 m.

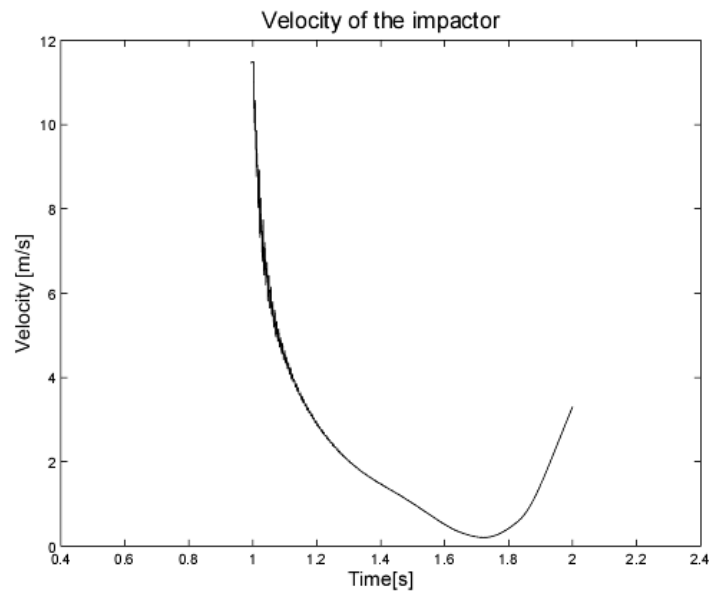


**Figure 9-61** Integrated signal of the accelerometer; velocity at lateral impact of the BWOFF for a drop test at 7.2 m.

### 9. 2. 3. High Speed Camera

The results from the HSC are discussed. This camera was used to register the events with high accuracy (1000 frames per second) as is shown in Figure 9-62. With some effort the different phases can be noticed again (splashing, rising-up and separation phase). However, this was not as clearly visualised as for the small tests probably due to the larger distance. The HSC was another means of determining the drop speed. The impact velocity is calculated with the help of a Labview program that follows the markers (made by T. Versluys from the Department of Coastal Engineering). Results are quite similar with those of the shock accelerometer since the average for the drop tests of 4.8 m is 9.6 m/s and the standard deviation 0.19 m/s. For the drop tests of 7.2 m the average impact speed is 11.97 m/s and the standard deviation 0.2 m/s.

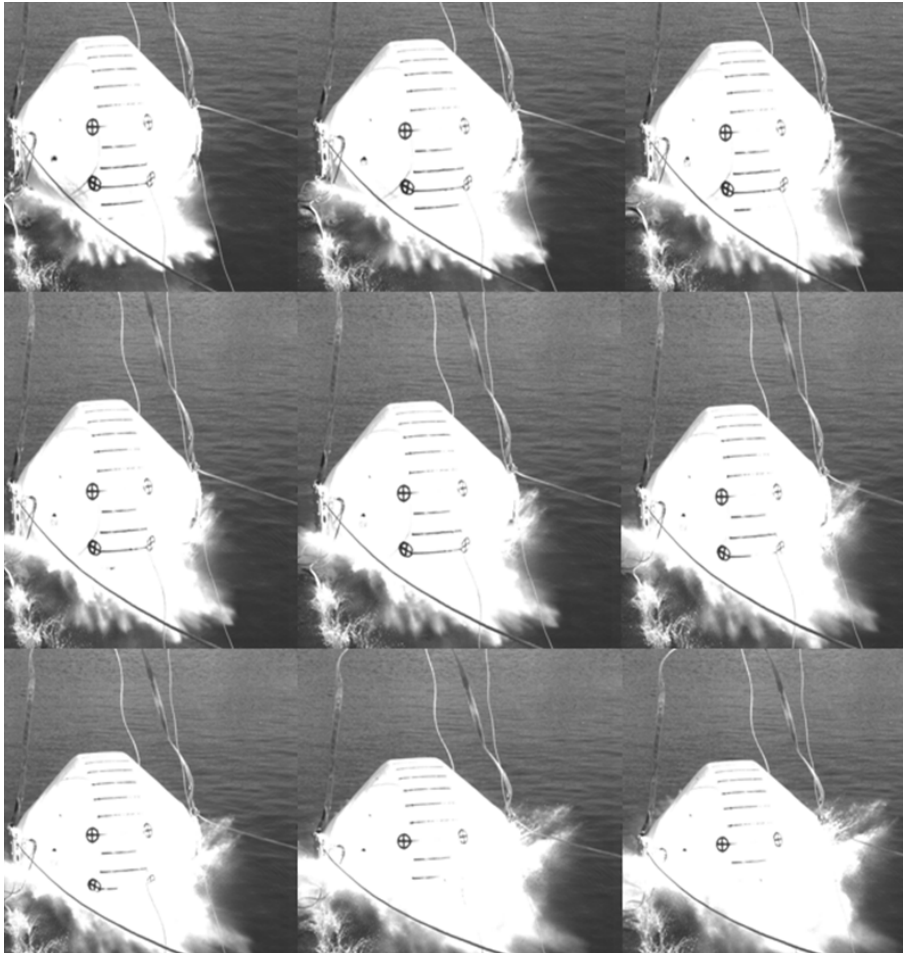


**Figure 9-62** Lateral outdoor drop test from 4.8 meter; sequential images from the HSC measurements during impact of the BWO.

#### 9.2.4. Pressure Sensors

As was mentioned before, five pressure sensors have been used during the drop tests. However, for each kind of test (bottom or breaking) only some sensors were useful. The sample rate was 75 000 Hz. For the zero degrees tests the shock pressure sensor A06 and A07 were measured. In the preparation phase it was assumed to have some results from the A23C as well for the 30 degrees tests. This was indeed the case as is discussed further in this paragraph. However, for the zero degrees tests this sensor is not taken into account due to its too small range. The results of the A06 and A07 at drop height 4.8 meter for the zero degrees tests, which means with the pressure sensors down, are shown in Figure 9-63 and shortly discussed afterwards.

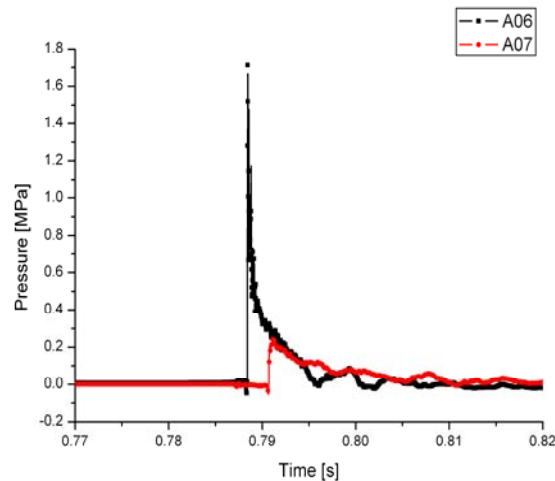


**Figure 9-63** Pressure sensors A06 and A07 signals for BWOF when dropped at zero degrees.

In Figure 9-63 the signal of the sensor A06 on the BWOF gives a peak pressure equal to about 1.8 MPa. The average value over ten experiments is 2.23 MPa with a standard deviation of 0.46 MPa. The A07 peak takes place a bit later and is also a lot smaller, which is in consent with their respective location on the buoy as is shown again in Figure 9-64. This average value is 0.2 MPa with a standard deviation of 0.03 MPa. Next, a representative graph for one of the BWF tests is given in Figure 9-65. There, the average value of the A06 sensor is 3.5 MPa with a standard deviation of 0.14 MPa. For the BWF the average of the A07 is 0.21 MPa over ten experiments with a standard deviation of 0.07 MPa. As mentioned, the results given in Figure 9-63 and Figure 9-65 are from zero degrees tests i.e. the buoy falls with the pressure sensors down. However, also ten tests per buoy were done at 30 degrees i.e. the point absorber is turned over a circle segment of 30 degrees. The average of the

A06 for these tests is 0.31 MPa for the BWF (Figure 9-66) and 0.305 MPa for the BWOE (Figure 9-67) with respective standard deviations of 0.05 MPa and 0.06 MPa. Here, also the A23C sensor was read out. There, the average peak pressure for the BWF is 0.34 MPa and for the BWOE 0.31 MPa with respective standard deviation of 0.03 MPa and 0.02 MPa.

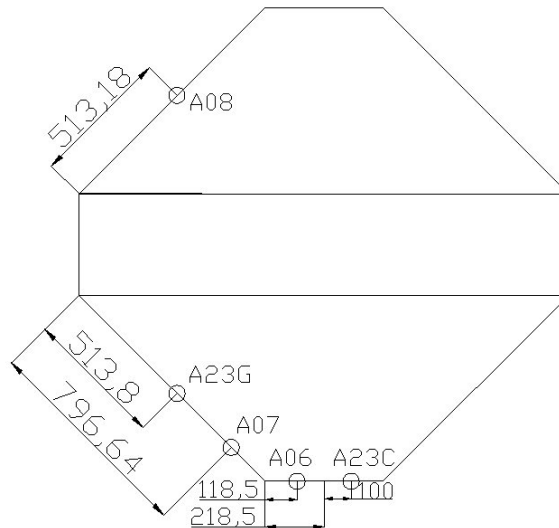


**Figure 9-64** Technical drawing of the location of the pressure sensors; note A06 and A07.

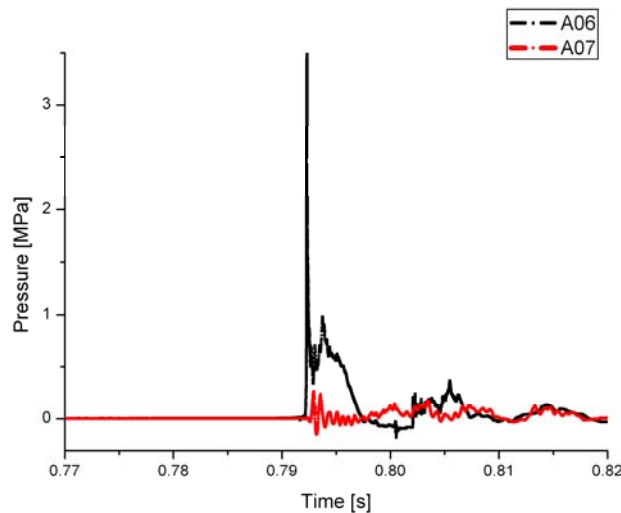


**Figure 9-65** Pressure sensors A06 and A07 signals for BWF when dropped at zero degrees.

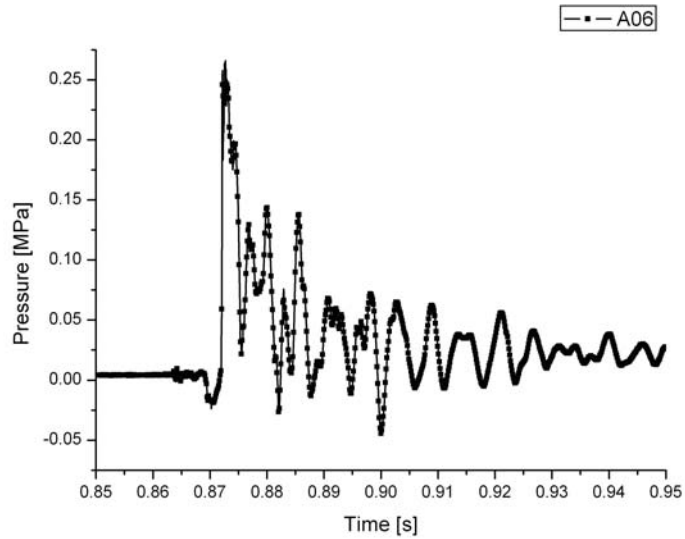


**Figure 9-66** Pressure sensor A06 signal for BWF when dropped at 30 degrees.

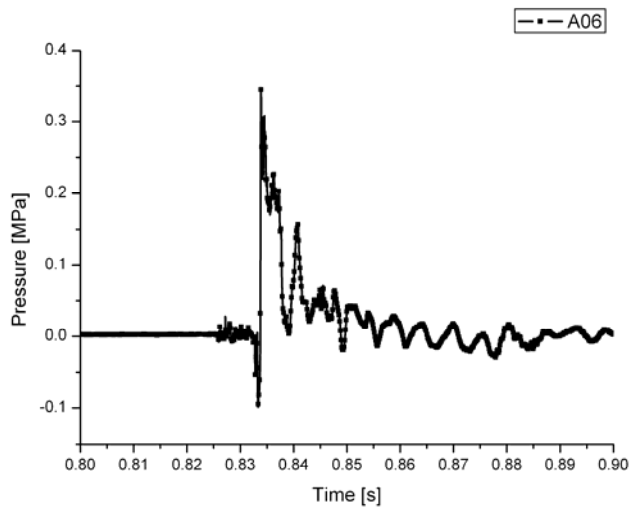


**Figure 9-67** Pressure sensor A06 signal for BWOE when dropped at 30 degrees.

Next, the results of the three drop tests *at drop height 7.2 meter* were the peak pressure of the A06, which was  $2.77 \pm 0.21$  MPa and the peak pressure of the A07 which was  $0.24 \pm 0.1$  MPa. This peak pressure is higher than the one for the same buoy at 4.8 m (2.23 MPa) but lower than the one for the BWF at 4.8 meter (3.5 MPa).

---

Lin & Shieh (1997) performed experimental drop tests on acrylic cylinders as was explained in Chapter 7. Their dimensionless pressure coefficient for cylinders at zero degrees,  $C_p(0)$ , peaks at about 110 to 120. However, there is a quite large deviation for these experiments. For the experiments at 30 degrees the values are almost the same for all impact velocities, namely a  $C_p$  of about 7.5 [3].

For the watersportbaan experiments at 4.8 meters, the dimensionless pressure coefficient at zero degrees,  $C_p(0)$  is 76 for the BWF and 48 for the BWOF. At thirty degrees the experimental coefficient,  $C_p(30)$ , equals 7.4 for the BWF and 6.7 for the BWOF. The  $C_p(0)$  of the three drop tests at 7.2 meter for the BWOF equals 39 calculated with the impact velocity obtained from the shock accelerometer signal.

Additionally, in the master thesis mentioned in Chapter 7 [4] it was shown that for cylinders at zero degrees,  $C_p(0)$ , drops by a factor two for a certain deformable (hollow) cylinder in comparison with a rigid one. Of course this factor is dependent on different input parameters but fact is that the pressure decreases for more deformable structures. This finding is also in good agreement with the drop tests on both buoys at 4.8 meters.

The drop tests were useful for gaining more knowledge about deformable behaviour under slamming conditions. Within the Seewec project, cost is of course an issue. The discussion about using or not using the expensive foam (expensive due to production cost) stays important. The discussed measurements are coming from Buldra-scale buoys at a drop height of 4.8 meters. These tests could be seen as the representation of the one year storm in the proposed sea climate. Now, it is seen that the proposed DNV norm (0.31 MPa) is maybe conservative in some areas (on the cone it is and of the same order of magnitude over thirty degrees on the cylinder) but it is certainly not at peak pressures (zero degrees). This difference is of course larger for the BWF since the measured peak pressure is higher than for the BWOF.

As shown in Chapter 5, for the full scale prototype using the BWOF would be critical (measure for Tsai Wu larger than one) *for the return level of 25 years* according to numerical simulations with the DNV standard. The average pressure used according to DNV was 0.472 MPa. For the BWF simulation at full scale according to this same DNV norm, the BWF should survive. Following only the DNV norm it seems clear that the BWF is the better buoy for these conditions.

Now, with the gained knowledge for the one year storm (4.8 meter drop height) and supposing the same trend is followed for the 25 year storm (7.2 meter drop height), the BWOF could be considered as an option. At the location where the DNV under

predicts the peak value, this under prediction is a lot worse for the BWF. Additionally, using foam would mean ca. 25% increase in material cost, also extra man hours would be needed to place the foam onto the buoy. An industrial process study would be necessary to avoid extra man hours on placing the foam. However, it should be considered whether this additional effort is still worthwhile considering the findings.

### 9.2.5. Strain Gauges

Finally, the measurements of the strain gauges channels are discussed. To fix thought the location of all measured strain gauges is shown again in Figure 9-68.

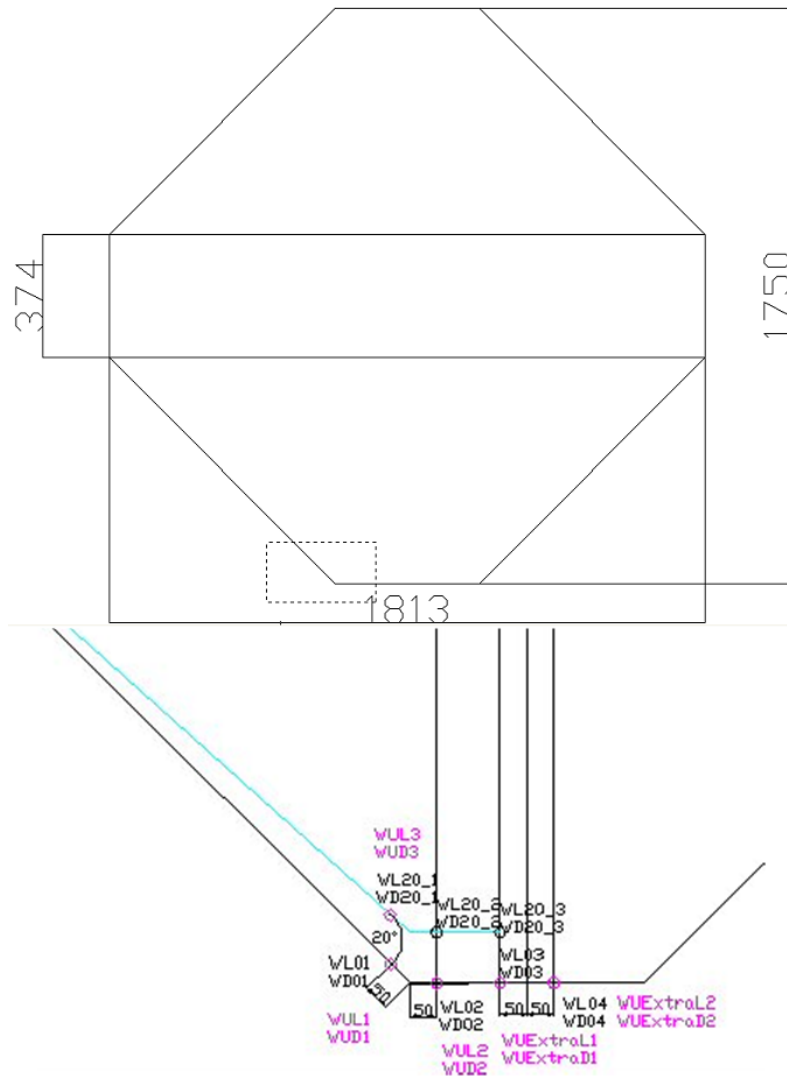
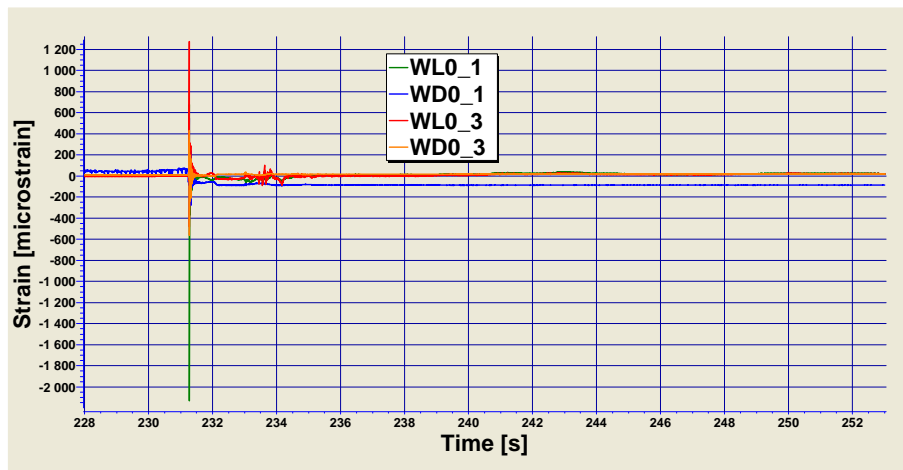


Figure 9-68 The position of the strain gauges for the ‘Watersportbaan’.

There are fourteen internal strain gauges and ten external ones (labelled extra with ‘U’). However, the maximum number that could be measured was 20 strain gauges. This means that there were four extra gauges (labelled ‘extra’). The sample rate was 10 kHz which was the highest possible.

At 7.2 meters only three drop tests were done with the P0 meridian down for the BWOFF and none with the W0 meridian (strain gauges) down. Hence, the comparison with finite element analysis is made with the drop tests of both buoys at 4.8 meter. As explained before, this simulates the yearly storm at the proposed sea climate with a celerity of 9.75 m/s. In the finite element the DNV norm is used which equals a constant pressure of 0.31 MPa. To fix thoughts, in Table 9-4 a representative group of four strain gauge signals (two on the cone and two in the middle) is shown for the BWOFF.



**Table 9-4** Representative strain gauge signals in time; WL0\_1, WD0\_1, WL0\_3 and the WD0\_3 of the BWOFF.

The average and standard deviation of ten BWOFF and ten BWF drop tests from 4.8 m with the W0 meridian down are given in Table 9-5. There is mentioned which strain gauge is mounted on or near the cone (C) or in the middle (M). Also the finite element results are summarised in the same table. These calculations were done with a constant pressure which is 0.31 MPa according to DNV for the proposed 1 year storm with a wave celerity of 9.75 m/s.

Out of this table it is shown that the strain gauges in the middle (M) give higher measurements than calculated. This was expected since the local measured pressures are a lot higher than the applied constant pressure in the simulations. For the strain gauges on or near the cone (C) it is the other way round: the strain gauge

Composite floating point absorbers for wave energy converters

measurements give lower values than the calculated ones which seems also logical. At that location the distributed pressure is lower than the simulated constant pressure. There are some exceptions in this trend, namely the WUD\_1, and the WU\_extraL2 for the BWOFF and the WL20\_3 for the BWF.

		BWOFF [microstrain]			BWF [microstrain]		
		FEA	Experiments		FEA	Experiments	
			Average	Standard Deviation		Average	Standard Deviation
WUL_1	C	770	347	69	-1400	-180	55
WUD_1	C	630	864	240	1200	789	91
WUL_2	C	420	298	86			
WU extraL1	M	-1300	-1696	287	-800	-1015	320
WUL_3	C	770	111	49	-960	-534	136
WUD_3	C	420	205	60	850	488	290
WL0_4	M	400	466	45	-700	-1083	33
WD0_4	M	-500	-885	185	-600	-876	232
WU extraL2	M	-1300	-1168	280	-800	-1023	150
WL0_1	C	-2300	-1833	310	-1300	-1006	123
WD0_1	C	780	532	258			
WL0_2	C	-2300	-1508	78			
WD0_2	C	780	143	76	1500	1468	323
WL0_3	M	400	1691	456	-700	-1542	172
WD0_3	M	-500	-511	60	-600	-932	66
WL20_1	C	-1600	-497	132	-1300	-300	18
WD20_1	C	550	327	86	950	533	24
WL20_2	C	-1600	-379	110	-1300	-271	17
WD20_2	C	550	430	48	950	449	187
WL20_3	M	400	702	79	-700	-193	89
WD20_3	M	-300	-1777	105	-400	-1701	77
WU extraD1	M				-900	-1675	233
WUD_2	C				1200	827	57

**Table 9-5** Calculated results with a constant pressure of 0.31 MPa and measurements for the BWOFF and the BWF at 4.8 meter.

### 9. 3. DROP TESTS BOTTOM SLAMMING

The results of the drop tests are not discussed within this doctoral thesis since the work of the outdoor slamming tests was shared with the Department of Coastal Engineering. Hence, the results of the bottom slamming tests can be found in [2]. In Figure 9-69 some pictures during bottom slamming tests are shown.



**Figure 9-69** Pictures during bottom tests.

## 9. 4. FRACTURE

### 9. 4. 1. Introduction

As for the fatigue test, the buoy is tested on its side over a segment of 60 degrees to simulate breaking wave slamming but this time the purpose is the determination of the maximum load that the buoy can resist. The set-up is quite the same as for the fatigue test but another load cell with a higher range (2000 kN) was used since the predicted failure load for the BWF (strongest buoy) was about 1320 kN. A building-up load program was applied. The first step was a load of 300 kN (equal to the load used for the fatigue test). Once it was stable, the load was increased up to 450 kN. Next step was 600 kN and from then on the load was increased further in steps of 100 kN. Each load step lasted for ten minutes with one exception at 450 kN which lasted longer (about one hour) since that load could be considered equal to the 25 year storm which is calculated from the DNV norm as explained in Chapter 3. Also, this one hour of stable testing was used to compare the measurements of the strain gauges with the simulations of the 25 year storm. For the fracture experiment the load was measured, the fourteen 'M' strain gauges were read out and also five signals of LVDT sensors were registered. In this chapter the results of those three kinds of sensors are discussed. Again, as was explained in Chapter 8, for the experiments at Magnel a more extensive finite element model was made inclusive the shell and the rubber. The measurements were compared with this simulation instead of with a constant pressure directly applied on the buoy. For fracture the Tsai Wu measure was iterated until it was about one, which resembles with a force of respectively 1320 kN for the BWF and 880 kN for the BWO. Now, in the finite elements that force was used to compare it with the measurements.

### 9. 4. 2. Load

First, the load sensor is treated. The measured force as a function of time (equal to the load step plan) for the BWF is given in Figure 9-70. However, the results of the other sensors for this first test are only correct until about 1000 kN. At that load it seemed that the displacement was too large for the length of stroke of the actuator. The load step program still went on to be certain whether this suspicion was right. It was clear that this was indeed the case and it was decided to stop the test. Next, some metal discs were mounted between the shell and the actuator to enlarge the maximum possible displacement for the machine. The experiment was restarted, but this time the load was built up smoothly and was not held at each step for ten minutes anymore. In Figure 9-71 this second measurement of the load is given. For the results of the strain gauges and LVDT sensors it is better to use the measurements from the first experiment up to a load of 1000 kN (which equals a

time of 9000 s within this test) and as soon as a result for a higher load is desired it is better to use the measurements of the second experiment. During this second test 1000 kN equals a time of 2600 s and fracture occurred at about 1280 kN, which equals a time of 3000 s there. In reality this fracture load value could be slightly higher due to the fact that the buoy had already been loaded and released again. However, it can not be estimated how big this effect was, so the measurement of 1280 kN is considered as the failure load for BWF.

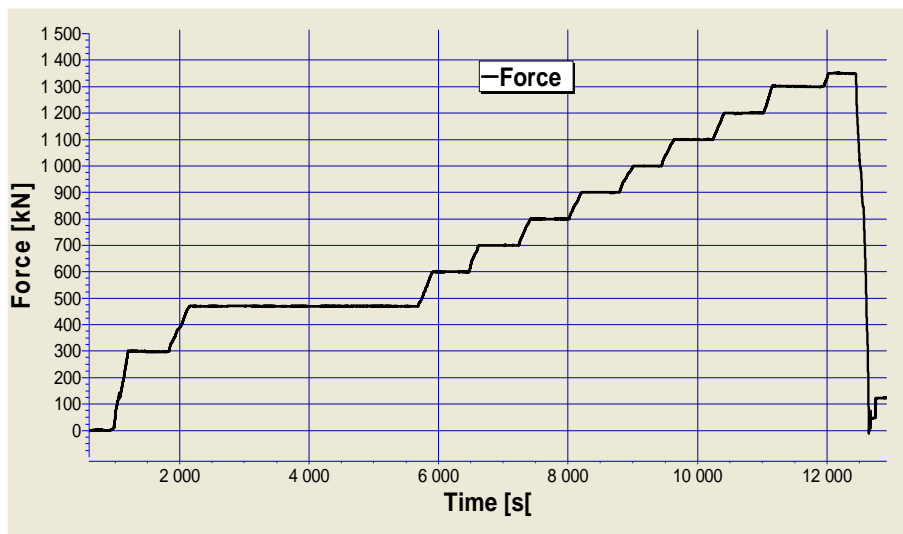


Figure 9-70 BWF fracture test; force as a function of time.

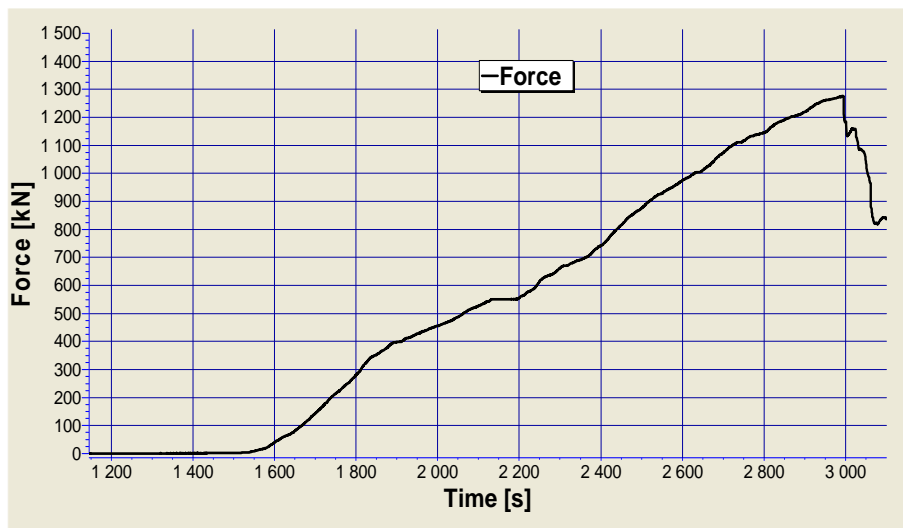
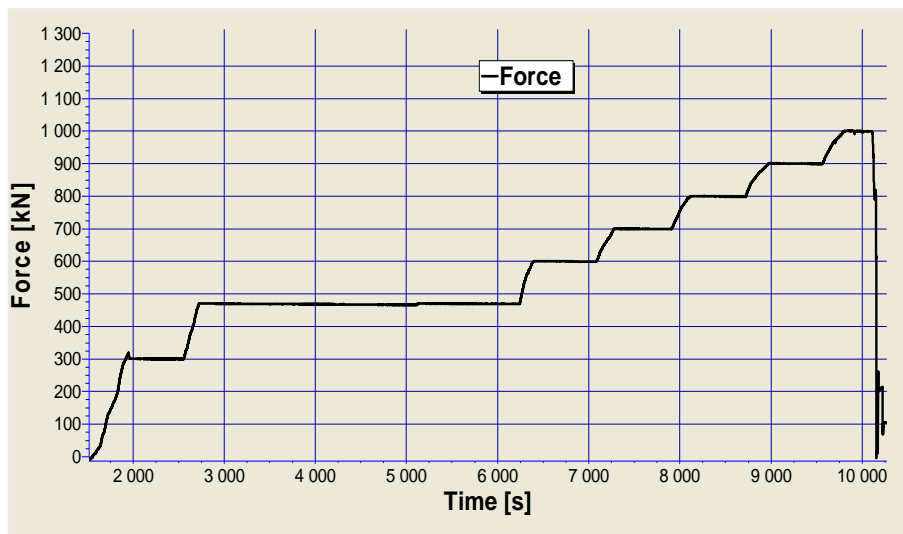


Figure 9-71 Second load measurement BWF.

This result matches very well with the FEA fracture simulation of the buoy. For fracture the Tsai Wu measure was iterated until it was about one, which resembles with a force of respectively 1320 kN for the BWF. In the finite elements including the shell and the rubber as explained in chapter 8 that force was used to compare it with the measurements. The measure for Tsai Wu is still about one; however it is slightly lower (0.991) than for the simulation with the constant pressure (0.9948).

The measured force as a function of time for the BWOF is given in Figure 9-72. The fracture load of the BWOF is 1000 kN. This result is higher than predicted with the FEA simulation of this buoy. The measure for Tsai Wu reaches 1.078 which is about one (predicted failure) for an applied constant pressure (equal to a force of 880 kN) directly on the buoy. Again, also for the BWOF the calculation with this force was re-done on the full model with a general rubber and the shell. The measure for Tsai Wu was still about one however it was again slightly lower (0.996) than for the simulation with the constant pressure.



**Figure 9-72** BWOF fracture test; force as a function of time.

The difference between experiment and simulation is larger than for the BWF. Additionally, for the BWF the real fracture load is a bit smaller than the one predicted through simulation. For the BWOF this is vice versa. One explanation could be the fact that the BWF fracture test occurred in two times and hence probably broke faster than it would have done the first time. A second possible reason is the shell. The same shell is used for both buoys and the shell was built to fit the diameter of the BWF. There is a difference in outer diameter between both buoys since they are built on the same mandrel and since the buoy with foam and

eight wound layers is thicker than the buoy with seven wound layers and without foam. Hence, when it was used for the fracture test for the BWOF it probably did not distribute the load in the same way as for the other buoy. However, these are only assumptions and their influence can not be determined exactly. The fact remains that the measured results for both buoys are quite similar to the calculated ones. Also, it has to be stated that fracture occurs very gradually which is a good thing. This means that when one buoy breaks at sea, the whole structure can stay operational and no damage occurs to other parts of the structure. Some pictures of fracture are shown in Figure 9-73. The fracture occurred at the predicted location namely on the edge of the cone/cylinder.



**Figure 9-73** Buoys at fracture.

#### 9. 4. 3. Strain Gauges

The signals of the strain gauges for both buoys are discussed. The values of the strain gauges at circa 450 kN (which simulates the 25 year storm) measured during the one hour lasting creep test, are compared with the finite element results. This value was also compared with the finite element results because it is the survival condition load (25 year storm). Additionally, the measurement lasted for an hour and it was assumed that the measurements of the strain gauges would give stable results there. Experimental and numerical values on all strain gauges at this load (450 kN) are summarised in Table 9-6. For the BWF these are the values from the first test and read from the respective graphs given further in this paragraph at a time of 2200 until 5800 seconds. For the BWOF these are read from the respective graphs at a

time of 2600 until 6300 seconds. To give a more detailed overview of the creep and of the fracture results, the fourteen ‘M – strain gauges’ are again divided in three groups as is shown in Figure 9-74. These groups are chosen since the difference between the experimental and finite element results show a similar trend.

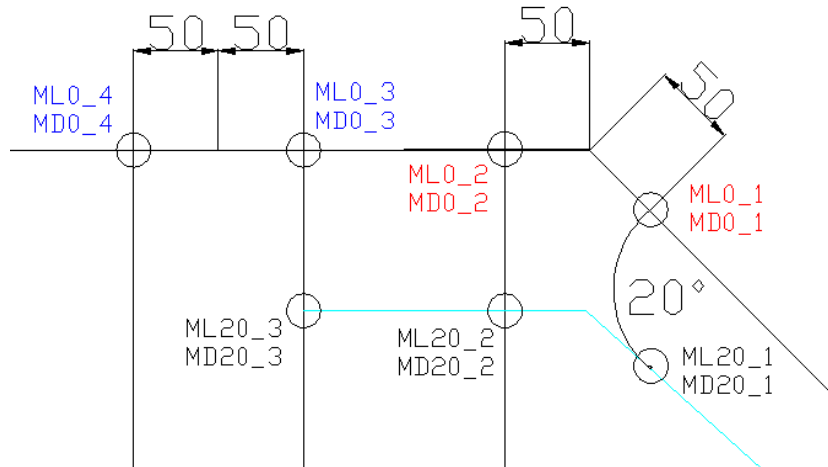


**Figure 9-74** The inner ‘Magnet’ strain gauges divided in three groups.

	BWF (experimental)	BWF (calculations)	BWOF (experimental)	BWOF (calculations)
ML0_1	-1000	-2000	-200	-3600
MD0_1	1400	2400	1800	1200
ML0_2	-600	-2000	-2300	-3600
MD0_2	/	2400	500	1200
ML0_3	1500	-830	/	630
MD0_3	-2000	-1300	-3000	-850
ML0_4	1000	-830	600	300
MD0_4	-2000	-1300	-3000	-850
ML20_1	-1000	-1700	-3300	-3250
MD20_1	1000	2400	800	1200
ML20_2	/	-830	-200	-3250
MD20_2	300	2400	1200	1200
ML20_3	0	-830	500	630
MD20_3	-1000	-960	-3800	-850

**Table 9-6** All results of the strain gauges during the one hour at 450 kN; calculations and experiments.

Also, all peak results of the strain gauges at fracture are summarised in Table 9-7. The values of the simulations are at a Tsai Wu measure of one. This means that progressive failure is not taken into account but only the initiating of failure. However, at this moment a lot of other Tsai Wu values were close to one (higher than 0.8) which shows that real failure is near.

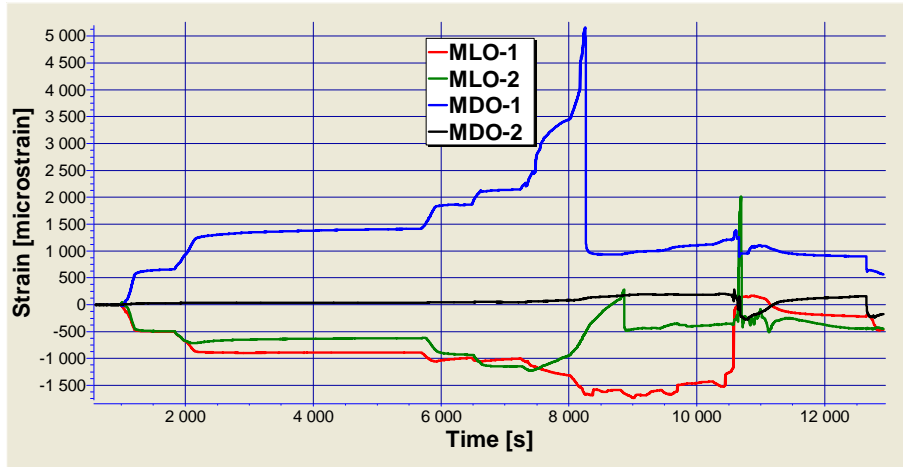
The values of the experiments are read from the respective measurement graphs at the moment of fracture which is at 1280 kN for the BWF and at 1000 kN for the BWO. Next, when strain gauges failed too early the last measured value has been used here. It can be seen that some of the strain gauges measure higher strains than calculated and vice versa as was the case for the fatigue tests. Nevertheless the order of magnitude is in good agreement considering the assumptions made (used rubber and shell). Additionally, the signs are correct. Some of the strain gauges did not work anymore. It has to be kept in mind that they were already present during the outdoor drop tests. Detailed explanation about these results is given within this paragraph.

	BWF (experimental)	BWF (calculations)	BWO (experimental)	BWO (calculations)
ML0_1	-2000	-6500	-200	-7600
MD0_1	1200	7600	3000	2600
ML0_2	-800	-6500	-4200	-7600
MD0_2	/	7600	0	2600
ML0_3	-500	-2600	/	1300
MD0_3	-4000	-4000	-5200	-1400
ML0_4	-1000	-2600	700	600
MD0_4	-1200	-4000	-1700	-1400
ML20_1	-700	-5800	-4800	-6100
MD20_1	1000	5700	700	2600
ML20_2	/	-5800	-3000	-6100
MD20_2	2400	5700	2200	2600
ML20_3	0	-2600	300	1300
MD20_3	-1300	-2100	-3000	-1400

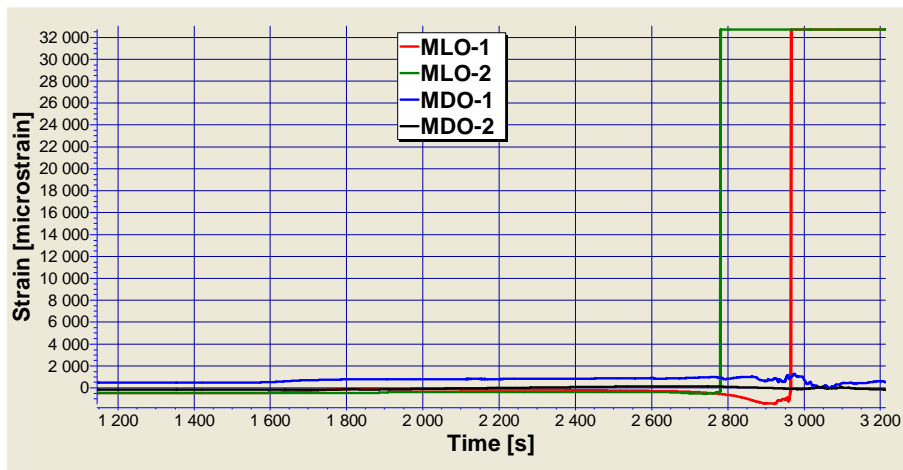
**Table 9-7 All results of strain gauges at fracture; calculations and experiments.**

Each group of signals is now given for the BWF as well as for the BWO. As mentioned earlier in this Chapter the experiment for the BWF was performed in two times. Before 1000 kN, thus for the comparison of the measurements during creep,

the results of the first experiment have to be used and after 1000 kN, thus for the measurements during fracture, the results of the second experiment are the most reliable ones. As such, in Figure 9-75 and Figure 9-76 a first group (MLO\_1, MD0\_1, MLO\_2 and MD0\_2) of the BWF are shown.



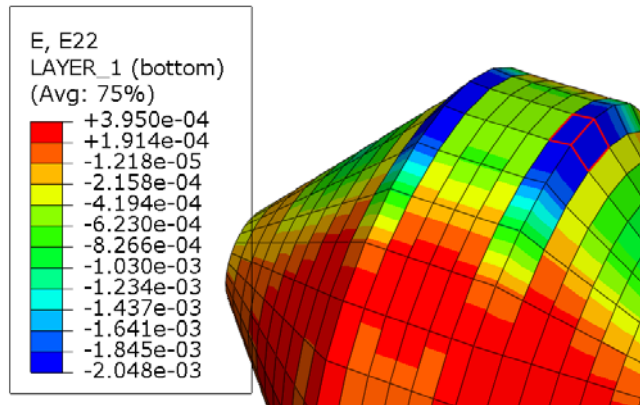
**Figure 9-75** BWF fracture; signals of MLO\_1, MD0\_1, MLO\_2 and MD0\_2; valid up to 9000 s which is 1000 kN.



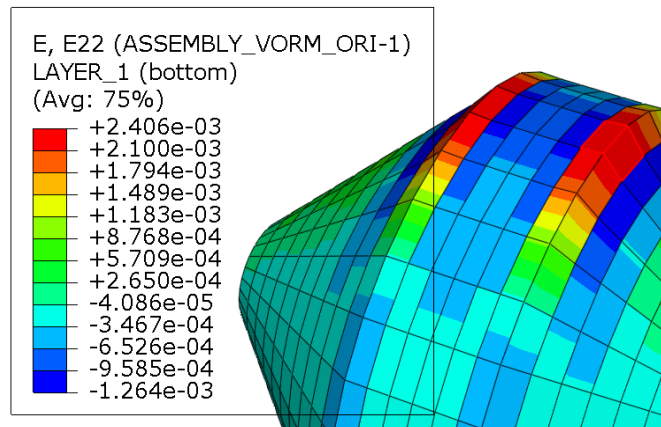
**Figure 9-76** BWF fracture; signals of MLO\_1, MD0\_1, MLO\_2 and MD0\_2; valid between 2600s (1000kN) & 3000s (1280kN).

Figure 9-77 shows the calculated longitudinal strain distribution on the inner side of the buoy with foam at 450 kN and Figure 9-78 shows the transverse strain distribution. Again, as for the fatigue simulations, these distributions are always given in the cylindrical axes system where the longitudinal direction is axial and the

perpendicular direction perpendicular. The red squares in both distributions mark the location of ‘group one’ of the strain gauges.



**Figure 9-77** Longitudinal strain distribution in the inner layer of the BWF at 450 kN.



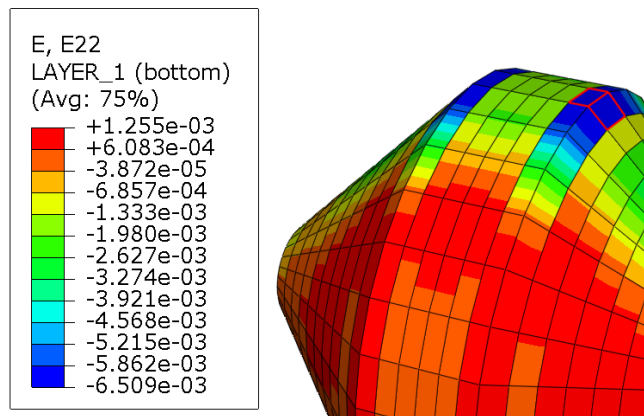
**Figure 9-78** Transverse strain distribution in the inner layer of the BWF at 450 kN.

As for the fatigue test, the longitudinal strain gauges on the cone (the ML0\_1 of this group and the ML20\_1 of the third group) should always be read out of the simulations in a local axes system along the slope of the cone instead of in the cylindrical one. However, again as was the case for the fatigue simulations, the values in such a local axes system are almost the same as the ones in the cylindrical axes system. Hence, for fracture, these distributions are not mentioned anymore.

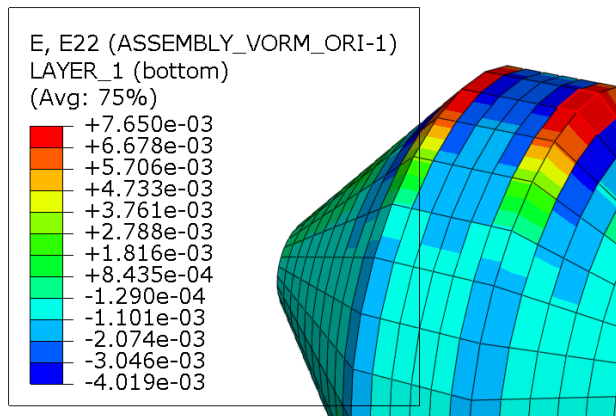
The measurements of this first group of strain gauges of the BWF during the one hour creep test at 450 kN are about a factor two smaller. Hence, the calculations

seem to over predict the measurements. However, the trend (compressive/tensile) is the same.

Figure 9-79 shows the calculated longitudinal strain distribution on the inner side of the buoy with foam at 1320 kN (Tsai Wu measure is one for that force) and Figure 9-80 shows the transverse strain distribution. The red squares in both distributions mark the location of ‘group one’ of the strain gauges.



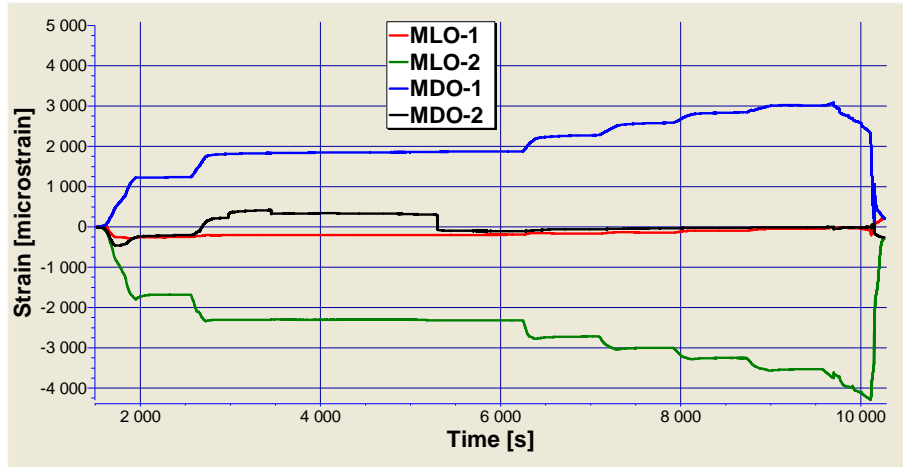
**Figure 9-79** Longitudinal strain distribution in the inner layer of the BWF at 1320 kN.



**Figure 9-80** Transverse strain distribution in the inner layer of the BWF at 1320 kN.

The measurements of this first group of strain gauges of the BWF at fracture are this time at least a factor two smaller. Hence, as for the creep test of this first group of strain gauges, the calculations seem to over predict the measurements. However, again the trend (compressive/tensile) matched.

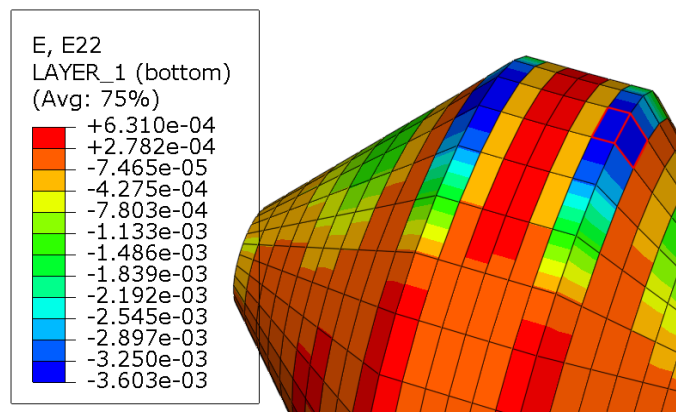
The same group of strain gauge signals for the BWOFF are given in Figure 9-81.



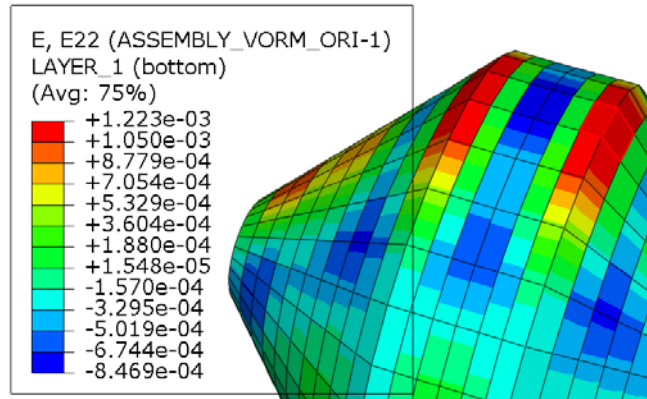
**Figure 9-81 BWOFF fracture; signals of four strain gauges; ML0\_1, MD0\_1, ML0\_2 and MD0\_2.**

Figure 9-82 shows the calculated longitudinal strain distribution on the inner side of the buoy without foam during the one hour creep test at 450 kN and Figure 9-83 shows the transverse strain distribution. The red squares in both distributions mark the location of ‘group one’ of the strain gauges.

Figure 9-84 shows the calculated longitudinal strain distribution on the inner side of the buoy without foam at 880 kN and Figure 9-85 shows the transverse strain distribution. The red squares in both distributions mark the location of ‘group one’ of the strain gauges.



**Figure 9-82 Longitudinal strain distribution in the inner layer of the BWOFF at 450 kN.**



**Figure 9-83** Transverse strain distribution in the inner layer of the BWOFF at 450 kN.

Again, as for the BWF, the finite element calculations seem to over predict the measurements of the first group of strain gauges of the BWOFF during the one hour creep test at 450 kN with the exception of the MD0\_1 strain gauge where the calculated value is an under prediction of the measurement. However, it should be noticed that the strain gauge ML0\_1 stays about constant at -200 microstrain which could indicate that it is broken. Additionally, the strain gauge MD0\_2 falls down to zero after a short while which could also mean it has broken. For this first zone it could be concluded that only the ML0\_2 and the MD0\_1 gave useful results.

The finite element calculations over predict the measurements of the first group of strain gauges of the BWOFF at 880 kN with the same exception as during the creep test, the MD0\_1 strain gauge, where the calculated value is a small under prediction of the measurement.

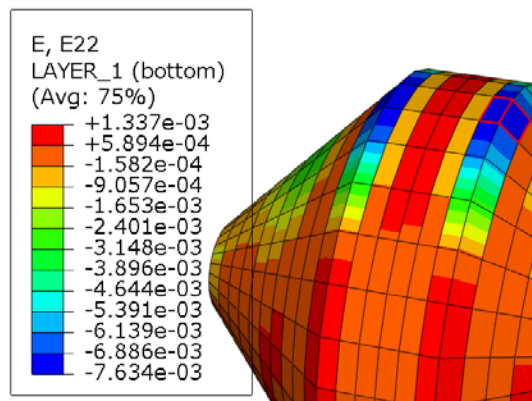


**Figure 9-84** Longitudinal strain distribution in the inner layer of the BWOFF at 880 kN.

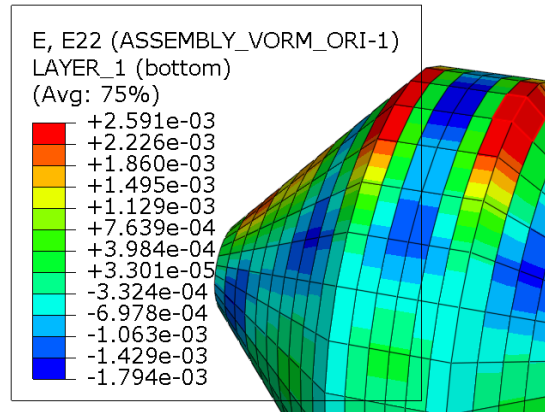


**Figure 9-85** Transverse strain distribution in the inner layer of the BWO at 880 kN.

In Figure 9-86 and Figure 9-87 the signals of a second group (ML0\_3, MD0\_3, ML0\_4 and the MD0\_4 strain gauges) for the BWF are given.

Figure 9-88 shows the calculated longitudinal strain distribution on the inner side of the buoy with foam at 450 kN and Figure 9-89 shows the transverse strain distribution. The red squares in both distributions mark the location of ‘group two’ of the strain gauges.

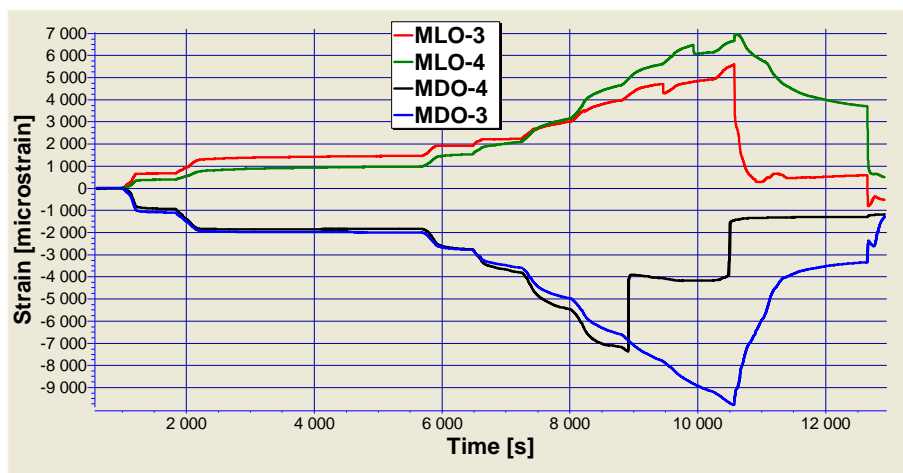


**Figure 9-86** BWF fracture; signals of ML0\_3, MD0\_3, ML0\_4, MD0\_4; valid up to 9000 s which is 1000 kN in this experiment.

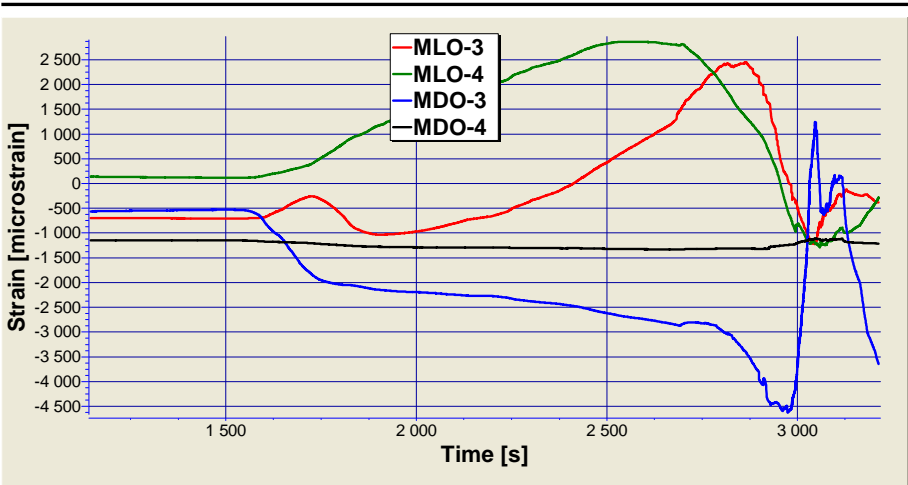


Figure 9-87 BWF fracture; signals of ML0\_3, MD0\_3, ML0\_4, MD0\_4; valid between 2600s (1000kN) & 3000s (1280kN).

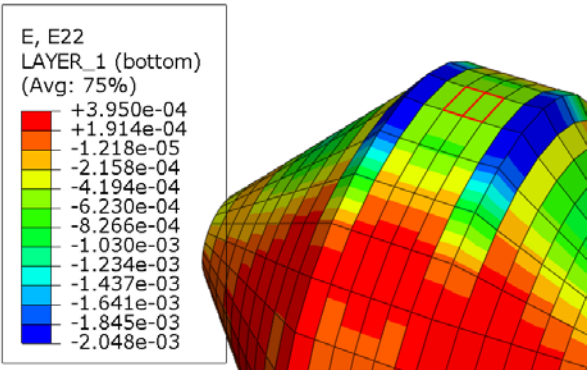


Figure 9-88 Longitudinal strain distribution in the inner layer of the BWF at 450 kN.

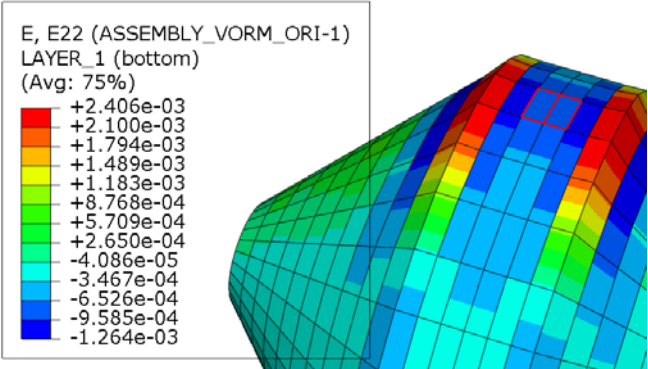
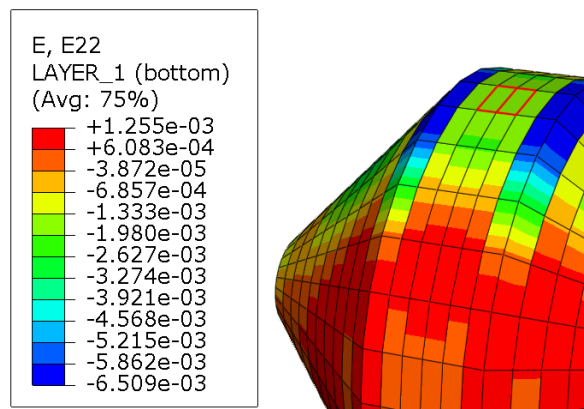


Figure 9-89 Transverse strain distribution in the inner layer of the BWF at 450 kN.

The measurements of the transverse strain gauges of this second group of the BWF during the one hour creep test at 450 kN match well with the finite element calculations. However, the calculations seem to under predict (35 %) the measurements. The two longitudinal strain gauges do not match; in the calculations a negative value occurs while in the measurements it is positive.

Figure 9-90 shows the calculated longitudinal strain distribution on the inner side of the buoy with foam at 1320 kN and Figure 9-91 shows the transverse strain distribution. The red squares in both distributions mark the location of ‘group two’ of the strain gauges. The measurements of the strain gauges of this second group of the BWF at fracture are lower than the finite element calculations. Hence, the calculations over predict the measurements but the trends are again correct.



**Figure 9-90** Longitudinal strain distribution in the inner layer of the BWF at 1320 kN.

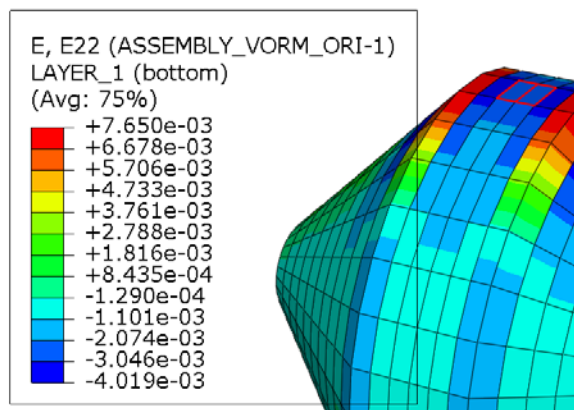


**Figure 9-91** Transverse strain distribution in the inner layer of the BWF.

The same group of strain gauge signals for the BWOFF is given in Figure 9-92. The longitudinal and transverse strain distribution is given respectively in Figure 9-93 and in Figure 9-94.

The measurement of the perpendicular strain gauges of this second group of the BWOFF during the one hour creep test at 450 kN are about a factor 3 higher than the calculations. The longitudinal strain gauge measured 600 microstrain while 300 microstrain was calculated.

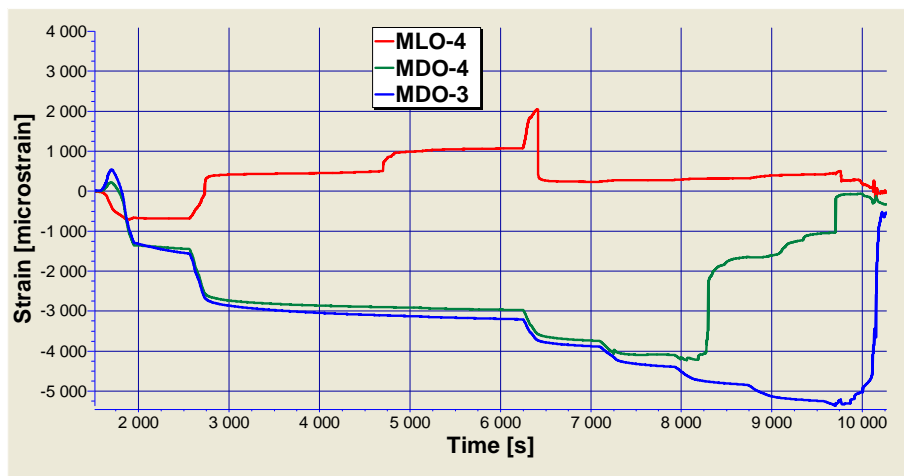


Figure 9-92 BWOFF fracture; signals of four strain gauges; ML0\_3, MD0\_3, ML0\_4, MD0\_4.

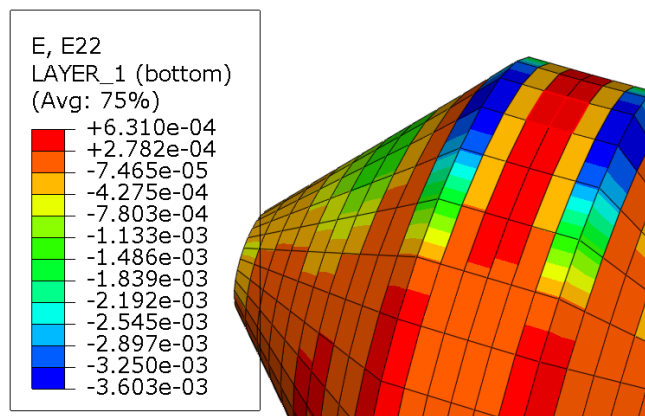
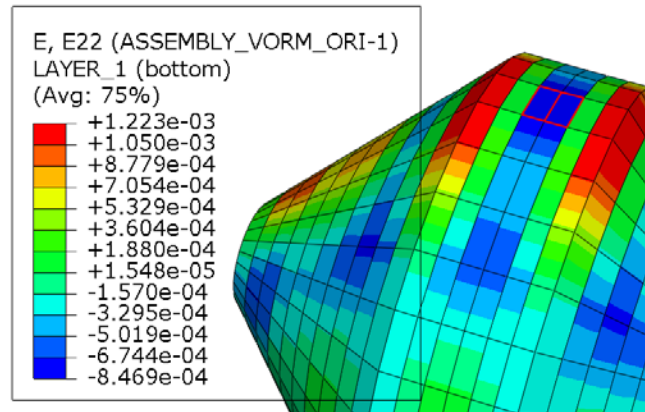


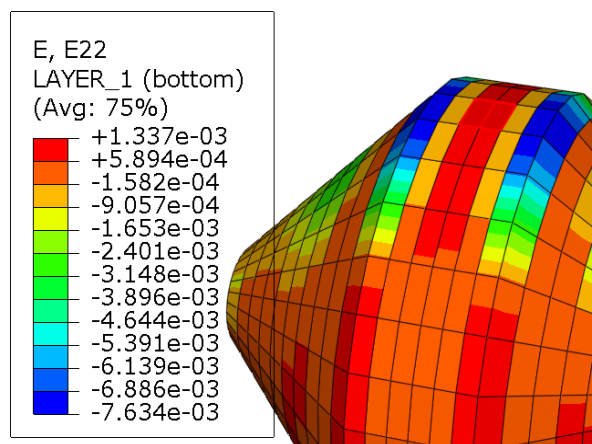
Figure 9-93 Longitudinal strain distribution in the inner layer of the BWOFF at 450 kN.



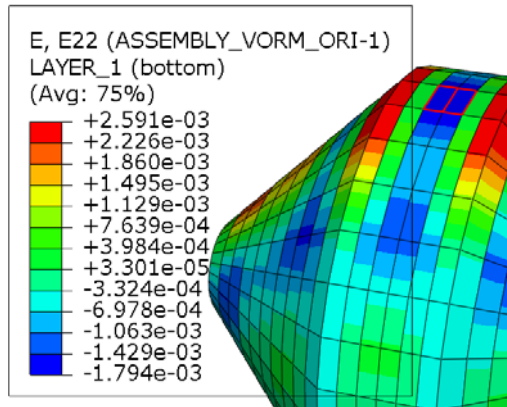
**Figure 9-94** Transverse strain distribution in the inner layer of the BWOFF at 450 kN.

Figure 9-95 shows the calculated longitudinal strain distribution on the inner side of the buoy without foam at 880 kN and Figure 9-96 shows the transverse strain distribution. The red squares in both distributions mark the location of ‘group two’ of the strain gauges.

The measurements of the perpendicular strain gauges of this second group of the BWOFF at 880 kN are an under estimation of for the transverse strain gauges. One matches very well while the other is a factor 3 higher. For the longitudinal strain gauge the experimental value (700 microstrain) is about the same as in the finite element calculation (600 microstrain).



**Figure 9-95** Longitudinal strain distribution in the inner layer of the BWOFF at 880 kN.



**Figure 9-96** Transverse strain distribution in the inner layer of the BWO at 880 kN.

In Figure 9-97 and Figure 9-98 the measurements of the ML20\_1, MD20\_1, ML20\_2, MD20\_2, ML20\_3 and the MD20\_3 for the BWF are given.

Figure 9-99 shows the calculated longitudinal strain distribution on the inner side of the buoy with foam during the one hour creep test at 450 kN and Figure 9-100 shows the transverse strain distribution. The red squares in both distributions mark the location of ‘group three’ of the strain gauges.

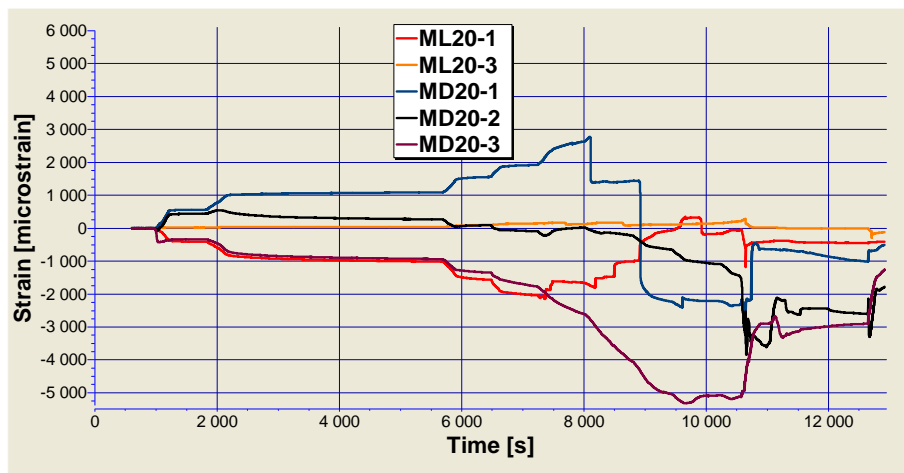


**Figure 9-97** BWF fracture; signals of ML20\_1, MD20\_1, MD20\_2, ML20\_3 and the MD20\_3; valid up to 9000 s (1000 kN) .

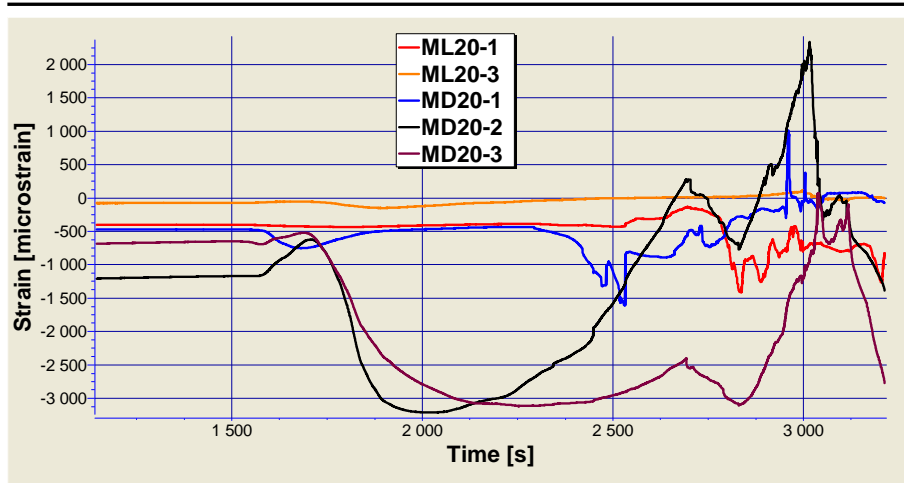


**Figure 9-98** BWF fracture; signals of ML20\_1, MD20\_1, ML20\_2, MD20\_2, ML20\_3 and the MD20\_3; valid between 2600s & 3000s (1280kN).

The calculations of the strain gauges of the ML20\_1 and the MD20\_1 of the BWF at 450 kN over predict the measurements during the one hour creep test with about a factor two. The MD20\_3 gives a rather strange result (300 microstrain) while it should be 2400 microstrain. Two strain gauges, the ML20\_2 and the ML20\_3 failed. For the MD20\_3 about the same value is found (4%).

Figure 9-101 shows the calculated longitudinal strain distribution on the inner side of the buoy with foam at fracture and Figure 9-102 shows the transverse strain distribution. The red squares in both distributions mark the location of ‘group three’ of the strain gauges.

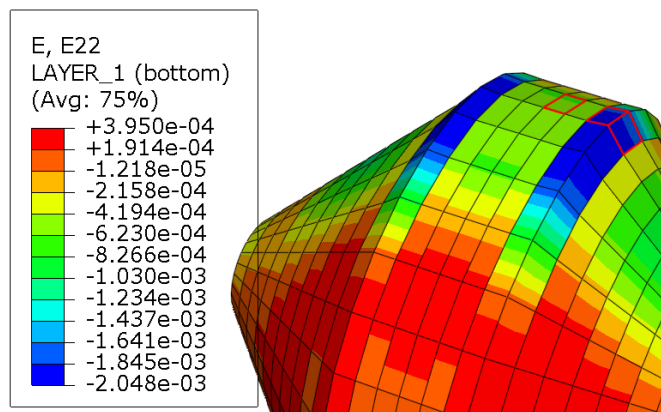


**Figure 9-99** Longitudinal strain distribution in the inner layer of the BWF at 450 kN.

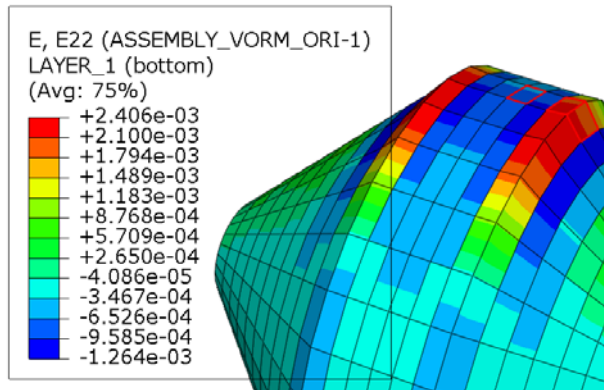


**Figure 9-100** Transverse strain distribution in the inner layer of the BWF at 450 kN.

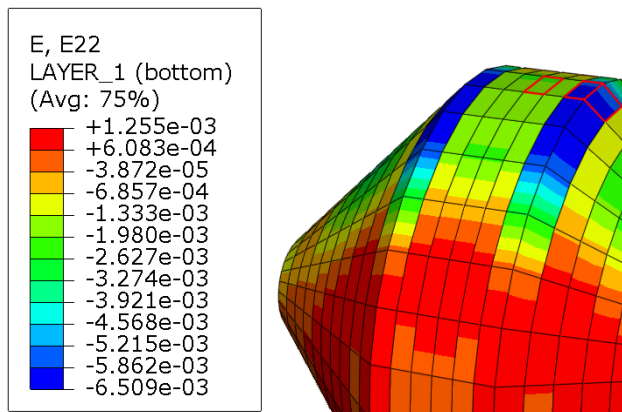


**Figure 9-101** Longitudinal strain distribution of the inner layer of the BWF at 1320 kN.

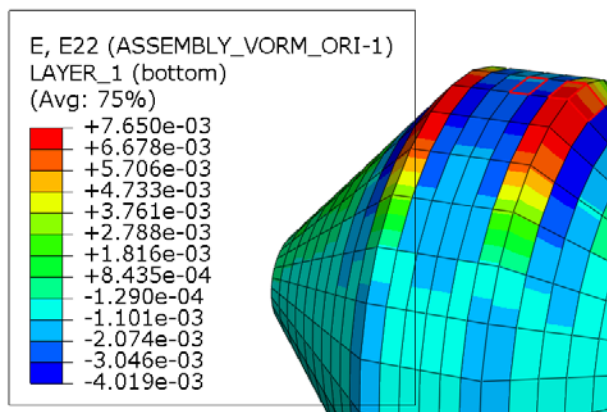


**Figure 9-102** Transverse strain distribution of the inner layer of the BWF at 1320 kN.

The measurements of the strain gauges of this third group of the BWF at 1320 kN are at least a factor two lower than the finite element calculations. Hence, the calculations over predict the measurements. The two strain gauges that failed at 450 kN, the ML20\_2 and the ML20\_3, did of course not work at 1320 kN.

Again, the same group of strain gauge signals for the BWOFF are shown in Figure 9-103.

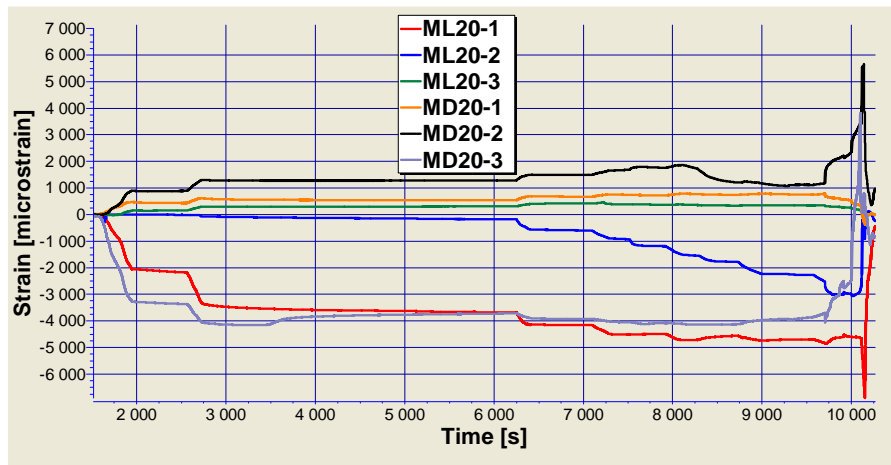


**Figure 9-103** BWOFF fracture; signals of five strain gauges; ML20\_1, MD20\_1, ML20\_2, MD20\_2, ML20\_3 and the MD20\_3.

Figure 9-104 shows the calculated longitudinal strain distribution on the inner side of the buoy without foam during the creep test of one hour at 450 kN and Figure 9-105 shows the transverse strain distribution. The red squares in both distributions mark the location of ‘group three’ of the strain gauges.

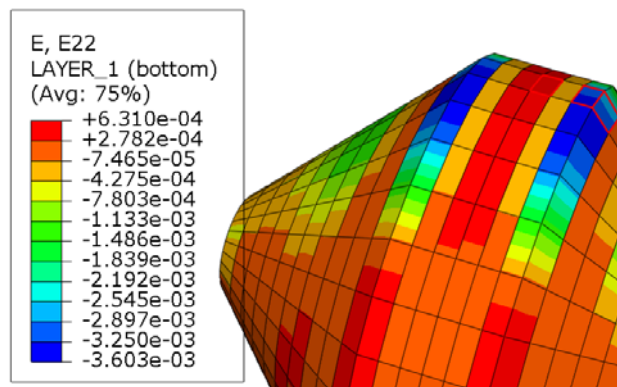


**Figure 9-104** Longitudinal strain distribution in the inner layer of the BWOFF at 450 kN.

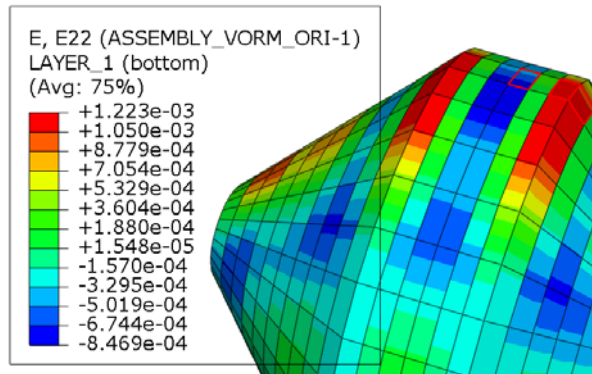


**Figure 9-105** Transverse strain distribution in the inner layer of the BWOFF at 450 kN.

Some of the measurements of four of the strain gauges of this third group of the BWOFF during the one hour creep test at 450 kN match well with the finite element calculations (from 0 up to 50 %). However, two signals differed a lot from the calculations; the ML20\_2 was over predicted in such a way that they did not match at all (-200 microstrain experimental and -3250 microstrain simulated) and the MD20\_3 under predicted with a factor 4.

Figure 9-106 shows the calculated longitudinal strain distribution on the inner side of the buoy without foam at 880 kN and Figure 9-107 shows the transverse strain distribution. The red squares in both distributions mark the location of ‘group three’ of the strain gauges. The measurements of the strain gauges of this third group of the BWOFF for the fracture test at 880 kN were over predicted by the finite element calculations except for strain gauge MD20\_3 which was under predicted with 53 %.

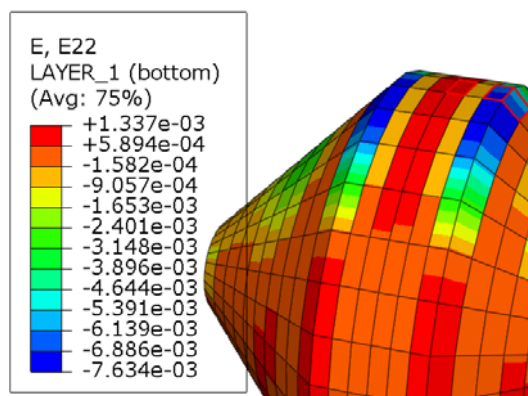


**Figure 9-106** Longitudinal strain distribution in the inner layer of the BWOFF at 880 kN.

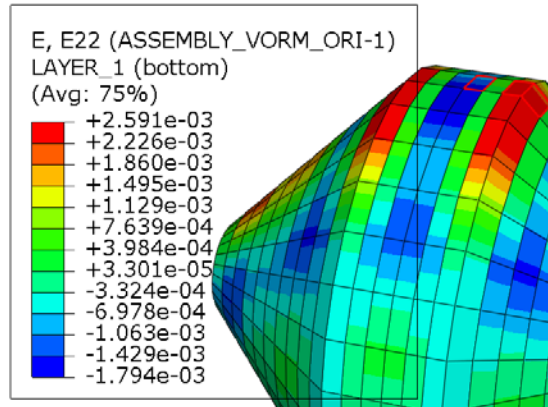


**Figure 9-107** Transverse strain distribution in the inner layer of the BWF at 880 kN.

#### 9. 4. 4. LVDT sensors

The third and final sensor results for the fracture tests are the results of the LVDT sensors. Those are given, again for both buoys, and explained where possible. Again, as for the results of the strain gauges for this buoy, the results of the first test of the BWF can not be considered correct for a load higher than 1000 kN (9000 s). As was explained earlier within this paragraph, a second faster test was done with the help of metal discs. It is the results at fracture hence of this second experiment that are assessed here. For this buoy the sensors were located as is shown in Figure 9-108. The solar 50-1 and solar 50-2 were mainly used for safety reasons.

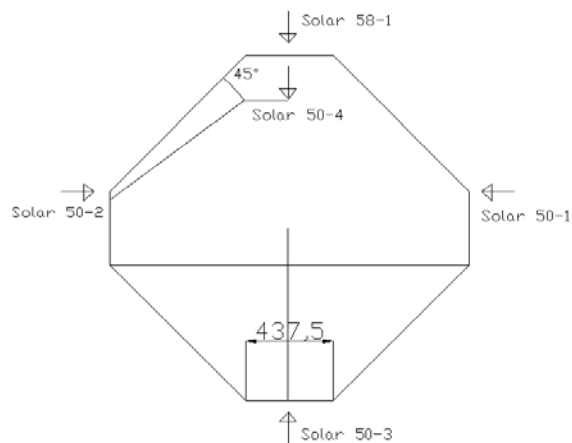


**Figure 9-108** Positions of the LVDT sensors for the BWF fracture.

The solar 58-1 is situated on top of the buoy while the solar 50-3 is mounted on the bottom of the buoy. The solar50\_4 measures the displacement at the 45 degrees

meridian next to the shell. As is expected lower and upper LVDT sensors give a similar but opposite displacement as is also shown in Figure 9-109. The displacement is a relative signal hence here an increase in signal is a positive displacement and a decrease a negative one.

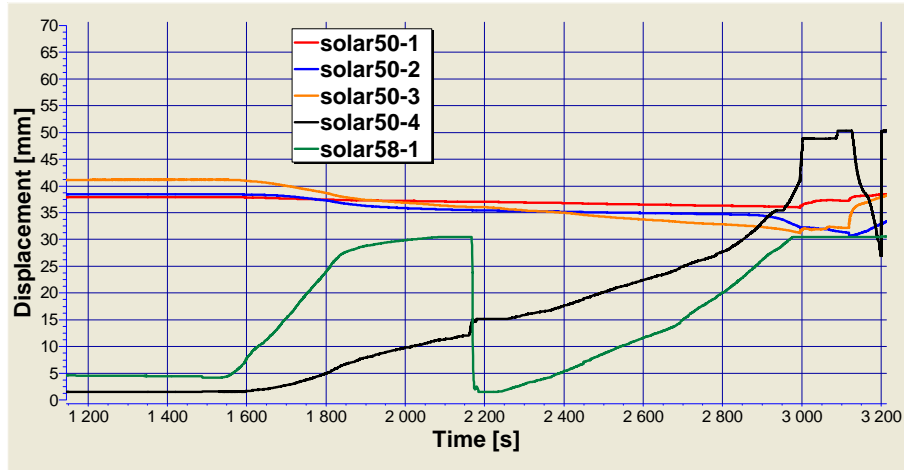


**Figure 9-109** BWF; Signals of the five LVDT sensors; second BWF fracture test.

The displacement of the lower sensor is about -10 mm. The finite element simulations as is shown in Figure 9-110. The red squares mark the location of the sensor. The calculated displacement value is -6.8 mm which is in good agreement with the measurement. However, it slightly under predicts the real value.

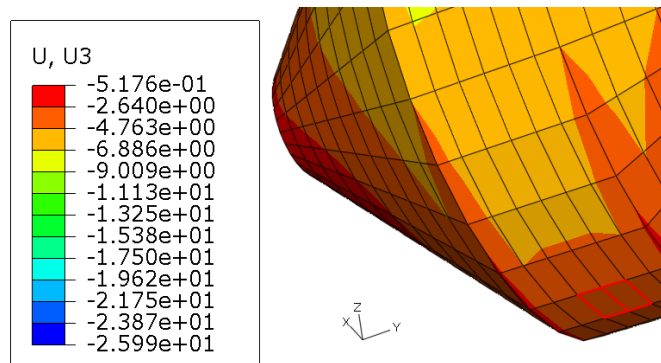


**Figure 9-110** Distribution of the vertical displacement; red squares show the location of the solar 50-3.

Next, in the finite element simulation one of the edges is fixed. Hence, the axial displacement on the other side can be compared with the subtraction of the solar 50-

2 and the solar 50-1. The result of this subtraction equals 4 mm. The value of the simulation is 3.8 mm which is in very good agreement with the measurements.

The positions of the LVDT sensors for the fracture test on the BWOFF are given in Figure 9-111. Next, in Figure 9-112 the signals of the five LVDT sensors are shown for the BWOFF.

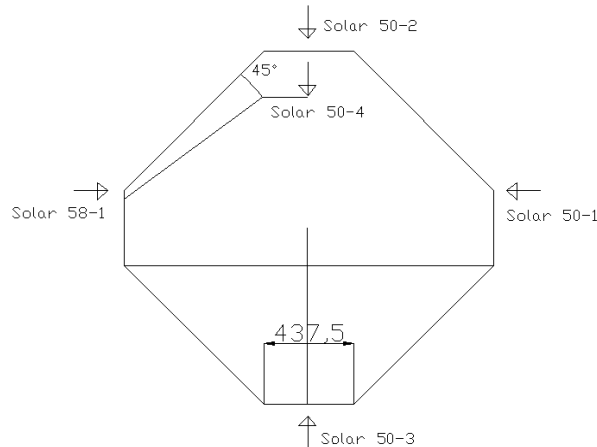


**Figure 9-111** Positions of the LVDT sensors for the BWOFF fracture.

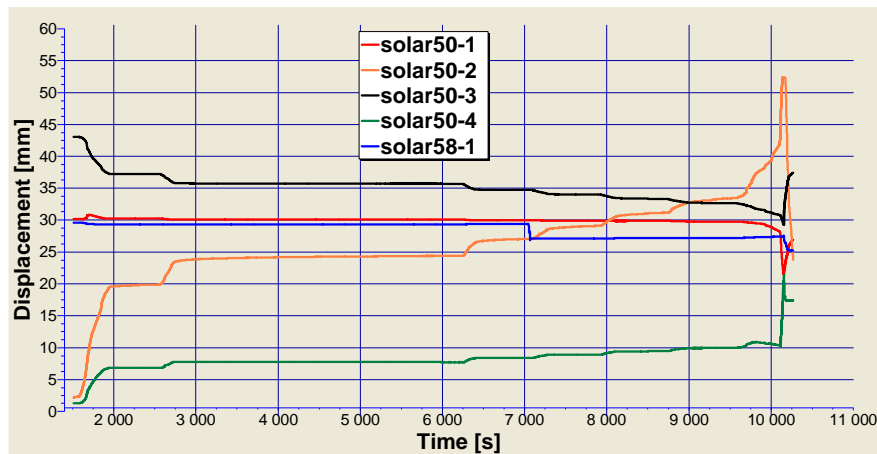


**Figure 9-112** BWOFF; Signals of the five LVDT sensors.

Again, the upper (now the solar 50-2 and the solar 50\_4) and lower (solar 50-3) LVDT sensors give a similar but opposite displacement. Again, an increasing curve means a positive displacement and a decreasing curve a negative displacement. The solar 50-4 is on top of the buoy but it measures the displacement just near the shell, which means at the 45 degrees meridian. At the bottom of the point absorber, the maximum displacement of the solar 50-3 is about -14 mm which is in good

agreement with the simulation shown in Figure 9-113. The red squares mark the location where the LVDT sensor is situated and there a value of -10 mm was calculated. However, again the simulations under predict the measured value.

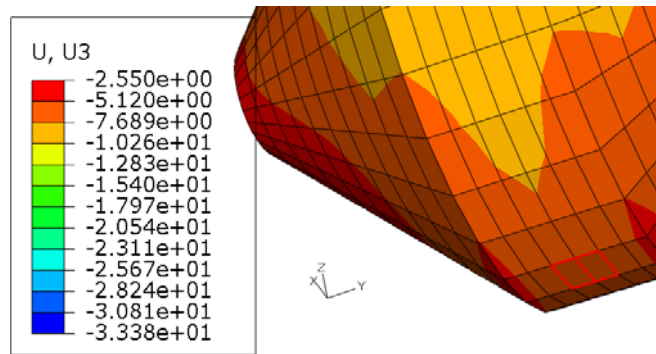


**Figure 9-113 Distribution of the vertical displacement, the red squares mark the location of LVDT ‘solar 50-3’ with a displacement of -10 mm.**

As for the BWF, the axial displacement on one side in the simulation can be compared with the subtraction of the two axial LVDT sensors, here solar 50-1 and solar 58-1. This subtraction results in 4 mm while the simulated value is 4.2 mm.

Several issues were dealt with in this extensive testing program. We learned that the indoor strain gauges and LVDT sensors at start of the fatigue test were of the same order of magnitude as the simulations. Next, for the outdoor drop test the results of the pressure sensors were important. Here it was shown that the pressure at zero degrees is a lot lower for the more deformable buoy. Important consequence is that there could be opted for the BWOF at full scale while with the DNV norm this is not an option at all. However, this decision stays of course nuanced. Also, the trends in the strain gauge measurements were, as expected, higher in the cylindrical part of the buoy and lower on and near the cones. Finally, for fracture the strain gauges measurements showed the same trends as in the finite element calculations but in value some of them matched but others differed quite a lot (factor 2 or 3). This could be due the fact that, at the time of this fracture test, the strain gauges and their connection survived already an extensive testing program. The fact that the axial and vertical displacement did match and additionally the load at fracture was very accurate for both buoys is in favour of that explanation.

## 9. 5. REFERENCES

1. I. De Baere, Experimental and Numerical Study of Different Setups for Conducting and Monitoring Fatigue Experiments of Fibre-Reinforced Thermoplastics, Ghent University, PhD dissertation, 2008.
2. G. DeBacker, Optimisation of a wave energy converter for south Nordsea conditions, Ghent University, Faculty of Engineering, PhD in preparation, foreseen for end 2009, .
3. M.-C. Lin and L.-D. Shieh, Flow visualization and pressure characteristics of a cylinder for water impact. Applied Ocean Research, 1997. 19: p. 101-112.
4. K. Stoop and S. Vermeulen, Numerieke simulatie van de vloeistof-structuur interactie bij hydrodynamische impact, Ghent University. Faculty of Engineering, Master thesis academic year 2007-2008.



## Chapter 10

### CONCLUSIONS AND FUTURE RESEARCH

*In this chapter, the most important conclusions are summarised and some ideas for future research are given.*

#### 10. 1. CONCLUSIONS

This doctoral research was about composite floating ‘point absorbers’ for wave energy converters (WEC). The focus laid on the survivability design, production method and large-scale testing. The work done is situated within the Seewec project of the European sixth framework. Within this WEC structure there are vertical moving point absorbers (or buoys) present to absorb the energy of the waves. Composite materials were proposed materials for these buoys. For the survivability design a very critical load is ‘slamming’. Slamming is a phenomenon, known in the maritime sector, as the repeated short impact of water on a floating or sailing structure. The buoys suffer from both bottom and breaking wave slamming. In the calculations the acknowledged DNV norm is used which means that a constant pressure is applied on a sector of the buoy.

In this way the first objective to establish a finite element model with composite layers to withstand slamming was met. Finite element calculations were performed on several shapes such as an egg, tulip, pencil and a smaller cone/cylinder/cone shape. On these shapes calculations were done with bottom and breaking wave slamming according to the DNV standards with and without internal stiffeners, foam core and for both proposed materials (SMC/STY). Finally, this has lead to the proposal of a ‘cone/cylinder/cone’ shape. According to the DNV load a sandwich buoy, with skins consisting out of four layers composite and PVC core in the middle, was suitable to withstand the DNV slamming load. Nevertheless, the production of a sandwich buoy was a more cost consuming method.

A second objective of this dissertation was choosing an effective production method. For this continuous interaction occurred with Spiromatic for filament winding and in a lesser extent with Standfast Yachts for vacuum infusion. Also, preparations were made to perform slamming tests (drop experiments) on laboratory scale. The existing filament winding machine was made up to date and a slamming set-up was designed and built which was also an objective. Most test objects were made on the filament winding machine. For the final shape of the point absorber, a cone/cylinder/cone a special production technique focussing on re-using the mandrel was proposed. This method used a re-usable cone mandrel which was used to produce two cones of the same point absorber. Next, these two were mounted over a

filament wound composite tube. Finally, this whole was over wound with the proposed layers. The production ‘method of the cones’ was used on laboratory scale as well as on large scale and has proven viable.

Gaining experience of the mechanical behaviour of composites under slamming loads, another important objective of this dissertation, was done by performing a relevant literature survey, experimental testing on several shapes and by using numerical methods. Laboratory scale testing was done on four chosen test objects: a cone with deadrise angle of 45 degrees, a rigid and a hollow cylinder and a scaled shape of the cone/cylinder/cone point absorber. The peak value in literature is higher than the measured value hence the models are conservative. The same was the case in the numerical model of Peseux and his experiments. Also, the cone simulations of Stoop & Vermeulen for the cone were conservative. This is probably due to the fact that the cone is rigid in the simulations but in reality never is entirely rigid. Additionally, in the models a constant impact velocity was applied while in experiments a decrease occurs. Also, incompressibility was assumed. Hence, for the cone of 45 degrees it could be concluded that the 3D Wagner formulation for the peak pressure as well as the DNV constant pressure are conservative. Next, two cylinders (a rigid and deformable one) were tested. The main finding is that the peak pressure is almost a factor two lower for the hollow cylinder than for the rigid one. Note that the impact of an object on a water surface is a fluid structure interaction problem. The hydrodynamic pressures that occur at water entry of the body, lead to deformations of that body. Additionally, these deformations influence the pressures and at the Department of Fluid Dynamics also at Ghent University, the first calculations done on the rigid and deformable cylinder showed again that the dimensionless pressure coefficient drops down with about a factor two. Hence, simulations and experiments both show that the peak pressure is a lot lower for the deformable cylinder which is a very important finding. The cylinder experiments and VOF calculations showed that the DNV constant pressure should be used with caution since this constant pressure underestimates the peak pressure. Hence, the influence of a very high local peak pressure on material behaviour should be considered in the design of cylinder shaped point absorbers. It could also be reflected on using different slamming coefficients according to the kind of material used.

Next, the production and testing of two large-scale point absorbers has been done. Especially to assess the influence of the deformability on the peak pressures a buoy with foam (BWF) with four wound layers, PVC foam and again four wound layers and a buoy without foam (BWOF) with seven wound layers were made. An extensive testing program was foreseen on both samples to simulate breaking wave

---

slamming. Fatigue, slamming and fracture tests were done to achieve as much data as possible with these two large scale samples.

The fatigue and fracture tests were done indoor in the laboratory Magnel at Ghent University. During these tests, the applied force, strain gauges and displacement sensors were measured. In these tests, the point absorber is loaded on its side, over a sector segment of 60 degrees which is an experimental simulation of the breaking wave slamming. The force used for the fatigue experiments equals the yearly storm condition for the proposed sea climate. Both the measurements of the strain gauges and the LVDT for the fatigue tests are in the same order of magnitude of the finite element calculations. However, the absolute values of the strain gauges were only accurate at the beginning of the experiment. Later on, drift occurred and there was only looked at the decreasing or increasing of the amplitudes. For the fracture tests a building-up load program was applied. The first step was a load of 300 kN (equal to the load used for the fatigue test). Once it was stable, the load was increased up to 450 kN. Next step was 600 kN and from then on the load was increased further in steps of 100 kN. Each load step lasted for ten minutes with one exception at 450 kN which lasted longer (about one hour) since that load could be considered equal to the 25 year storm which is calculated from the DNV norm. There, the strain gauges were compared with finite element simulations and were again in the same order of magnitude. Next, both buoys broke very near the predicted fracture load. Also at these loads, the measurements of the strain gauges and the displacement sensors are in the same order of magnitude of the simulations. The location of fracture was the same one as predicted.

The slamming experiments, or 'drop tests', were done on the '*Watersportbaan*' which is a canal in Ghent. During these tests, strain gauges, pressure sensors and an accelerometer were measured. All outdoor experiments were registered with the high speed camera. The impact velocity was determined by means of a shock accelerometer. Lateral drop tests were done at 4.8 meter for both buoys which equals about the celerity of the 1 year storm for the proposed sea climate. Again, the values of the strain gauges match quite well with the simulations. However, the measured deformations in the cylindrical part of the buoy are larger than calculated and in the conical part it is the other way around. This was expected since now the simulations are the ones which use the DNV standards hence a constant pressure which is lower than measured in the cylindrical part of the buoy and higher on the cones. The maximum peak dimensionless pressure coefficient for the BWF at zero degrees is 76 and for the BWOF 48. At thirty degrees, it is 7.4 for the BWF and 6.7 for the BWOF. Again, it is clear that the peak pressure decreases for more deformable structures. At thirty degrees there is not a lot of difference anymore between both

buoys. The last experiments carried out on the canal were drop tests from 7.2 meter at zero degrees which simulates the 25 year storm for the proposed sea climate. There the same conclusions were drawn concerning the measurements of the strain gauges and the simulations.

Note that the full scale BWOF model fails for the 25 year storm according to DNV. The BWF full scale model survives that load. For the conical areas and 30 degrees on the cylinder this DNV standard is conservative. However, for the 0 degrees the DNV underestimates the local peak pressure. This underestimation is worse for the BWF than for the BWOF. Also, the BWF is equal to an increase in production cost of about 25 % in comparison with the BWOF.

When the DNV constant pressure is used to assess slamming loads on cylinder shaped bodies (small scale cylinders and large scale buoys) it should be noted that the local peak pressure is not taken into account. In that case it may be better to opt for a more deformable cylinder to decrease the magnitude of such a peak pressure. Until now only fluid structure interaction calculations could take the extent of deformability into account. This is very difficult to simplify into a coefficient since the 'measure of deformability' is not easy to assess. Hence, the practical design of a point absorber to survive slamming loads should take the shape and the used material into account.

## 10. 2. FUTURE RESEARCH

After finishing this research there are still some topics worthy of further research. A project is already approved by the Fund for Scientific Research (*Fonds voor Wetenschappelijk Onderzoek*, FWO) which concerns slamming on composites.

One of the challenges of this sequel project is the effect of this very local peak pressure that moves very fast in time along the surface of the structure, on the local deformation of the composite material. Very often a composite structure is built up in a layered manner, with strongly anisotropic plies. The peak pressure due to slamming causes a sort of pressure wave that propagates through the thickness of the structure and can show strong discontinuities at the interface between different layers, what might lead to delaminations.

A second important area is about the kind of damage that is caused by the repeated wave impact in the composite structure and how this gradual deterioration of the composite material could be modelled in terms of maximum stresses/strains during one single slamming wave impact.

Also, the exact influence of the deformability of the composite structure on the slamming event is unknown, while taking into account the deformability of the structure can precisely lead to more efficient design, reduced material consumption and weight reduction.

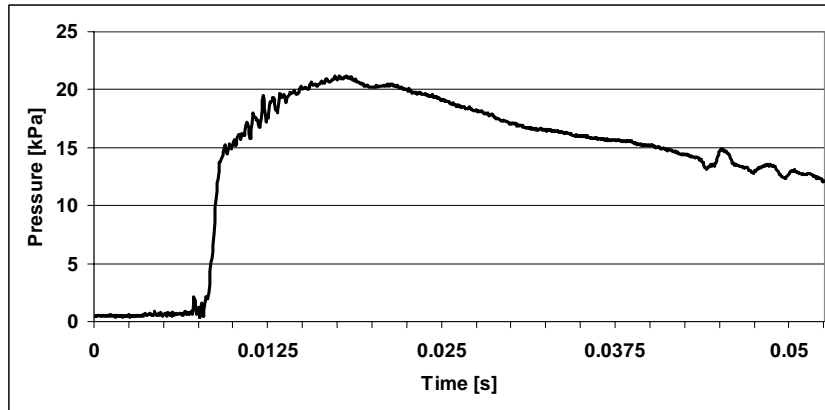
Finally, the simultaneous measurement of structural deformations and fluid motions has not been reported in international literature up till now. For the measurement of the motion fields in the water during the slamming event, a so-called Particle Image Velocimetry (PIV) set-up could be used. Therefore a sufficiently large concentration of tracking particles should be dispersed in the water volume. These tracking particles are monitored with the high speed camera which is measured simultaneously with the motion of the composite component which is important given the very short duration of the experiment. This work is planned within the sequel project and will be carried out by the Free University of Brussels.



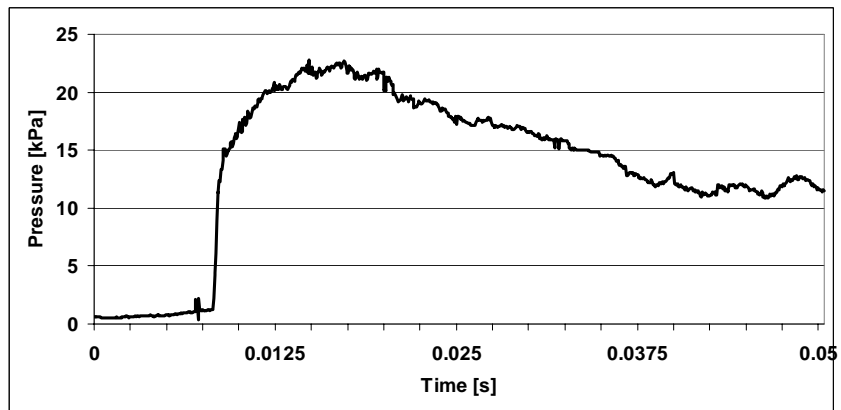
## PRESSURE TIME HISTORIES OF THE LABORATORY TESTS

Cone

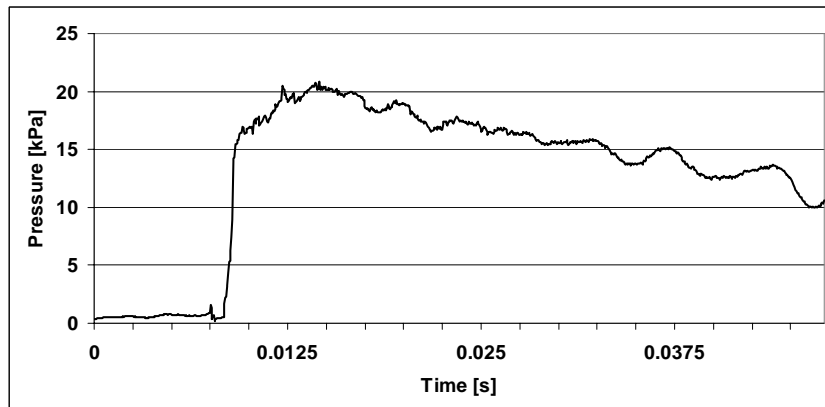
Test 1



Test 2



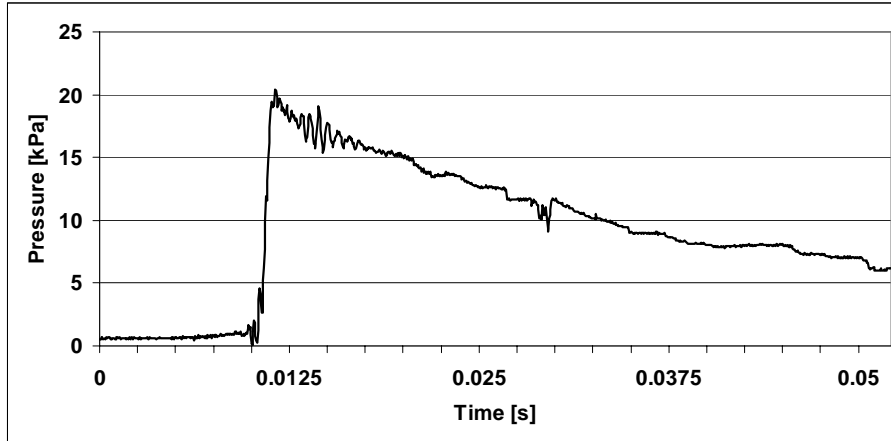
Test 3



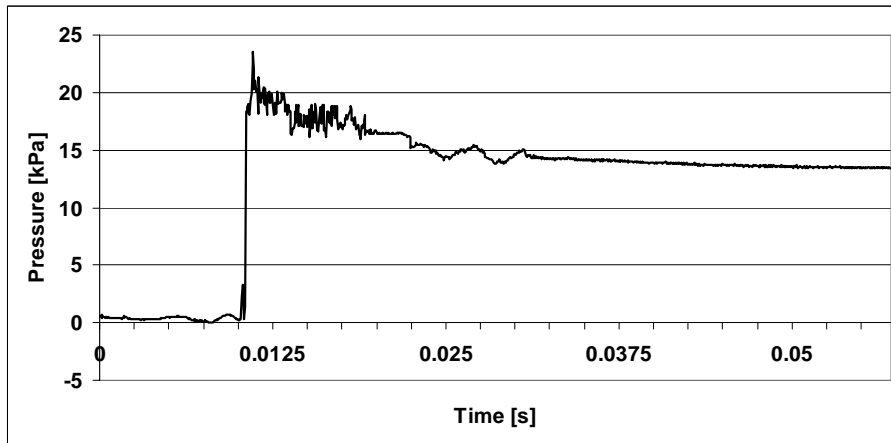
Appendix

---

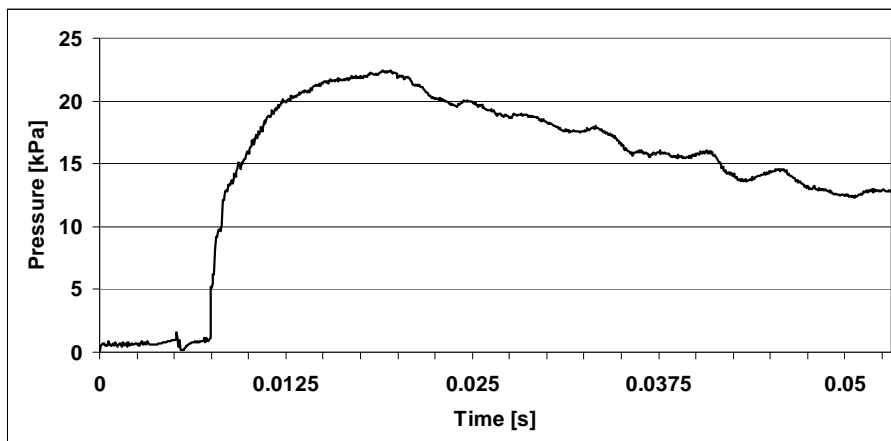
Test 4



Test 5



Test 6

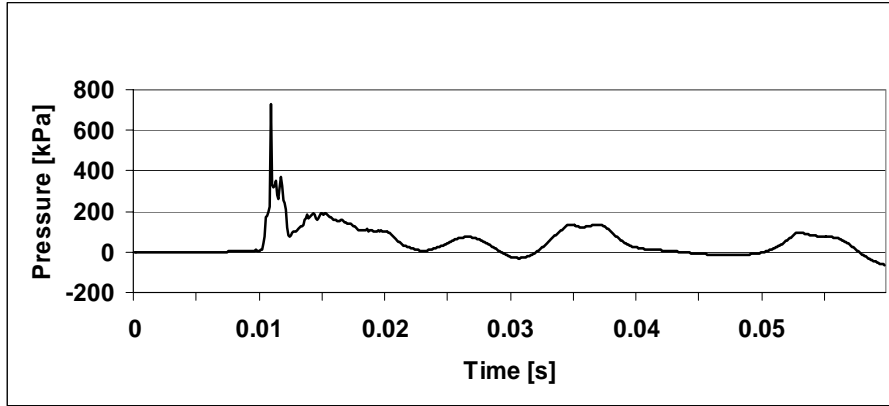


Appendix

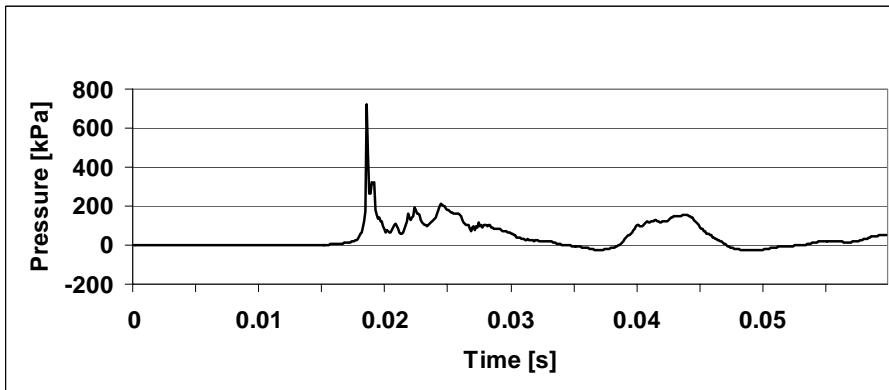
---

Full cylinder

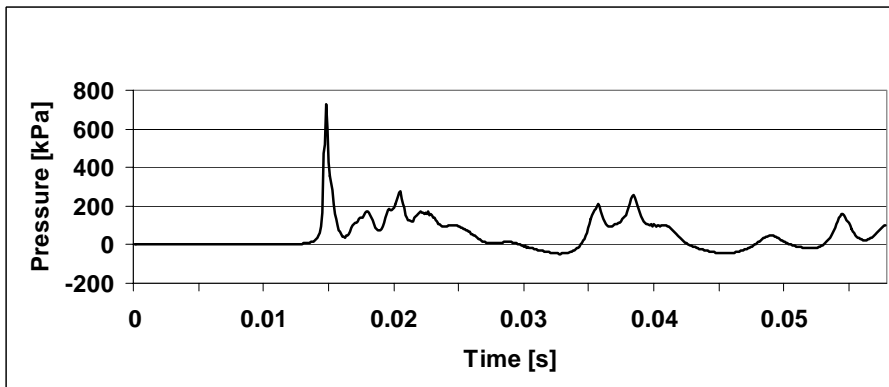
Test 1



Test 2



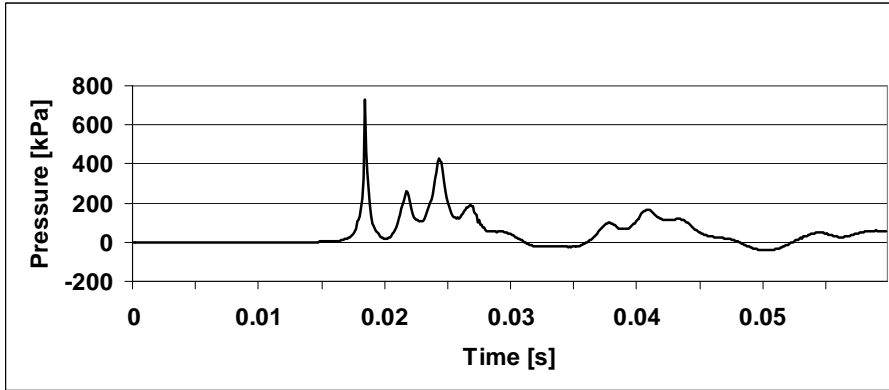
Test 3



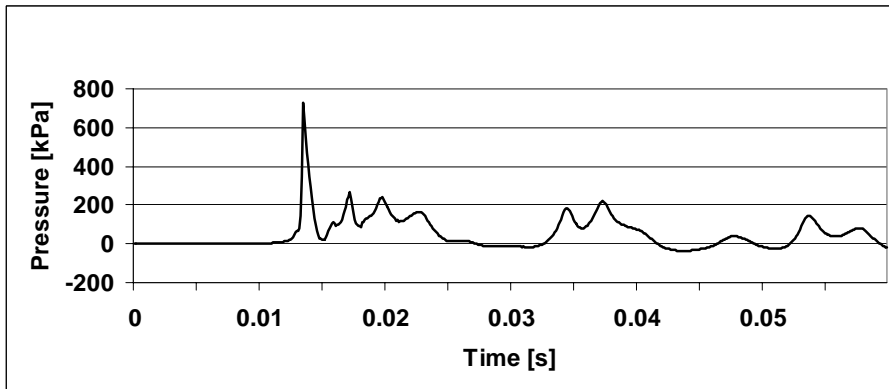
Appendix

---

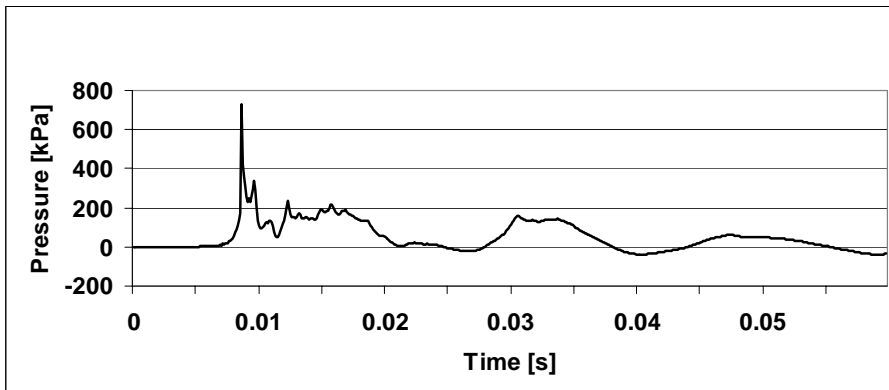
Test 4



Test 5



Test 6

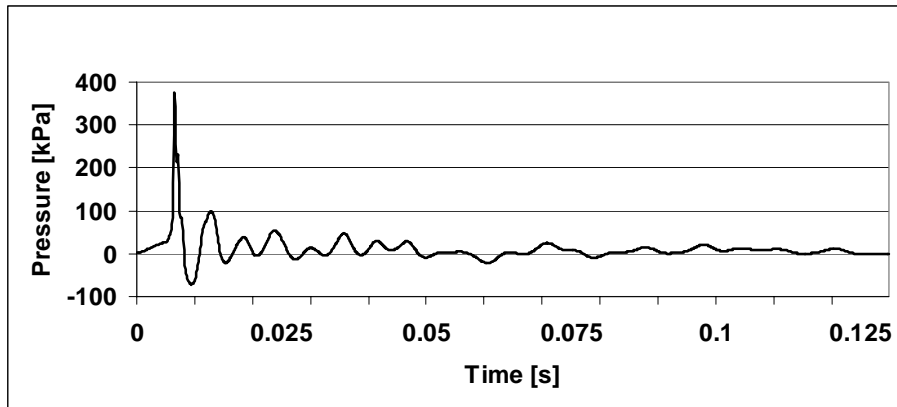


Appendix

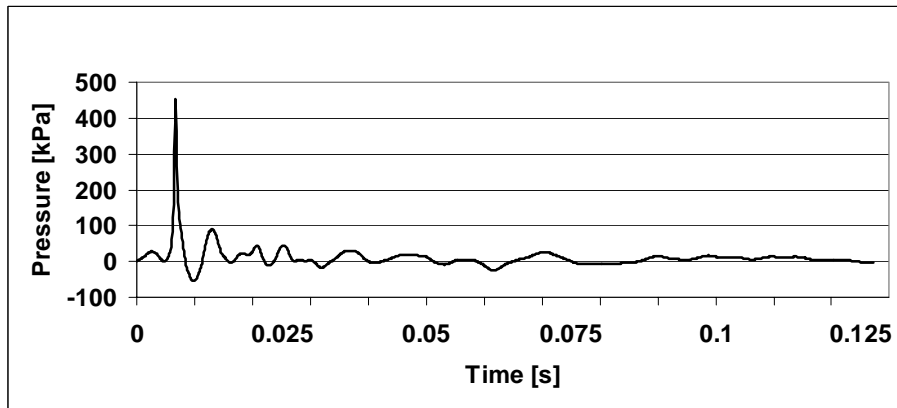
---

Hollow cylinder

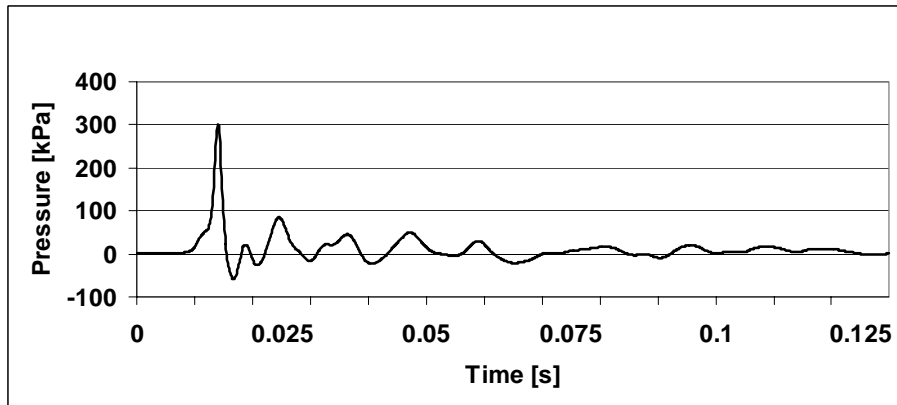
Test 1



Test 2



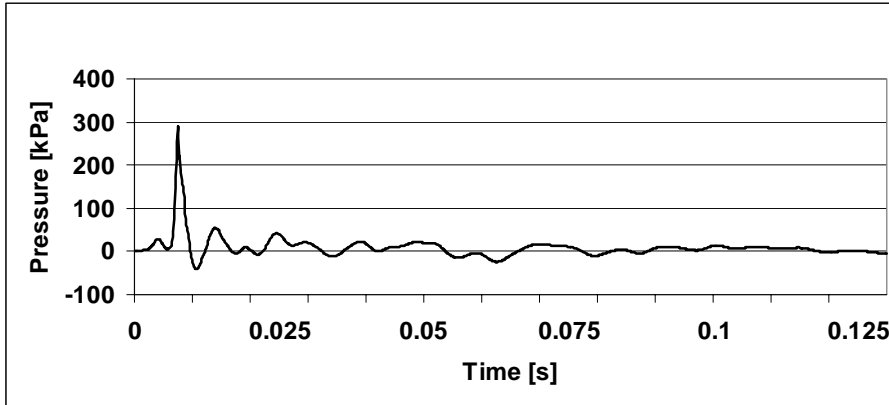
Test 3



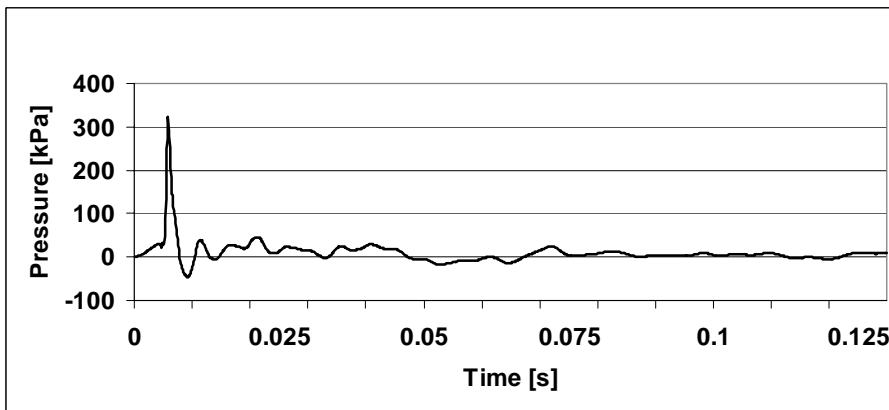
Appendix

---

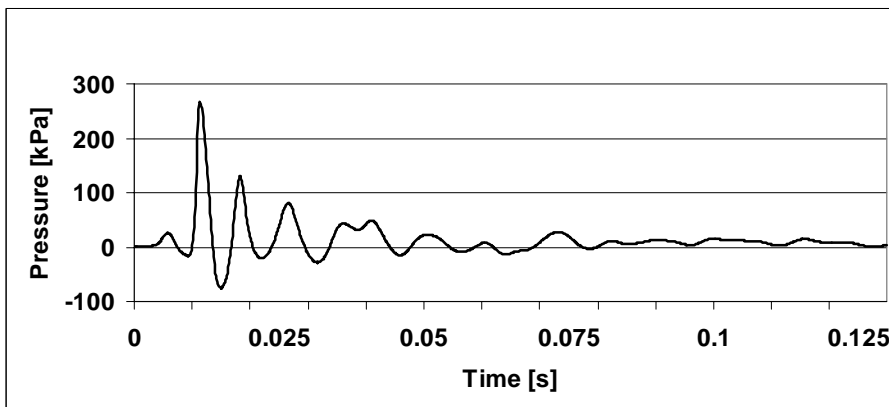
Test 4



Test 5



Test 6

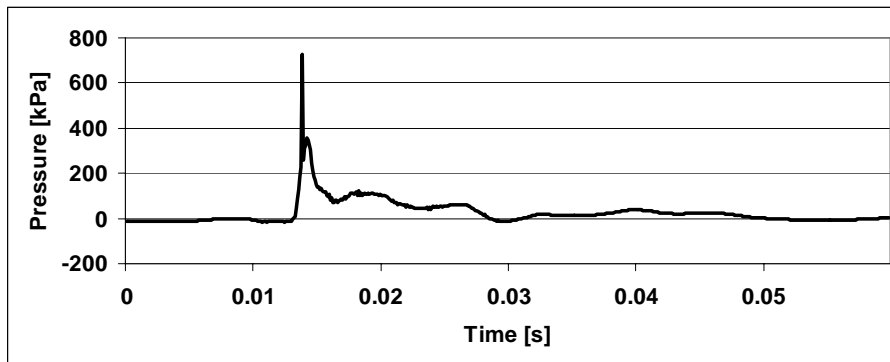


Appendix

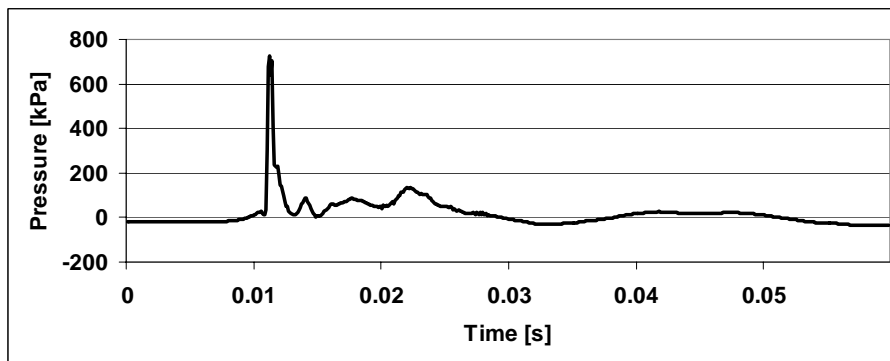
---

Small point absorber

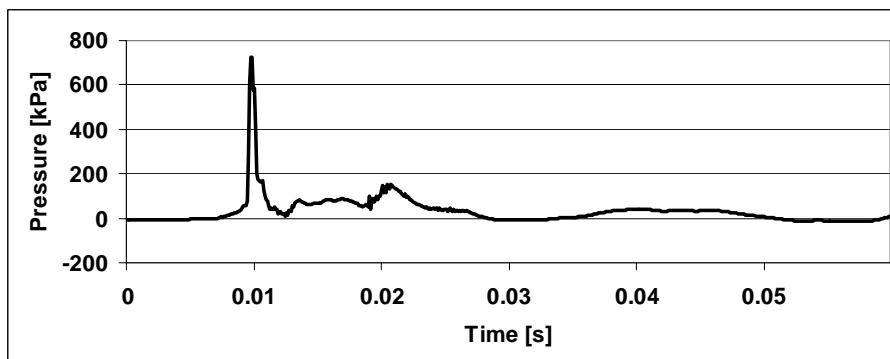
Test 1



Test 2



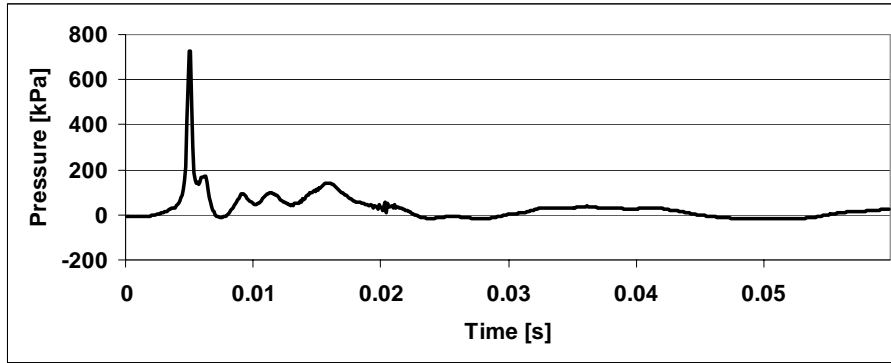
Test 3



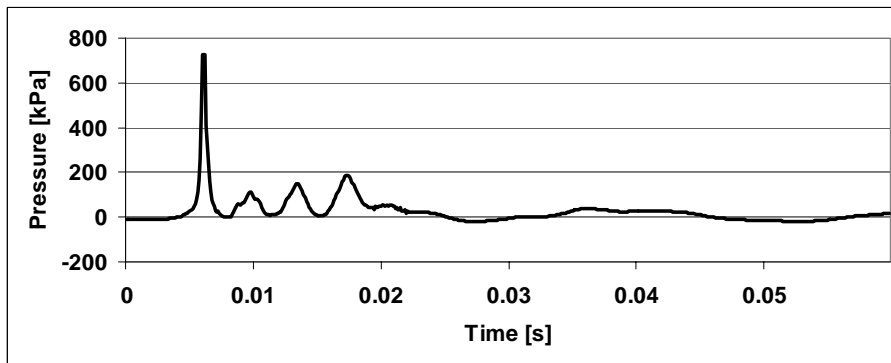
Appendix

---

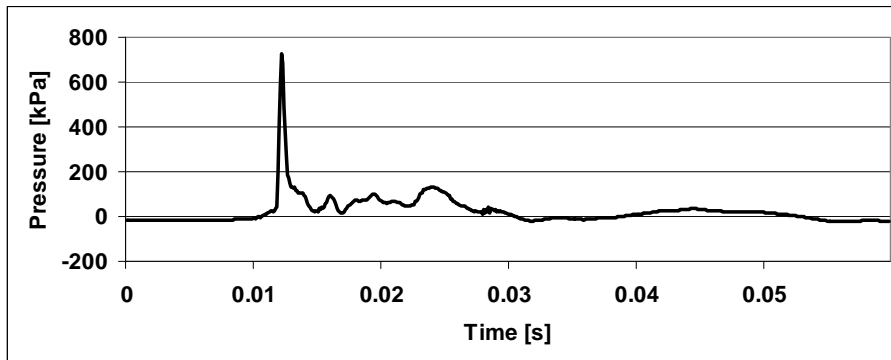
Test 4



Test 5



Test 6



## LIST OF PUBLICATIONS

### Publications in international journals of the Science Citation Index (SCI)

- [2009-1] Blommaert, C., Van Paepegem, W. and Degrieck, J. (2009). Design of Composite Material for Cost Effective Large Scale Production of Components for Floating Offshore Structures. Accepted for *Special Issue of Plastics, Rubber and Composites: Macromolecular Engineering.*
- [2009-2] DeBacker, G., Vantorre, M., Beels, C., De Pre, J., Victor, S., De Rouck, J., Blommaert, C., Van Paepegem, W. (2009). Experimental Investigation of Water Impact on Axisymmetric Bodies. Accepted for *Applied Ocean Research.*

### Publications in conference proceedings

- [2008-1] Blommaert, C., Degrieck, J. and Van Paepegem, W. (2008). Design of composite material for cost effective large scale production of components for floating offshore structures. Proceedings of the 13<sup>th</sup> European Conference on Composite Materials (ECCM-13), Stockholm, Sweden, 2-5 June, 2008.
- [2009-1] Degroote, J., Blommaert, C., Haelterman, R., Van Paepegem, W. and Vierendeels, J. (2009). Partitioned simulation of the impact of a deformable circular cylinder on a water surface. Proceedings of the 3<sup>rd</sup> International Conference on Computational Methods for Coupled Problems in Science and Engineering, Ischia Island, Italy, 8-10 June 2009.
- [2009-2] Blommaert, C., Van Paepegem, W., Dhondt, P., De Backer, G., Degrieck, J., De Rouck, J., Vantorre, M., Van Slycken, J., De Baere, I., De Backer, H., Degroote, J., Vierendeels, J., De Pauw, P., Matthys, S. and Taerwe, L. (2009). Large scale slamming tests on composite buoys for wave energy applications. Proceedings of the 17<sup>th</sup> International Conference on Composite Materials (ICCM-17), Edinburgh, United Kingdom, 27-31 July 2009.

## List of publications

---

### Awards

- [2009-3] JEC PARIS 2009 Innovation Awards, 24/03/2009 – Owens Corning, Spiromatic and Ghent University (Department of Material Science and Engineering)

### Local (in Belgium) media attention

- [2008-1] News paper, *Het Laatste Nieuws*, "Spectaculaire experimenten op de Watersportbaan", 24/10/2008, p 15
- [2008-2] News paper, *Het Nieuwsblad*, "Energie uit golven heeft wel degelijk een toekomst", 24/10/2008, p 29
- [2008-3] News paper, *De Gazet van Antwerpen*, "UGent haalt energie uit golven", 25/10/2008, p 66
- [2008-4] Television Regional News, *AVS*, 23/10/2008
- [2008-5] Television National News, *VRT*, 23/10/2008
- [2008-6] Radio interview, *Radio 2*, "Meisjes en wetenschap", 23/10/2008